Development of a

Novel Intracortical Electrode

For Chronic Neural Recordings

Harbaljit Sohal

Submitted for the degree of

Doctor of Philosophy

July 2013

Institute of Neuroscience

ABSTRACT

Micromotion, attributable to the modulus mismatch between the brain and electrode materials, is a fundamental phenomenon contributing to electrode failure for invasive Brain-Machine Interfaces. Spike recording quality from conventional chronic electrode designs deteriorates over the weeks/months post-implantation, in terms of signal amplitude and single unit stability, due to glial cell activation by sustained mechanical trauma.

Conventional electrode designs consist of a rigid straight shaft and sharp tip, which can augment mechanical trauma sustained due to micromotion.

The sinusoidal probe has been fabricated to reduce micromotion related mechanical trauma. The electrode is microfabricated from flexible materials and has design measures such as a sinusoidal shaft, spheroid tip and a 3D polyimide ball anchor to restrict electrode movement relative to the surrounding brain tissue, thus theoretically minimising micromotion.

The electrode was compared to standard microwire electrodes and was shown to have more stable chronic recordings in terms of SNR and LFP power. A longer chronic recording period was achieved with the sinusoidal probe for the first generation.

Quantitative histology detecting microglia and astrocytes showed reduced neuronal tissue damage especially for the tip region between 6-24 months chronic indwelling period for the sinusoidal probe. This may be linked to the more stable chronic recordings.

This is the first demonstration that electrode designs wholly incorporating micromotion-reducing measures may decrease the magnitude of gliosis, with possible chronic recording longevity enhancement.

ACKNOWLEDGMENTS

I would like to express my sincere gratitude to my supervisors (Prof. Stuart Baker, Dr. Andrew Jackson, and Prof. Anthony O'Neill) for the highly unique opportunities presented to me during this PhD study. Also I would like to thank them for their priceless support with the project and thesis write-up. Their belief in me was instrumental for this project and I can only repay them back by becoming the best possible scientist/engineer.

For microfabrication, I would like to thank Konstantin and Irina for effectively teaching me microfabrication techniques. I would also like to thank Chris for his support during the early stages of my PhD. I would like to particularly thank Konstantin for his continuous and outstanding advice throughout the PhD.

For histology, I would like to thank Dr. Gavin Clowry for his support in protocols and general discussion about histological techniques.

I would like to thank the veterinary (Paul Flecknall, Aurelie Thomas, and Claire Richardson) and surgical (Caroline and Denise) staff for their support before, during and after rabbit surgery. A big thank you to those involved with the daily care for my rabbits, Sue, Michelle and Laura, I know at times this was difficult.

I will take this opportunity to also thank the bunnies that I used for this study. Although their names are merging into a blur, you were all crucial to this study.

In no particular order, I would like to thank my friends and members of the Newcastle Movement lab for their daily interactions, socialising and often, great incite: Cyril, Bonne, Evelyne, Fiona, Michael, Hamid, Ken, Tobias, Lauren, Stephan, Felipe, Ferran, Demitris, Jonas, Katherine, Stevie, Sabine, Claire S, Claire W, Karen, Edina, Jen, Terri, Tom, Ed, Emma, Daniel, Rai and John.

In particular, from my friends and lab, I have to thank: Cyril for providing great friendship and amusement throughout my PhD; Bonne, Ken, Terri, Tobias, Ed, Emma and John for being my public house buddies, providing great conversation/inspiration and banter throughout my time in Newcastle; Lauren and Stephan for being great friends and sharing great times on conferences especially in the States; Claire Schofield for the much needed daily coffee breaks; Felipe for the inspiring engineering debates;

Daniel for entertainment provided in London; Rai for her support during the first half of the project.

For their support throughout the PhD I would like to thank my family: my mother (Surinder), sisters (Nina, Neelam, Seema and Nisha), nephews (Nathan, Arjan and Amrith), nieces (India, Aishani, Shanti and Amrita) and brother-in-laws (Richard, Charlie, Davider, Gary, and Martyn) without them I would only know the world of electrodes: Yes everything should be sinusoidal!!!

Finally I would like to thank and dedicate my PhD thesis to my father, Harbhajan Sohal. Although he is no longer with us today, I want to thank him for always making me believe that no problem is unsolvable as long as you put your mind to it. For this Daddy and for everything you have ever done for me I will always be grateful and I will carry on making you proud.

PUBLICATIONS

Conference abstracts

Sohal et al. (2010). “A Novel Flexible Sinusoidal probe To Enhance Longevity of Chronic Neuronal Recordings”. In: 40th Society for Neuroscience Annual Meeting 2010. 85.8/AAA16. Society for Neuroscience. San Diego, CA.

Sohal et al. (2012). “The sinusoidal probe: Towards increasing chronic recording longevity through decreased micromotion related trauma ”. In: 42nd Society for Neuroscience Annual Meeting 2012.277.17/NN16. Society for Neuroscience. New Orleans, LA.

TABLE OF FIGURES

CONTENTS

Chapter 1: Introduction and Background

1.1 Introduction

In this thesis, a novel flexible microelectrode was microfabricated and tested *in vivo*. Current electrode designs are based on inflexible materials, such as silicon, which fail to accommodate the natural movement of the brain. Their rigid straight shafts combined with their sharp tips fail to accommodate brain movement and damage the finite number of cells that they are record from over chronic (>1 week) time points. This is known as micromotion induced damage (Gilletti and Muthuswamy, 2006). This thesis is divided into 6 chapters and covers the background and motivation, microfabrication, bench testing, *in vivo* chronic testing and ad hoc histology for the newly developed sinusoidal probe. Our flexible probe has three design features to minimise micromotion induced damage from conventional silicon probes: a sinusoidal shaft, a shepherical tip and a polyimide ball anchor. These measures were hypothesised to restrict the movement of the electrode relative to the recording tissue and reduce micromotion induced damage.

Spinal cord damage often leads to partial or complete paralysis. The brain region that corresponds to movement is active, but spiking actvitiy (Hubel, 1959, Hubel and Wiesel, 1959), is not relayed to the muscle through the damaged spinal cord. In invasive brain-machine-interface (BMI), spiking activity can be extracted through electrodes, analysed and decoded (Koyama et al., 2009) to bring about movement (Schwartz, 2004) through an external effector (e.g. robotic arm) (Figure 1.1) or trigger functional stimulation (e.g. in the spinal cord) (Fetz, 1999). Through BMI, a tetraplegic subject moved an artificial limb and changed television channels simply by using brain signals (Hochberg et al., 2006). A limitation in BMI field advancement is the failure of invasive chronic electrodes attributable to device failure and immune activiation (Polikov et al., 2005). Such a limitation is not clinically acceptable due to the long life expenctancy post injury for spinal cord patients. Current short electrode performance times contrast poorly with the long life-times of current devices such as the pacemaker, cochlear implant and deep brain stimulation electrodes (Hatsopoulos and Donoghue, 2009).

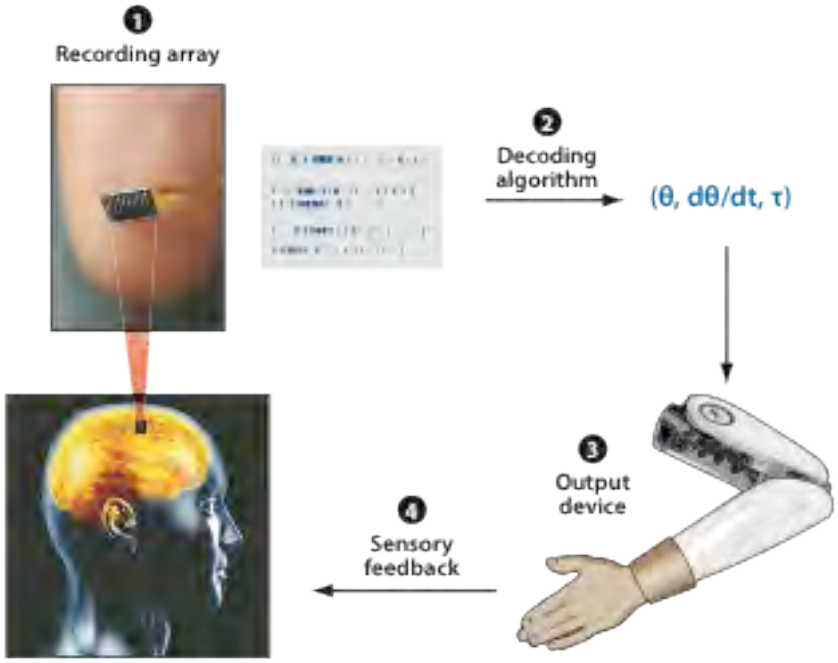

Figure 1.1. The principles behind BMI. Movement signals are captured from the brain with the use of electrodes. Signals are interpreted with an appropriate algorithm and relayed to the output device to produce movement with (closed-loop) or without (open-loop) sensory feedback (image adapted from (Hatsopoulos and Donoghue, 2009)).

In electrode design it is essential to investigate both biological and engineering considerations. This thesis will explore the development of a novel intracortical probe for chronic neuronal recording. Within this thesis, the probe design has been optimised from the orginal design, microfabricated and chronically tested in terms of both neuronal recording and tissue responses over various chronic indwelling periods *in vivo*. All of this was achieved with no prior engineering or microfabrication experience.

As this thesis required knowledge of various scientific and engineering approaches, this chapter will cover: the immune response to electrodes, strategies to reduce the immune response, current chronic electrode designs and material considerations. This review of the literature will then lead to a detailed understanding for the design and microfabrication considerations for the sinusoidal probe.

1.2 Immune response to electrodes: The glial reaction

Activation of the brain's immune system causes electrode failure (Polikov et al., 2005). The chronically implanted electrode is foreign, which the immune system reacts against in a process known as gliosis. This leads to immune protein accumulation resulting in tissue isolation and ensheathing of the recording sites.

Glial cells consist of both microglia and astrocytes. Microglia are involved with the brain's healing response and constitute 10% of the total number of glia. These cells arrive in the brain after a prenatal infilitration of the central nervous system (CNS) by blood-born haematopoetic cells (Santos et al., 2008), and reside in a ramified state until injury activation (Figure 1.3) (Fawcett and Asher, 1999). Astrocytes (Figure 1.3), so called due to their star like appearance, make up 30-65% of glial cells in the CNS. Astrocytes provide growth cues during CNS development, support neuronal circuits by buffering ions and recycle neurotransmitters such as glutamate, provide energy substrates for neurons, control neuronal vasculature, and modulate firing activity of neurons (Leis et al., 2005, Koehler et al., 2006, Giaume et al., 2010, Hamilton and Attwell, 2010).

The general reproducible distribution of glial cells around chronic electrodes (Biran et al., 2005, Polikov et al., 2005, Winslow and Tresco, 2010) is shown in Figure 1.2. Microglia surround the electrode for up to 50-100 μm, an area designated the "kill zone" due to the lack of viable neurons. Surrounding the microglia are astrocytes, which can be seen up to 300 μm from the implant, where the viable neurons can still be found.

Activation cues and subsequent actions are summarised for both microglia and astrocytes in Figures 1.4 and 1.5 respectively. In short, electrode insertion and micromotion causes neuronal tissue irritation. This leads to the slow release of microglia activation cues from neurons such as neurotransmitters (purines:Adenosine Triphosphate (ATP) and Uridine Triphosphate (UTP) and glutamate), chemokines (attractant molecules), matrix metalloproteinase (MMP) and Triggering receptor expressed on myeloid cells 2 (TREM 2; macrophage that engulfs cell debris). Microglia morphologically change from the resting to amoeboid state, leading to increased phagocytosis, chemokine (attracts more microglia and astrocytes), and cytokine release. Nitric oxide is released, oxidating proteins, through the formation of super oxide (Kawano et al., 2007). Damaged neurons and microglia release factors that activate

astrocytes. This leads to increased inflammation, release of neuronal growth inhibitors and general upregulation. Astrocyte proliferation is not beneficial for single unit recordings as they can influence neuronal firing activity, potentially adding noise to the system. Recently, a bi-directional link with astrocytes and neurons has been found where astrocytes can influence neuronal activity (Sasaki et al., 2012).

Astrocytes can confer neuronal protection. Release of anti-inflammatory molecules and growth factors allow remaining viable neurons to survive (Rolls et al., 2009). It is essential that strategies trying to reduce gliosis do not abliterate the astrocytic response due to their supporting role (Giaume et al., 2010).

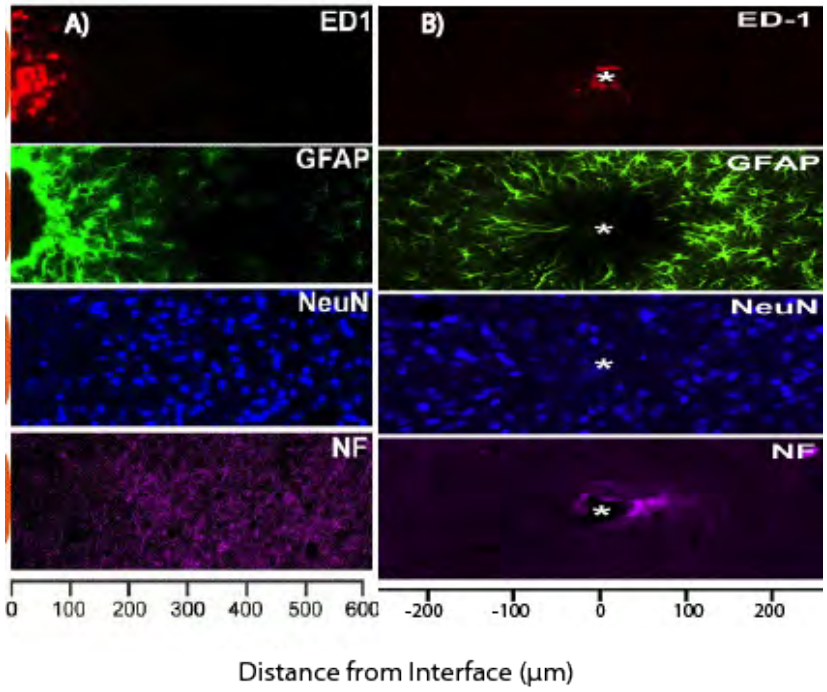

Figure 1.2. The general distribution of glial cells relative to the electrode implant. This relative distribution is highly reproducible and independent of the electrode type. Images are obtained by tagging cell specific proteins ("markers") via primary antibodies. Secondary antibodies, carrying a fluorescent marker can then attach to the primary antibody, allowing cell visualization under a fluorescent microscope. ED1- microglia/macrophage marker. GFAP- astrocyte marker. NeuN- neuron marker. NF- neurofilament marker. A) The distribution of gliosis mediators and neurons around a conventional single shank silicon probe. The orange line at zero indicates the implantation site (Biran et al., 2005) B) The distribution of gliosis mediators and neurons around a microwire electrode. The star at zero distance indicates the implantation site (Winslow and Tresco, 2010). Generally, a microglial reaction is found at 0-50 µm and an astrocytic response at 100-300 µm. Interestingly the viable neurons seem to be confined to an area of the astrocytic reaction. The lack of viable neuron confinment to the area of high microglia expression is known as th "kill zone" in the literature.

Although microglia and astrocytes contribute to electrode failure, recent studies have elucidated other failure mechanisms. In studies using rats, neuronal function was compromised by blood brain barrier degeneration and local demylination, with implantation of microwire and planar silicon microarrays for a 12 week indwelling period (Winslow et al., 2010b, Winslow and Tresco, 2010). Blood-brain-barrier functionality is vital to maintain the homeostatic environment around neurons, as is myelin for optimal neuronal conduction.

Lind and colleagues found that an electrode in the middle of a row of implants was surrounded by a smaller astrocytic scar than single implants within the same hemisphere. Also, a large number of implants did not aggrevate the tissue reaction, allowing for the implatantion of multiple electrodes within the same hemisphere (Lind et al., 2012).

Good surgical technique is required to reduce the glial response. In an elegant study, Kipke and colleagues showed the damage caused by targetting surface blood vessels with electrode implants by using two photon microscopy. Destroying surface vasculature often leads to sub-surface vasculature damage creating decreased tissue perfusion around the area where the electrode tip would reside. Further, blood proteins such as albumin are released and attach to the electrode; a known potent microglial activator (Kozai et al., 2010c). Both would increase the likelihood of neuronal damage and subsequent electrode failure. Reducing vasculature damage during surgery is vital. Interestingly, Kruger (2010) showed that electrode longeivity can be increased by avoiding classical insertion through the dura, and confining implantation through white matter in a monkey, leaving the recording area intact. Multi-unit activity was recorded for seven years using such an approach; limiting surface vasculature and recording area damage during surgery is optimal (Kruger et al., 2010).

A)

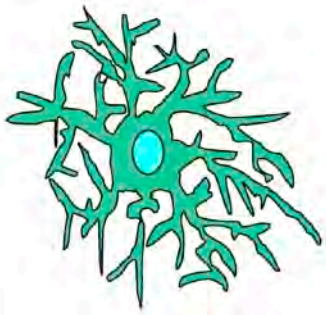

Resting or Ramified Microglia

- No Fc receptors, no macrophage specific receptors
- Large, dense chromatin masses in small flattened nucleus
- 5-10% of glial population
- Many long, thin processes

Activated or Amoeboid Microglia

- Upregulation of lytic enzymes
- Retraction of cytoplasmic processes to stouter, thicker pseudopodia
- Accumulation of phagocytosed material and lipid droplets
- Ameboid and motile abilities
- Release of inflammatory factors MHC I, II expression
- Active Proliferation

B)

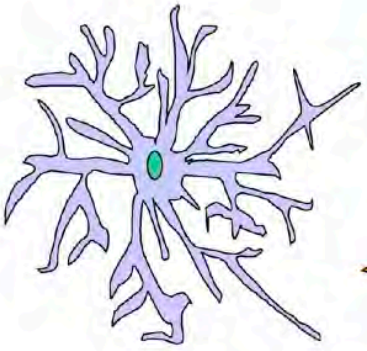

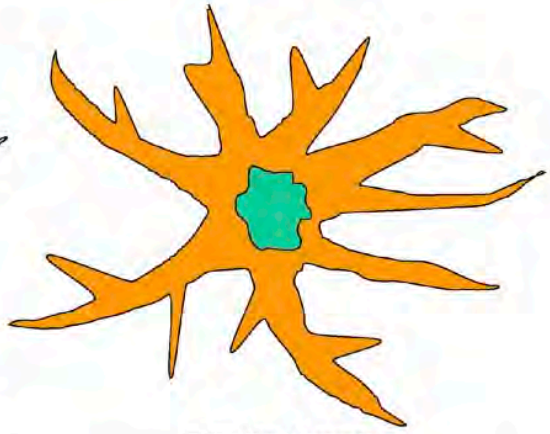

Normal Astrocyte

- 8-10 nm diameter GFAP filaments
- Round nucleus
- 10-40 nm glycogen particles
- Large mitochondria
- Gap junctions with other astrocytes
- Maintain proper neuronal environment
- 30-65% of glial population

Reactive Astrocyte

- Large increase in GFAP filaments, glycogen deposits
- Irregular nucleus
- Increase in mitochondria and multiple Golgi complexes
- Hypertrophy
- Phagocytosis
- Proliferation
- Migration
- Extracellular matrix production
- Production of neurotrophic and inflammatory factors

Figure 1.3. The morphological changes and resulting effects from the activation of both microglia (A) and astrocytes (B) from resting to reactive states. Image adapted from (Polikov et al., 2005).

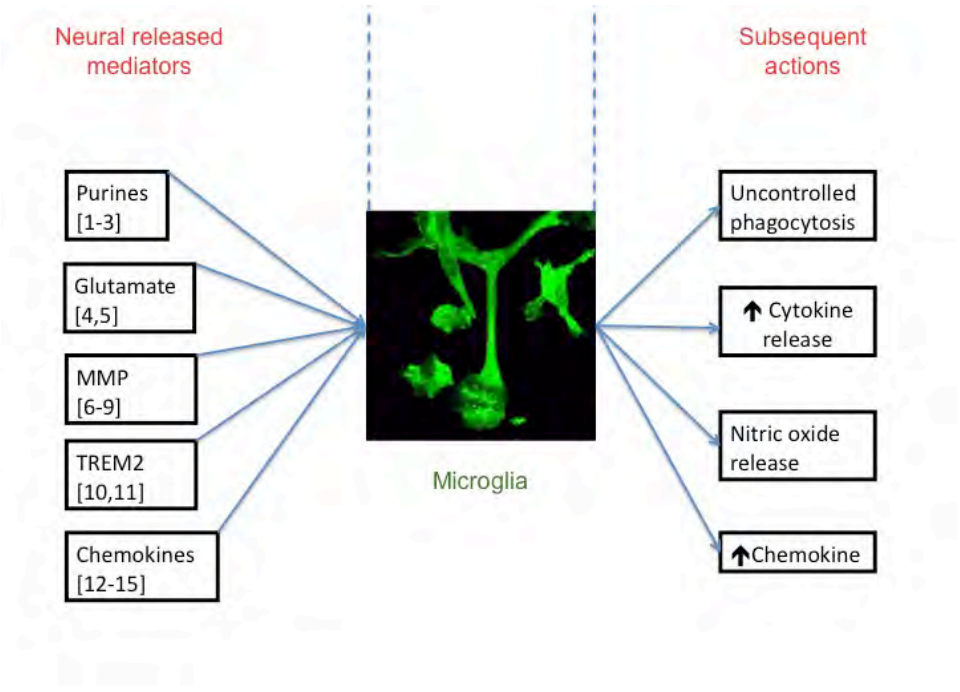

Figure 1.4. The actions of neuronal mediators released from damaged neurons. Chemokines are generally involved in attracting other glial cells to the site of injury. MMP= Matrix Metalloproteinase. TREM2= triggering receptor expressed on myeloid cells 2. The following numbers relate to those in the Figure: 1.(Wang et al., 2004) 2. (Inoue, 2007, Koizumi et al., 2007)3.(Inoue, 2007) 4.(Liu et al., 2009) 5.(Pocock and Kettenmann, 2007)6. (Choi et al., 2010)7.(Woo et al., 2008)9.(Yong et al., 2007) 10.(Stefano et al., 2009) 11. (Takahashi et al., 2005)12.(Limatola et al., 2005) 13.(de Jong et al., 2005)14. (Abbadie et al., 2009) 15. (Biber et al., 2008)

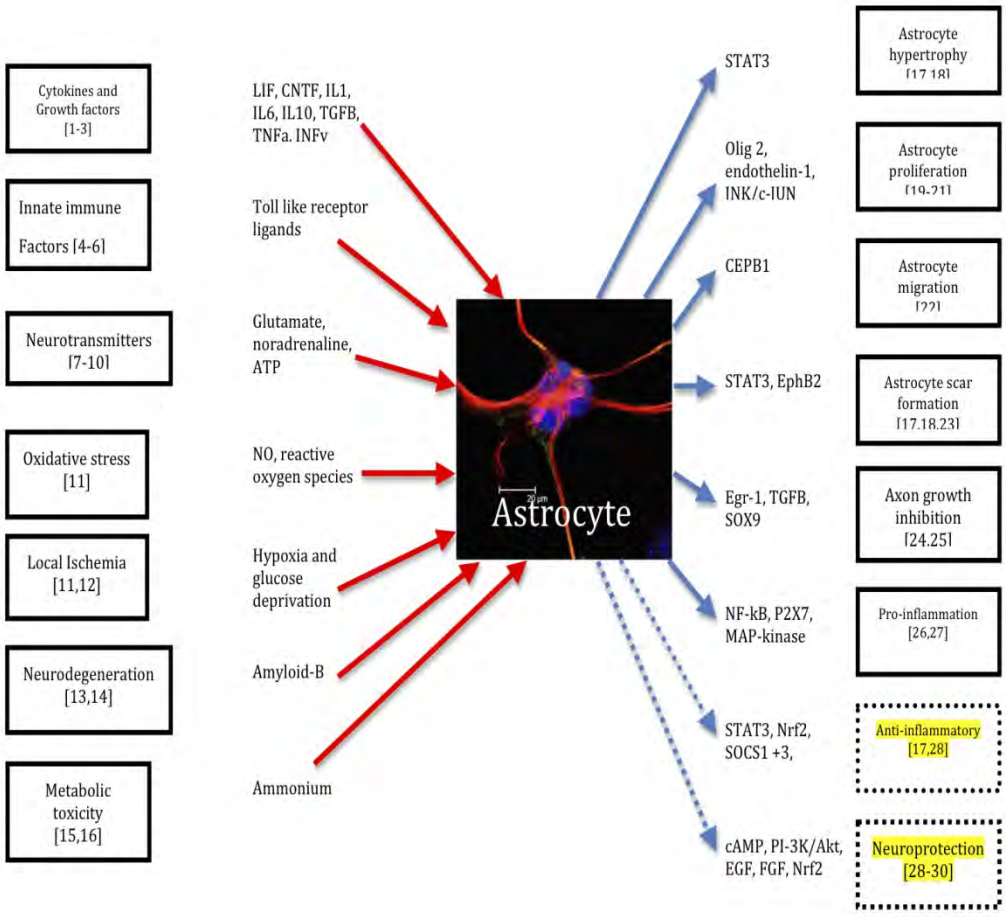

Figure 1.5. The actions of neuronal/microglial mediators on astrocytes. Although astrocytes can inhibit neuronal axon growth, they can convey anti-inflammation and neuroprotection. Understanding the complexities of the reaction is vital to design biological strategies to attenuate the glial response. An attractive proposition to attenuate the astrocytic response may be found in Nrf2 upregulation. The following numbers relate to those in the Figure: 1.(John et al., 2003) 2.(John et al., 2005)3. (Di Giorgio et al., 2007) 4.(Mallard et al., 2009) 5.(Khuda et al., 2009) 6.(Farina et al., 2007) 7.(Reyes-Haro et al., 2010) 8.(Giaume et al., 2010)9.(Bekar et al., 2008)10.(Neary et al., 2005) 11.(Takano et al., 2009) 12.(Cao et al., 2010) 13.(Allaman et al., 2010) 14.(Simpson et al., 2008) 15.(Pichili et al., 2007) 16. (Rao et al., 2005) 17.(Lee et al., 2010) 18. (Herrmann et al., 2008) 19.(Chen et al., 2008) 20.(Murphy et al., 2010) 21.(Gadea et al., 2008) 22.(Jones et al., 2008) 23.(Conover et al., 2000) 24.(Beck et al., 2008) 25.(Gris et al., 2007) 26.(Brambilla et al., 2009) 27.(Sun, 2010) 28. (Calkins et al., 2010) 28.(Li et al., 2006) 29. (Figiel et al., 2003). LIF= leukemia inhibitory factor, CNTF= ciliary neurotrophic factor, IL-1= Interleukin-1, IL-6= Interleukin-6, IL-10= Interleukin-10, TGF-ß-transforming growth factor, beta, TNF-α= Tumour necrosis factor-alpa; INFγ= Interferon-gamma; ATP= Adenosine tri-phosphate; NO= Nitrous Oxide; STAT3= signal-transducer and activator of transcription protein-3; Olig2= oligodendrocyte transcription factor 2; JNK/C-JUN= c-Jun N-terminal kinases; EphB2= Eph receptor B2; EGR-1= early growth response protein 1; SOX-9= SRY (sex determining region Y)-box 9; NF-κB= nuclear factor of kappa light polypeptide gene enhancer in B-cells; P2X7- purinergic receptor P2X, ligand-gated ion channel, 7; map-kinase= mitogen-activated protein kinase; Nrf2= nuclear respiratory factor-2; SOCS1 = suppressor of cytokine signaling 1; SOCS 3= suppressor of cytokine signaling 3; cAMP= cyclic adenosine monophosphate; PI-3K/AKt= phosphoinositide-3-kinase/ serine/threonine protein kinase Akt; EGF= epidermal growth factor; FGF= fibroblast growth factor.

1.2.1 Biological strategies to reduce the extent of the glial reaction

It is contentious whether a fast or slow insertion speed during electrode insertion reduces initial gliosis. Nicolelis and colleagues used a slow insertion for their microwire electrodes (Nicolelis et al., 2003), although Edell and colleagues believe this causes prolonged irritation and damage using a standard silicon probe (Edell et al., 1992). As electrodes are inserted, it severs vasculature, extracellular matrix, and neuronal and glial cell processes. In a landmark study, Bjornsson and colleagues showed that silicon electrodes with a sharp tip and fast insertion gave reduced electrode displacement from the intended implant site, rupture and severing of blood vessels and decreased dragging of blood vessels and neuronal tissue (Bjornsson et al., 2006). This suggested that fast insertion was to be preferred.

Another study showed that different silicon electrode tip geometries (Figure 1.6) cannot reduce gliosis (Szarowski et al., 2003).

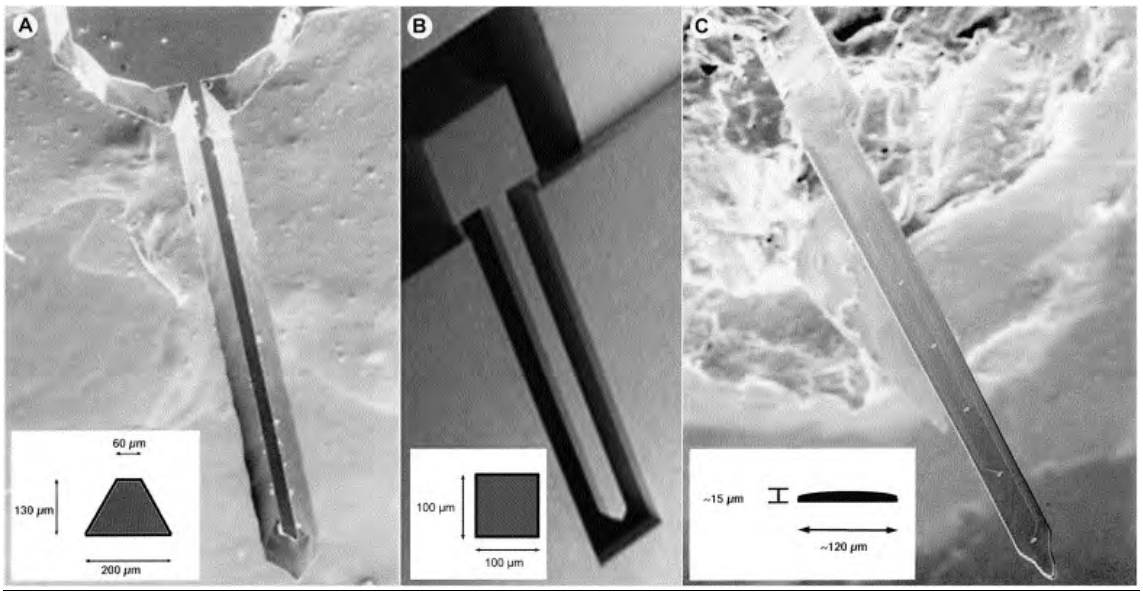

Figure 1.6. Different silicon electrode geometries (A-C) cannot attenuate gliosis. The corresponding pictographs at the bottom show tip view geometries of the individual silicon probe used with corresponding dimensions (Szarowski et al., 2003).

Device fixation method and implant size can influence the magnitude of the tissue response around electrodes (Figure 1.7). In a recent study, Thelin and colleagues showed over a 6 and 12-week indwelling period that small diameter (50 µm) implants elicited smaller tissue responses compared to large diameter (200 µm). In addition fixing the electrode to the skull caused a larger tissue response, due to enhanced

micromotion (Thelin et al., 2011). This corroborates the findings of earlier studies (Biran et al., 2007). Therefore smaller diameter, freely floating devices are preferred.

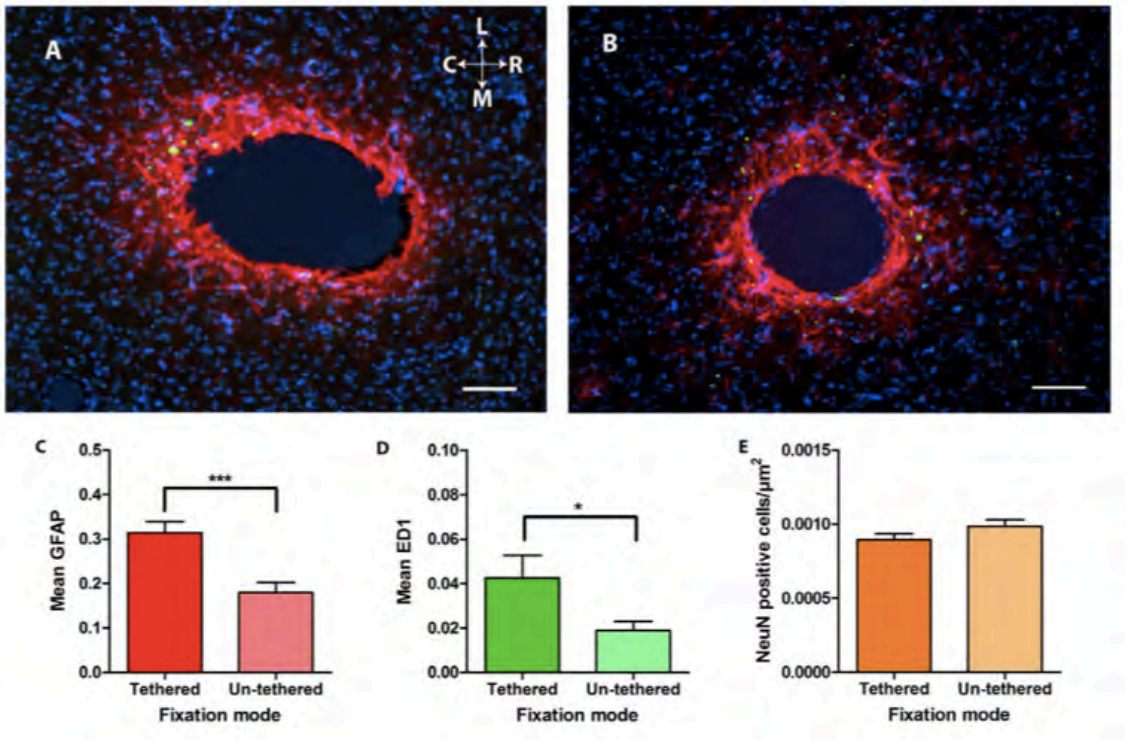

Figure 1.7. The glial response to tethered (A) and untethered (B) implant over a 12 week period. A reduced astrocytic (C) and microglial (D) response is observed (Thelin et al., 2011). * = p <0.05. *** = p<0.001. GFAP (Red), ED1 (green), DAPI counterstain (blue). Scale bar is 100 μm.

Local and systemic drugs have been used to reduce gliosis. The most promising systemic drug, dexamethasone (corticosteroid), reduces the initial astrocytic reaction; a 6 day treatment regimen with 200 μg/kg, was more effective than a single injection (Spataro et al., 2005). Similarly, reduced gliosis resulted with dexamethasone seeded neuronal probes (Kim and Martin, 2006).

Local drugs can be infused using hydrogels (Nisbet et al., 2008) or microfluidics. The latter comprises of fluid channel incorporation into the electrode for drug delivery (Retterer et al., 2004, Rohatgi et al., 2009). Through microfluidics, Rohatgi and colleagues altered neuronal activity with a constant infusion of tetrodotoxin (Rohatgi et al., 2009). A microfluidic approach delivers drugs effectively and thereby could potentially mediate the glial response. However, microfluidics is expensive, complex and the inclusion of a fluidic channel acts as another source for infection with no contingency plans for channel blockage.

Neural stem cells have been proposed to attenuate gliosis. Purcell and colleagues fabricated a parylene-C device, seeded with embryonic day 14 neuronal stem cells within an alginate hydrogel. Neuronal loss and glial encapsulation was mitigated during the initial week but exacerbated 6-week post implant. This failure was attributed to neuronal stem cell death and scaffold degradation (Purcell et al., 2009a, Purcell et al., 2009b). However, embryonic day 14 neuronal stem cells contain a mixture of both neuronal progenitor and glial progenitor cells (Rietze and Reynolds, 2006). An electrode is foreign, the extracellular environment surrounding the electrode would be rich with gliosis mediators which therefore could make neural stem cells differentiate into a glial fate; a potential source of glia.

A similar study used neuronal progenitor seeded probes, showing attenuation in initial gliosis. However, this study did not investigate the chronic response, although testing is in progress (Azemi, 2010). Such a strategy may yield future success.

Purcell and colleagues hypothesised that microglial and astrocytic proliferation could be minimised with the introduction of a cell cycle inhibitor, flavopiridol, at the implant site. Mature neurons do not divide and proliferate. Flavopiridol was shown to reduce cyclin D1 in microglia surrounding probes at a 3-day time point. *In vivo* impedance was reduced, although this did not improve signal-to-noise ratio or unit detection rate compared to controls (Purcell et al., 2009c). The authors do argue that such a method could be used to lower stimulation thresholds for devices; an improvement in recording quality may have resulted over a longer recording period.

In short, gliosis can be acutely attenuated with a fast insertion technique and dexamethasone. For the chronic glial reaction hydrogels, like laminin-1 (He et al., 2006, Nisbet et al., 2008), have shown promise in increasing electrode recording longevity.

1.3 Engineering

1.3.1 Electrode characterisation

Recording electrodes are characterised by impedance at 1 kHz, signal-to-noise of electrophysiological recordings and post-hoc histology. Impedance rise indicates a decrease in the surface area for recording. Signal to noise ratio can be calculated to determine the electrode efficiency to capture spiking activity over noise; the primary measure to determine the usefulness of chronic electrodes (Rousche and Normann, 1998, Williams et al., 1999, Suner et al., 2005).

1.3.2 Current popular electrodes used for neuronal recordings

1.3.2.1 Utah array

Utah array (Rousche and Normann, 1998) fabrication starts with a micromachined and acid etched silicon substrate which forms the basic structure (Figure 1.8). This comprises 100 needles (1 mm length), surrounded by a glass dielectric, arranged in a 10 x 10 configuration. Prior to the metallisation of the electrode tips, the silicon needles are boron doped to enhance their electrical properties (Campbell et al., 1991). The needle tips are converted into electrodes with the application of a four-part multilayer of platinum, titanium, tungsten and platinum on the first 50-100 μm of the tips. The unmetalised silicon electrode shafts are insulated with a 2-3 μm layer of polyimide (Rousche and Normann, 1998) or parylene-C (Suner et al., 2005). A bondpad consisting of the same metal as the electrode tip is deposited onto the backside of each electrode, and a Pt-Ir wire is soldered to the bondpad and miniature connector. One wire is used as a reference electrode.

Utah array chronic recording capabilities have been assessed in cats and monkeys. In cats, an 11 electrode-array was implanted into the cerebral cortex for over 2-13 months, with single and multi-unit activity measured. After 6 months, 6 out of 11 electrodes gave activity, although by 13 months this was reduced to only 2 out of 11 electrodes. 4 out of 11 electrodes were damaged during insertion, a characteristic of most electrode designs (Rousche and Normann, 1998). In monkeys, reliable recordings were achieved over a 569-day period post implant, with a good mean SNR of 4.8 for electrodes implanted into the primary motor cortex. A recording period of 1264 days post-implant

was achieved in another subset of monkeys (Suner et al., 2005). The SNR measurement from Suner and colleagues has been used consistently throughout the electrode literature (Ward et al., 2009). For the signal for a specific isolated spike, the peak-to-peak amplitude (A) of the mean waveform was calculated. For the noise, the mean waveform is subtracted from all waveforms, with the standard deviation calculated from the resulting values. Noise is then calculated as 2 x the average standard deviation (ε). SNR was then calculated as A/ ε. From this study a good (SNR= 11.2), fair (SNR=3.2), poor/noise (SNR≤ 1.4) SNR values from specific waveforms have been calculated (Figure 1.8C).

The Utah array has Food and Drug administration (FDA)-approval in the United States for human use. In a landmark paper, a patient implanted with the device could control a robotic hand and control a television (Hochberg et al., 2006). The same group also showed that a robotic arm can be successfully manipulated to reach and grasp a flask using neuronal signals from a tetraplegic subject, with this implanted array (Hochberg et al., 2012).

A recent study shows that after a 1000 day implant period in a tetraplegic, meaningful data from the electrodes can be captured to allow repeatable, accurate point and click control of a computer device (Simeral et al., 2011).

The recent iteration of the Utah array has resulted in the creation of the wireless and non-wireless Utah Slant Array. This array has electrode needles at varying lengths (0.5, 1, 1.5 mm) to allow brain recordings, simultaneously from different cortical layers (Branner et al., 1999, Sharma et al., 2010, Sharma et al., 2011). Although chronic *in vivo* recording data is lacking, the array has been shown to withstand 150 days of PBS soaking at 37^{o}C (Sharma et al., 2010).

An advantage of the array is the high channel count. A limitation for the Utah array is the failure to penetrate deep brain structures owing to the short (~ 1 mm) electrode shaft length. Similarly, the array cannot sample neuronal activity at various locations in the direction normal to the cortical surface (Nordhausen et al., 1994). However, multi depth recording is now possible with the Utah Slant Array (Figure 18B). The array has a fixed geometry, the whole device has to be implanted and individual electrodes cannot be manipulated to avoid surface vasculature, avoidance of which is vital as it may lead to reduced tissue perfusion at the potential recording area (Kozai et al., 2010c). Also the

pneumatic insertion method could cause additional brain trauma as high pressures are used for insertion (Rousche and Normann, 1990).

The interconnect cabling has been shown to be problematic. Early studies showed cable damage, although the authors argue this was due to the use of insulated gold wires (Nordhausen et al., 1993). Suner and colleagues reported repeated damage to the array relating to interconnect cable failure with the modern insulated platinum/iridium wiring in monkeys (Suner et al., 2005), although this might be confined to behaviour related issues in the animals, such as tugging on wires and excessive head movement.

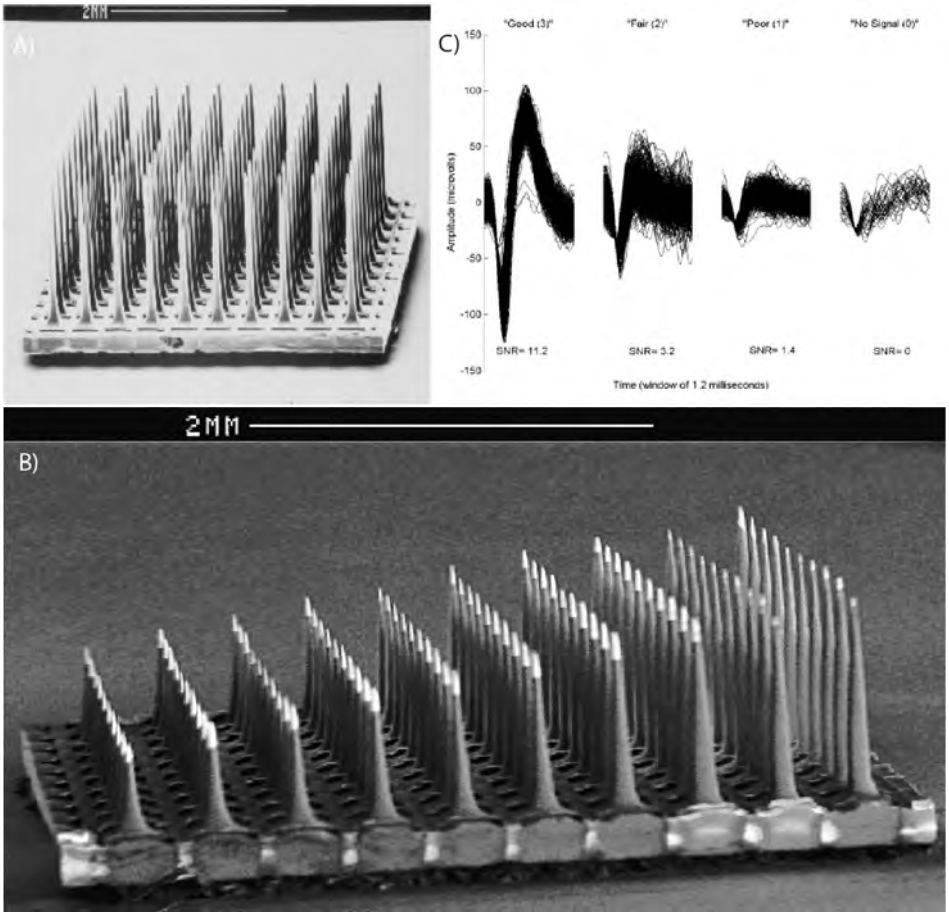

Figure 1.8. The Utah (A) and Utah slant array (B) array consists of a substrate material of boron doped silicon with parylene-C insulation, with platinum recording sites. Images show the array without interconnect cabling. (C) Clasification of single-unit waveforms corresponding to SNR values from Suner and Colleagues. For the signal for a specific isolated spike, the peak-to-peak amplitude (a) of the mean waveform was calculated. For the noise, the mean waveform is subtracted from all waveforms, with the standard deviation calculated from the resulting values. Noise is then calculated as 2 x the average standard deviation (ε). SNR was then calculated as a/ ε (Suner et al., 2005).

1.3.2.2 Michigan probe

Michigan probe (Figure 1.9) fabrication begins with selective boron diffusion into a silicon wafer to define the shape and thickness of the device. Next, the lower dielectric layer (silicon dioxide and nitride) is deposited using chemical vapour deposition. Conductive interconnect material, polysilicon is deposited, patterned and insulated with the same lower layer dielectric. Metal is deposited to form the electrode sites (iridium) and bond pads (gold) using lift off technology. Next, the undoped silicon is chemically etched away. Dielectrics in the recording site area are removed using a dry etch to re-open the recording sites (Hetke et al., 1994, Kipke et al., 2003).

Chronic recording capabilities have been assessed in two studies using the rat motor cortex. In the first study, spiking activity could be found for 18 weeks, with 13 out of 14 implanted probes remaining functional throughout the assessment period. The authors report that histological evidence from tissue surrounding the probe indicated the development of a stable interface sufficient for sustained electrical contact (Kipke et al., 2003), although a longer implant period would have been better evidence of this. In the second study 5/6 of the implants recorded activity for more than six weeks, with four implants remaining functional for more than 28 weeks (Vetter et al., 2004). In both studies the chronic recording extremities (18 and 28 weeks) is too short for the electrode to be clinically viable.

An advantage of this array is the staggered recording sites allow multi-depth cortical recordings within the same electrode shank. Neuronal signals are captured normal to the cortical surface, allowing for multi-depth recording and allowing researchers investigate the interactions between different layers in the cortex (Vandecasteele et al., 2012). However, a limitation for the probe is the complexities in creating a three-dimensional electrode array (Nordhausen et al., 1994), as additional assembly is required to create the array platform (Hoogerwerf and Wise, 1991, 1994) .

Figure 1.9. The Michigan probe electrode consists of a substrate material of silicon with silicon dioxide/nitride insulation with 16 iridium-recording sites linearly arranged on the end of four shanks to allow for recordings from different layers of specific brain regions. Shank length= 3 mm. Probe thickness= 15 µm. Site area= 1250 μm^2 (Ward et al., 2009). Recently, it is possible to obtain customised probes from the michigan probe spin-off company (NeuroNexus,USA), where multi-depth recording sites can be arranged in a circular format to allow for better isolation of neuronal activity (www.neuronexus.com). Further, customisable probes are now available with up to 128 recording sites.

1.3.2.3 Microwire arrays

A microwire (Figure 1.10) consists of a blunt metal wire (diameter 20-100 µm) with a non-cytotoxic insulator. Nicolelis and colleagues implanted 96-704 teflon coated stainless steel microwires per monkey in up to five cortical areas. After 18 months, at least 58 neurons could be isolated from one subject (Nicolelis et al., 2003). A higher yield of neurons might have been expected over an 18-month period. Kruger (2010) showed that it is possible to record multi-unit activity from neurons after a 7-year microwire implant (Kruger et al., 2010). However, the highly invasive surgical procedure, confining microwire implantation through white matter from brain underside to reach the motor cortices is unlikely to be adopted by research groups.

Microwires can be moved post-implant. In a study by Jackson and Fetz, microwires were adjusted to maintain large-amplitude action potential recordings for over 184 days from the monkey cortex (Jackson and Fetz, 2007). Such a strategy is advantageous over

other electrode types, which cannot be moved easily whilst inserted. A disadvantage of microwires is their inability to access deep brain structures due to bending and deviation during insertion (Edell et al., 1992), although this accessibility is less problematic than the Utah array electrode due to their short shank lengths.

Microwires can also be combined into a bundle of four to produce a tetrode. This allows for better unit isolation and with the use of linear correlation algorithms, the SNR obtained can be enhanced. However, this is dependent on the same cells or activity being recorded across > 2 microwire recording sites (Gray et al., 1995).

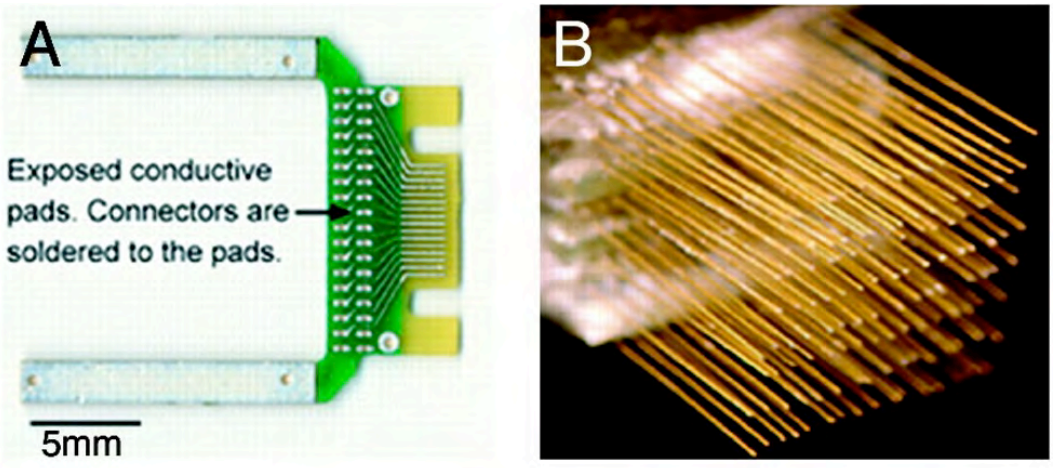

Figure 1.10. Microwire consists of a conducting wire surrounded by a non-cytotoxic insulator e.g. tungsten and Teflon coated. A) The connector used in Nicolelis' chronic implant experiment which were stacked up with attached microwire to form high density arrays (B) (Nicolelis et al., 2003). By using such an array, neuronal activity was recorded over 18 months.

1.3.2.4 Cone/Neurotrophic electrode

The first cone electrode (Figure 1.11) consisted of an insulated gold wire fixed inside a hollow glass cone, with a piece of sciatic nerve placed in the glass cone pre-implant into the rat cortex. Cortical neurites were able to grow into the cone from surrounding neurons allowing single and multi- unit recording for many months (Kennedy, 1989). In follow up experiments, cone electrodes containing sciatic nerve or neurotrophic medium were implanted into the cerebral cortex of rat and monkeys with spiking data recorded 15 months post implant (Kennedy et al., 1992).

The modern day electrode is of the neurotrophic variety due to the ethical problems using sciatic nerve in humans. The electrode contains four wires inside its tip and has a smaller connector. These electrodes have been implanted into the human motor speech cortex with signals obtained for over 4 years in two subjects (Bartels et al., 2008). The cone electrode is not the industry standard due to the commercialisation of the more "popular" electrodes and the low channel count, even though it was the first electrode implant in the human brain (Kennedy and Bakay, 1998).

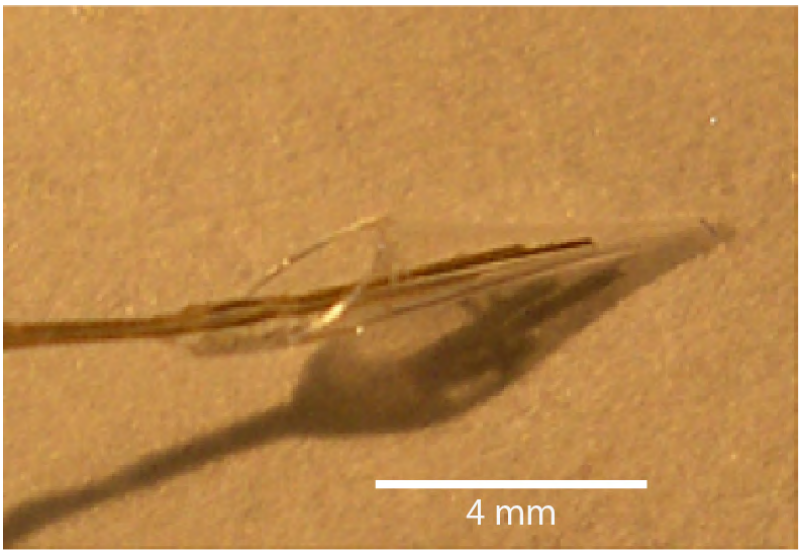

Figure 1.11. The cone/neurotropic electrode. The glass tip contains insulated gold wires for recording the activity of the myelinated neurites that grow into the tip. Neuronal signals inside the tip are electrically insulated from surrounding neuronal activity by the glass. The most recent version of the electrode has four wires inside its tip to maximize the number of discriminable signals recorded from ingrown neurites, and has a miniature connector. Flexible coiled, insulated gold wires connect to electronics on the skull that remain subcutaneous.

1.3.2.5 Moxon Ceramic probe

The ceramic-based multisite electrode array (Figure 1.12) has four separated recording sites patterned onto the length of a ceramic shaft, the size of a microwire electrode, similar in design to the Michigan probe. The authors argue that this electrode is superior as ceramic is more rigid than silicon, thus allowing easier insertion, although this rigidity may lead to enhanced micromotion related tissue damage (Polikov et al., 2005). The electrode only lasted 8 weeks, with a two-fold decrease in SNR three weeks post

insertion in Long Evan rats (Moxon et al., 2004), which could be attributable to the probe stiffness.

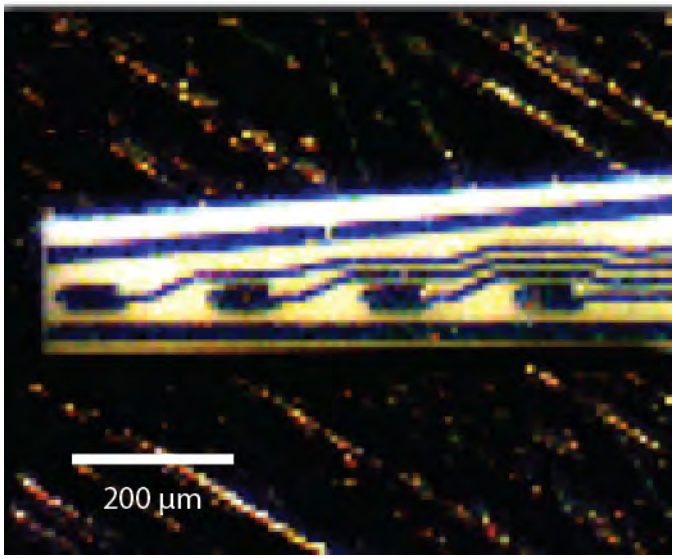

Figure 1.12. The ceramic array has a substrate material of ceramic with 4 chromium and platinum recording sites linearly arranged on 4 shanks. Image is shown of the recording end. Shank length= 7 mm, probe thickness= 44 µm and site area= 1760 µm^2 (Moxon et al., 2004). The array was fabricated to allow better penetration through the dura, with a stiffer material than silicon (ceramic).

1.3.2.6 Flexible Arrays

Flexible array design stems from the idea that current electrodes fail by causing a heightened tissue response due to mechanical mismatch between the brain and electrode material, known as micromotion (Gilletti and Muthuswamy, 2006). The brain is constantly deforming and moving due to being buoyant in cerebrospinal fluid. The theoretical modulus of elasticity for the brain is in the order of 5-30 kPa (Miller et al., 2000) , whereas current silicon devices have a modulus of around 150 GPa.

Current flexible electrodes are centred on the use of polymers such as parylene-C (Young's modulus: 2.86 GPa), polyimide (~2.3 GPa), polydimethylsiloxane (360-870 KPa) or SU-8 (4.02 GPa) with a suitable metal for recording, although chronic recording data is lacking. A microelectrode array for measuring evoked potentials in the central nervous system showed electrode failure after 16 days using a combination of two polyimides (PI-2525 and PI-2771) (Myllymaa et al., 2009).

To further minimise electrode movement relative to the recording tissue, such electrodes can incorporate anchoring features. Kohler and colleagues (2009) have an electrode with such features, where angular spikes anchor the electrode in place (Kohler et al., 2009, Ejserholm et al., 2011). Similarly, Fan and colleagues (2011) have developed a fish-bone electrode, where a spear like structure anchors the electrode in place (Fan et al., 2011). For both designs (Figure 1.13), chronic recording and histological data is lacking. The latter may be attributable to the issues with removing the devices prior to brain slicing or trying to cut through the devices. Spikes to anchor the device may cause an augmented tissue response and electrode failures, as the recording sites are located at the anchoring sites for both electrode designs.

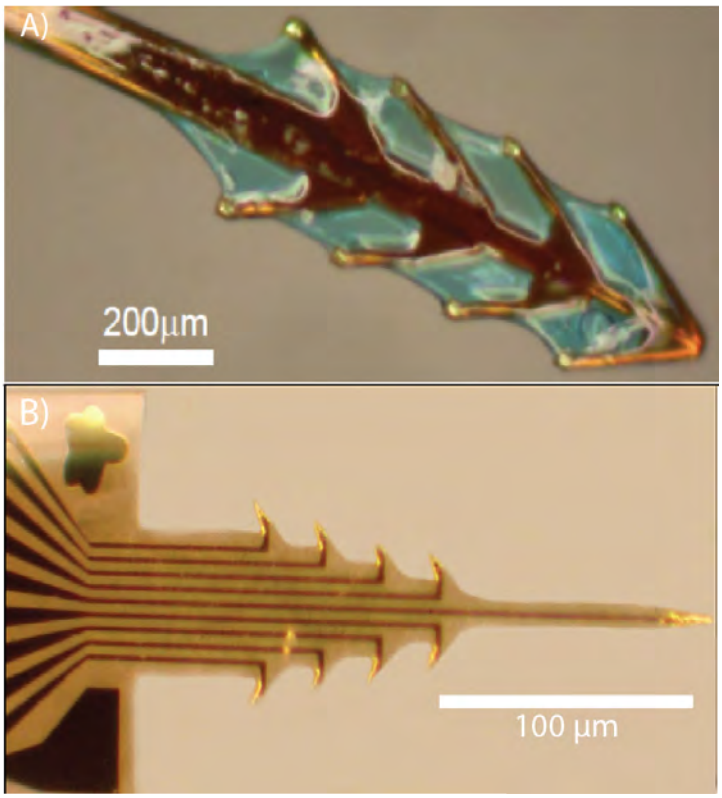

Figure 1.13. The Fish-bone electrode (Fan et al., 2011) (A) and Christmas tree like electrode (Ejserholm et al., 2011) (B). Both of these electrodes are polymeric and have angular sharp anchoring features to restrict the movement of the recording sites relative to the tissue. Such features may irritate the tissue.

Flexible arrays require specialised brain insertion techniques, due to their inability to penetrate through the dura, and potential deviation away from the intended recording regions. Such insertion techniques are based on either attaching the flexible electrode to an insertion device, which can later be removed or by temporarily increasing probe

stiffness to allow for successful device insertion. Kozai and Kipke used an electronegative, self-assemble monolayer coated insertion shuttle, based on the Michigan probe to insert their flexible polyimide and PDMS devices (Figure 1.14). Ethanol was used to temporarily adhere the flexible devices to the silicon insertion shuttles, which were removed after insertion (Kozai and Kipke, 2009). Fan and colleagues (2011), temporarily strengthened their polyimide based, fish-bone electrode with the use of a biodegradable silk polymer to provide mechanical stiffness during insertion (Fan et al., 2011). Similarly, gelatin/glycerol has been used to successfully implant and preserve nanowires in the brain (Witteveen et al., 2010). Stieglitz and colleagues used molten sucrose to temporarily strengthen their arrays prior to insertion (Hassler et al., 2011).

Another strategy is the use of polyethylene glycol (PEG). PEG can be used to strengthen electrodes prior to insertion and "washes" off with saline in a matter of minutes. Using this technique, strengthened polyimide based probes, were successfully inserted into the brain with electrode impedance values returning back to pre-PEG applications levels (Takeuchi et al., 2004).

Recently, smart materials have been developed that can change their modulus depending on temperature. A nanocomposite consisting of poly(vinyl acetate) and tunicate whiskers has been shown to decrease its tensile storage modulus from 5 GPa to 12 MPa within 15 minutes (Capadona et al., 2008). This nanocomposite can be incorporated into microfabrication to provide device stiffness upon insertion, with a Young's modulus change from 3420 (dry) to 20 (wet) MPa, for parylene-C insulated, Titanium/gold electrodes (Harris et al., 2011b).

Each insertion method has limitations. To strengthen the electrode temporarily, devices still have to remain sharp for successful penetration. A sharp tip will still cause damage to the surrounding brain tissue, regardless of device flexibility, due to the modulus mismatch. Related, insertion shuttle fabrication can become another additional microfabrication cost.

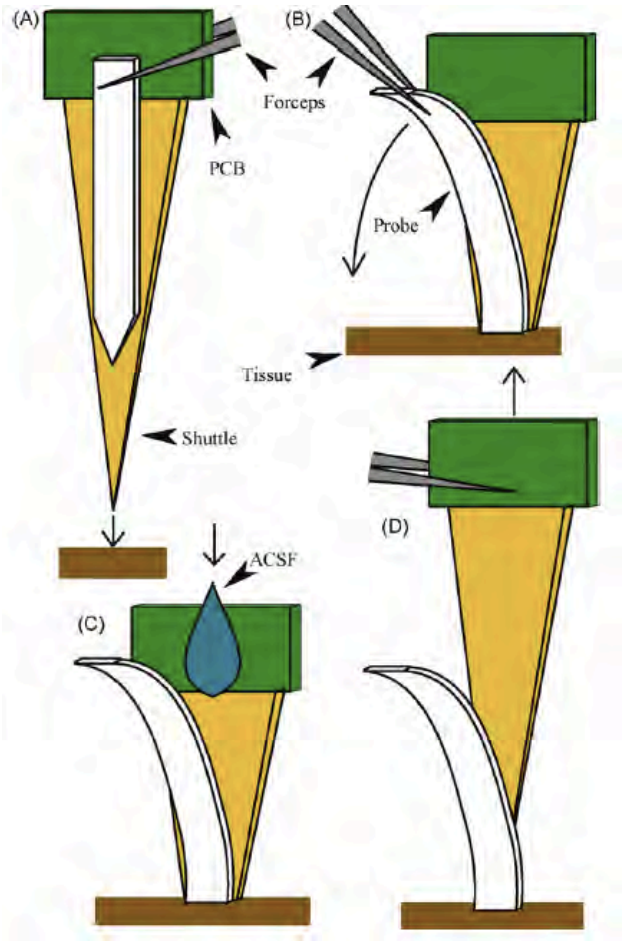

Figure 1.14. The sequential steps (a-d) for inserting flexible devices with a modified Michigan probe coated with a self-assemble monolayer (Kozai and Kipke, 2009). An electronegative, self-assemble monolayer coated insertion shuttle, based on the Michigan probe is used to insert their flexible polyimide and PDMS devices. ACSF= artificial cerebrospinal fluid. PCB= printed circuit board.

1.3.2.7 Wireless arrays

Wireless arrays could minimise tethering forces associated with ribbon cable shearing forces, however they also need to be effectively powered. Kim and colleagues believe that such designs would minimise the inherent infection risk due to transcutaneous wired connections, signal contamination from forcing signal through wired connections and minimise tethering forces associated with micromotion (Kim et al., 2009). Untethered devices reduce the tissue response to electrodes over a 6 and 12-week indwelling period in rats (Biran et al., 2007, Thelin et al., 2011).

The wireless Utah array (Figure 1.15) has been designed and tested. Devices need to be powered and will dissipate heat into the brain. A temperature rise by more than 1^{o}C can have lasting effects on brain tissue (LaManna et al., 1989). Kim and colleagues show

that temperature increases at a rate of 0.029 ^{o}C/mW with the use of finite element analysis and *in vivo* testing. This equates to a temperature increase of 0.38 ^{o}C for a power dissipation of 13 mW through the Utah array, which is the maximum expected power dissipation for the integrated internal circuit (Kim et al., 2006, Kim et al., 2007).

Similarly, the circuit board needs to be encapsulated, and with Parylene-C use, there was no change in the integrity of the device with a 150-day, saline soak period for the array (Sharma et al., 2010, Sharma et al., 2011).

The device is in its infancy, so there is no chronic recording data available. However, while recording artificial neurons with saline soaking, it was shown that there is no loss in recording quality, in terms of signal-to-noise ratio (Sharma et al., 2010). The input signal for the artificial neurons consisted of a biphasic cyclic pulse of 2 V peak-to-peak with a frequency of 6 pulses/s for a 0.4 ms duration.

Such a design could yield success. However, this device is still silicon based, a potential pitfall when minimising micromotion. Although promising, there is a limitation for wireless devices. Currently, the wireless signals transmitted are not encrypted, which could lead to device tampering. If a layer of encryption is added, power consumption and subsequent heat dissipation into the brain could increase, resulting in unsafe and unusable devices. Recently, an independent group show that their wireless Utah array exhibits similar single unit and activity fall out as the original non-wireless probe over a 13 month indwelling period, thus highlighting the problem of modulus mismatched devices (Borton et al., 2013).

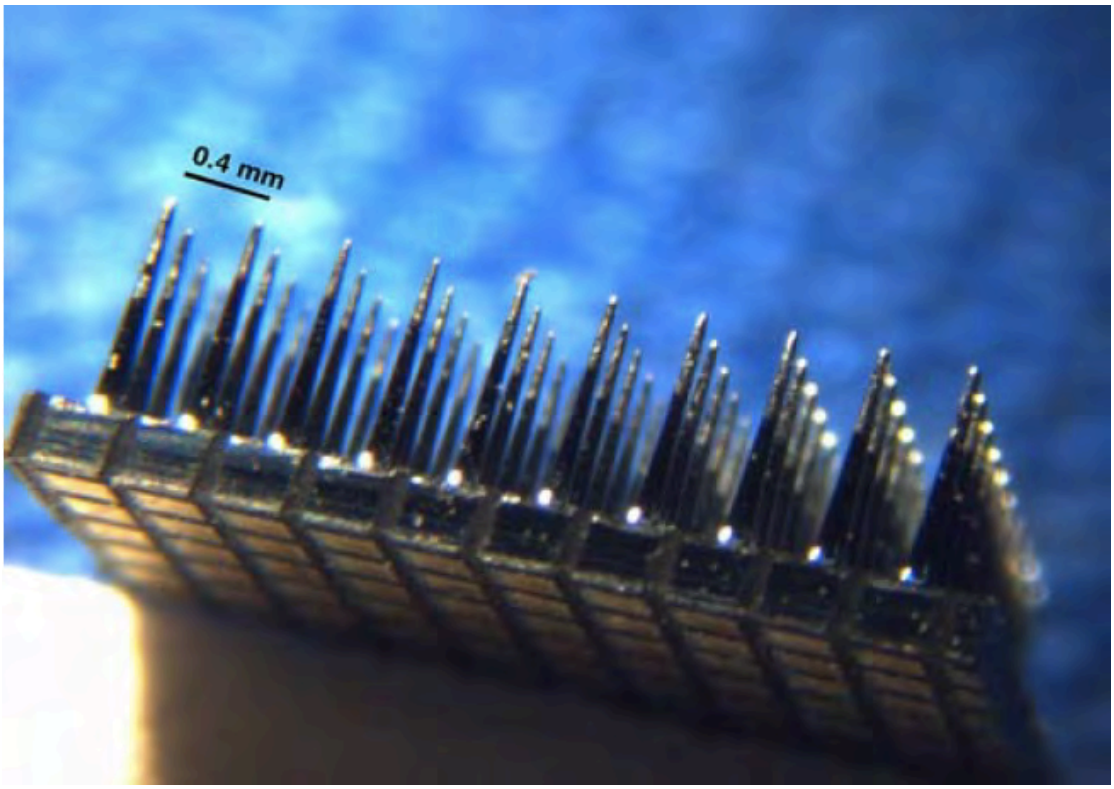

Figure 1.15. The wireless Utah array (Kim et al., 2006). Wireless arrays could minimise tethering forces associated with ribbon cable shearing forces, however they also need to be effectively powered to minimise heat dissipation into the brain.

1.3.2.8 General considerations: independent testing?

The performance of the above electrodes have been analysed by the groups, which have fabricated them. These groups solely develop their own arrays and major comparisons of different arrays from independent groups is thus lacking in the literature. Ward and colleagues investigated the chronic recording capabilities of the Cyberkinetics iridium oxide array, Cyberkinectics silicon ("Utah array"), Moxon Thin-film Ceramic, NeuroNexus ("Michigan probe") and Tucker-Davis Technology (TDT) microwire arrays and demonstrated no superior electrode for long-term neuronal recordings in measures of impedance, charge capacity, signal-to-noise ratio, recording stability and elicited immune response in a 31-day period in a Long Evans rat animal model (Ward et al., 2009). The electrodes were implanted in either the visual or motor cortex depending on specific manufacture recommended use; a possible confounding factor when performing comparisons in the study. Longer duration independent studies are needed to investigate chronic electrode performance.

1.3.2.9 General considerations: Unit stability

Although recording time length has been determined by the above groups, with the ability to capture spiking activity for the maximum time period, unit stability from day-to-day is scarcely reported. Unit stability, the requirement to record from the same group of neurons day-to-day is needed for optimal brain machine interface performance. Rousche and Norman (1998) reported that the same neuron can be tracked visually with the use of their waveform on-screen for a maximum of a few weeks using the Utah array (Rousche and Normann, 1998). For the same array, Suner and colleagues (2005) measured wave form clusters and interspike interval distributions over a 91-day period, although they did not determine whether the same neurons were present daily (Suner et al., 2005). For microwires, Nicolelis and colleagues (2003) recorded activity from primate cortex and with similarity of unsorted waveform clusters in principle component space, found 80% of the original units were stable after two days and 55% were stable through 8 days (Nicolelis et al., 2003). Jackson and Fetz (2007) used the correlation coefficient between unsorted waveform averages and reported that 50% of original units were stable for a week, and 10% were stable through to 2 weeks (Jackson and Fetz, 2007). Dickey and colleagues (2009) used both average spike waveforms and interspike interval histograms to show that for a Utah array implanted in rhesus macaque monkeys that 57, 43 and 39% of original units were stable for 7, 10 and 15 days respectively. They claim by using this method they reduced the number of false positives (Dickey et al., 2009).

It is beneficial to show both unit stability and recording longevity to determine intracortical electrode performance. Stability will lead to performance longevity. If a different cell is recorded every week due to cell death, eventually the total number of cells will diminish. Thus a low stability may indicate poor long term (>1 year) longevity.

1.3.3 Intracortical electrode material choice

The majority of the electrodes have designs relating to the Utah array, Michigan probe or microwires but use different electrode configurations or materials to optimise longevity. An important component in electrode design is the metal and dielectric choice.

1.3.3.1 Metal

Allergenicity, impedance, stimulating properties, flexibility, chronic recording capabilities and in some cases radiographic visibility can characterise recording metals.

Increased allergenicity leads to an augmented tissue response. Evidence of metal allergies can be found in medical case studies. One such example is that of a woman who developed nickel dermatitis after a surgical implant, with symptoms subsiding after removal (Barranco and Solomon, 1973). According to Geddes, there is a hierarchy of allergenic metals: nickel, chromium, cobalt, beryllium, mercury, copper, gold and silver, exposure of which should be avoided (Geddes and Roeder, 2003).

Electrode impedance decreases with increasing area, surface roughness, current density and frequency. An equivalent circuit for impedance measurement from an electrode bathed in electrolyte (e.g. saline) is shown in figure 1.16.

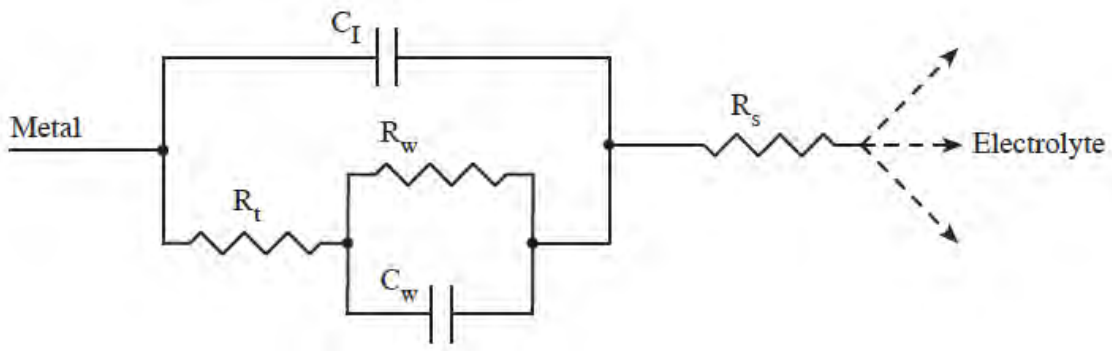

Figure 1.16. An equivalent circuit for impedance measurement for an electrode in an electrolyte solution. R_t is the charge transfer resistance caused by the diffusion of reactants to and from the electrode. C_I is the interfacial capacitance forming from the interaction of water molecules and solvated ions at the electrode interface. R_W and C_W form the Warburg element due to the frequency dependent nature of alternating current. R_S is the spreading resistance caused by the spreading of current to a distant ground or counter electrode (Merrill et al., 2005).

Below, a detailed explanation of the circuit element for impedance has been formulated from appropriate literature (Borkholder, 1998, Merrill et al., 2005, Cogan, 2008).

When a metal is placed in an ionically conducting solution, the metal and the solution are electroneutral. Electrochemical reactions occur immediately where electrons are transferred between the metal and the electrolyte that influences further chemical

reactions. Both reduction and oxidation reactions occur, where they compete until a stable equilibrium is achieved. The electron field generated by these reactions influence the electrolyte. Water dipoles orient themselves in the field forming a layer at the metal surface. Beyond the dipoles are solvated ions that form a layer known as the outer Helmhotz plane (OHP). There is also specific adsorption of ions at the electrode surface interspaced with the orientation of water dipoles, known as the inner Helmhotz plane (IHP). This creates an electrical double layer at the boundary.

The solvated ions forming the OHP act like a dielectric and forms what is known as the interfacial capacitance (C_I). This can be considered as a simple capacitor. Next in the circuit is the charge transfer resistance, which is due to the diffusion of reactants to and from the electrode. As impedance is measured with a sinusoidal waveform in the form of an alternating current, the situation changes when this current is so large that the reactants are no longer able to diffuse from the bulk to the interface fast enough. This additional impedance must be placed in series with the charge transfer resistance, since physical diffusion and charge transfer occurs in a series process. The reactants diffuse to the interface where they contribute to redox reactions. The charged particles will move in response to the applied sinusoidal field, varying the spatial concentration of the ions around the interface rather than a linear graded distribution. Ions will still be concentrated near the OHP. As the excitation increased, it becomes more difficult for the ions to follow the field. At high enough frequency, the ions cannot follow the field at all, resulting in this diffusional impedance tending towards zero. To model this frequency dependant impedance, the Warburg element (R_w and C_w) was created, which consists of a half cell potential, a series capacitance and resistance, in parallel with the faradic impedance. The final circuit element that must be included is the spreading resistance (R_s). This models the effects of current spreading from the electrode to a distance counter electrode in solution or loss to ground in the *in vivo* state.

Using the Warburg element/model, it is possible to calculate the low-current-density capacitance, which can be compared for different metals when in contact with physiological saline. From the literature, Platinum black provides the best Warburg capacitance, followed by platinum-iridium, copper, rhodium, stainless steel, platinum, palladium and aluminium (Geddes, 1997, Geddes and Roeder, 2003). Data are not available for gold or tungsten, the latter of which is a good supposed recording metal (Hubel, 1957, Freeman et al., 2010).

Electrode decomposition when stimulating is important. In a landmark study, a constant-current stimulator was used to produce a 0.5/0.5 ms, 50 Hz bidirectional wave which was applied to metals for 24 hours a day for up to 9 months. Electrodes were weighed before and after stimulation. Microelectrodes 5 μm thick made from iridium, rhodium, platinum and palladium have lifetimes on the order of decades. Gold was classed as mediocre, with tungsten and stainless steel as unacceptable for use as chronic microelectrodes (White and Gross, 1974).

The flexibility of a material is measured by the Young's modulus. Platinum is the most flexible of the electrode metals, although iridium and tungsten can be made more flexible by sintering with platinum and tungsten respectively (table 1.1). Flexible metals are important in reducing micromotion, although too flexible a metal choice may cause electrode insertion issues (Moxon et al., 2004).

Metal	Young's Modulus (GPa)
Gold	79
Platinum	168
Iridium	528
Tungsten	400
Titanium	110

Table 1.1. The Young's modulus of metals used in electrode design. A decreased Young's modulus shows an increase in flexibility. Metals can be alloyed (sintered) to form more flexible metals.

Radiographic imaging can monitor device integrity. The best metals for imaging are those that have atomic numbers ranging in the 70s. The most visible will be gold, platinum, platinum-iridium, tungsten and tantalum (Geddes and Roeder, 2003).

In short, the best metals are those that have low impedance, good flexibility, non-allergenic and have good stimulation stability. The latter is important in electrode design for recording and stimulation. Platinum and iridium both singularly and as an alloy are the optimal choice in electrode metals. Tungsten has been effectively used for recording electrodes (Hubel, 1957). Gold is scarcely used due to stimulation

decomposition and allergenicity, although seems attractive due to established micromachining techniques and flexibility.

1.3.3.1.1. Decreasing electrode impedance

Strategies have reduced impedance at electrode recording sites, which is linked to a reduction in noise and signal loss. Such strategies involve increasing the recording site surface area (Borkholder, 1998). Recent studies have used the electro-deposition of platinum black on to gold and platinum electrodes, which has lowered impedance for recording electrodes (Pang et al., 2005, Musa et al., 2009). However, platinum black can rub off during insertion causing augmented gliosis (Geddes and Roeder, 2003, Griffith and Humphrey, 2006), although this could be minimised by ultrasonicated electrodeposition (Desai et al., 2010) .

Similarly, Negi and colleagues compared the electroplating of conventional Utah array tips with platinum and iridium oxide. Platinum and iridium oxide were used due to their ability to transfer between ionic and electronic current and to resist corrosion. Iridium oxide had a higher charge injection capacity and lower impedance than platinum films, making it a promising chronic recording and stimulation material (Negi et al., 2010). On the contrary, a biocompatibility study by Thanawala and colleagues showed the superiority of platinum over iridium oxide in promoting neuronal cell growth (Thanawala et al., 2007). However, *in vivo* studies are needed to corroborate these findings.

Conductive polymers (for a review see (Green et al., 2008)) can be used to decrease impedance (George et al., 2005, Widge et al., 2007, Shimada et al., 2009). Ludwig and colleagues used electrochemically deposited poly(3,4-ethylenedioxythiophene) (PEDOT) at the recording sites of conventional Michigan probes. These probes were inserted into the motor cortex of Sprague Dawley rats for a six week period, and the PEDOT recording sites outperformed control sites with respect to SNR, number of recorded units and impedance (Ludwig et al., 2006, Negi et al.).

Recording site surface area could be increased without metal electrodeposition. Micro-roughening the metal sites by a short duration chemical/dry etch could increase surface area to decrease impedance. The selectivity of the recording area remains unaltered.

1.3.3.2. Dielectrics

The mechanical and electrical properties of dielectrics are shown in table 1.2.

Material	Parylene-C	PI-58789	PI-2611	PDMS	Durimide	Kapton	General comment
Young's Modulus (GPa)	2.76	2.3	8.5	360-870 KPa	2.9	2.28-2.48	Lower values = less stiff and more flexible
Tensile strength (MPa)	69	260	350	2.24	170	234	Higher values= less flexible
Dielectric constant (1 kHz)	3.1	3.5	2.9	2.3	--------	3.4	Higher the better
Dielectric constant (1 MHz)	2.95	--------	-------	-------	3.3	---------	Higher the better
Elongation at break (%)	200	120	100	160	73	80-82	Higher the better= more "stretchy"
Water absorption (%)	0.06	1.77	0.5	-------	1.3	0.8-1.3	Lower value = better barrier
Glass transition temperature (^{o}C)	80-100	> 400	360	-------	>350	--------	--------
Melting temperature (^{o}C)	290	580	------	-49-40	>510	360-410	--------

Table 1.2. The electrical and mechanical properties of dielectrics in electrode design. From the literature higher water absorption for the dielectric leads to a decreased life expectancy. Biocompatibility factors need to be taken into consideration when choosing a dielectric for electrode design. Some data was not available for specific dielectrics (dotted line). Data were obtained from specific manufacturer data sheets: parylene-C (http://scscoatings.com); polyimide (PI; http://hdmicrosystems.com); durimide (http://fujifilmusa.com); kapton (http://dupont.com).

1.3.3.2.1 Polyimides

Polyimides (PI) are polymers of imide monomers, and contain a functional group consisting of two carbonyl groups bound to nitrogen. PI are deposited by spinning, where a PI 'blob' is placed centrally on a vacuum held wafer, which is spun at a desired spin rate to obtain the dielectric thickness. Spun PI undergo baking regimes and etching to complete imidization and dielectric layer shaping respectively.

PI have been used successfully in peripheral nervous system (PNS) implants, including sieve electrodes for peripheral nerve regeneration (for a review see (Stieglitz and Meyer, 1999)), with implanted electrodes lasting between 2-12 months with no signs of delamination.

A microelectrode array for measuring evoked potentials in the CNS showed electrode failure after 16 days using a combination of two polyimides (PI-2525 and PI-2771) (Myllymaa et al., 2009). Moreover, the Michigan probe fabricators observed that polyimide on their test cables disappeared after two years in buffered saline soak tests resulting in the incorporation of a silicon ribbon cable (Hetke et al., 1994). Both studies corroborate the unreliable performance of PI.

Generally, PI have a higher water absorption rate than other dielectrics (table 1.2). From the literature, specific PI with a higher water absorption rate delaminate more rapidly leading to device failure. Another limitation in using PI is the ability to make the layer pinhole free during spin deposition, due to particle/bubble contamination. Microholes (Figure 1.17) can develop which enable fluids to interact with the metal layer, resulting in decreased metal and dielectric adhesion (Rubehn and Stieglitz, 2007).

The literature suggests that PI is a poor insulator for chronic intracortical electrodes. The successes for PNS electrodes may be attributable to the greater dielectric thickness and implemented multi-layer deposition strategies (Chen et al., 2009). PI-2611 is consistently used for peripheral implants but due to its high young's modulus value (8.5 GPa) it is too rigid for use in flexible brain implants to minimise micromotion.

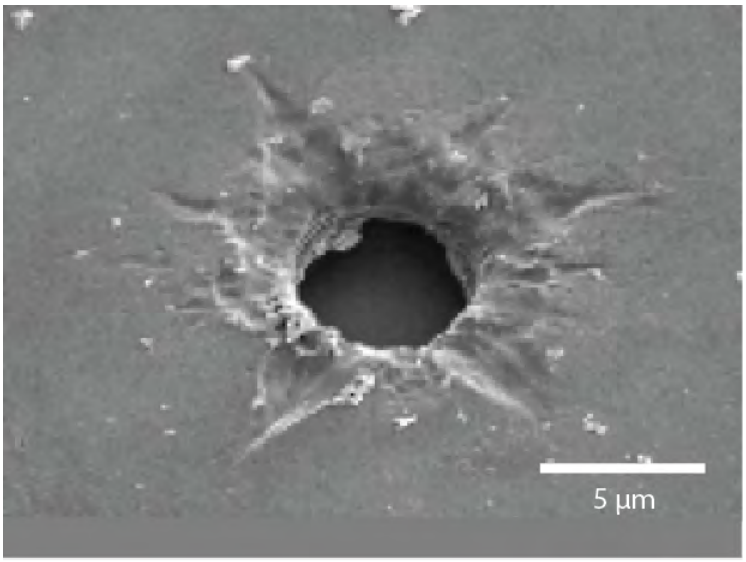

Figure 1.17. An optical microscopy image of a pinhole that can form during the spin deposition of PI. These pinholes can allow fluids through that in turn can lead to the decreased adhesion between the metal and dielectric resulting in device failure (Rubehn and Stieglitz, 2007).

1.3.3.2.2 Parylene-C

Parylene-C deposition is shown in Figure 1.18. Highly conformal layers are obtained from chemical vapour deposition.

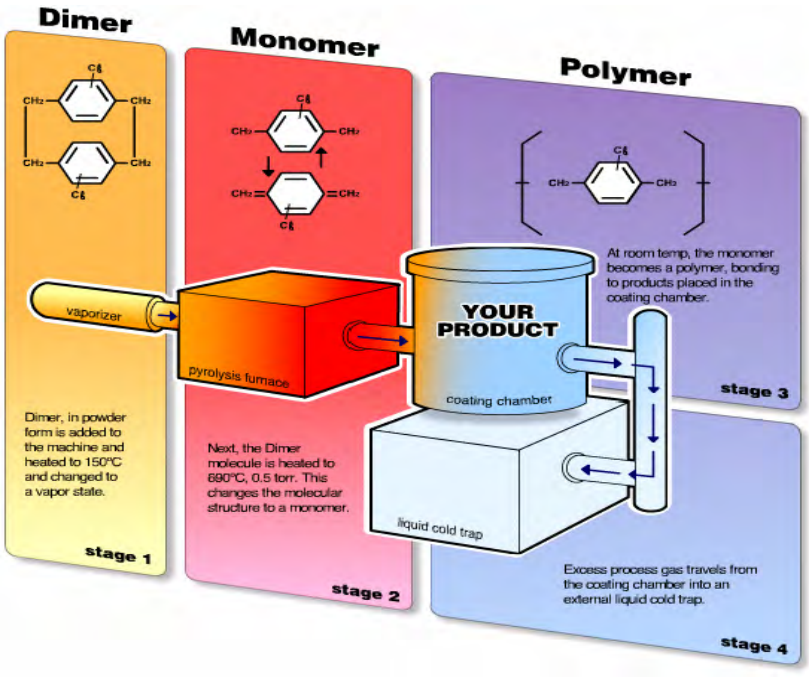

Figure 1.18. The deposition process of parylene-C. It is noteworthy that because of the highly specialised, multi-stage deposition of parylene-C, many fabrication laboratories prefer using PI due to cost effectiveness involved with purchasing/maintaining the four chamber equipment (http://scscoatings.com)

The intracortical recording capabilities of parylene-C based microprobes were first characterised in the 1970s. Schmidt and colleagues showed single unit activity for up to 223 days in one monkey, with all 12 implants showing activity for a total of 141 days. (Schmidt, 1976, Schmidt et al., 1988). Similarly, Loeb and colleagues obtained monkey cortical single unit activity for up to 100 days with their parylene-C-gold-Parylene-C probes (Loeb et al., 1977a). Both studies report limited delamination during chronic insertion. *In vitro* testing has ascertained the high biocompatibility of parylene-c using cell culture (Kato et al., 2009). More importantly, parylene-C has obtained a Class VI USP biocompatibility rating for medical devices in the United States. Kozai and colleagues have shown that parylene-C also reduces the extent of biofouling post-electrode insertion by minimising the adhesion of blood proteins that can aggravate the tissue response in comparison to silicon probes (Kozai et al., 2012a).

Accelerated saline soak tests show the superior delamination resistive properties of parylene-C. Parylene-c can last up to 5 months and 12 months at 55^{o}C (Kazemi et al., 2004) and 77^{o}C (Wahjudi et al., 2009) respectively with a predicted 10-year lifetime at 37^{o}C.

Interestingly, the superior quality of Parylene-C is emphasized as the fabricators of the Michigan probe use it in their new electrode arrays. Reasons given for the use of parylene-C include Class VI USP biocompatibility rating, excellent insulating properties, low water uptake and well established micromachining methodologies (Seymour and Kipke, 2007). The modern Utah array utilises parylene-C rather than polyimide, which has resulted in better reliability (Suner et al., 2005) and the array is also FDA approved. Parylene-C is also emerging as the superior dielectric for retinal implants (Weiland et al., 2009).

Taken together, Parylene-C is highly biocompatible, shows good *in vivo* chronic performance and has good mechanical properties. With a young's modulus of 2.86 GPa and an elongation of break value of 200 %, parylene-C is highly suitable for use in large deflection applications (Pang et al., 2005), a key requirement to reduce micromotion.

1.3.3.2.3 Durimide

Durimide is a novel photosensitive PI in electrode design. Kato and colleagues designed an intracortical electrode using this particular PI. An advantage in using such a PI is the

elimination of the dry etching process, which is used to shape other insulating layers such a Parylene-C. This will allow more options in optimisation of the configuration and size of electrodes and enables lower cost fabrication (Kato et al., 2008).

In vivo characteristics for recording capabilities are lacking but are in progress (Lee, 2004, Kato et al., 2008). Critically, the water uptake value (table 1.2; 1.3% at 50 % humidity) is still comparable to conventional PIs. Therefore this polyimide may still have problems providing a better dielectric performance than parylene-c.

In vitro cell culture studies have shown that durimide is noncytotoxic, and possesses a better cell adhesion properties when fibroblasts were cultured than PI-2611 (Sun et al., 2009). Similarly Lee and colleagues showed good adhesion of 3T3 fibroblasts to their durimide based electrode probe (Lee, 2004). However cultures of fibroblasts do not truly reflect properties of neurons, especially when trying to analyse adhesion of glial cells and neurons, which can only reliably be measured *in vivo*.

1.3.3.2.4 Kapton

Kapton has been used on NASA spaceships to no avail for wiring insulation. However, for biomedical applications it remains a material of interest. Kapton has been shown to be more biocompatible than parylene-C in the reduction of neuronal loss and cortical gliosis (Loeb et al., 1977b) and is a superior cell growth promoting polyimide compared to other dielectrics (Sun et al., 2009). However, the fabrication and deposition of such a material is not well established, and is currently limited to roll form (Kitzmiller et al., 2007).

In short, the best dielectric choice from the literature is Parylene-C. However fabrication laboratories are still using PI due to simpler and cost effective deposition, as specialist machines are required for the four-chamber parylene-C deposition. Unlike PI, Parylene-C provides a very uniform and pinhole free layer.

General dielectric biocompatibility can be increased by surface micro-roughening (Song, 2009). This allows better integration and adhesion of cells due to the mimicking of the cell's extracellular matrix (Polikov et al., 2005). However, this may enhance the undesirable electrode encapsulation by glial cells.

1.3.3.2.5 Polydimethylsiloxane (PDMS)

PDMS is a viscoelastic polymer that acts either as a liquid or solid depending on the temperature; it is an important component in silly putty. PDMS has rarely been used for intracortical electrode design. Kozai and Kipke, used a PDMS based probe simply to show that an adapted insertion needle could accommodate PDMS substrate insertion (Kozai and Kipke, 2009).

However, PDMS has been used for stretchable array fabrication, although not chronically. Yu and colleagues showed that it is possible to create a stretchable array out of PDMS and gold electrode tracks for recording hippocampal brain slices. Array stretching is required to induce injury to culture, mimicking traumatic brain injury for use in an *in vitro* model. The array was shown to be biocompatible with very limited cell death occurring, in cell cultures over a two-week period. An interesting feature about this array is the ability to withstand large, rapid and repeated biaxial deformation up to 20 %, promoting device flexibility (Yu et al., 2006).

Recently, a similar array has been created with 60 electrodes, which reliably capture action potentials and local field potentials both *in- vitro* and *vivo* from cardiac and brain tissue, over acute time points (Blau et al., 2011).

Although PDMS may seem attractive due to its high flexibility, it has a lower dielectric constant than parylene-c and polyimide (table 1.2). Also, as it is spin coated on to wafers, there is a problem of air bubble emergence causing pitting and device failure; a similar problem as that for polyimide. These factors may restrict PDMS use in Intracortical electrode fabrication.

1.3.3.2.6 Smart materials

Nanocomposites have been recently developed and introduced to intracortical electrode fabrication. Harris and colleagues have fabricated non-functional microelectrodes made from a mixture of poly(vinyl acetate) and tunicate whiskers from sea cucumber dermis which decreases its tensile storage modulus from 5 GPA to 12 MPa within 15 minutes under physiological conditions, resulting in a brain-matched modulus (Harris et al., 2011b). The electrodes were compared with traditional microwires in terms of nuclei density within 100 um from the device at 4 and 8 week post-implant in to the rat brain.

There was a greater nuclei density at 4 weeks for the nanocomposite devices compared to microwire, although at 8 weeks the density around the wire recovered to match that of the nanocomposite. The authors also show that the glial scar was substantial for the microwire, compared to the nanocomposite (Harris et al., 2011a) .

A similar nuclei distribution level around both electrodes indicates that the nanocomposite confers no advantage over the traditional microwire. Nanocomposite use in fabrication is limited. It has to be laser cut, technology that not all clean rooms possess and only thin films can be patterned using this technique (Hess et al., 2011). Interestingly, the nanocomposite has only been used either to provide mechanical stiffness to parylene-C probes during insertion (Hess et al., 2011) or in non-functional microelectrodes (Harris et al., 2011a). No dielectric properties have been reported, so it is reasonable to assume that the nanocomposite use in microfabrication is currently limited.

1.3.4.2.7 General considerations: Biocompatibility

In the literature, biocompatibility is normally assessed with the use of cell cultures, where viable cell numbers on the substrate is calculated (Sun et al., 2009). In an elegant study, Winslow and colleagues showed that this approach is simplistic for evaluating responses to intracortical electrodes. Comparing the number of adherent microglia cultures, the glass substrate had a considerable number of cells compared to parylene-C (50 cells/mm^2 vs. 9 cells/mm^2). Microglia attraction to parylene-c should be limited. However, the authors report that silicon probes, coated with and without parylene-c have a similar glial response. *In vitro* cultures are not representative of the complex abiotic-biotic interface (Winslow et al., 2010a). The best indicator of material biocompatibility is the *in vivo* environment.

1.4 Conclusions

It is important to reduce the tissue response to electrodes for them to work optimally. Current electrodes are not optimally designed to limit the mechanical trauma caused by micromotion. Although the Utah array is FDA-approved, the high channel count increases the probability of neurons being captured over time; unit stability is poor.

Current flexible electrodes still have features, which cause pronounced neuronal tissue damage, such as sharp anchoring structures. There is a clear need to develop an electrode that is designed to fully combat the effects of micromotion related mechanical trauma to lead to the possible enhancement of single unit recording longevity.

1.5. Project aims

Micromotion is a key contributing factor for chronic intracortical electrode failure. Current designs for flexible devices do not fully try to combat the modulus mismatch between the electrode material and brain. We propose a new design that might be beneficial in reducing micromotion, hence enhancing electrode longevity.

We propose three changes to current electrode designs. Instead of a straight rigid shaft, we propose a sinusoidal shaft. Instead of a sharp tip we propose a rounded tip, to reduce mechanical trauma. Finally, instead of angular anchoring structures, we propose a spherical structure.

The spherical anchor will restrict the movement of the recording tip, while the sinusoidal shaft will move relative to the recording tissue, thus acting like a spring like device. A spherical structure may also be beneficial to attract neurons (Winslow and Tresco, 2010).

The period between the sinusoids must not be too small, to avoid a serrated knife effect. As we will have a rounded tip, a specialised, low-cost insertion method must be developed.

This thesis will explore the design considerations, fabrication, bench and *in vivo* testing for the newly developed “sinusoidal probe”.

Chapter 2: Device fabrication

2.1 Introduction

As discussed in chapter 1, there is a necessity to develop an electrode that was designed to combat micromotion fully. This chapter will explain the design considerations and the fabrication processes in manufacturing the "sinusoidal probe." In this chapter we show a successfully optimised probe design that addressed the problem encountered with the electrode bondpad for the first sinusoidal probe generation. Further, microfabrication was successfully optimised for parylene-C (dielectric) and WTi (metal) patterning with limited dimension loss. These materials were chosen as they showed optimum *in-vivo* longevity, flexibility and recording considerations. We also showed that aluminium was the best sacrificial layer due to etchant selectivity and lithographic measures. This chapter will explain in detail the optimisation of the overall design and individual microfabrication steps for the sinusoidal probe.

2.2 Material choice

Material choice was important for our flexible electrode design. The optimum dielectric was parylene-C. Parylene-C has excellent mechanical and electrical properties, including a low modulus of elasticity, 2.86 GPa, and elongation at break of 200 %, corroborating use for large deflection applications. Similarly, parylene-C has a high dielectric constant and a very low water uptake at 50% humidity, the latter, which is linked to improved dielectric long-term performance (table 1.2). Most importantly, parylene-C already has FDA approval for use as a biomedical material in human implants and is used as the insulator for the wiring on cardiac pacemakers. Also parylene-C has obtained the highest biocompatibility rating; class VI, from the United States Pharmacopeia (USP).

Tungsten-titanium (WTi) was used as the metal layer. Tungsten is classically a very good recording metal and has been used extensively for the past 50 years to record from the brain. However, with a modulus of elasticity of 400 Gpa, it is not flexible. Therefore tungsten was sintered with titanium, with the purchase of a combined metal sputtering target (YM: 110 GPa), to increase flexibility (table 1.1).

The overall electrode consisted of a parylene-C-WTi-parylene-C sandwich, with design features to minimise micromotion. The electrode was fabricated on a silicon substrate, with a sacrificial layer utilised for device release.

2.3 Sinusoidal probe: first generation

The initial electrode was designed and fabricated before the commencement of this thesis.

The electrode consisted of three WTi recording sites encased in parylene-C. The recording end was a parylene disc of 100 µm diameter, out of which the three metal electrode sites protrude. There were three electrode recording sites to isolate single-unit activity through triangulation recording. The electrode body was 20 µm deep and 35 µm wide, and 5.5mm long, consisting of 10 sinusoidal cycles of 100 µm amplitude and 500 µm period. Each electrode connected to a bondpad, which was approximately 400 μm^2 (Figure 2.1).

The 10 sinusoidal cycles of 100 µm amplitude and 500 µm period was calculated to give the optimum compression ratio for the electrode length.

Mask designs were sent to Scottish Microelectronics Centre, Edinburgh, Scotland who fabricated the devices.

Figure 2.1. The sinusoidal probe first generation. The recording end was a parylene disc of 100 µm diameter, out of which the three metal electrode sites protrude. There were three electrode recording sites to isolate single-unit activity through triangulation recording. The electrode body was 20 µm deep and 35 µm wide, and 5.5mm long, consisting of 10 sinusoidal cycles of 100 µm amplitude and 500 µm period. Each electrode connected to a bondpad, which was approximately 400 μm^2. Recording sites had an area of 96 μm^2 and the distance beween the recording sites were 40 µm centre to centre. Distance between the electrode recording tracks are 5 µm edge to edge.

Fabrication for the sinusoidal probe first generation is summarised in Figure 2.2. The electrode was fabricated on a silicon substrate with a sacrificial layer (silicon dioxide) to aid device release. Sequentially the first parylene-C, WTi and second parylene-C layer are deposited with subsequent metal and dielectric etching steps. Finally, electrodes are released by sacrificial layer etching.

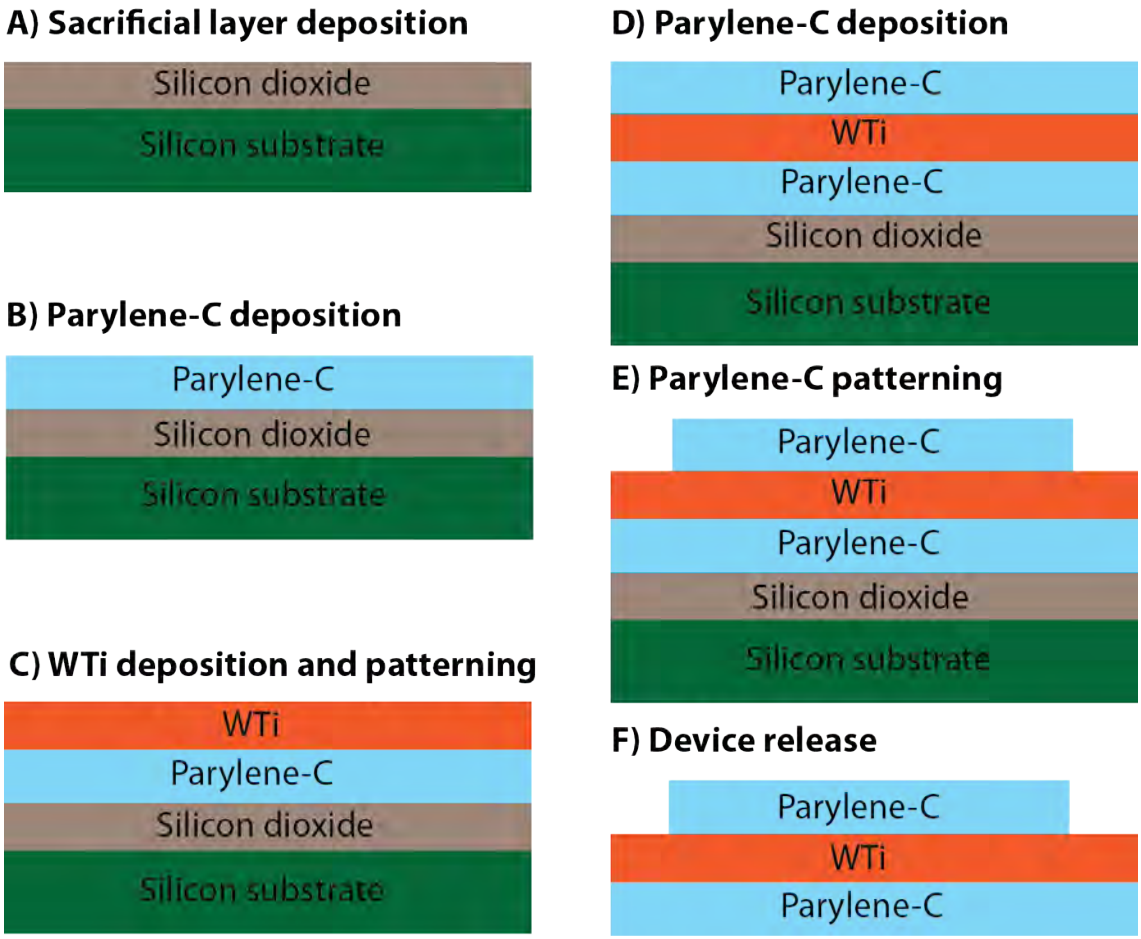

Figure 2.2. The edge-on fabrication steps for the Sinusoidal probe first generation. A) Thermal oxidation growth of 1 µm silicon dioxide as a sacrificial layer. B) Parylene-C deposition using a CVD process. C) WTi metal deposition and patterning. D) Second layer parylene-C with subsequent patterning (E). F) Device release using BHF etching of silicon dioxide. Device release took longer than anticipated, which partially damaged the other layers. The design of the bondpad also failed the acquisition of three separate contacts to the electrode recording sites. An optimised design was needed.

2.4 Problems with probe first generation

Two problems were encountered with this electrode design. Post-wire bonding, three separate electrode connections were unattainable as individual bondpad spacing was inadequate. Device release was problematic as release took over 24 hours. The predicted release time was approximately 10 minutes or less through BHF (5:1 40% NH_4F : 49% HF) or HF (49%) etching of silicon dioxide samples through clean room and literature observation (Williams et al., 2003).

Further optimisation was needed for the sinusoidal probe. For the next generation, design and fabrication emphasis was on obtaining three separate electrode contacts and optimising device release.

2.5 Sinusoidal probe: Second generation

The second electrode iteration was designed and fabricated, in house, at Newcastle University. The electrode was designed to eliminate the problems encountered with the first electrode generation. The design maintains the sinusoidal shaft and spheroid tip, but the electrode length was reduced to 3 mm to be cross-species compatible. At the current electrode length of 5.5 mm, recording from cells in smaller species was problematic, as electrodes were angled during insertion to obtain cells, as the brains are smaller. Therefore a 3 mm electrode length is a trade-off for targeting cells, without major angling, for smaller size brains (e.g. rabbit, and rat), while maintaining the ability to record from larger animals (e.g. macaque monkeys). Further, a 3 cm ribbon cable was incorporated and the bondpad re-designed to fit a standard connector (micro ps1/ps2 series, Omnetics Connector Corporation, USA); this eliminated the need to bond separate wires and made the process more refined.

Mask designs for the electrode are shown in Figure 2.3. The fabrication consists of a two-mask process, one mask for WTi and parylene-C layer patterning respectively. Masks were designed to allow for fabrication on a three-inch wafer, the maximum size that can be handled by the available mask aligner. Thirty-three electrodes can be obtained from one wafer.

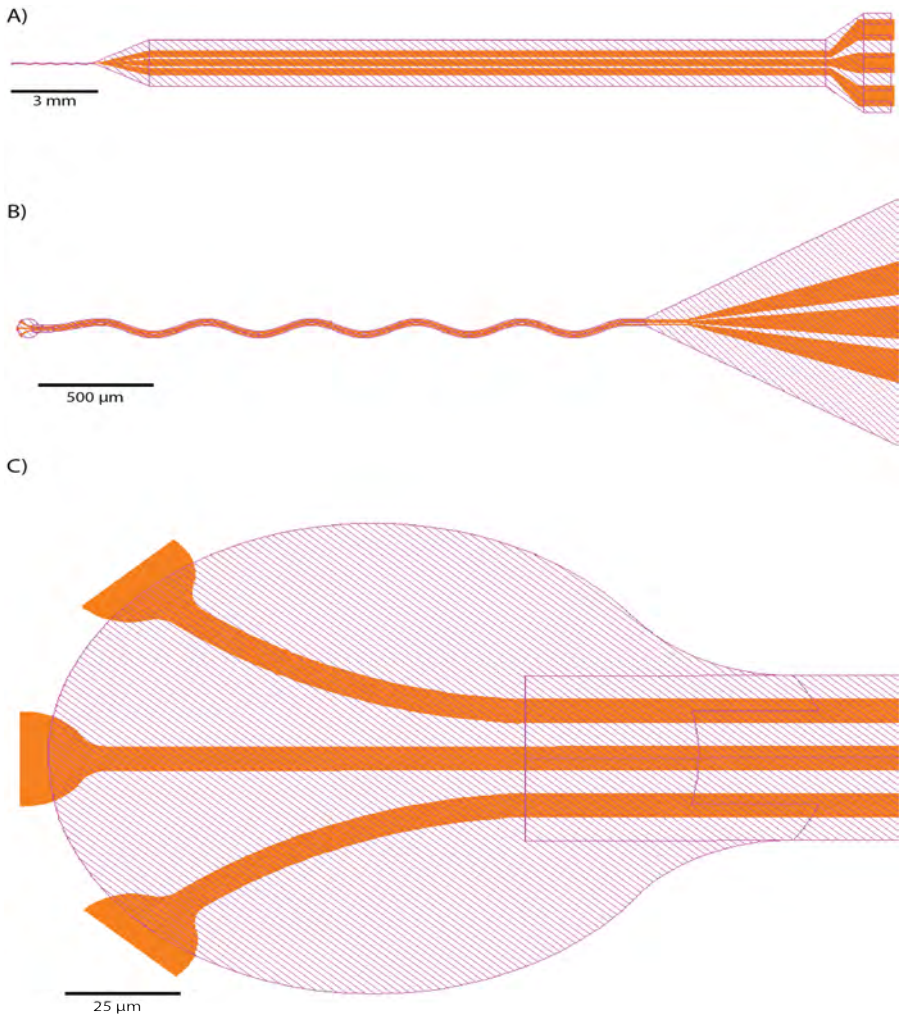

Figure 2.3. Mask designs for Sinusoidal probe second generation, orange and pink shows the WTi and Parylene-C layers respectively. The first generation sinusoidal part had similar dimensions but an increased length of 5.5 mm. A) The 3 electrode probe (3 mm length) with integrated ribbon cable (3 cm length). B) Close up of the electrode tapering to the integrated ribbon cable. C) Probe recording end with 3 electrode recording sites. Recording sites had an area of 96 µm^2 and the distance beween the recording sites were 40 µm centre to centre. Distance between the electrode recording tracks are 5 µm edge to edge.

The fabrication steps for the second generation are shown in Figure 2.4. From the first generation, aluminium was considered a better sacrificial layer than silicon dioxide. Further, deposition and etching parameters were optimised for both the dielectric and metal layers. The rest of the chapter will describe the fabrication reasoning and optimisation for the individual sequential fabrication steps relating to Figure 2.4.

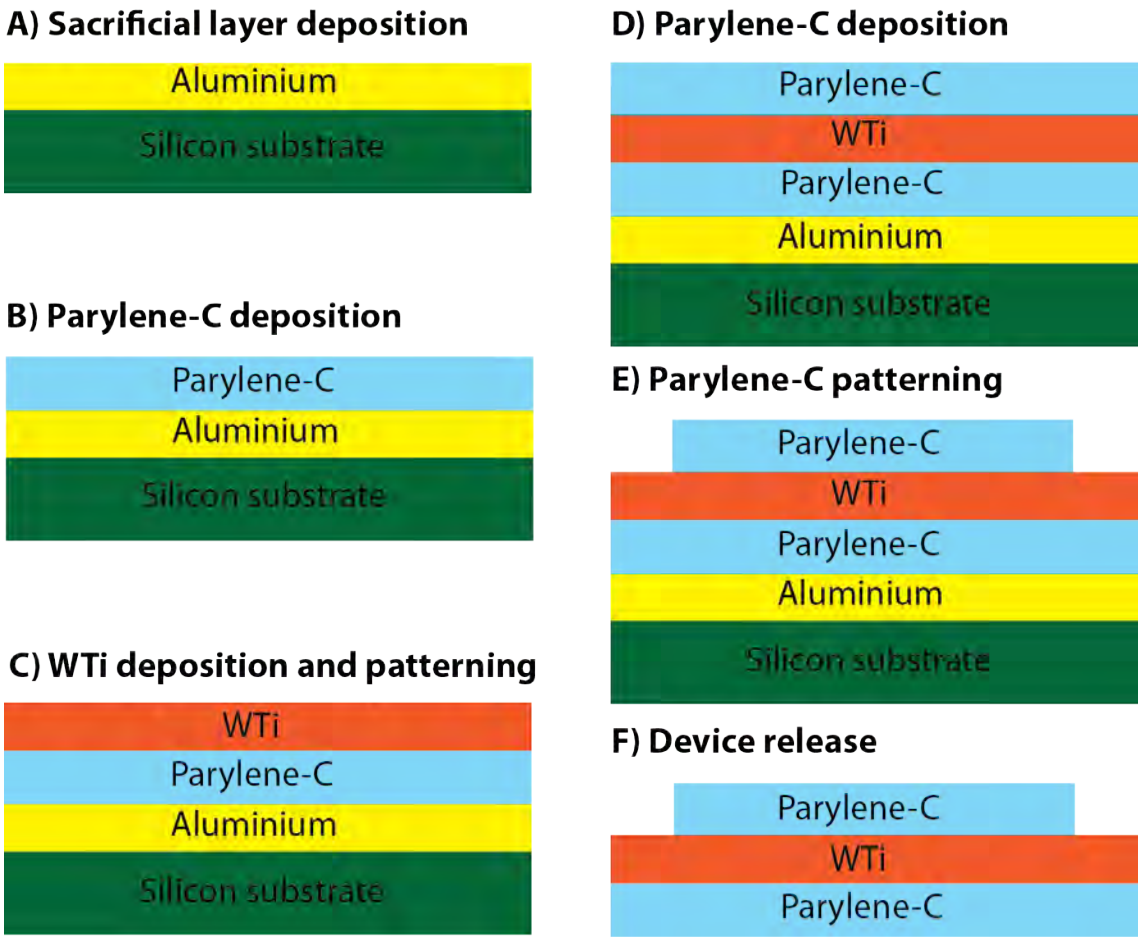

Figure 2.4. Summarised edge-on fabrication for the sinusoidal probe. A) Ebeam deposition of 1 µm aluminium as a sacrificial layer. B) Parylene-C deposition using a CVD process. C) WTi metal deposition and patterning using SF_6. D) Second layer parylene-C with subsequent patterning with oxygen plasma (E). F) Device release using peeling or aluminium etch (80% H_3PO_4 + 5% HNO_3 + 5% HAc + 10 % H_2O) .

2.6 Choice of sacrificial layer

2.6.1 Problems with current sacrificial layer

The sacrificial layer on our first probe generation was silicon dioxide. This was thermally grown within a steam environment to realise a 1 µm thick layer. Silicon dioxide can be etched by using either hydrofluoric acid (HF-49%) or buffered hydrofluoric acid (BHF- 5:1 40% NH_4F : 49% HF) with an etch rate of 2300 and 100 nm/min respectively (Williams et al., 2003). Through extrapolation, device release for etching through a 1 um layer should take 10 minutes with BHF, and 26 seconds with HF.

Electrode device release was problematic and took over 24 hours. Bathing electrodes in either BHF or HF (49%) partially etched our parylene-C and WTi, compromising

electrode functionality for some electrodes over this time period (table 2.1). Further, a lengthy release time would risk dielectric swelling, through clean room observations. There was a need to optimise device release.

	HF	BHF	KOH	Al etch
Parylene-C	4.4	0.16	0.42	?
WTi	slow	1.5	>300	?
SiO_2	2300	100	7.7	0
Aluminium	works	11	12900	530

Table 2.1. Etch rates (nm/min) for specific etchants on materials considered for fabrication, adapted from (Williams et al., 2003). HF (49%), BHF(5:1 40% NH_4F : 49% HF), KOH (30%) and Al etch (80% H_3PO_4 + 5% HNO_3 + 5% HAc + 10 % H_2O)

Metal sacrificial layers have been used to aid device release. Kozai and Kipke used aluminium as a sacrificial layer with KOH (30%) assisted-device release (Kozai and Kipke, 2009). A problem with using KOH is that it would inevitably attack the WTi layer, quickly. Therefore, the use of aluminium as a sacrificial layer and subsequent etching with Al etchant (80% H_3PO_4 + 5% HNO_3 + 5% HAc + 10 % H_2O) was considered as a device release mechanism.

2.6.2 Aluminium sacrificial layer testing

To evaluate aluminium as a potential sacrificial layer, three tests were performed. This included etchant selectivity, surface profiling and contrast testing.

2.6.3 Aluminium etchant selectivity testing

The etchant used to etch aluminium should have a high selectivity for aluminium over the other layers. Etching of aluminium with Al etch would give a five time faster release than BHF use to etch silicon dioxide (table 2.1). However, Al etch selectivity for the WTi and Parylene-C layers were unknown.

To test the selectivity for Al etch, first generation probes were subjected to Al etchant for 96 hours. Images were taken at 0, 0.5, 1, 24, 48, 96 hours via optical microscopy and the etchant topped up daily. Microscope settings were constant and obtained images were converted to grayscale and intensity measurements were taken in the Matlab environment (Image processing toolbox, Mathworks), for both the WTi and parylene-C layers (3 points per image) for 10 electrodes.

After a 96-hour soak period, there was no change in the appearance for the WTi and parylene-C layers. This was further corroborated with the intensity measurements for the 10 electrodes (Figure 2.5). This strongly implies that Al etch was highly selective for aluminium.

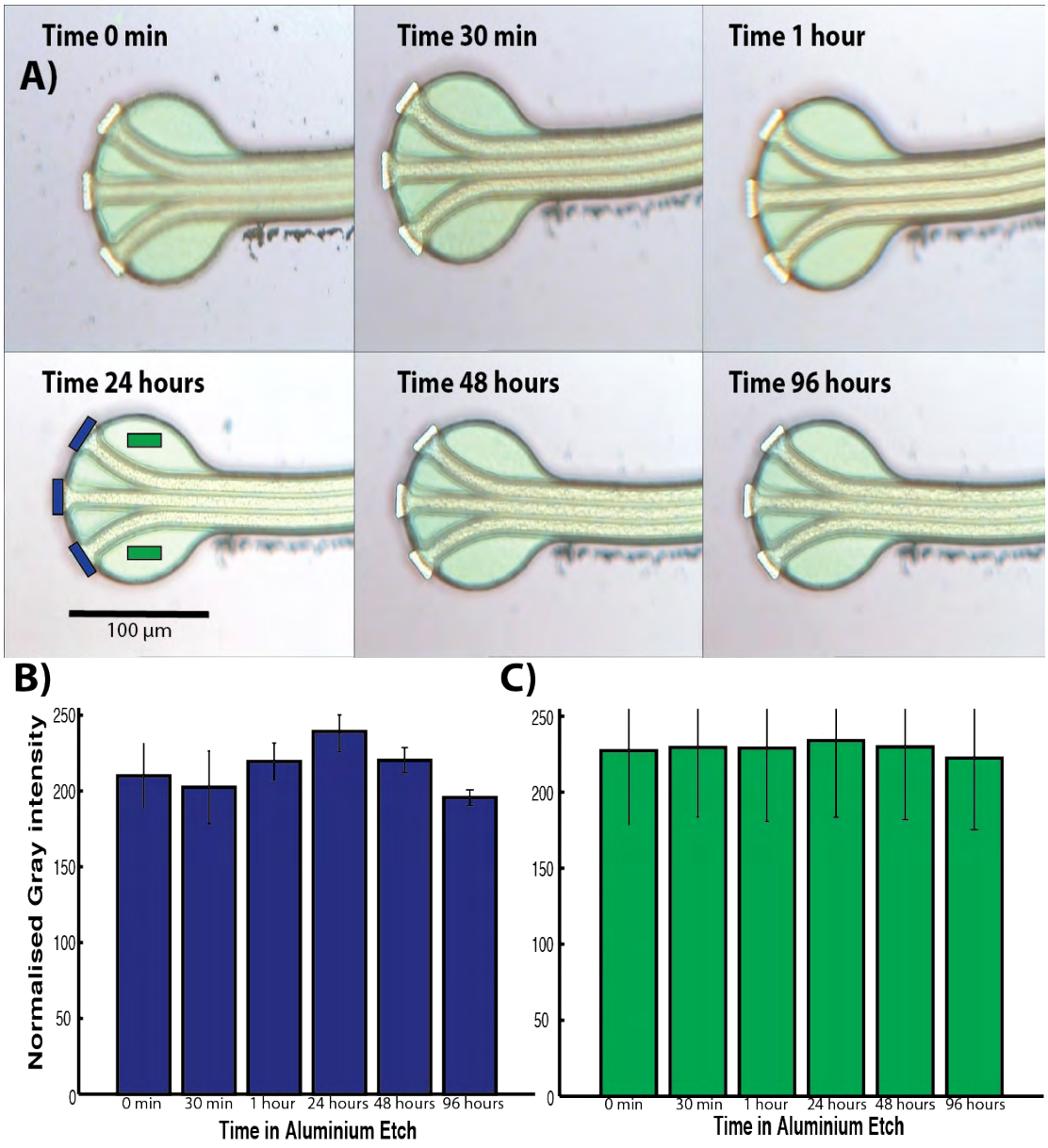

Figure 2.5. First generation electrodes over a 96 hour soak period. A) Representative image of a single probe through the soak period. Blue and green rectangles show the regions of interest for intensity measurements for

WTi and Parylene-C respectively. B) Intensity analysis (±SEM) for WTi electrode tips (n=30, one per recording site). C) intensity analysis (±SEM) for parylene-C layer (n=30 points). No significant differences were found between the time periods for the effect of Al etch on parylene-C and WTi as corroborated by ANOVA analysis.

2.6.4 Silicon vs silicon dioxide vs aluminium: surface profiling

Surface profile testing was performed to evaluate the explanation for poor device release with silicon dioxide use. The literature suggests that parylene-C based electrodes can be peeled off the silicon substrate after device fabrication (Takeuchi et al., 2004). However, this was not evident for silicon dioxide used in our first generation electrodes. As silicon dioxide was thermally grown, there was a possibility that unequal film growth may have led to the formation of a rough surface, hence augmenting adhesion between the parylene-C and silicon dioxide layers. This possibility was explored with the use of optical and atomic force microscopy (AFM).

2.6.4.1 Optical and Atomic Force microscopy

Optical micrographs were taken at x 5 magnification. Aluminium, silicon and silicon dioxide samples were also subjected to atomic force microscopy. Through AFM, a 10 by 10 μm area was measured for the surface profile of each sample.

The 1 μm silicon dioxide layer was optically rough at only x 5 magnification compared to both aluminium and silicon (Figure 2.6 A-C). AFM corroborates this, however aluminium was slightly rougher than silicon. This was negligible as the overall aluminium layer had a consistent, minimal roughness (Figure 2.6 D-F). The unequal film growth for silicon dioxide led to differing etch rates and increased substrate-sacrificial layer adhesion due to surface roughness in our first electrode generation.

Further, silicon had a smooth profile, which may be the reason behind successful device peeling methods shown in the literature.

A device peeling method was determined to be a simpler and less time consuming method for electrode release. Silicon was a better candidate for this sort of device release, due to overall surface smoothness. However, a failure in this process would lead to device release failure, as no sacrificial layer is present to aid device release.

Aluminium was the best candidate as a sacrificial layer as it had a similar overall smooth profile like silicon. Importantly, if a device peeling method was not achieved, the sacrificial layer could be etched away to release devices as an alternate release mechanism as corroborated through Al etch selectivity testing.

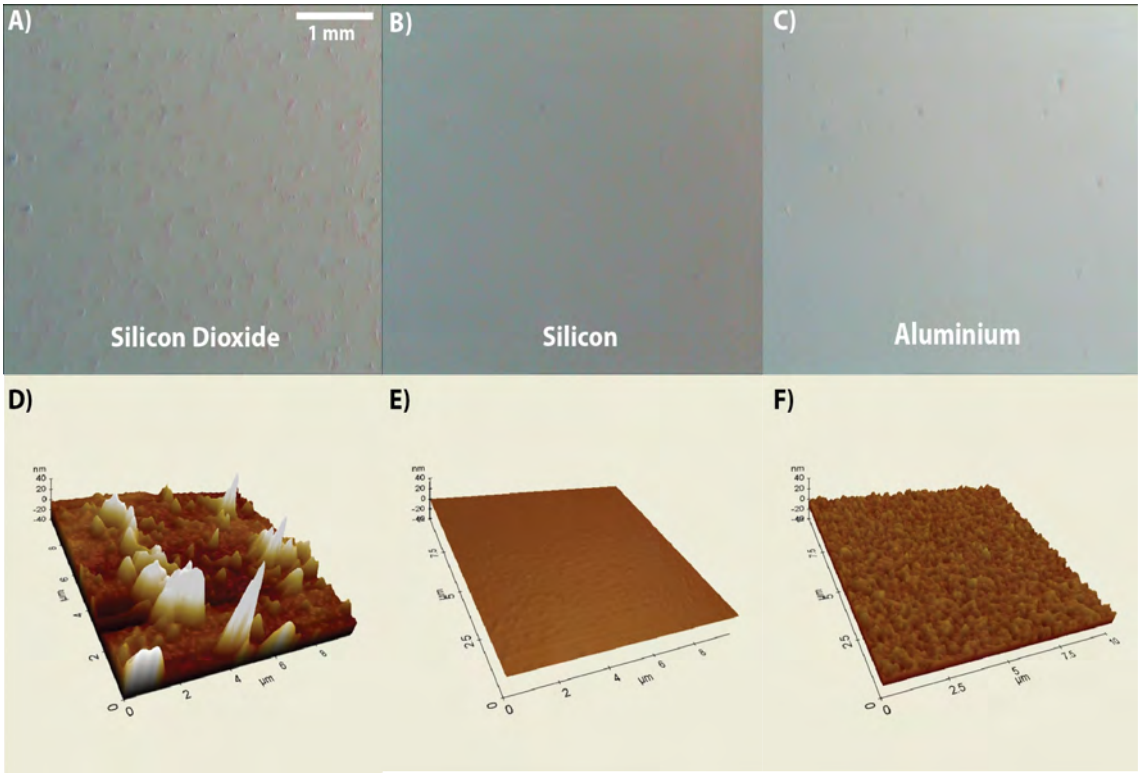

Figure 2.6. Optical (A-C) and Atomic Force (D-F) microscope images for silicon dioxide, silicon and aluminium. Overall silicon dioxide had unequal film growth leading to enhanced surface roughness, which was may have been the cause of inadequate device release for the first probe generation. Aluminium and silicon had similar minimal roughness.

2.7 Aluminium vs WTi vs Silicon, contrast testing

The final test to corroborate aluminium use as a sacrificial layer was contrast testing to ensure alignment marks visualisation for successful alignment of our two masking layers. The contrast between silicon and WTi was too similar to allow clear alignment mark visualisation (Figure 2.7). Therefore the aluminium layer deposition was also optimal to allow clear visualisation for the WTi based alignment marks, due to greater contrast between the two metals, over silicon. For quantification purposes, an image was taken for WTi (1 µm: Sputter deposited), Aluminium (1 µm: E-beam evaporation deposited) and a silicon wafer (Figure 2.7). Ensuring that all the microscope settings were the same, the images were converted to grayscale and intensity measurements

were taken in the Matlab environment (Image processing toolbox, mathworks, USA), for 20 points across the material to account for potential deposition non-uniformity. The mean greysale intensity is shown in Figure 2.8.

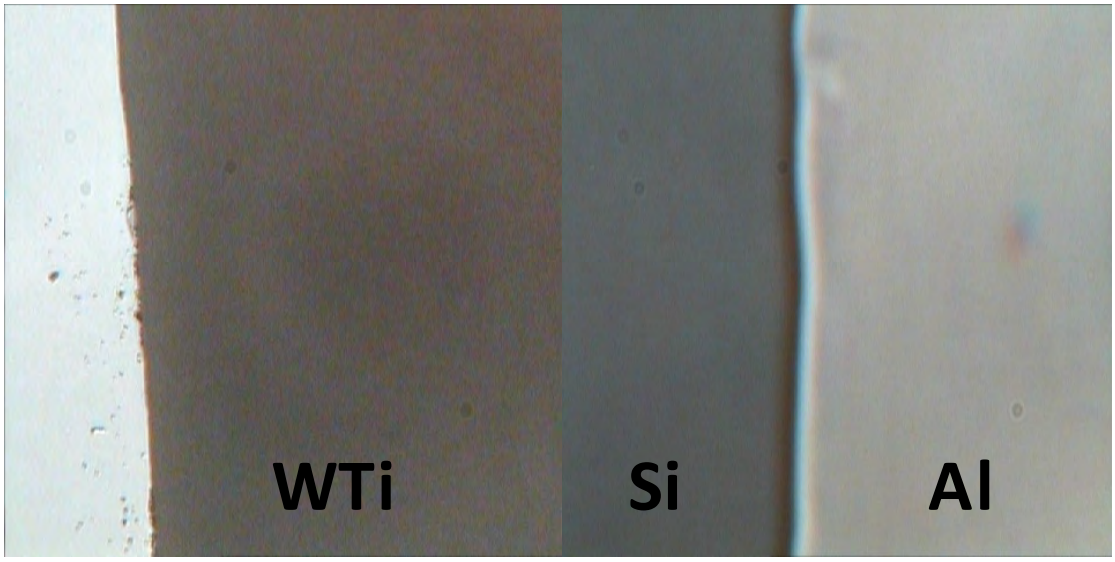

Figure 2.7. Contrast between WTi, Si and Al as shown by optical microscopy

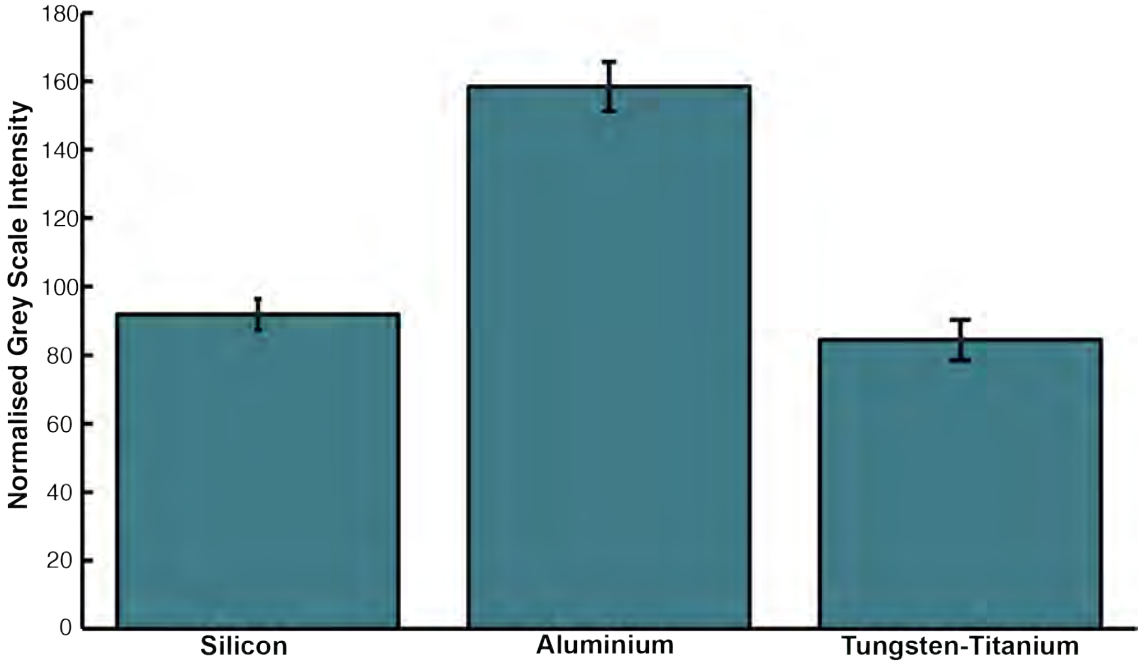

Figure 2.8. Intensity analysis for silicon, aluminium and tungsten-titanium. Three samples contributed to the measures. Silicon 92±5.1, aluminium 159 ±8.2, and tungsten-titanium 84 ± 6.3 (mean normalised grey intensity ± SEM).

From both Figure 2.7 and 2.8, WTi on aluminium provided clearer alignment mark visualisation and allowed better mask alignment for our layers.

From testing, aluminium was the best candidate as a sacrificial layer. In short etching the aluminium sacrificial layer gave a potential quicker device release method compared with previous release methods and enabled release through device peeling.

2.8 Dielectric deposition and patterning

2.8.1 Parylene-C

Parylene-C is deposited via chemical vapour deposition (Figure 1.17). The process starts by placing di-para-xylylene (dimer) into the vaporiser and the substrate to be coated into the deposition chamber. The system is pumped down to medium vacuum, and the di-para-xylylene is heated to 150 ^{o}C where it sublimes into vapour. This vapour enters the pyrolysis furnace, maintained at 690 ^{o}C, where the di-para-xylene is cleaved into identical monomers (para-xylylene). In a chamber at room temperature, the monomers reunite on all exposed surfaces as polymers (poly-(para-xylylene)) leading to a highly conformal layer known as Parylene-C. The coating thickness can be controlled by the amount of dimer used. The normal deposition rate is 5 μm/hour for parylene-C.

Due to the lack of in-house facilities, samples were sent to an external company for parylene-C deposition (Paratech Coating Limited, Northampton, UK).

2.8.1.1 Mask choice

Parylene-C was etched using oxygen plasma etching, a conventional etch method used throughout fabrication (Meng and Yu-Chong, 2005). Through clean room observations a photoresist mask was readily etched by oxygen plasma and therefore a metal masking layer was used for parylene-C etching.

Aluminium was initially the best mask choice for parylene-C as the masking layer could be concurrently removed from the sample, after parylene-C patterning, while etching the aluminium sacrificial layer to aid device release. To test the feasibility of such an approach, aluminium was deposited on to silicon samples, coated with parylene-C. AZ-

5214E photoresist (1.4 μm thick, post-soft bake; AZ Electronic Materials, Germany) was spun on (Electronic Microsystems Photo Resist Spinner, United Kingdom) to parylene-C coated wafers, soft-baked, exposed, and developed in accordance to manufacture guidelines for metal-lift off. After samples were inspected by optical microscopy for lithography quality, a suitable aluminium thickness (40 nm) was deposited via e-beam evaporation to serve as a masking layer (BOC-Edwards auto ebeam evaporator, United Kingdom). Post-aluminium deposition, samples were allowed to cool and subjected to acetone to remove photoresist from around the structures, to complete metal layer patterning. Aluminium deposition was repeated three-times on separate samples. Aluminium to parylene-C adhesion was extremely poor, resulting in the "flaking" of aluminium where structures should be present (Figure 2.9).

Although aluminium adhesion could be improved by surface roughening the parylene-C layer (Huang and Tai, 2009), this was unsuitable due to potentially augmenting the glial response to our electrodes due to enhanced cell attraction. Therefore titanium was considered as a masking layer candidate for parylene-C. Titanium is used to promote adhesion of other metals to substrates. Before gold is deposited on to silicon, a thin titanium layer is deposited to promote adhesion between gold and silicon. Therefore titanium adhesion to parylene-C was predicted to be good. Using the same protocol, titanium (40 nm) was deposited and subsequently patterned via lift-off and the structures were perfectly resolved and remained on samples (Figure 2.9). Therefore a titanium mask was chosen for parylene-C patterning, although mask removal required buffered hydrofluoric or hydrofluoric acid etching (Williams et al., 2003), adding another step in the fabrication process.

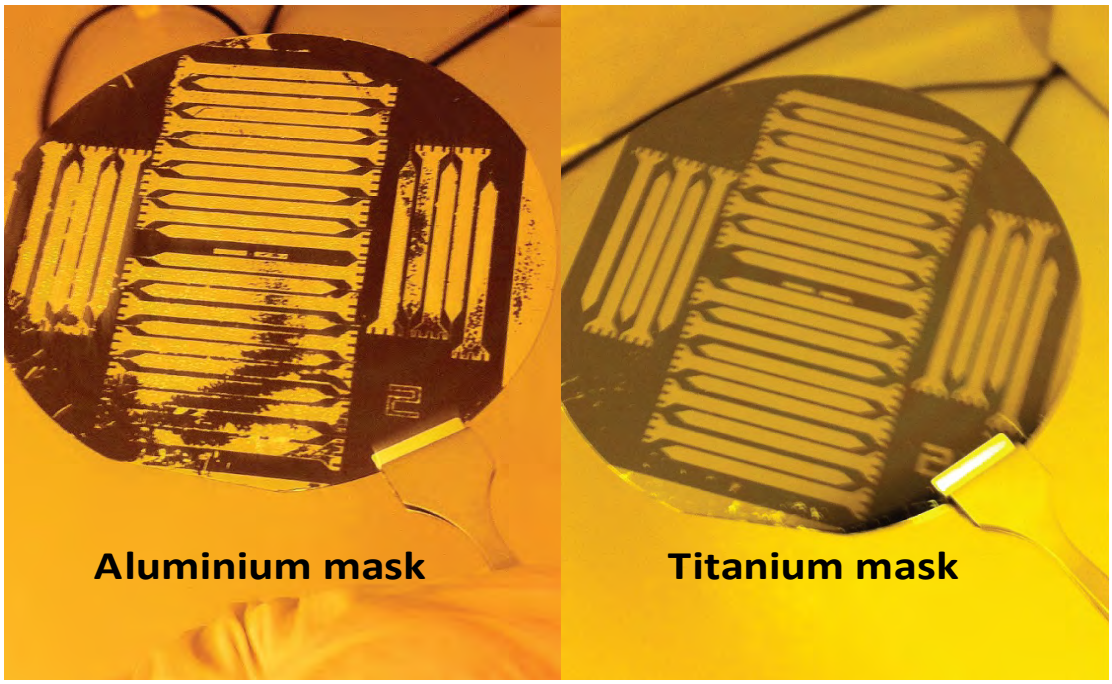

Figure 2.9. Aluminium and titanium mask on a parylene-C layer after lift-off. Aluminium mask shows metal flaking indicating bad adhesion. Titanium mask is more adherent and all features are resolved properly promoting its use as a mask for parylene-C RIE.

2.8.1.2 Optimising etch rate parameters for thick Parylene-C films

For reactive ion etching (RIE), three parameters were controlled in order to achieve the desired film patterning: power, pressure and gas flow rate. Power is related to the vertical anisotropic etching and pressure to isotropic chemical etching. Increasing the pressure and flow rate, increases the etch rate but due to isotropic etching there is a potential loss of critical dimension (required dimension from the original mask design) especially when etching thick layers. With our design such a critical dimension loss may result in defects in the electrode insulation. Therefore an etch recipe was found to increase the vertical etch for parylene-C etching while achieving a good etch rate. Wafers coated with parylene-C and the subsequent titanium mask was subjected to either 175 W and 50 mTorr or 200 W and 50 mTorr power/pressure settings in the RIE machine (Plasma-Therm 790, USA). The gas flow rate was kept constant at 18 SCCM for both conditions. The etch step was recorded periodically over a 30 minute time period with the use of a profilometer (Tencor P-1, USA). After the etch, samples were appropriately cleaved to check the sidewall profile with the use of optical microscopy. Sidewall angles were measured from the optical images in the Matlab environment (2009a, MathWorks, USA).

Figures 2.10 and 2.11 show the sidewall profile for 10 μm parylene-C after etching using different RIE parameters. Parameters of 200 W and 50 mTorr pressure was preferred due to the achieved vertical etch, as shown by the angle (89^{O}).

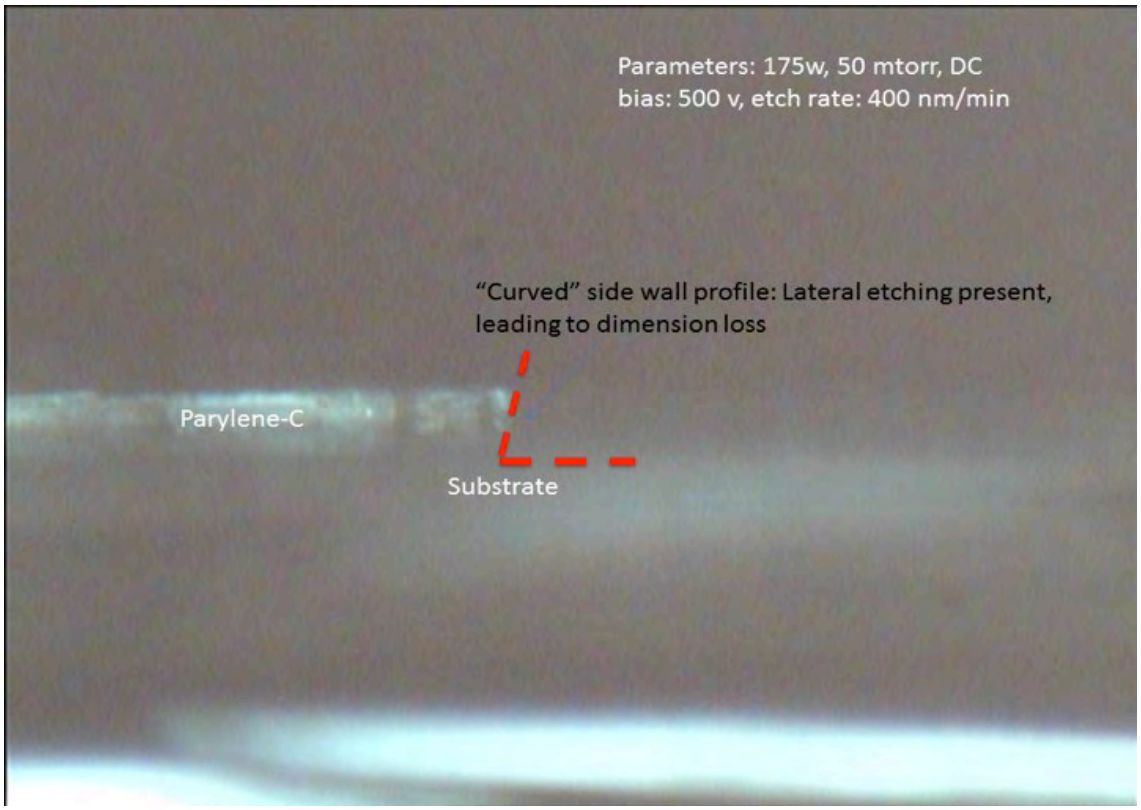

Figure 2.10. The side wall profile for parylene-C, after etching with oxygen plasma at settings of 175 W and 50 mTorr pressure. A side wall angle (dashed red-line) of 85^{O} was obtained.

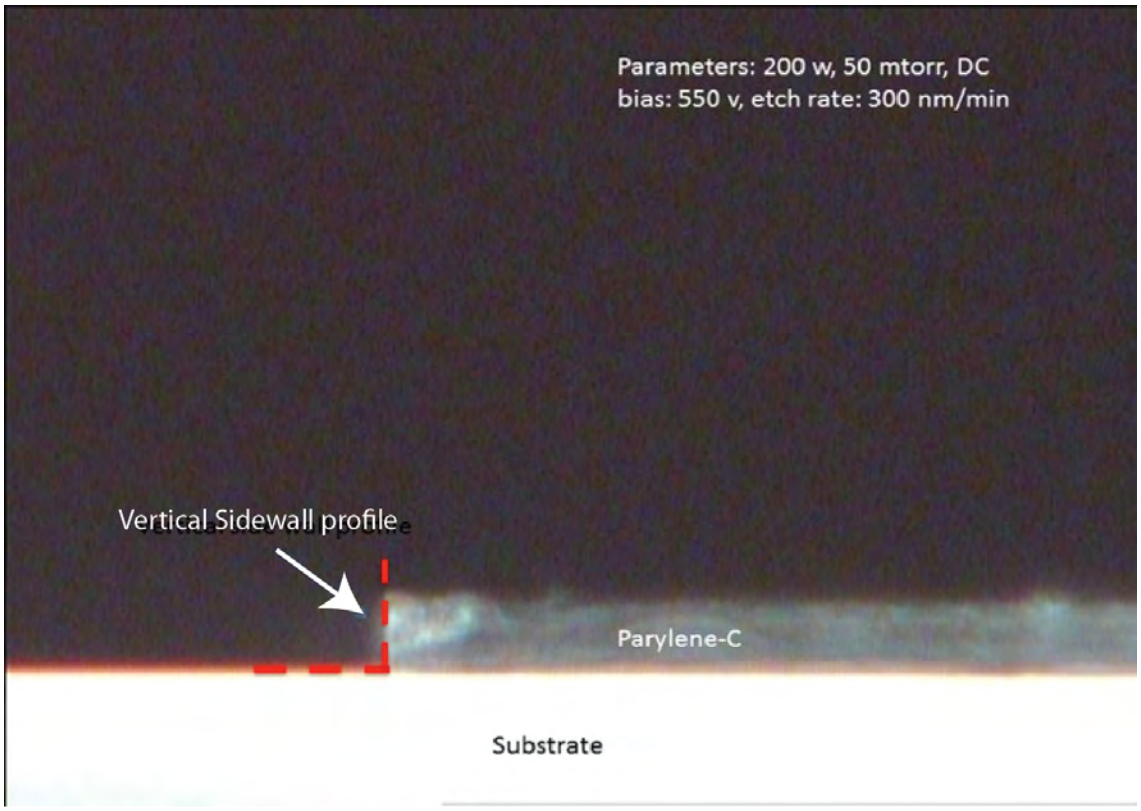

Figure 2.11. Parylene-C side wall profile, after etching with oxygen plasma at settings of 200 W and 50 mTorr pressure. A side wall angle (dashed red-line) of 89^{O} was obtained, showing the feasibility to use this etch recipe for parylene-C patterning.

2.8.1.3 Etch rate

The etch step and subsequent etch rate for Parylene-C at 200 W and 50 mTorr is shown in Figure 2.12. There was a decrease in the etch rate towards 30 minutes as the parylene-C may have been etched completely before this time period. The overall etch rate was 226 nm/min, if the full recording period was considered. Discounting the final recording period the etch rate was 301 nm/min. Both etch rates enabled a 20 μm parylene-C layer to be etched in under 90 minutes at these RIE settings. For the fabrication process, samples were checked for complete parylene-C etching after 70 minutes. If needed the etch recipe was run for more time with regular etch checks at 5 minute intervals to determine complete etching.

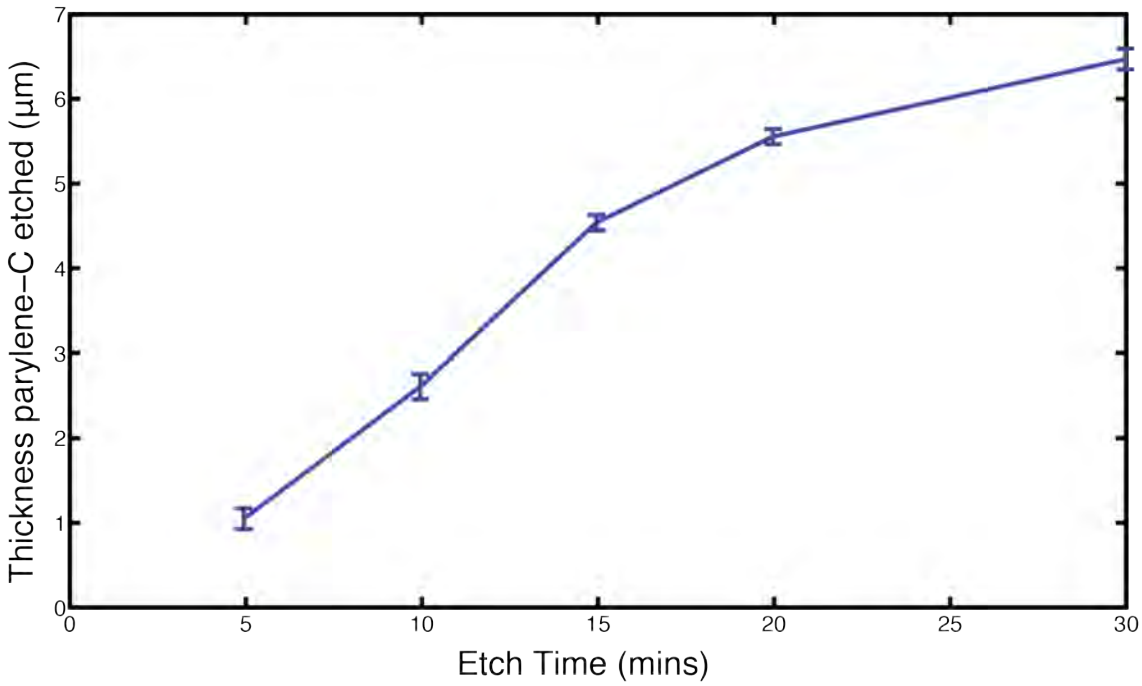

Figure 2.12. Thickness of parylene-C etched (±SEM) as a function of time (n=3 samples). There was a decrease in the etch rate between 20-30 mins as the parylene-C may have been completely etched before the extremity of this etching period. An overall etch rate of 301 nm/min is obtained discounting the final recording period. It was predicted to take 67 mins to etch a 20 µm thick parylene-C layer.

2.8.1.4 Titanium mask over the etch period

The titanium mask (40 nm), deposited by e-beam, was subjected to 200 W and 50 mTorr RIE over a 120 min time duration to check mask integrity. This time period was more than ample to allow for the complete etching of the parylene-C layer. There was no change in mask integrity over a 120 minute period, further corroborating the use of titanium as a masking layer for parylene-C. Also, any imperfections in the mask layer were directly translated to the underlying parylene-C (Figure 2.13). Therefore it was critical to have a successfully deposited titanium mask via lift-off.

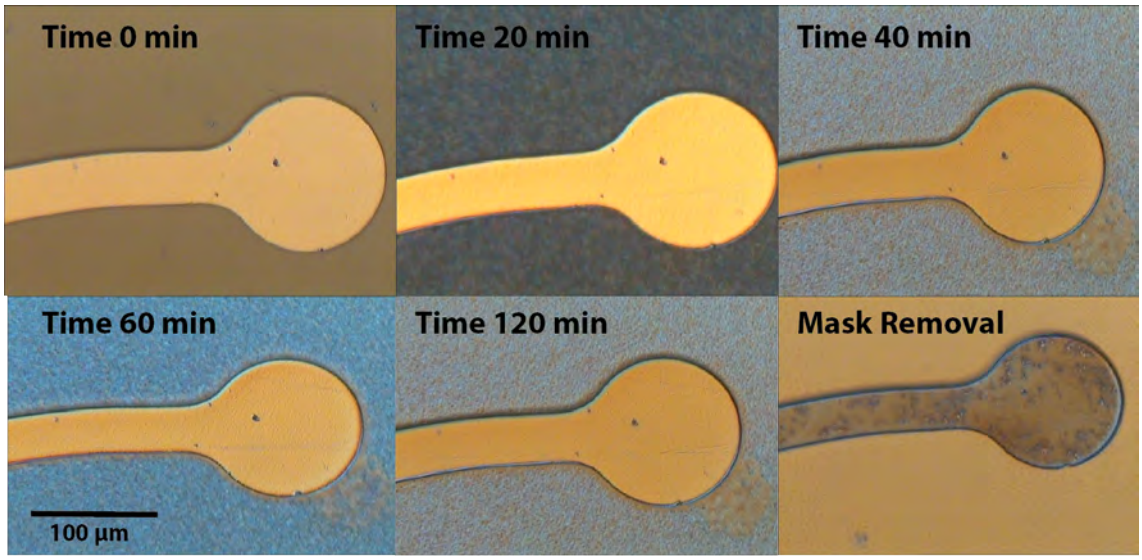

Figure 2.13. Titanium mask over a 120 min etch period. The titanium mask remained intact over the etch period showing that it was a suitable masking metal for parylene-C etching.

In summary, a titanium mask was preferred over aluminium due to enhanced adhesion and remains intact over a 2 hour etch period. The preferred RIE parameters were 200 W and 50 mTorr as corroborated by the highly vertical anisotropic etch.

2.8.2 Polyimide

Polyimide was utilised as a comparison dielectric. Although Parylene-C is superior in dielectric qualities, a direct comparison for polyimide and parylene-C was performed to ensure that the most superior dielectric was chosen for the electrode design.

2.8.2.1 Deposition

PI-5878G (HD MicroSystems, USA) was chosen to be a comparison dielectric to parylene-C due to similar electrical and mechanical properties (table 1.2). The polyimide was spin deposited on to a three-inch Si (300 µm thickness; single sided polished) wafer coated with an aluminium sacrificial layer via pastette deposition. To achieve a similar thickness as parylene-C, the polyimide had to be deposited in two layers with a soft-baking step in between. The polyimide was then soft-baked in accordance to manufacturers guidelines, 120 ^{o}C for 30 minutes in a convection oven (Figure 2.16). Further films were then fully cured in a N_2 environment at 350 ^{o}C for 2 hours to drive away any remaining solvent and for complete imidization.

2.8.2.2 Polyimide vs Parylene-C bubble test

Dielectric failure has been attributed to the accumulation of bubbles within the layer (Rubehn and Stieglitz, 2007), leading to pitting over time (Figure 1.16). A bubble test was performed on polyimide and parylene-C coated on three-inch wafers with an aluminium sacrificial layer. Ten, random images were taken for layers on x 5 optical magnification. The number of bubbles per image was counted manually with the use of ImageJ64 software (NIH, USA). A t-test was then performed to compare the two groups. The polyimide layer had a significantly greater number ($t= 6.2$, $P<0.001$) of bubbles than a parylene-C layer. An overall ratio for the number of bubbles in polyimide compared to parylene-C was calculated at 8:1. Therefore, we also show that parylene-C was superior to polyimide as the dielectric has less potential for device failure due to pitting (Figure 2.14). This difference may be attributable to the deposition methods used. Polyimide was deposited using plastic pipette deposition, which may lead to an increase in bubble formation in the polyimide solution before application onto the wafer.

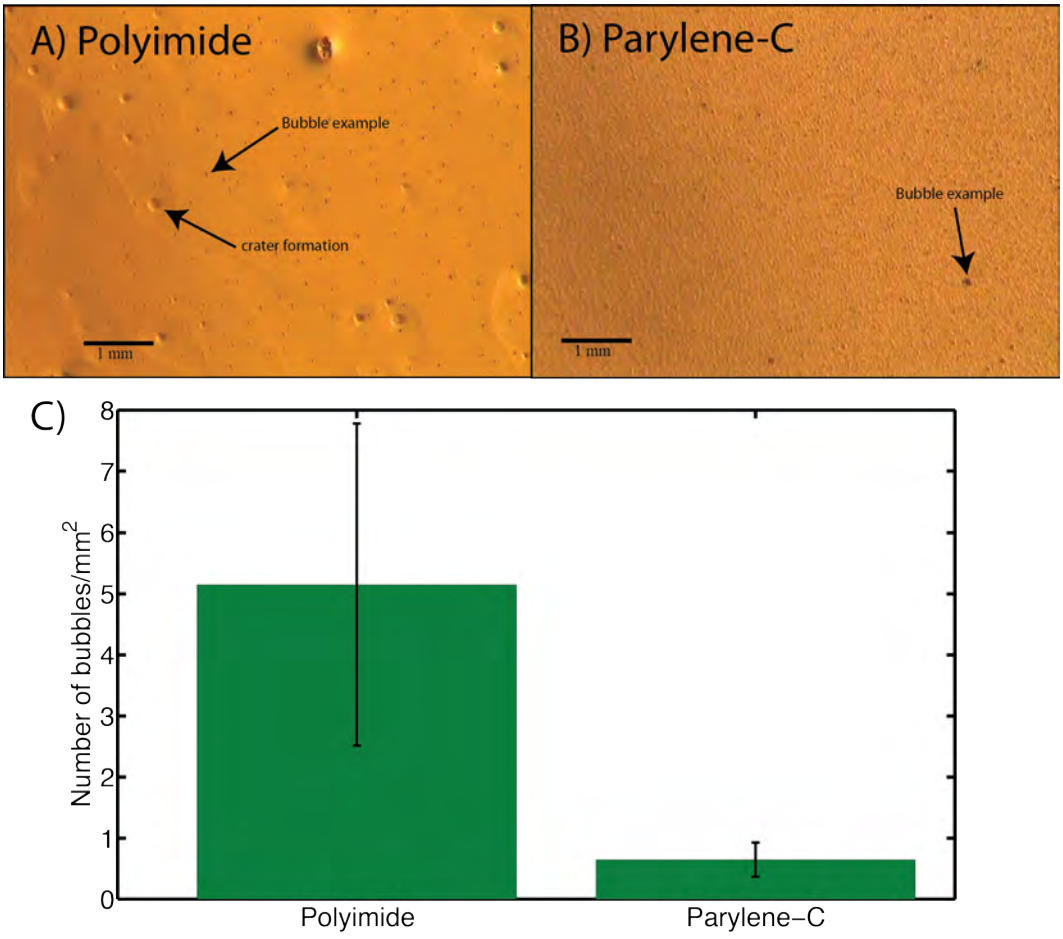

Figure 2.14. Representative image of a polyimide (A) and parylene-C (B) layer. Camera polarisation has been utilised to better visualise bubble formation. The parylene-C layer had a slightly rough aluminium layer underneath and roughness is visible due to the conformal coating nature for parylene-C; bubble visualisation remains unaffected. C) Bubble comparison test for a polyimide and parylene-C layer. Overall an 8:1 ratio is obtained for polyimide to parylene-C bubbles. For polyimide and parylene-C mean±sem values of 5.15±2.63 and 0.65± 0.28 bubbles/mm^2 are obtained respectively. The greater variation for polyimide further adds unpredictability about dielectric performance in respect to bubble formation.

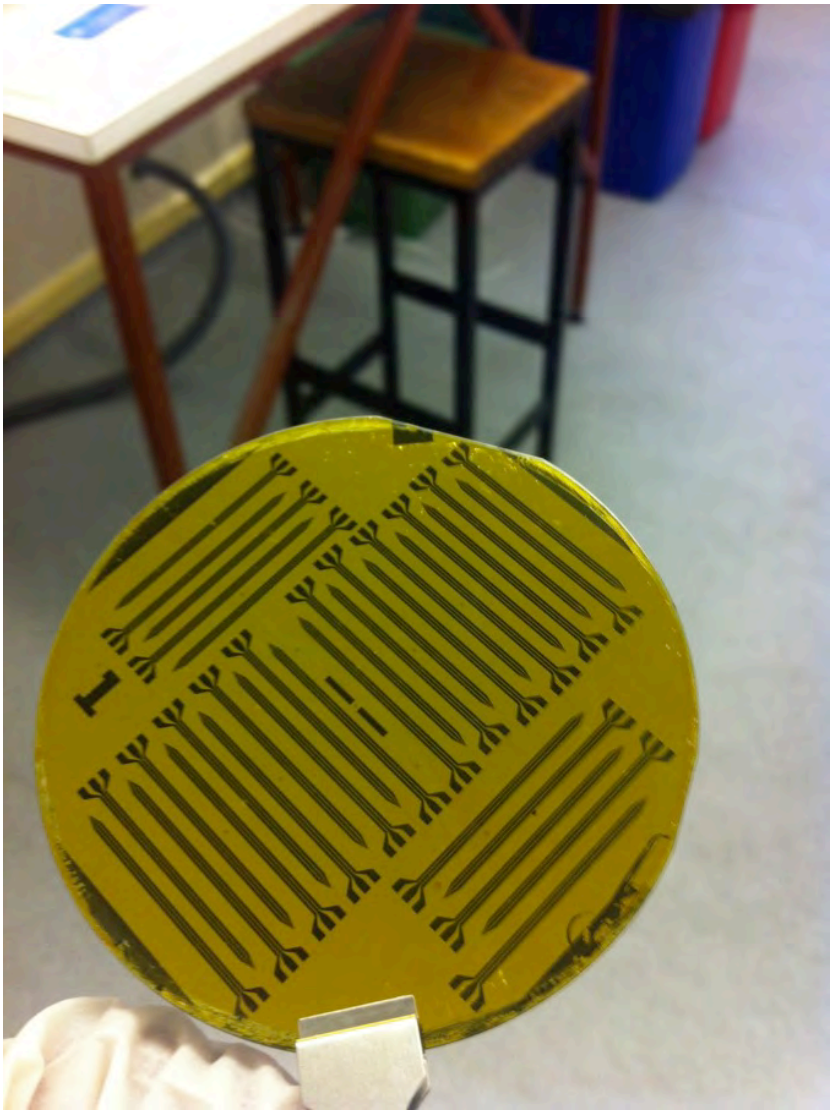

Figure 2.15. Polyimide based sinusoidal probes. Wafer diameter is 3 inches. Fabrication using polyimide was stopped due to the complexities in obtaining conformal and bubble free layers. This may have been related to the plastic pipette deposition used before the polyimide spin process.

2.8.2.3 Problems with polyimide

Problems were encountered with the polyimide layer. The layer proved to be very non-uniform with a large edge-bead, which was problematic when depositing and patterning a masking layer to etch the thick polyimide (Figure 2.14-2.15). Mask to sample contact was poor and alignment difficult, limiting optical lithography. The polyimide layer had many air bubbles trapped within the layer, which would inevitably lead to premature device failure. Device fabrication using polyimide was subsequently abandoned due to the complexities and limitations involved with fabrication and successful layer deposition.

2.9 Metal Deposition

To obtain thick metal films, sputter deposition was used. To achieve a 1 μm WTi layer, either a dual deposition from two separate targets, one tungsten and titanium, or from one sintered metal target was considered. The separate target approach was ruled out due to potential changes in deposition rates leading to different weight percentage metal composition. To simplify the process, a sintered target with WTi was purchased (Pi-Kem Ltd, United Kingdom); this is a common approach to WTi deposition across the industry.

WTi deposition rates were calculated before the successful deposition of a 1 μm layer. Alternative power settings were used on the sputtering machine (Kurt Lesker PVD, USA) and total deposition (nm) over a 30 minute period on silicon test samples was calculated using a profilometer (Tencor, USA). A 100 W power setting was desirable as the increase in WTi deposition rate between 100 and 150 W is negligible. Through clean room observation, running the sputtering machine at power settings above 100 W also risked machine over-heating over relatively long deposition periods.

From the deposition data, a 1 μm WTi layer was obtained in 135 minutes at 100 W; this protocol was used consistently throughout fabrication (Figure 2.16a).

For W deposition, a potential comparison electrode metal, a 100 W power setting was desirable (Figure 2.16b). A 1 μm tungsten layer was obtained in 109 minutes.

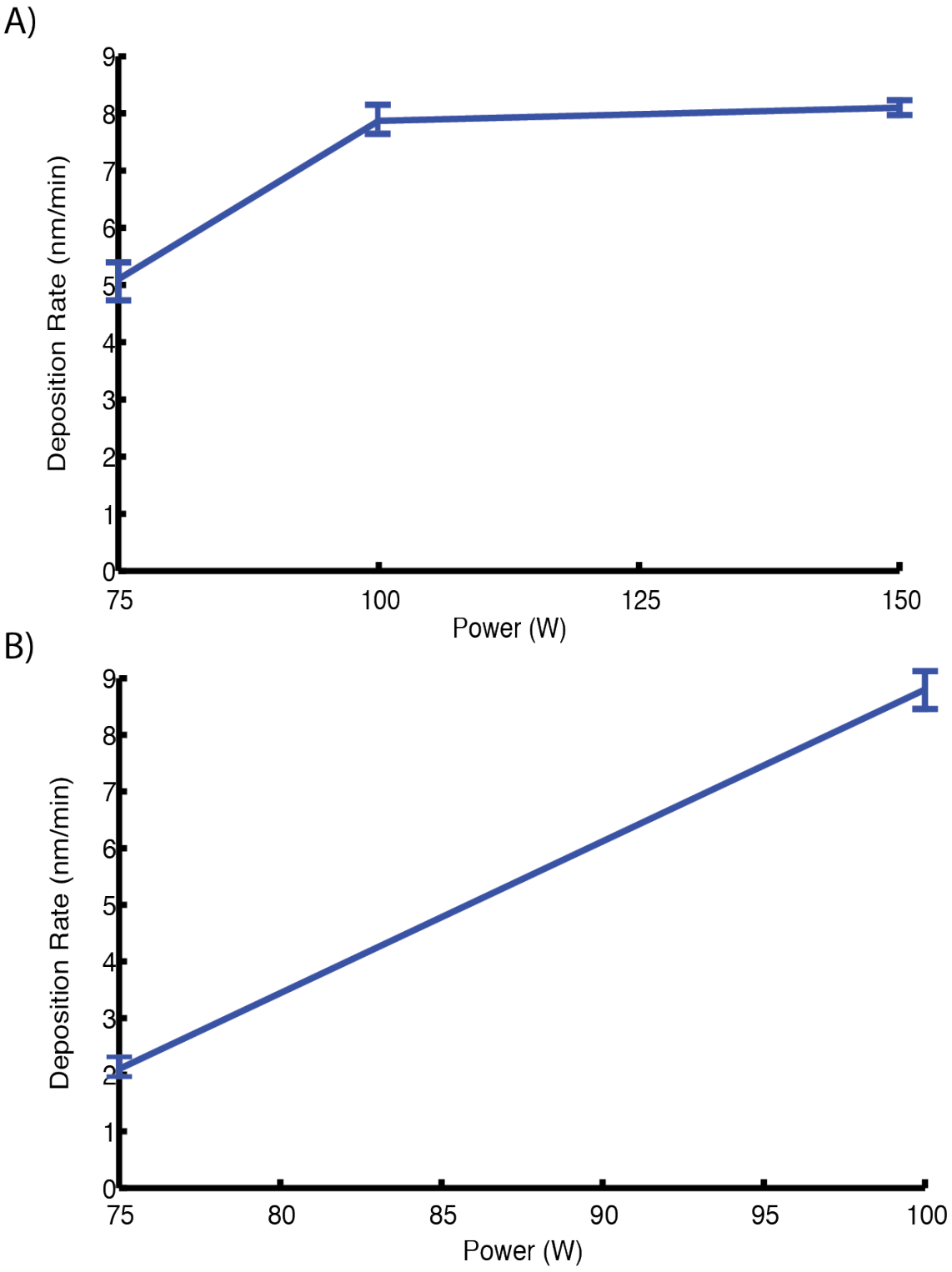

Figure 2.16. Deposition rate (±SEM) calculated over a 30 minute period for Tungsten-titanium (A) and Tungsten (B) for different sputtering machine power settings.

2.9.1 Metal patterning

WTi metal etch parameters were optimised to allow for the successful patterning of our electrode tracks, recording sites and bondpads. Both Wet and RIE etch processes were considered.

2.9.1.1 Wet Etching

Hydrogen Peroxide is known to etch tungsten, the primary constituent of the WTi film (Williams et al., 2003). We hypothesized that our metal film could be etched using such a wet etch. Our first generation electrodes were subjected to hydrogen peroxide (30%), with potential metal and dielectric etching observed with optical microscopy. Complete etching occurred for the metal after a 40 minute time period, with no visible effect on the parylene-C layer (Figure 2.18).

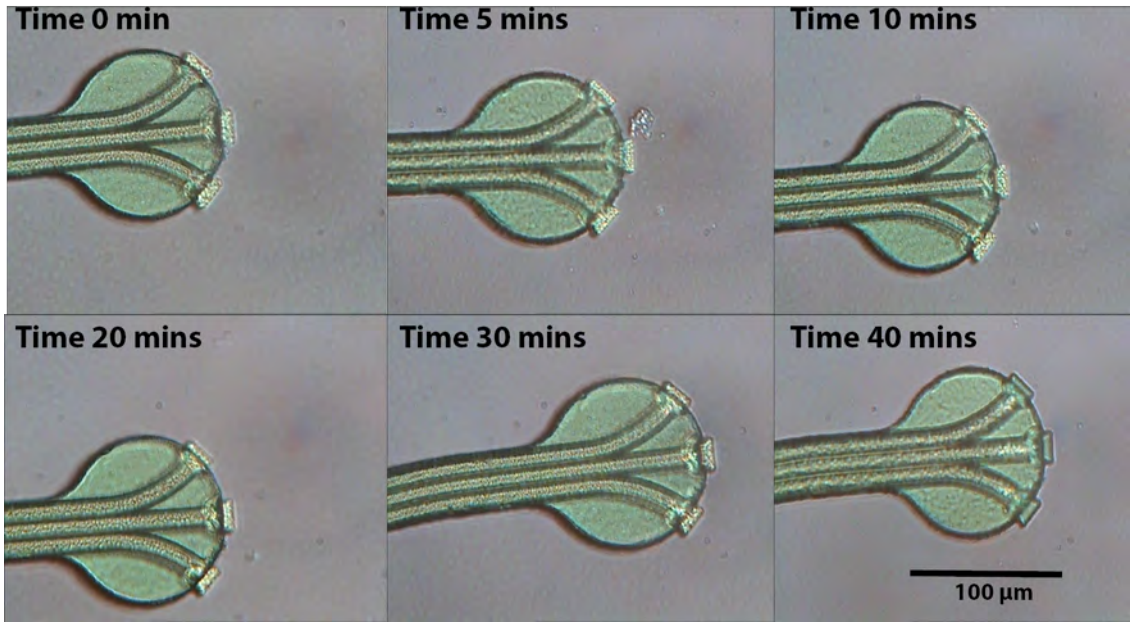

Figure 2.17. Representative images of a probe over a 40 minute time period in hydrogen peroxide. Note the metal was missing from the 3 recording sites at the 40 minute time point.

Although hydrogen peroxide etched a 1 µm tungsten-titanium layer over 40 minutes, the long etch duration would potentially lead to isotropic etching and dimension loss. A combination of ammonia hydroxide and hydrogen peroxide has been used in microfabrication to clean samples. We hypothesized that by combining the two chemicals, the reactivity of hydrogen peroxide might be enhanced, leading to a shorter etch duration and hence decreased potential for isotopic etching. Again our first generation electrodes were subjected to a mixture of ammonia hydroxide (30%) and hydrogen peroxide (30%) (1:1 ratio). WTi was completely etched between 3-5 minutes

with the parylene-C layer remaining unaffected as corroborated by optical microscopy (Figure 2.19). Photoresist remains unaffected over this time duration (Figure 2.20). Therefore this wet etch was confirmed to etch the WTi layer effectively.

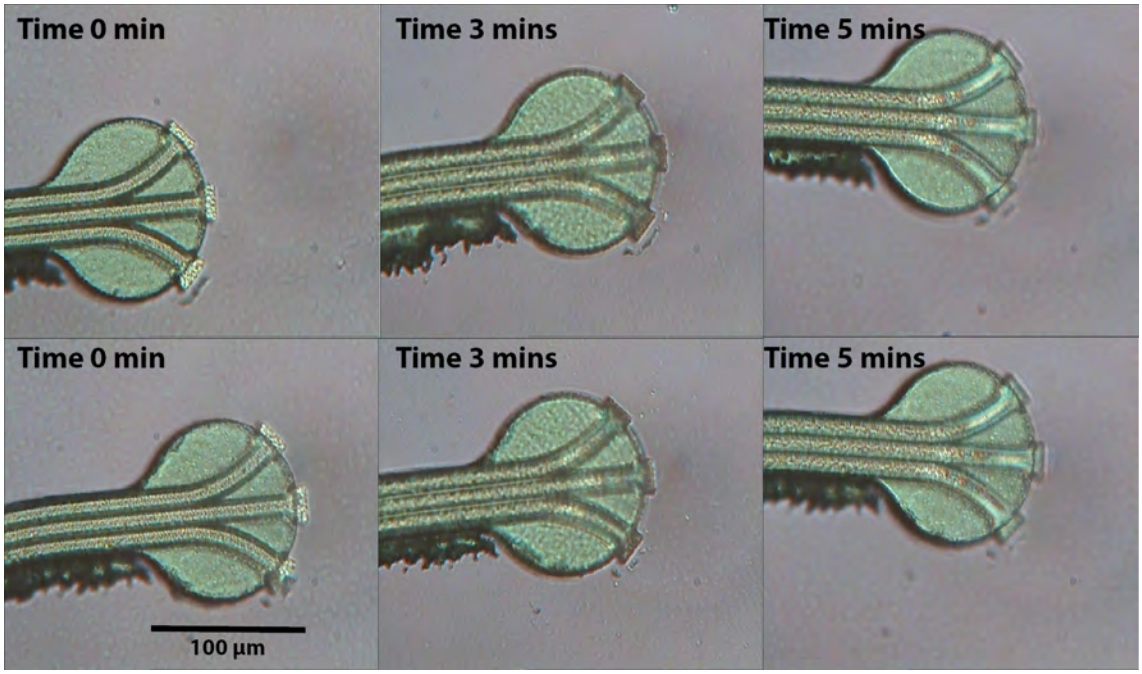

Figure 2.18. Representative images of two probes over a 5 minute time period in hydrogen peroxide (30%) and ammonia hydroxide (30%). Between 3-5 minutes the WTi was etched away with a mixture of hydrogen peroxide and ammonia hydroxide (note lack of metal for the three recording sites at time 5). This was a faster etch than using hydrogen peroxide alone, which was etched completely after a 40 minute etch period. The dark shading around the probe were lithography defects resulting from first generation probe microfabrication.

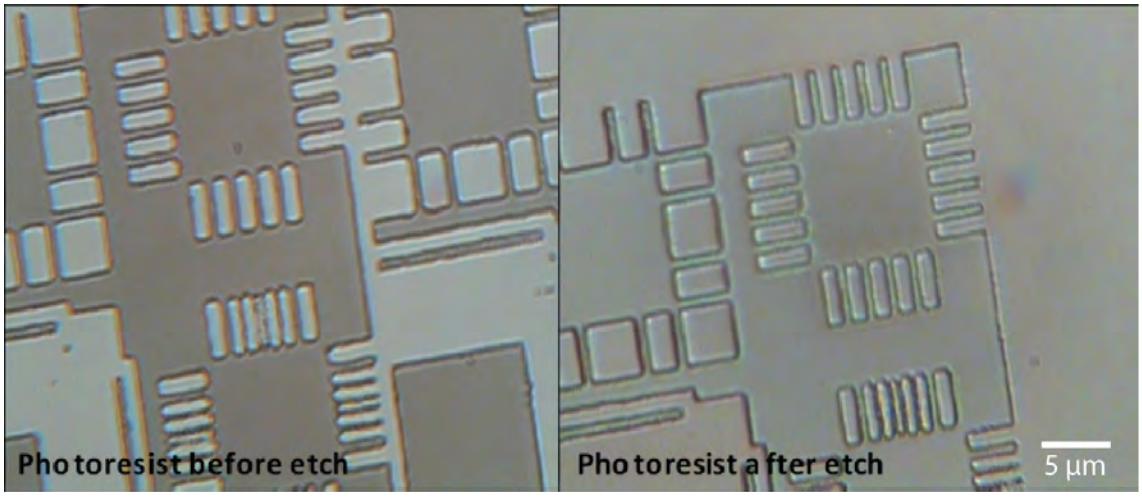

Figure 2.19. Photoresist over a 5 minute etch period in hydrogen peroxide and ammonia hydroxide solution. Photoresist remains intact over the etching period.

2.9.1.2 Lift-off

Using a lift-off process would allow the use of any metal in the fabrication process. To achieve a 1 μm metal layer a thicker photoresist (3-3.2 μm thickness, post-soft baked) was used (TI-35es, HD Microchemicals, Germany), as from experience AZ-5214E photoresist gave limited lift-off success at these metal thicknesses. For our parylene-C substrate, the lithography for TI-35es was very unpredictable, with similar parameters leading to different lithographical outcome (Figure 2.20). Therefore lift-off was not recommended for metal patterning, although further optimisation may lead to successful photoresist sidewall profile suitable for lift-off for thicker metals on a parylene-C substrate.

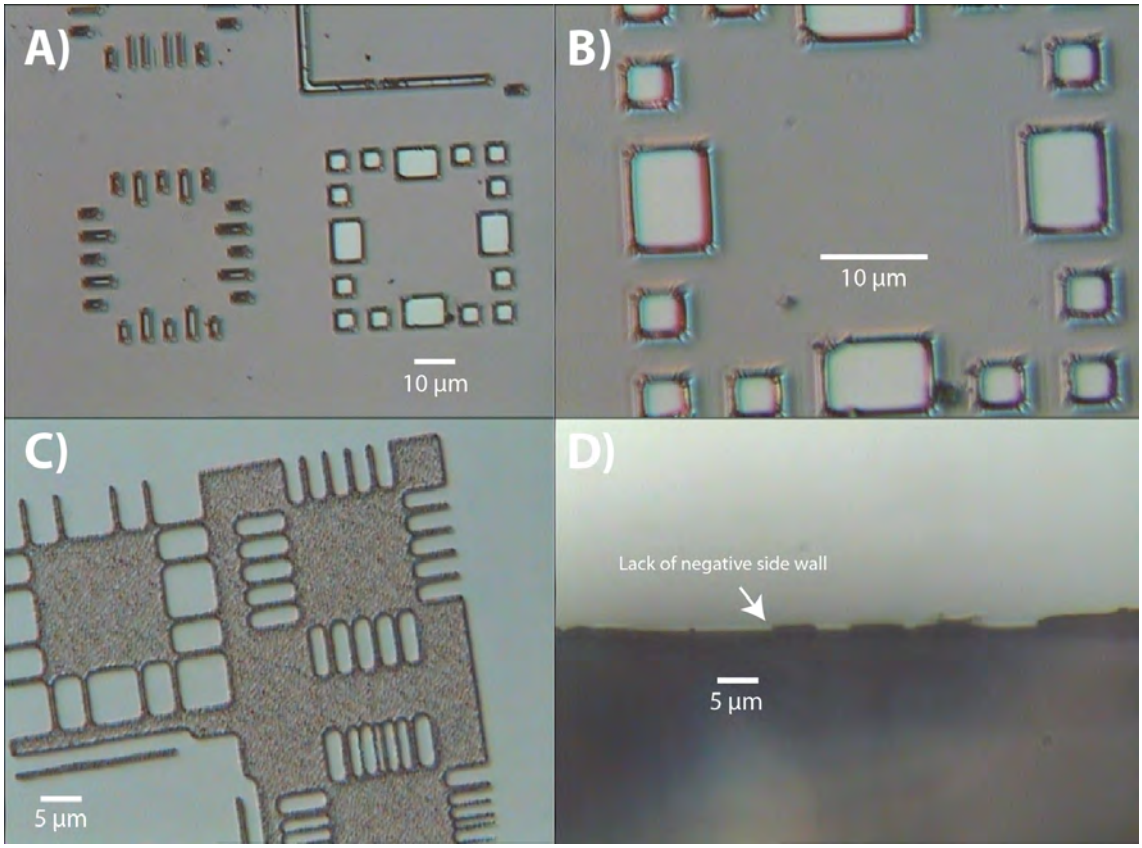

Figure 2.20. Lift off with thick photoresist. Although features have resolved well A) and B) and C), the edges are still rough that made lead to unpredictable lift off. Negative edge profiles are not achieved (D), which is required for successful lift off.

2.9.1.3 Dry Etching

Sulphur hexafluoride with/without oxygen has been shown to etch tungsten-titanium films (90/10 wt%) with an etch rate of 550 nm/min (Williams et al., 2003). Lithography was performed on wafers fabricated to the stage of WTi metal deposition. AZ-5214E photoresist (AZ Electronic Materials, Germany) was spun on (Electronic Microsystems Photo Resist Spinner, United Kingdom) to wafers, soft-baked, exposed with our first mask, and developed in accordance to manufacture guidelines. To make the photoresist more resilient to RIE, a hard baking step was employed at 115^{o}C in a convection oven for 30 minutes. An etch recipe of 200 W, 150 mTorr pressure and gas flow rate of 10 SCCM was used for a 3 minute etch duration with SF_6. This "over-etch" was employed to surface roughen our first parylene-C layer to promote adhesion for the second parylene-C layer. The WTi layer was successfully patterned using this recipe (Figure 2.21). After WTi etching, the photoresist required removing. Acetone was used to strip the hard-baked photoresist, although acetone ultrasonication was ruled out due to metal track damage (Figure 2.22).

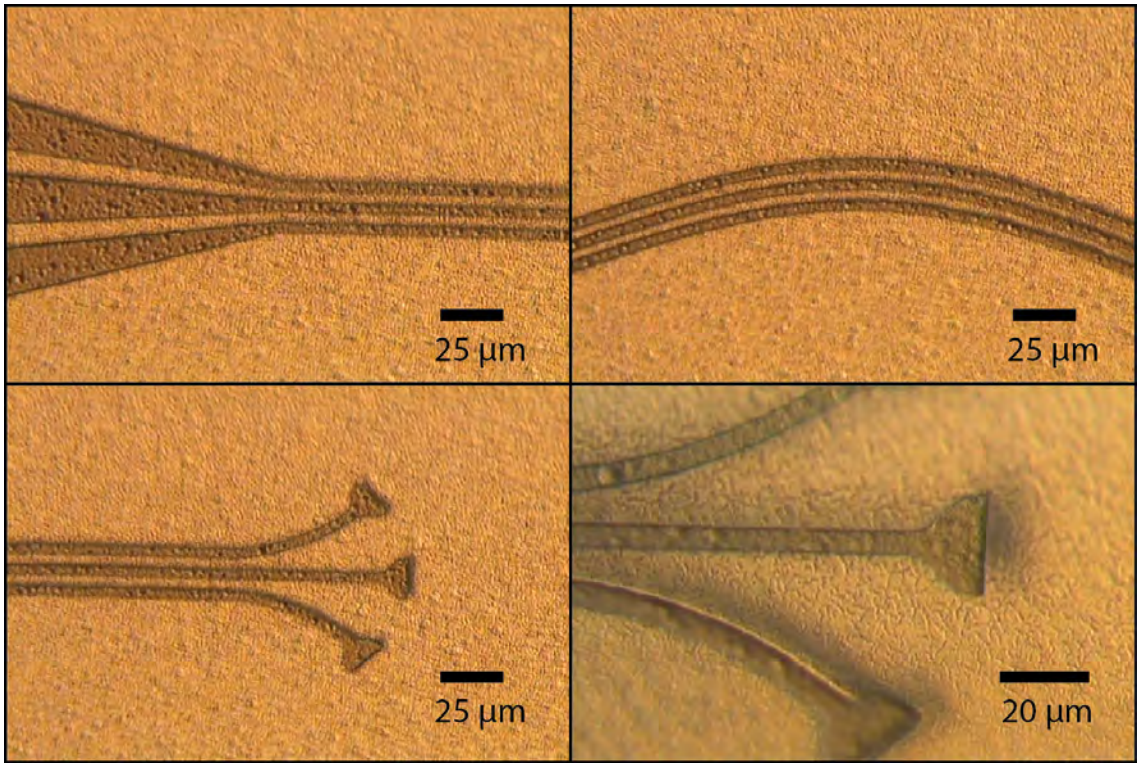

Figure 2.21. Patterned WTi layer with sulphur hexafluoride gas. Features are clearly defined with limited or no dimension loss.

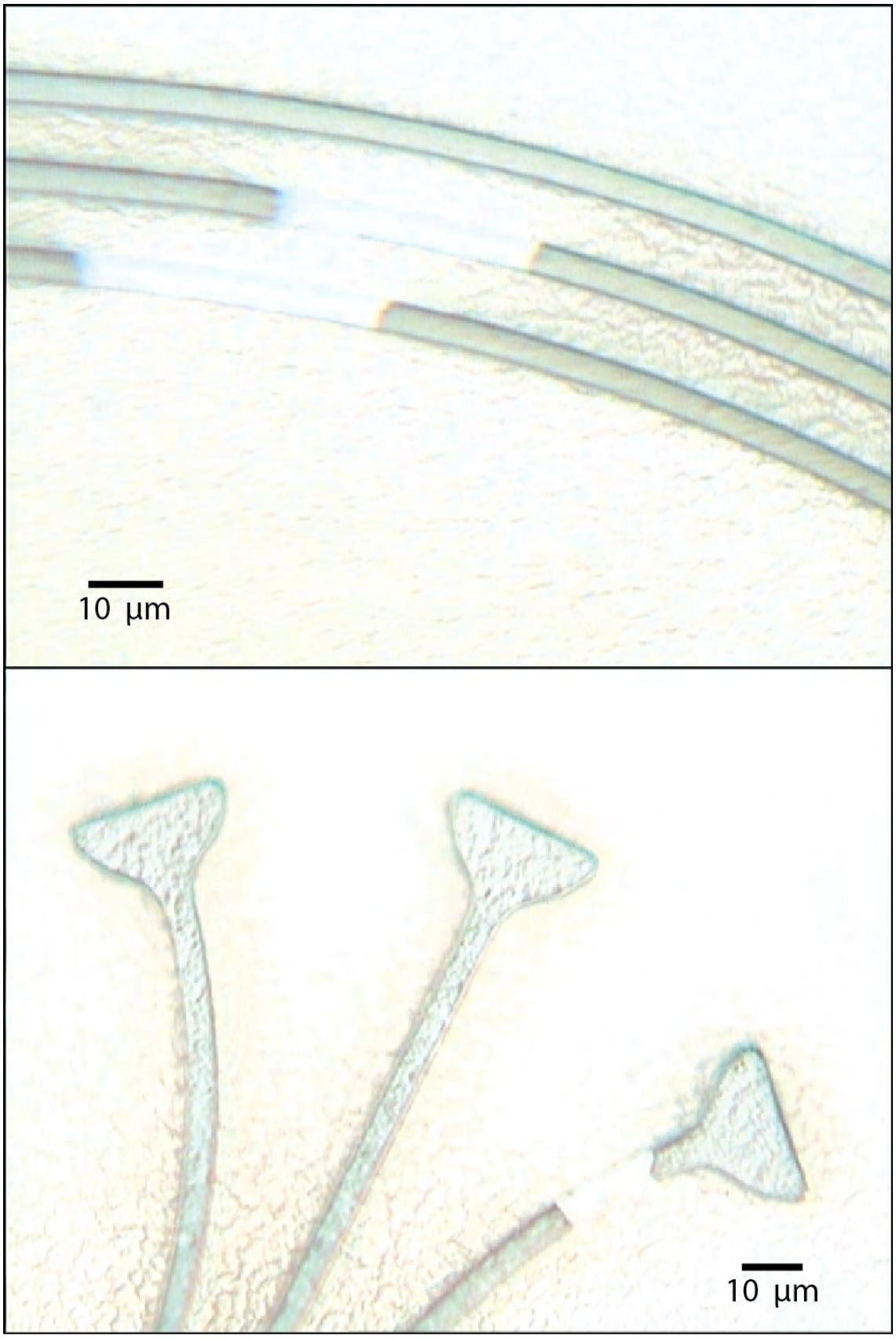

Figure 2.22. Damage to WTi layer after photoresist mask removal via ultrasonication

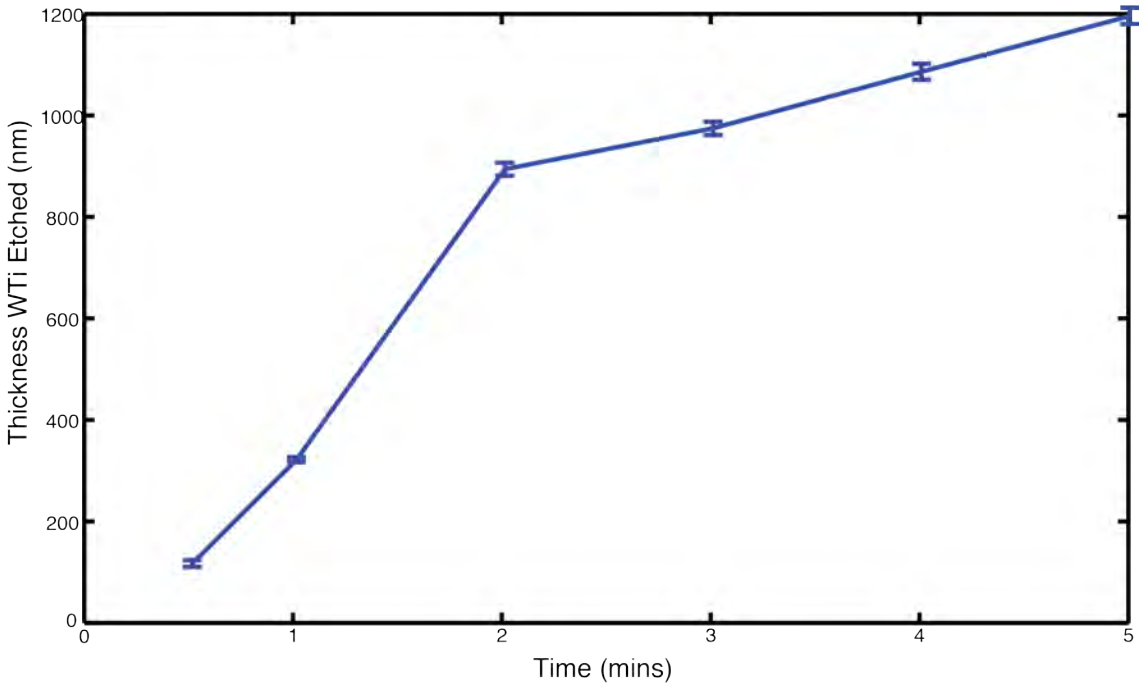

Figure 2.23. WTi thickness etched by SF_6 over a 5 minute period (±SEM, n=3 samples). Between 0.5--2 minutes the etch rate was 480 nm/min. WTi etching primarily occurred in the first two minutes. There was a decrease in the etch rate between 3-5 minutes as the underlying parylene-C layer was being etched, so these time points were not included when measuring the overall WTi etch rate.

Figure 2.23 shows the etching parameters for WTi. Most of the etching occurs between 0-2 minutes. There was a reduction in the etch rate between 3-5 minutes as the underlying parylene-C was now being etched.

Dry, over wet etching was preferred as the etch was very quick and reproducible with no visible dimension loss. The additional over-etching provided surface roughness to our first parylene-C layer to enhance adhesion between the two parylene-C layers. This did not occur with wet etching.

2.3 Optimised fabrication

Figure 2.24 shows the overall optimised fabrication. Fabrication began with e-beam deposition of 1 µm aluminium, a smooth surface was obtained, which may aid in device release. The first layer of parylene-C was deposited with a thickness up to 10 µm, through an external company. Next, a 1 µm WTi layer was sputter deposited with a power setting of 100 W, which gave a deposition rate of 7.5 nm/min. The layer was subsequently patterned with our first masking layer with SF_6 RIE with parameters of 200 W and 150 mTorr. A slight over-etch was employed to surface roughen the first parylene-C layer to aid parylene-C-to-parylene-C adhesion. Next the second parylene-C layer was deposited. Subsequently both parylene-C layers were patterned using oxygen RIE with parameters of 200 w and 50 mTorr with an etch rate of 226 nm/min, which gave a highly vertical sidewall profile, thus limiting dimension loss. A titanium mask was used for this process. Exposed WTi remained unaltered during parylene-C oxygen plasma etching. Finally, device release was shown to occur through two potential mechanisms: device peeling and aluminium etching with Al etch.

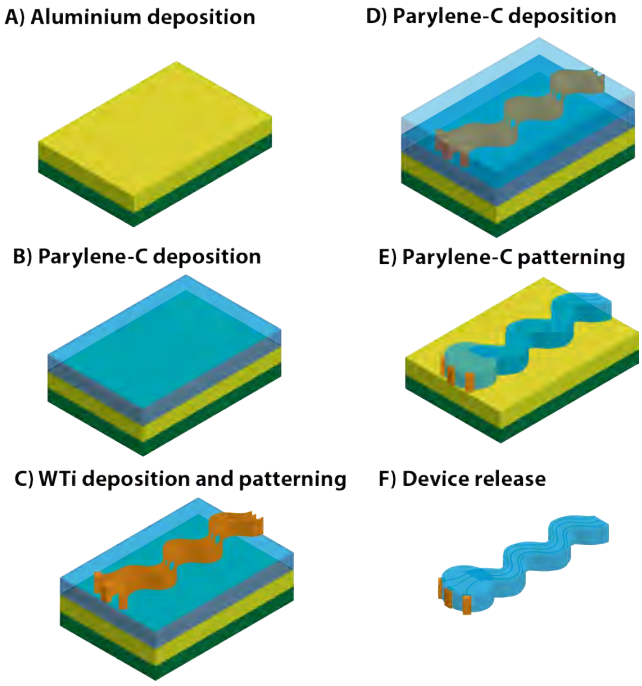

Figure 2.24. Optimised fabrication for the sinusoidal probe. A) Al deposition with a thickness of 1 µm using ebeam deposition B) Deposition of first parylene-C layer through external company C) Sputtering deposition of WTi from a combined target with an over-etch employed to surface roughen the first parylene-C layer and WTi etching to define electrode tracks, recording and bondpad regions. D) Deposition of second parylene-C layer through external company. E) Parylene-C oxygen plasma etching to define the overall electrode shape and re-open recording sites and bond pad. F) Device release through etching of Al sacrificial layer, or device peeling.

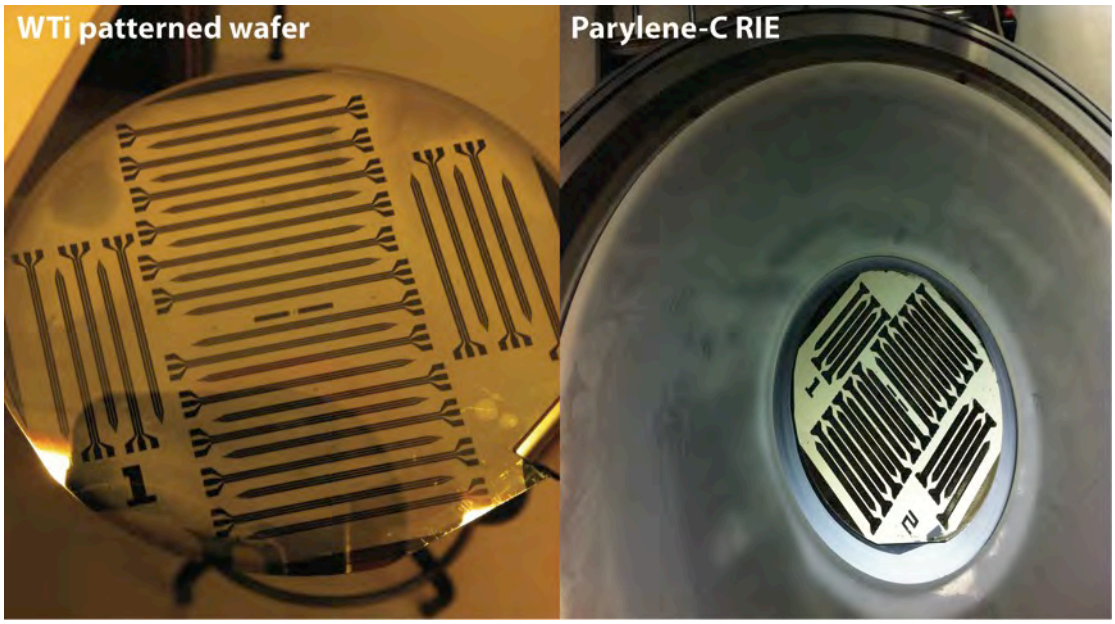

Figure 2.25. Completed patterning of our layers for the sinusoidal probe. Images show our 33 probe on three inch wafer after completed WTi and Parylene-C etching.

2.4 Conclusions

Parameters were optimised to allow for successful sinusoidal probe fabrication (Figure 2.24-2.25). Aluminium was shown to be the optimal sacrificial layer in terms etchant selectivity and lithographical measures. Sulphur hexafluoride dry etch was the best patterning mechanism for WTi, with minimal dimension loss and potential enhancement of parylene-C-to-parylene-C adhesion via over-etching. Oxygen plasma etching parameters for Parylene-C were optimised to achieve a highly vertical anisotropic etch, limiting dimension loss.

Chapter 3: Device testing and process optimisation

3.1 Introduction

Chapter 2 described the parameter optimisation to enable successful sinusoidal probe fabrication. This chapter will concentrate on the bench testing for successfully released devices post-fabrication and further fabrication optimisation. In total, a batch of 7 wafers were fabricated in the first round, followed by a further 10 wafers in order to achieve the project aims. We showed that emerging problems with titanium mask deposition with lift-off for parylene-C layer etching was minimised with conventional lithography. For device release, using tetramethyl ammonia hydroxide (TMAH 3%) etching of aluminium resulted in high functional yields than a device peeling method. To aid device insertion into the brain, a fine tipped steel electrode, placed inside 25 G needles, was the fully optimised device insertion method. The probe was temporarily attached to the fine tipped steel electrode with the use of polyethylene glycol (PEG). Horizontal connector movement during electrode detaching post-insertion was minimised with ribbon cable thermoforming and further PEG attachment of the ribbon cable to the plastic part of a 25 G syringe.

3.2 Emerging Problems with lift-off

The titanium mask for parylene-C RIE was successfully and repeatedly patterned by lift off for the first wafer batch. In the second wafer batch problems developed with 1 out of 11 attempts at lift-off proving successful. Lift-off was not successful, as sporadic metal breaks resulted in “fencing,” and dimension loss leading to insulation failure. Fencing occurred as the edge-profile for photoresist was positive rather than negative meaning that there was no discontinuity in the metal film to allow for patterned structures. Multiple lift-off parameters were tested and lift-off failed for test- and non-test samples.

After exhausting possible parameter perturbations for lithography processing, we hypothesised that lift-off failure was due to under-edge exposure, where ultraviolet light was reflected from underlying metal surfaces as parylene-C is transparent, resulting in photoresist exposure from the both the top and bottom (Figure 3.2). This resulted in uncontrolled sidewall slope formation and lift-off failure, irrespective of changes in

lithography parameters. Figure 3.1 shows under-edge exposure for our samples. There was a sharper defined line when titanium was deposited on parylene-C-WTi interface, rather than the parylene-C-WTi-parylene-C interface. The backscatter for UV light was greater for the latter due to reflection back from the aluminium sacrificial layer. Therefore, at the parylene-C-WTi-parylene-C interface edge definition was worse with observed "fencing." (Figure 3.1).

Parylene-C deposition on WTi patterned structures was conformal. Post-titanium deposition, alignment marks were still visible. Therefore conventional lithography was performed with subsequent patterning of the titanium mask using HF etch (1:50 HF:H_2O), after AZ-5214E photoresist deposition, patterning and hard-bake. After HF patterning, the hard baked AZ-5214E was removed with acetone. This resulted in successful titanium mask patterning and this lithography change was used successfully for the second batch.

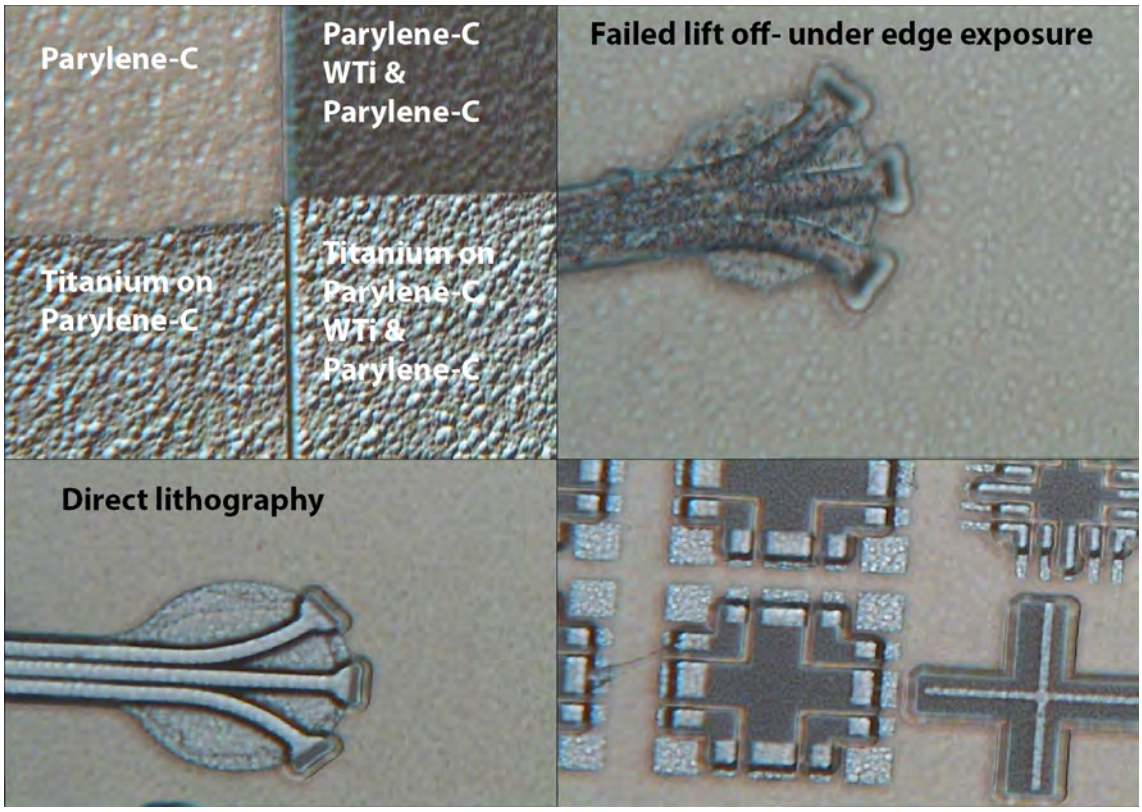

Figure 3.1. Image showing probe with and without conventional lithography. Under-edge exposure for lift off led to significant dimension loss. Conventional lithography resulted in all features resolved with good mask alignment.

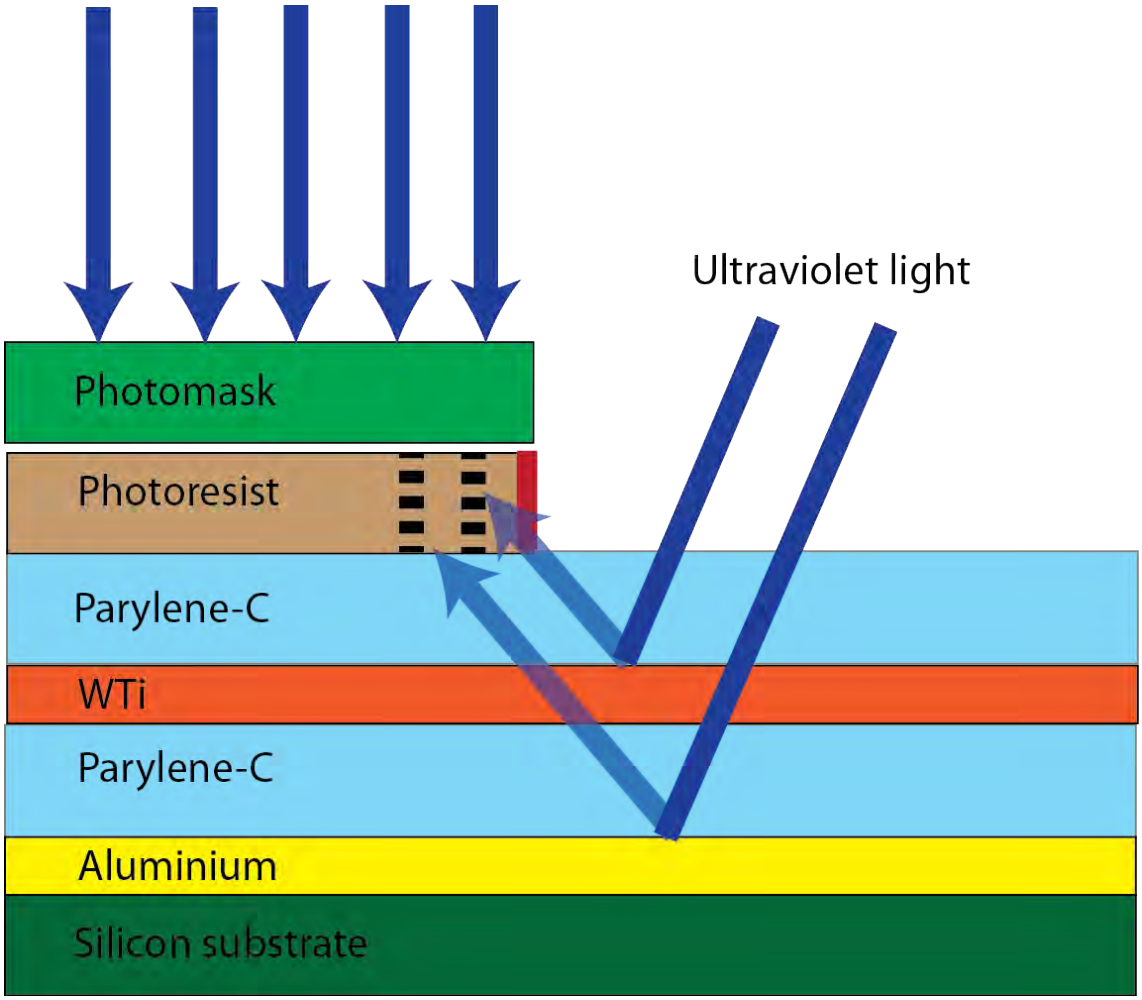

Figure 3.2. Edge on view showing internal UV reflection. Depending on the degree of UV reflection (blue arrows) from either WTi or Aluminium interfaces, the required edge (Red line) will shift (Dotted black lines) causing dimension loss and the "fencing" effect.

3.3 Device release

The titanium mask was removed after parylene-C RIE with BHF (5:1 40% NH_4F : 49% HF) for our first electrode batch. For the first wafer processed, this lead to premature device release with all 33 probes released in less than 10 seconds.

Figure 3.3. Premature device release with BHF use to remove titanium mask. Device interaction leads to probe damage.

Although this was initially determined as a success due to problems encountered with first generation device release, the probes interacted with each other causing damage (Figure 3.3). Also, probes were floating in HF, which was diluted with deionised (DI)

water to enable safe probe handling. DI water addition caused further probe tangling and damage. From this wafer there were limited functioning electrodes.

For the next wafer, an ethanol device release and peeling process was considered before titanium mask etching (Figure 3.4). After parylene-C RIE, another wafer was submerged in a small volume of ethanol. Visually, the devices began lifting-off from the wafer, although not completely, allowing device peeling.

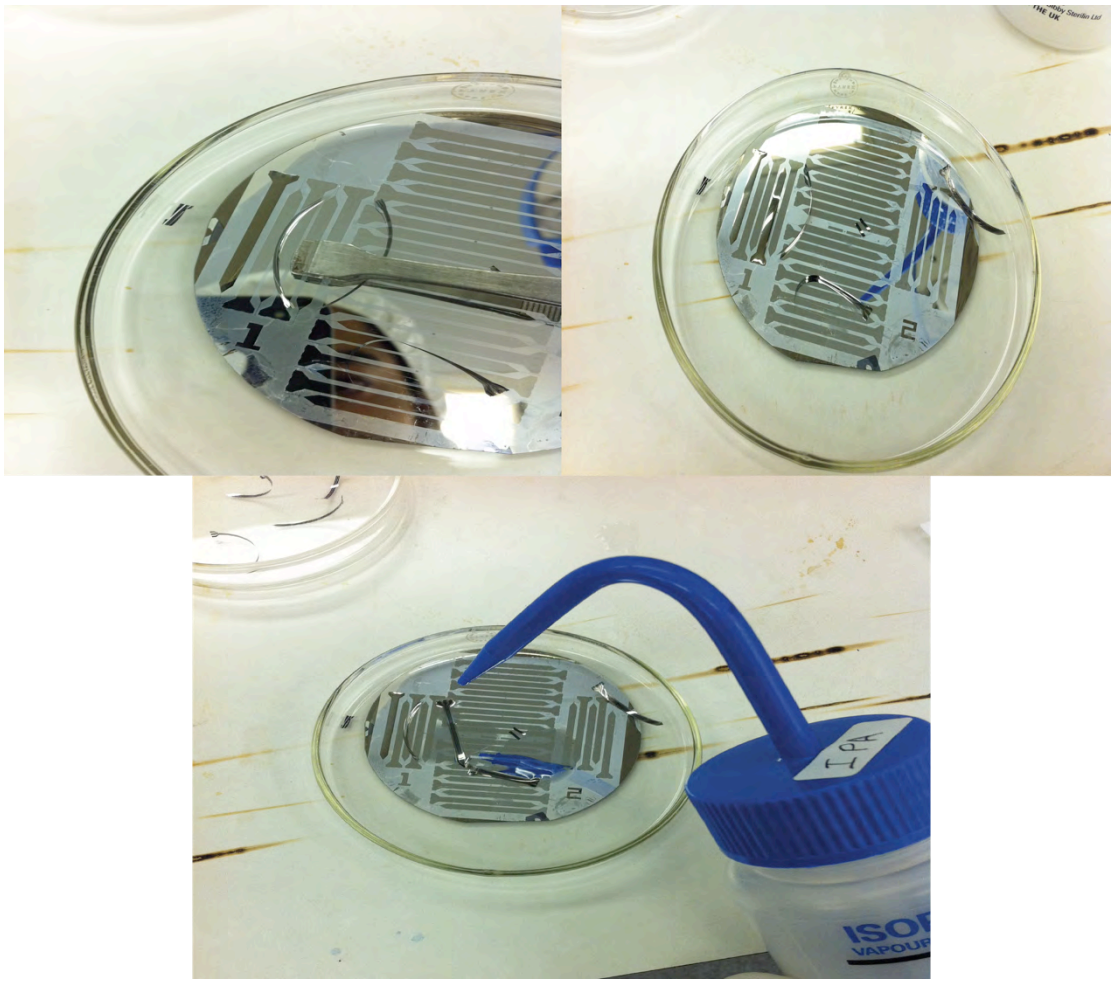

Figure 3.4. Ethanol device release method. Ribbon cable was release before the electrode, which occasionally caused electrode damage.

For the first fabricated batch, this device release method was reproducible and therefore used on subsequent wafers to minimise damage caused by bulk device release. However, it was ensured that devices were peeled or removed from the wafer in one attempt without allowing the ethanol dry, to minimise stiction. Stiction resulted in metal

track damage resulting from exaggerated horizontal plane movement (Figure 3.5), when manipulating the electrode via the ribbon cable while retrieving released devices.

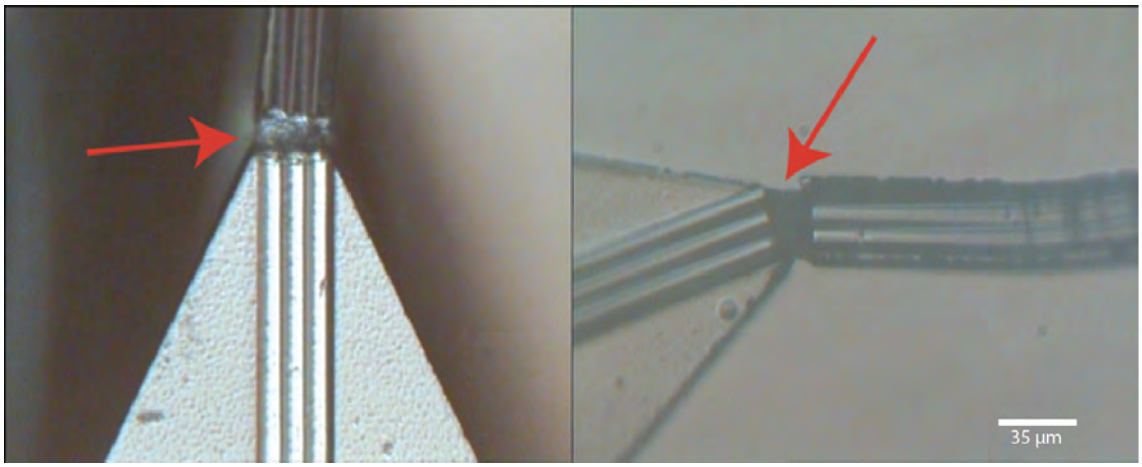

Figure 3.5. Electrode breakages (red arrows) resulting from stiction with the ethanol release method.

The titanium mask was removed with HF use. Firstly, a 1:10 HF:H_2O ratio was used, although this resulted in slight etching and discolouration of the bondpad (Figure 3.6). Subsequently, a 1:20 dilution was used to minimise WTi etching. Titanium mask removed devices were air-dried and appropriately stored for wiring.

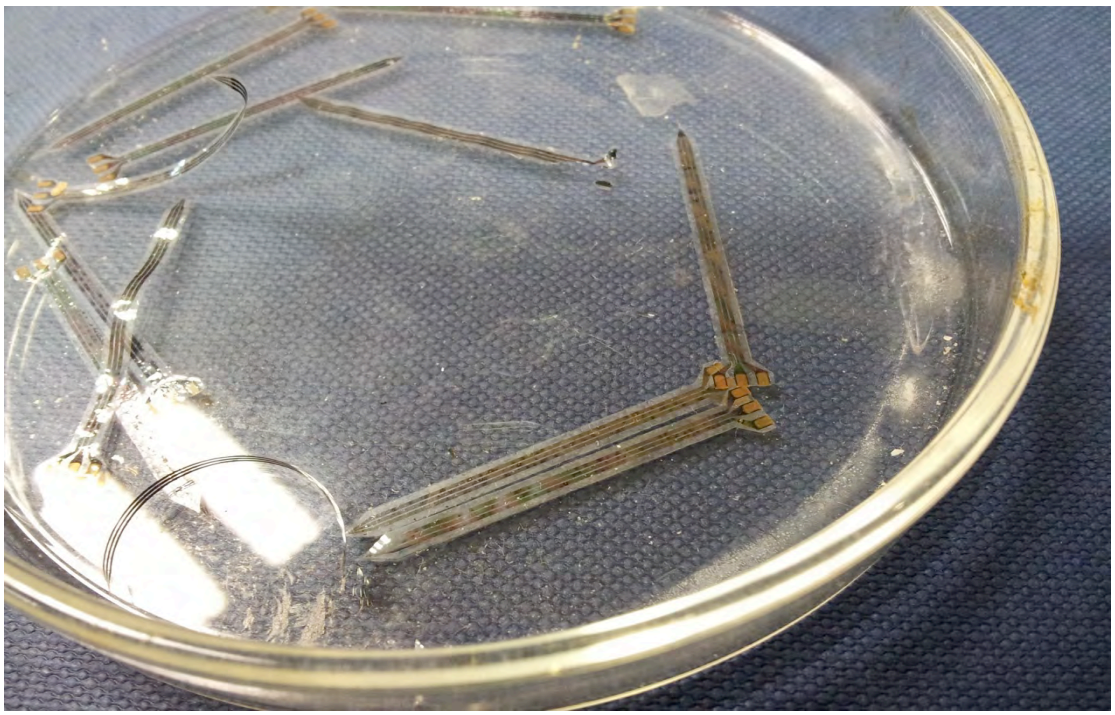

Figure 3.6. Bondpad decolourisation and etching of WTi due to more concentrated HF used to etch the titanium mask, post-parylene-C etching

3.3.1 Second batch device release

Problems were encountered with the second fabricated wafer batch. The adhesion between aluminium and first parylene-C layer was greater; the aluminium sacrificial layer had to be etched away to promote device release.

One wafer was subjected to aluminium etchant for device release. Al etch was heated up to 30^{o}C. Surprisingly, over a 1 hour time period Al etch etched away the WTi without successful device release, contrary to prior extensive testing (Figure 2.5). Therefore device release was further optimised.

Potassium hydroxide was chosen to etch away the sacrificial aluminium layer on another processed wafer. KOH (30% wt) has an etch rate of 12900 nm/min for aluminium (Williams et al., 2003). Although it was reported for sputter deposited WTi that KOH has > 300 nm/min etch rate, for separate sputtered tungsten and titanium the etch rate is zero (Williams et al., 2003). As WTi was sputter deposited, we hypothesised that KOH could be used to etch away the sacrificial aluminium layer with a good selectivity for aluminium over WTi. After 5 minutes, KOH etched the WTi, without successful device release. Parylene-C to parylene-C adhesion was affected due to effervescence due to the reaction of KOH with aluminium, resulting in device delamination. Therefore KOH was ruled out for device release.

Tetramethylammonium hydroxide (TMAH) is found in dilute concentrations in photoresist developer (MIF-326) and can etch aluminium through clean room observations. TMAH is also used to etch silicon anisotropically. Another processed wafer was subjected to TMAH to etch the sacrificial aluminium layer. This etch method was successful as all 33 devices were released within a 1.5 hour period without underlying damage to the parylene-C or WTi. When bare silicon was exposed, 25 % TMAH, rather than MIF-326 was used to ensure reactants were readily available for aluminium etching, as TMAH had a greater selectivity for silicon over aluminium. This release method was used consistently for the electrode second batch.

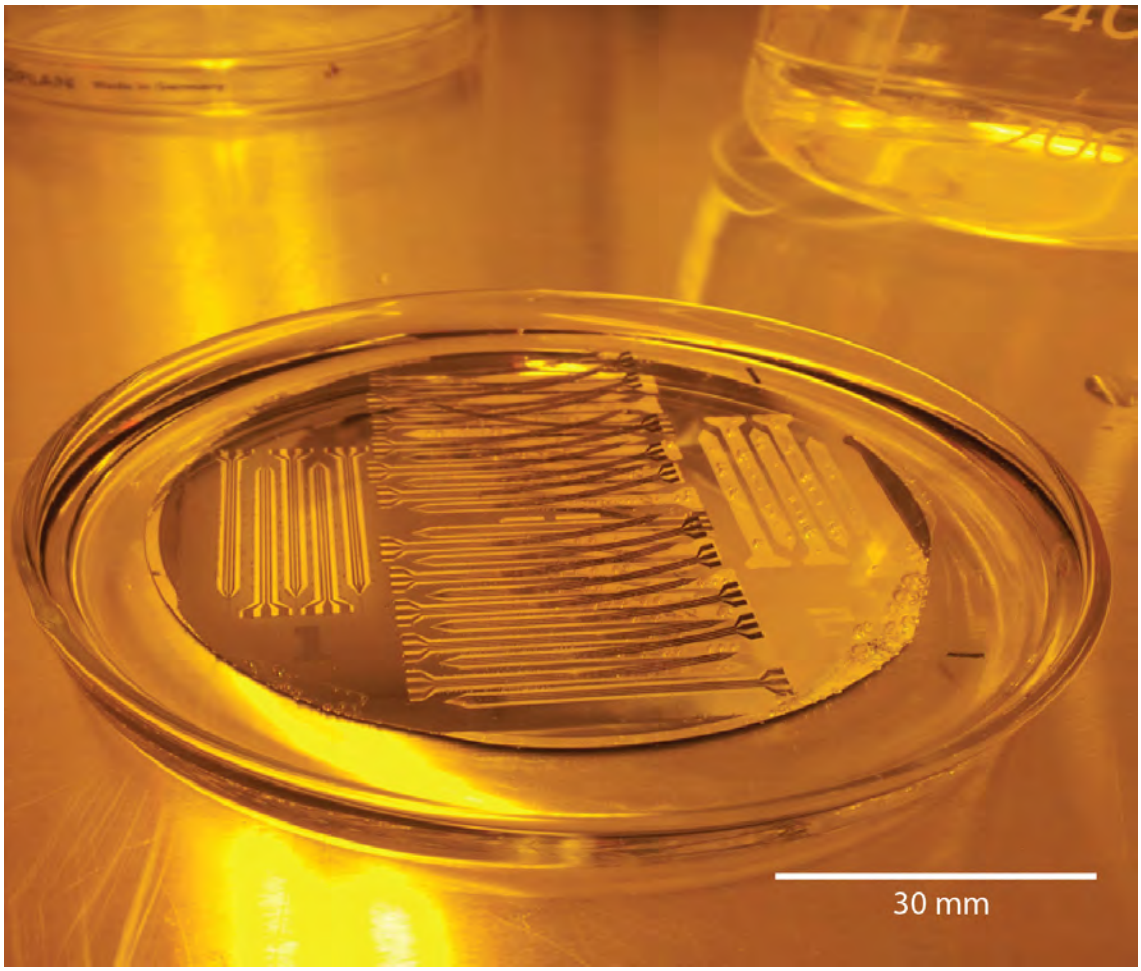

Figure 3.7. TMAH device release. Electrodes released in petri dish. The electrode was released before ribbon cable minimising damage, unlike the device peeling method.

3.4 Device connector bonding

Three methods were explored to bond the connector to our bond pad: gold wire wedge bonding, soldering and silver paint bonding. Solder provided mechanical bond support, an advantage of over both wedge bonding and silver-paint.

Gold wire wedge bonding was ruled out due to parylene-C flexibility, both parylene-C and WTi became scratched upon bonding machine probe contact. Soldering was also ruled out as contact of solder onto the bondpad "melted" the parylene-C in between the separate contacts. Therefore silver paint bonding was preferred and shown to be a highly reliable, quick and reproducible method of connector bonding (Figure 3.8).

Figure 3.8. Connector bonded to the electrode bondpad region using silver paint.

Silver paint bonded devices were insulated. Two insulating techniques were considered, either singular or combined use of two part epoxy (Araldite, UK) and polyimide. To check insulation integrity, leak impedance measurements were taken at 1 kHz pre- and post- epoxy and polyimide application.

Electrodes were considered insulated with a leak impedance rise towards infinity (> 5 MΩ on impedance meter).

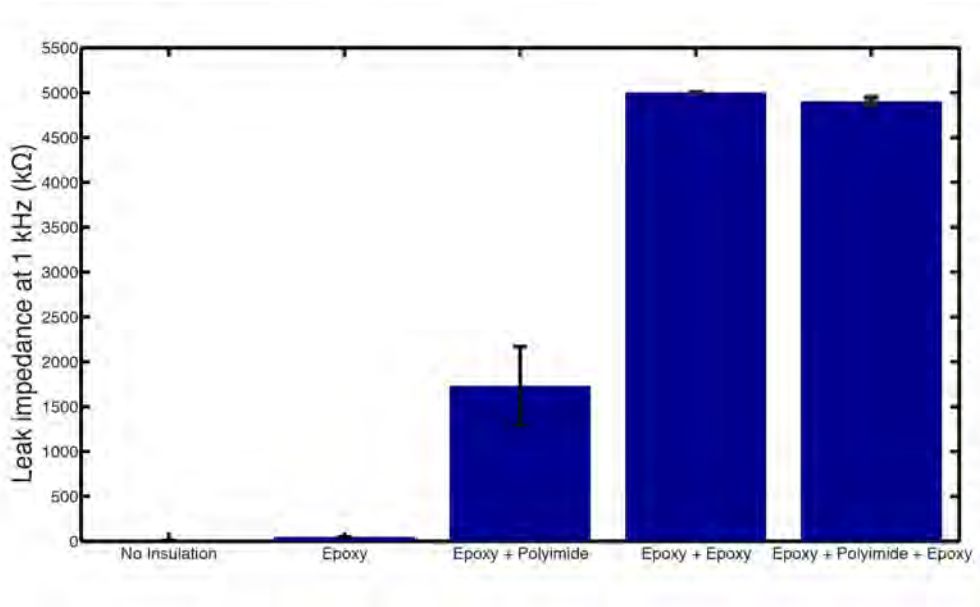

Figure 3.9. Five functional electrode recording sites silver paint bonded, insulated with epoxy, polyimide or combined epoxy and polyimide. Mean leak impedance values (±SEM) are shown for each insulation combination. An impedance rise towards 5000 kΩ is a rise towards infinity, where the specific electrode bondpad was considered to be insulated. The most effective insulation method was two coats of epoxy.

From Figure 3.9, two coats of epoxy was the most effective insulator. From clean room observations, epoxy can also be removed from connectors with N-Methyl-2-Pyrrolidone (NMP) for connector re-use due to unforeseen electrode breakages.

3.5 Impedance testing

3.5.1 Significance of Impedance measurements

Electrode impedance testing was crucial post-fabrication. A detailed explanation was given in Chapter 1 (figure 1.16), however a more specific example is given here for the *in vivo* scenario. The physical origins of the components are as follows: Z_{amp} is the input amplifier impedance, C_{shunt} is the shunt capacitance to ground from electrode to amplifier input, R_{metal} is the resistance of the microelectrode metal, $C_{electric}$ is the capacitance of the double layer at the electrode opening interface and electrolyte solution, R_{leak} is the leakage resistance due to charge carriers crossing the electric double layer, R_{sal} is the resistance to the saline bath between the electrode metal and ground electrode (spreading resistance), and e_{neuron} is the potential created in the volume conductor with respect to a point at infinity by extracellular current flow through neurons during spiking activity (Figure 3.10).

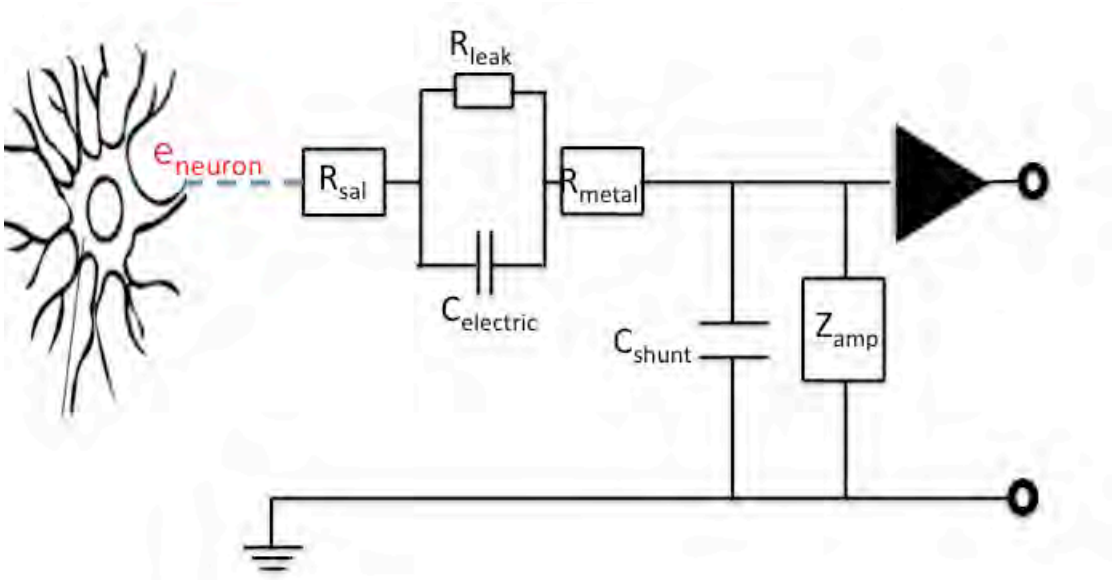

Figure 3.10. Microelectrode equivalent circuit explaining impedance.

From calculation, the dominant part of electrode impedance at 1 kHz is $C_{eletric}$. Electrode impedance is dominated by electrode opening size. Impedance values are obtained by recording current while submersing the electrode tip in saline solution and passing current through them. Impedance measurements can determine a successful connection between the connector and electrode, as well as determining the specificity for

recording from the obtained values. Low impedances allow electrodes to pick up a large number of neurons, where as a higher impedance may allow higher specificity.

Impedance impacts neuronal recording through two mechanisms; noise and shunt loss (Najafi et al., 1990, Ludwig et al., 2011). The random fluctuations of charged carriers at the electrode/electrolyte interface can contribute to noise; electron movement is known as thermal noise(Robinson, 1968, Hassibi et al., 2004). These fluctuations can be caused by the random or Brownian motion of electrons, diffusion of charged ions or REDOX reactions occurring at the electrode/electrolyte interface. Further compounding overall noise levels are instrumentation, biological (activity of other near by neurons) and pink noise (e.g. $1/f$). Sources of noise summate in quadratic form, meaning that the largest noise source will dominate the overall noise values (Ludwig et al., 2011).

The loss of signal from the electrode and measurement system to ground is known as shunt loss (C_{shunt}), which can occur in three ways. Firstly, there is a capacitive loss from the metal on the microelectrode to the surrounding biological fluids. Secondly, a resistive element induces loss of signal from the metal wiring from electrodes to the measurement system (R_{metal}). Finally, there is a capacitive signal loss in the measurement system (C_{shunt}) (Robinson, 1968, Najafi et al., 1990, Hetke et al., 1994, Ludwig et al., 2011).

Electrode impedances that are below 5 MΩ have acceptable levels of noise and shunt loss to allow for single unit recordings (Ludwig et al., 2011).

3.5.2 Electrode impedance testing

Electrode Impedance was measured at 1 kHz in saline, post-wiring with the use of an impedance meter. A sinusoidal voltage around 100 mV peak-to-peak was applied to individual electrodes. Electrode tips were placed in saline and then removed for subsequent storage post-testing. Two measurements were performed, one of individual recording sites and another of two/three recording sites to ensure that the individual electrode recording sites were electrically isolated from one another; the impedance values should summate. If impedance values did not summate, this was indicative of an electrical short and such electrodes were rewired.

Mean electrode impedance values for first and second batch wafers are shown in table 3.1.

	Number of recording sites	Mean 1kHz Impedance ±SEM (kΩ)
First Batch	78	1042 ± 155
Second batch: Wafer 1	75	465±128
Second batch: Wafer 2	90	1147±79
Second batch: Wafer 4	99	772±99
Second batch: Wafer 5	60	442±38

Table 3.1. Mean impedance (±SEM) values for first and second wafer batch.

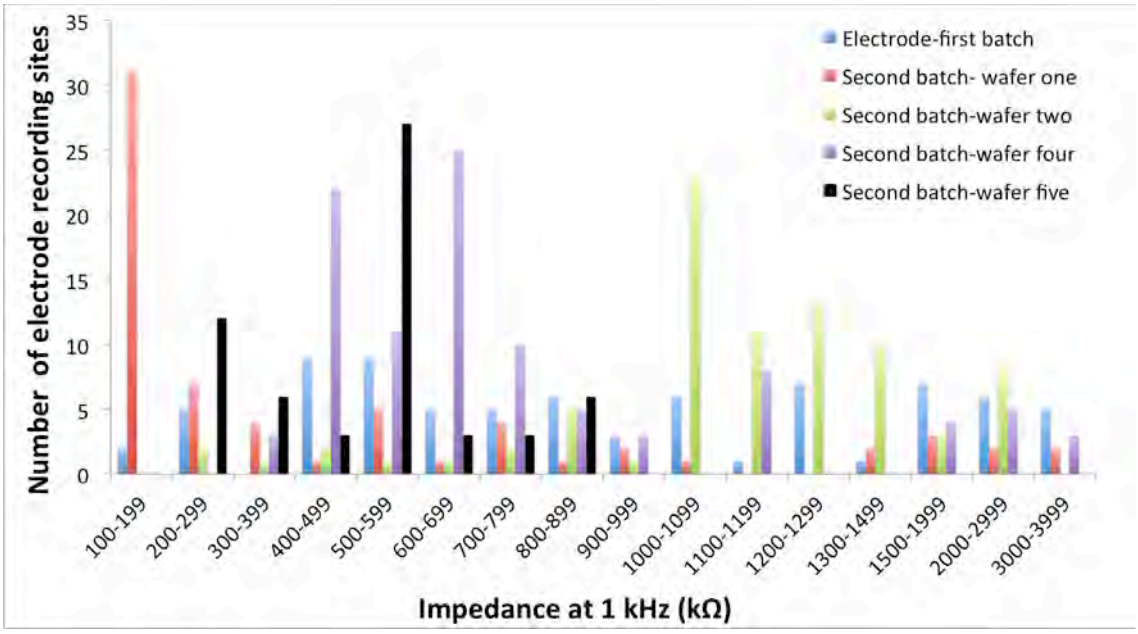

Figure 3.11. Electrode impedance ranges for all electrodes for first and second batch wafers

All recorded electrode impedances were acceptable for single-unit recording with impedances below 5 MΩ, which is the theoretical upper limit for single unit recording obtainment. Additionally, for each wafer there was always a single dominant impedance

range. Further, 79% of electrode recording sites had impedance values ≤ 1.2 MΩ, which was classed as a very good electrode impedance range for single-unit recording from our research group experience (table 3.1, Figure 3.11).

3.6 Functional electrodes

Figure 3.12 shows functional electrode numbers for both the first and second fabrication batch. For each wafer, all probes were released with both optimised release methods. For TMAH release, off wafer and post-wiring functional electrode numbers improved drastically. This release method was more controlled resulting in an increase in over probe functionality.

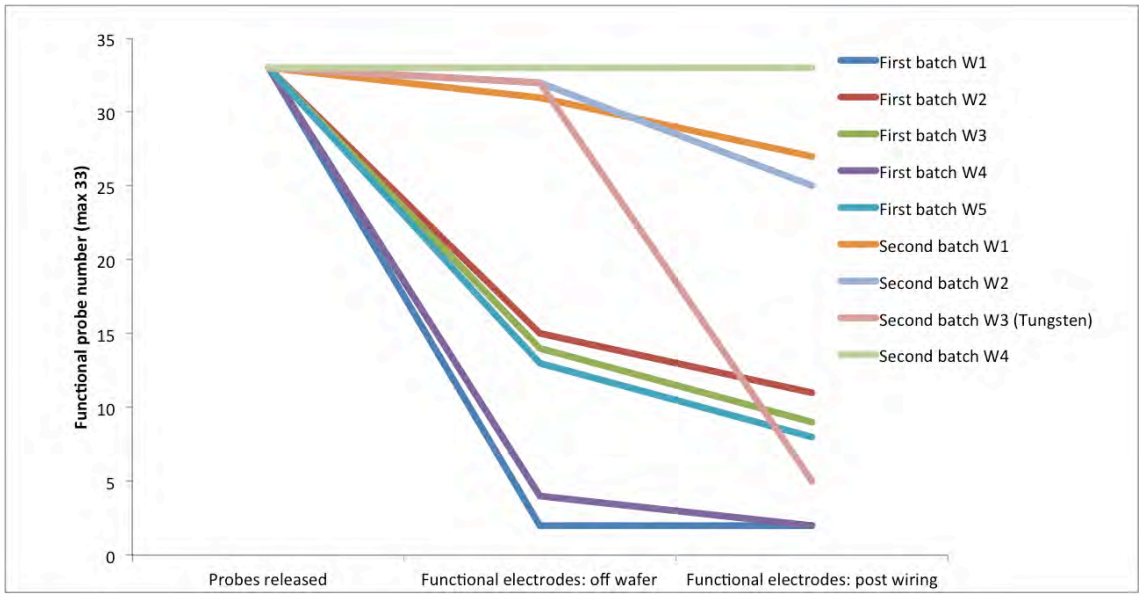

Figure 3.12. The number of functional electrodes for both first and second batches. Off wafer probes were characterised by the probe sinusoidal part being apparent and intact electrode tracks confirmed by optical microscopy. Second batch wafer 5 values were not included, as many electrodes remain unwired. However, 20 out of 20 electrodes were functional post-wiring. Post-wiring the second probe batch had higher functional yields due to optimised device release with the use of TMAH.

3.7 Polyimide-anchor application

A polyimide ball used as an anchor was added post-electrode wiring. VM 652 adhesion promotor (HD Microchemicals, Germany) was applied to the electrode recording tip under optical microscopy with a fine pastette. Immediately after, PI-5878G (HD Microchemicals, Germany) polyimide was applied with a fine pastette, so that a spherical structure formed at the recording site. The polyimide was subsequently soft-baked in accordance to manufacturers guidelines at 120 ^{o}C for 30 minutes in a

convection oven. To re-open the insulated recording sites, the probe tip was dipped into TMAH for a few seconds (Figure 3.13). Re-exposed recording sites were confirmed by optical microscopy and subsequent impedance measurement at 1 kHz, where values were expected to be similar to that pre-polyimide anchor application.

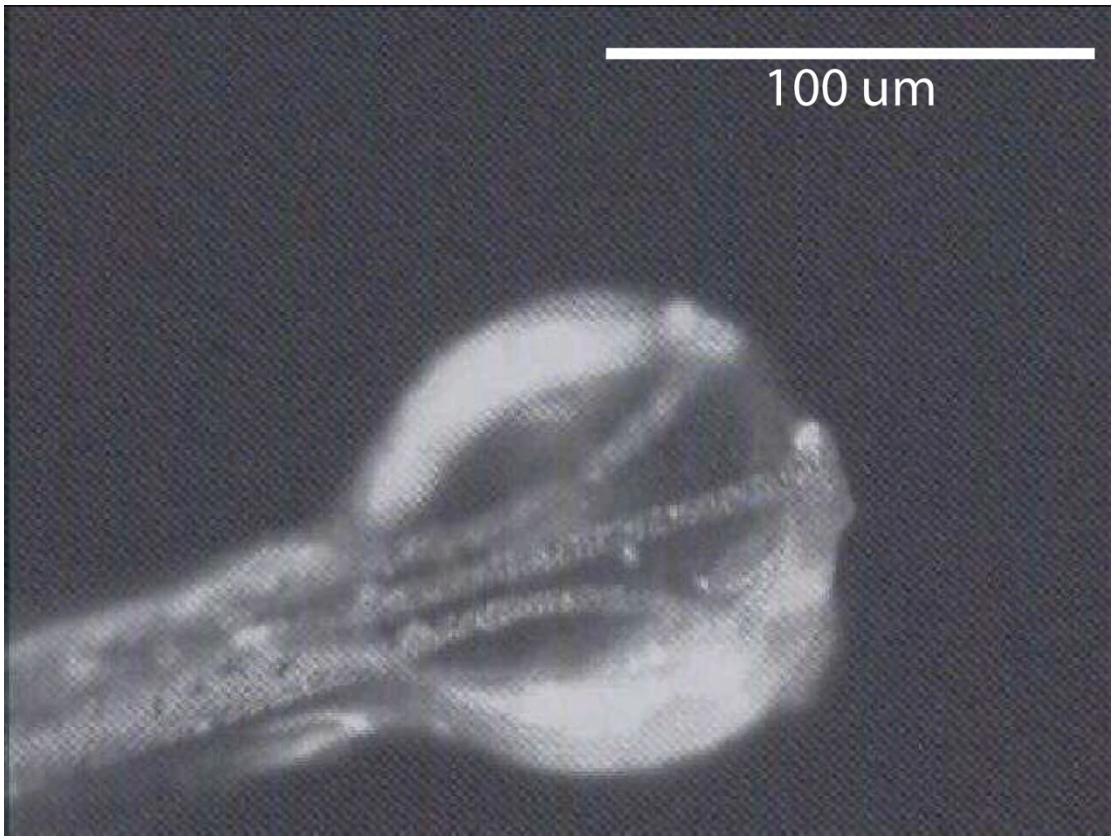

Figure 3.13. Sinusoidal probe with polyimide anchor applied to the recording end, with re-exposed electrode recording sites.

3.8 The rising impedance effect

From impedance measurements at 1 kHz, day-to-day impedance was varying for the same electrode measured previously. To characterise this effect further, a cohort of 5 electrodes (15 electrode recording sites) had their impedances measured over a three-week period. An impedance rise was observed over a 3-week period, which was reversed upon stimulation in saline with a DC power source (4V, 5-10s) (Figure 3.14)

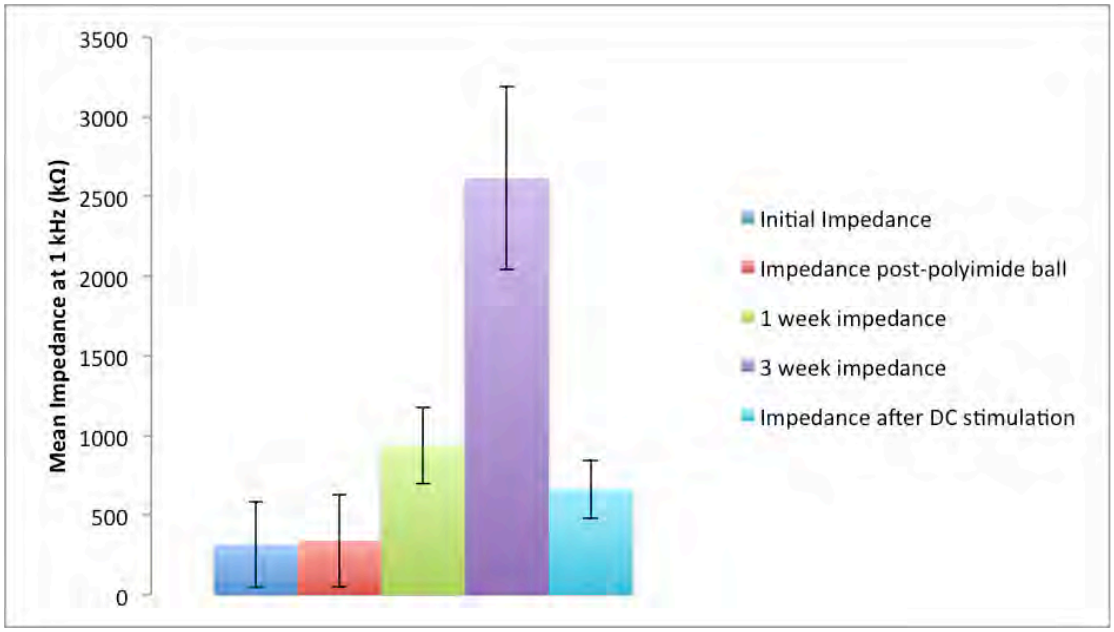

Figure 3.14. The mean impedance (±SEM) for wired probes over a three-week period, followed by DC stimulation (n=5 probes, 15 electrode recording sites). DC stimulation allowed for a potential REDOX reaction to occur, where the oxidised metal was reduced. This re-exposed the available recording site area, hence lowering the observed tip impedance at 1 kHz.

For the groups, a one-way ANOVA was performed to compare group means. A significant difference was found between the means of the groups ($F= 117$, $P<0.05$). A Post-Hoc Tukey's HSD test showed that the means for both the initial and post-polyimide ball impedance differed significantly from the means for both first and third week impedances. The first and third week impedance mean values were significantly different, indicative of a significant rise over this period. Importantly, the mean impedance value post-DC current stimulation with 4 V only significantly differed from the third week impedance value. This suggests that application of DC current reversed the rising impedance effect due to a potential REDOX reaction occurring where the oxidised electrode recording sites were reduced. Post-DC current stimulation, the

electrode impedances fell into acceptable impedance ranges associated with single unit recording (Ludwig et al., 2011).

3.9 Polyethylene Glycol (PEG)- Preservation of electrode impedance

We hypothesised that electrode impedance can be preserved with the application of PEG, post-impedance testing.

After measuring initial electrode impedances, PEG was applied to the recording sites for 5 electrodes. After two weeks, the PEG was washed off with warm saline with impedances tested. The pre and post PEG application impedances did not significantly differ from one another as confirmed by ANOVA ($F= 0.02$, $P>0.05$). Therefore, PEG application prevented further impedance rises, without the need to leave the electrodes soaking in saline (Figure 3.15).

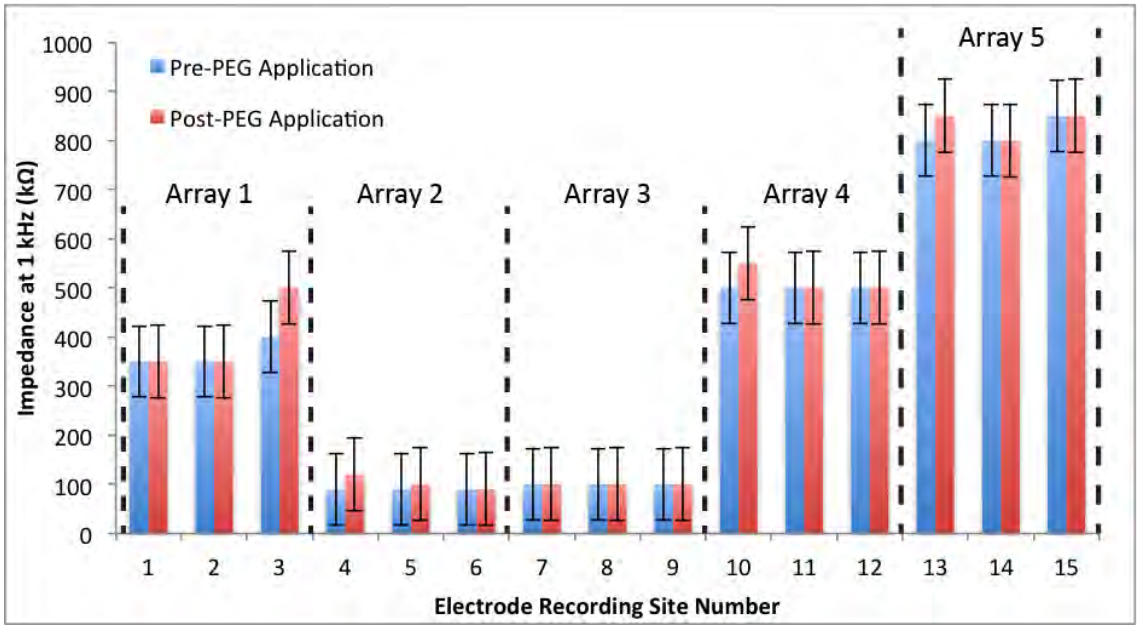

Figure 3.15. The impedance (±SEM) preservation for 15 electrode recording sites with PEG application. Each triplet combination represent an individual sinusoidal probe (Array 1-5). Higher impedances were recorded on some probes due to natural mask alignment error for our lithography. The arrays are shown either with perfect (Array 1, 4), over exposed (Array 2,3) and under exposed (Array 5) electrode recording site area.

3.9.1 Tungsten-based electrodes

We hypothesised that the rising impedance effect was related to the addition of 20% titanium to tungsten, which made the metal more susceptible to oxidation. As a

comparison metal, pure tungsten-based electrodes were fabricated, released using TMAH, cleaned in deionised water and stored for subsequent wiring. Electrode release was successful and wired electrodes had stable impedances, corroborating the contribution of titanium in the rising impedance effect.

Unwired electrodes showed device delamination, with metal loss from recording sites over a three-day period (Figure 3.16). Poor adhesion between the tungsten and parylene-C layer resulted in metal loss. Tungsten sandwiched between the two parylene-C layers was stable due to structural support from parylene-C conformal deposition. This indicates that the addition of titanium was needed for metal-substrate adhesion.

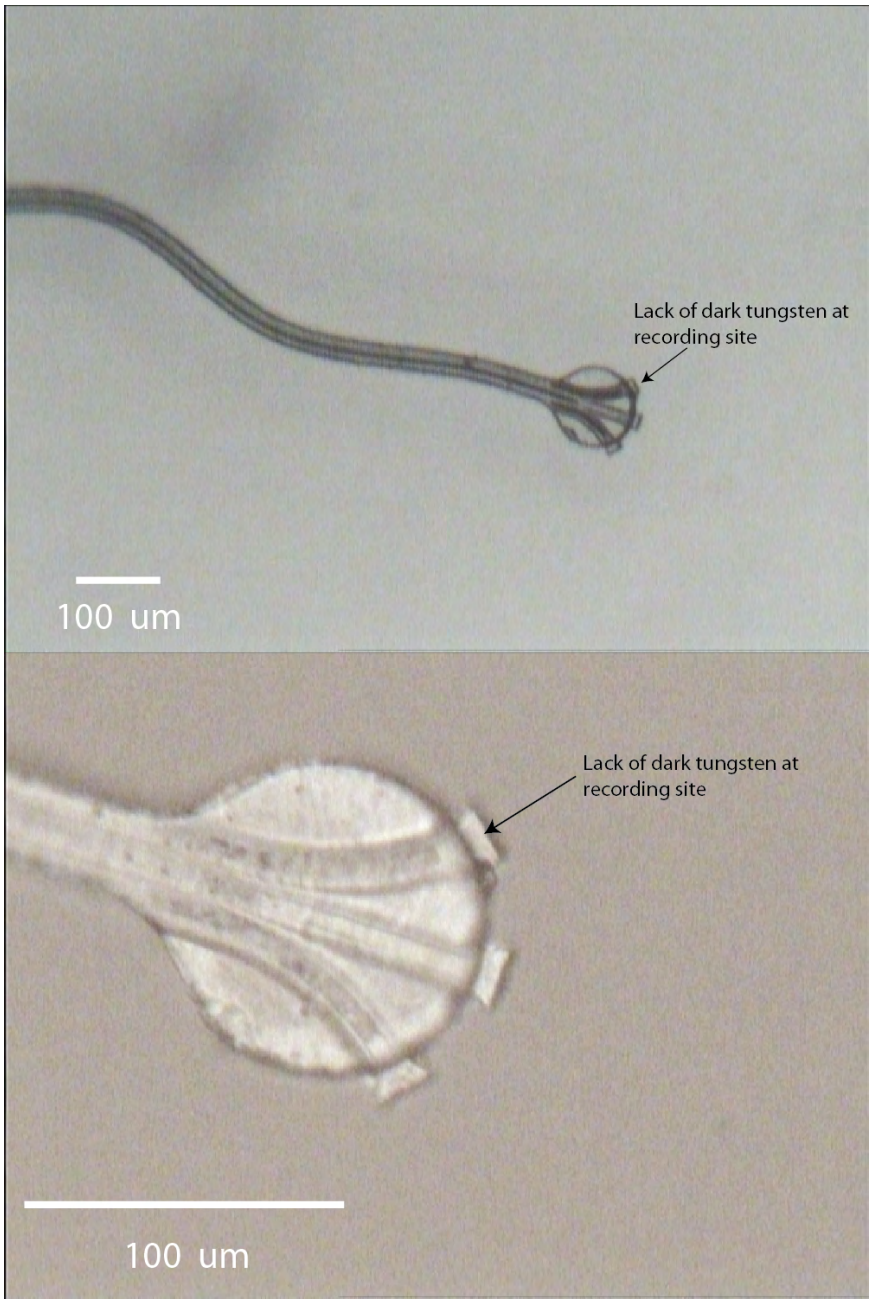

Figure 3.16. The loss of tungsten from electrode recording sites after a 3 day period as shown by the lack of dark (black) tungsten.

3.10 Device insertion method

The electrode was attached to a sharp and rigid carrier for successful brain penetration due to probe flexibility. PEG was used to attach the electrode to the carrier as it can be washed off with warm saline and so successfully liberate the electrode from the carrier.

For our first probe generation, the probes were temporarily attached with PEG to fine steel electrodes (0.229 mm diameter, 2-3 μm tips; Microprobe inc, USA) guided by optical microscopy. However, this method was not used for the second generation due to problems securing the ribbon cable and connector on a thin electrode.

Alternative probe insertion methods were explored. Post-polyimide ball application and soft-baking, the ribbon cable developed a curved shape. Flattening the electrode so that it conformed to a planar structure risked damaging the electrodes. Thus, to accommodate for ribbon cable curvature, Blu-tack (Bostick, UK) secured the connector to the insertion device, which enabled fine manipulation and alignment when using syringes. Firstly, 30 G needles, pre-filled with epoxy to prevent brain boring were utilised as a potential insertion needle. Probes were attached with PEG (Figure 3.17). However, upon preliminary insertion testing, the probe slid along the needle, rather than successfully entering the brain in an acute macaque experiment.

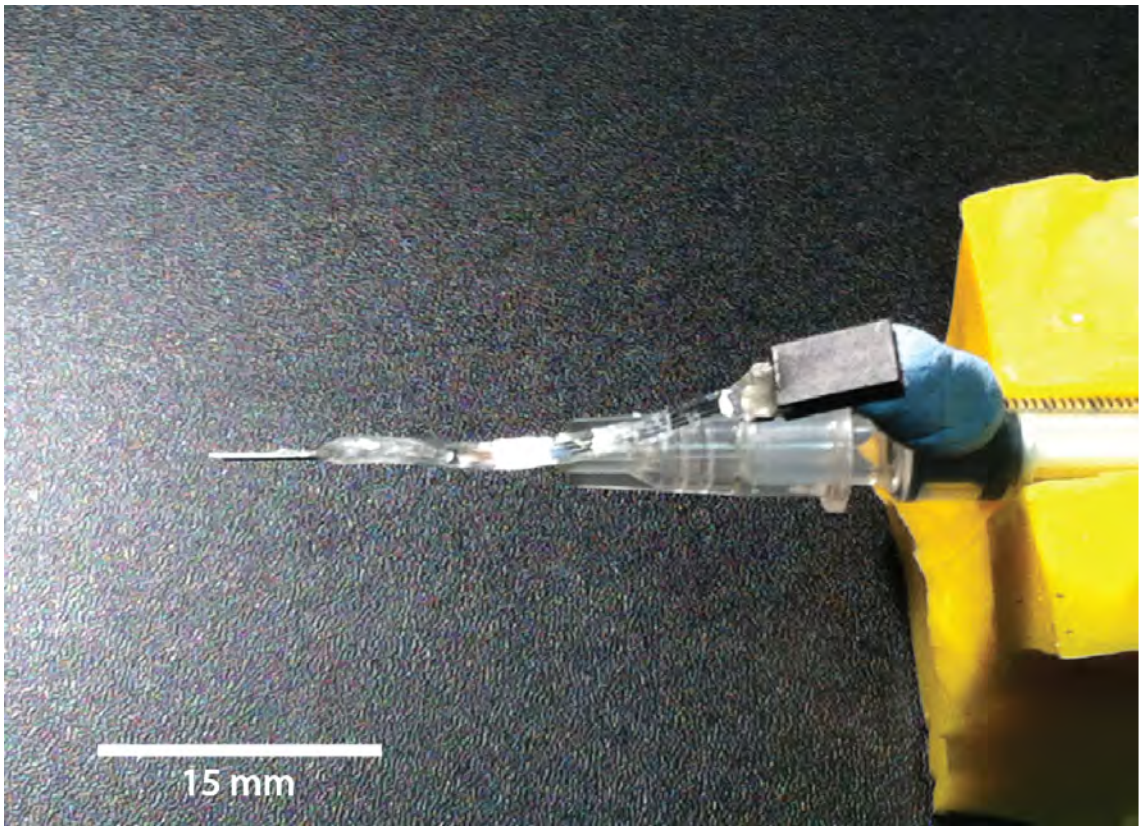

Figure 3.17. Electrode attached to syringe with a 30 G needle.

A half-needle insertion approach was considered. 25 G needles had fine tungsten rods inserted and a Dremel with a sanding disk was used to form a half needle. The probe was attached via the connector to a syringe using blu-tack and manipulated until the electrode lay inside the half-channel and this was filled with PEG (Figure 3.18). This method was utilised for the first surgery on Rabbit H, however brain swelling resulted due to this insertion method. Although there were 4 out of 8 successful insertions, the electrode polyimide anchor clung onto the half needle if any needle roughness from the dremeling process increased adhesion. Therefore 2 out of 4 probes were forced out the brain after successful penetration.

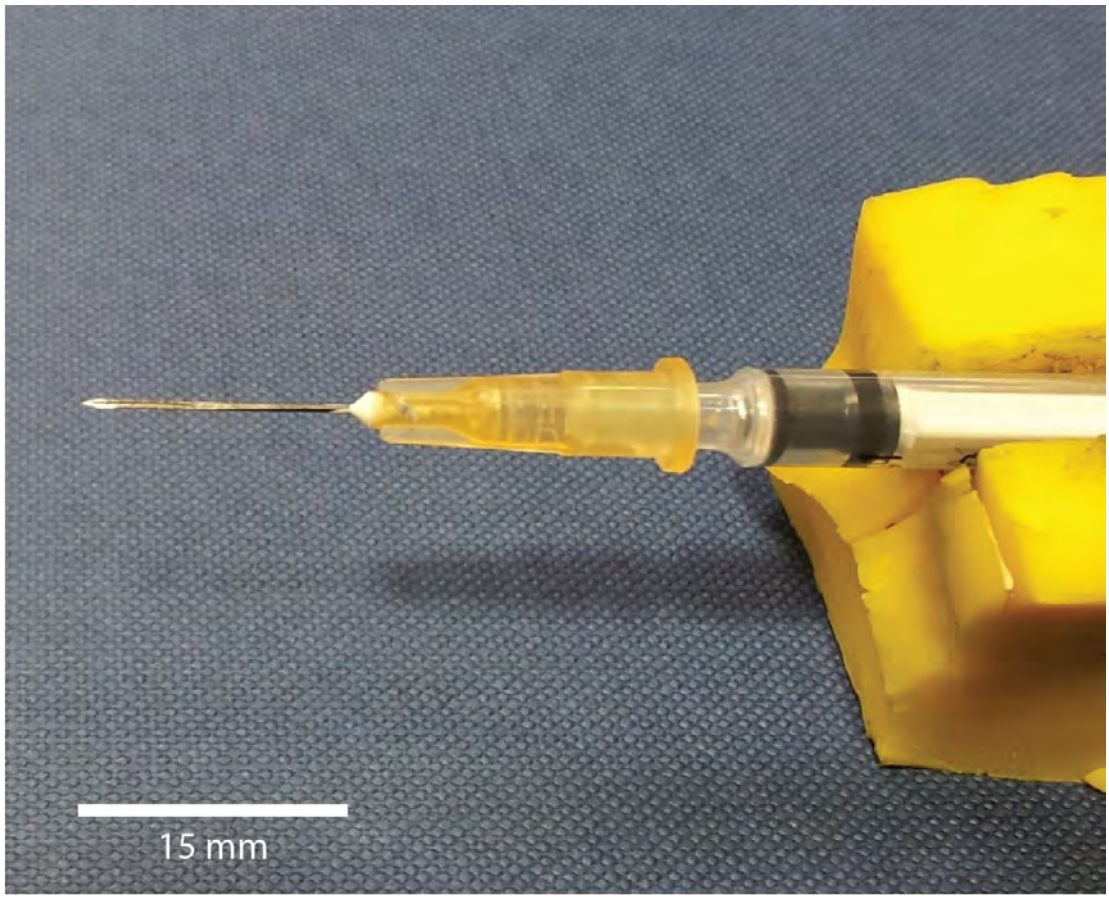

Figure 3.18. The half needle insertion approach. During surgery, electrodes were forced out of the brain due to surface roughness that remained from the Dremeling process for some of the constructed half needles.

An alternate insertion method was considered. 25 G needles were used, and fine tipped steel electrodes (0.229 mm diameter, 2-3 μm tips; Microprobe inc, USA) were placed in the needle and secured in place with epoxy. Probes were manipulated with Blu-tack and attached using PEG (Figure 3.19).

For surgical preparation, all electrodes and carriers were soaked in propan-2-ol (IPA) and attached under sterile conditions. Blu-tack was autoclaved successfully at 121^{o}C Further, probes were UV sterilised post-cold sterilisation for a three-hour period.

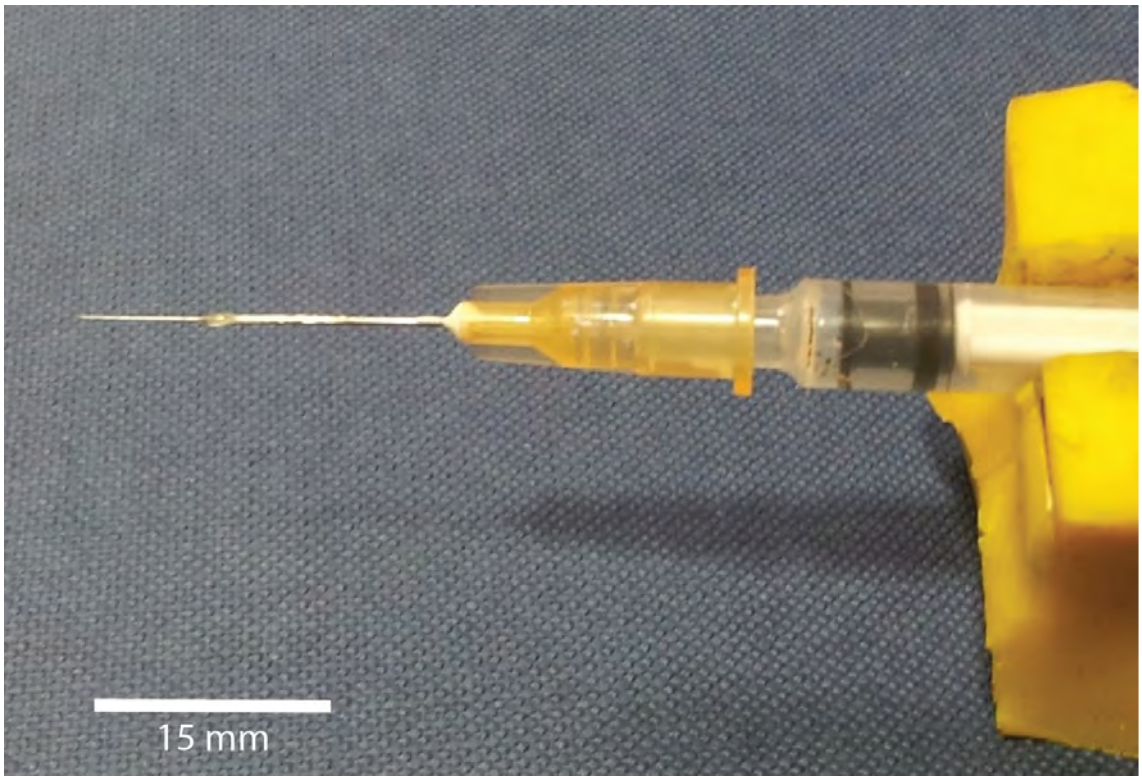

Figure 3.19. Fine tipped steel electrode inside a 25 G needle, secured with two-part epoxy. This was the optimised insertion method used.

3.10.1 Electrode insertion re-optimisation

Insertion devices, which used fine tipped steel electrodes inside a 25 G needle were tested in two rabbits, Rabbit-J and Rabbit-R. The connector was secured onto the insertion syringe with the use of blu-tack.

For Rabbit-J and Rabbit-R, most electrode breakages post brain insertion occurred when liberating the connector from the blu-tack. This resulted in horizontal plane movement for the probe, leading to electrode breakage. Small ribbon cable direction perturbations lead to enhanced shearing forces at the probe-ribbon cable tapering interface. A solution to prevent horizontal plane movement for the probe was needed. Reducing ribbon cable curvature further optimised insertion. A hot air gun was used to straighten probes, and a temperature (120^{o}C) used that prevented dielectric damage. Probe straightening allowed the connectors to be attached to the plastic part of the syringe needle with PEG use. The PEG was washed with saline for rapid connector liberation. Further, a part of the ribbon cable was secured to the insertion needle to minimise force transduction to the tapering point between the electrode and ribbon cable. The probe was attached with a thin PEG layer (Figure 3.20).

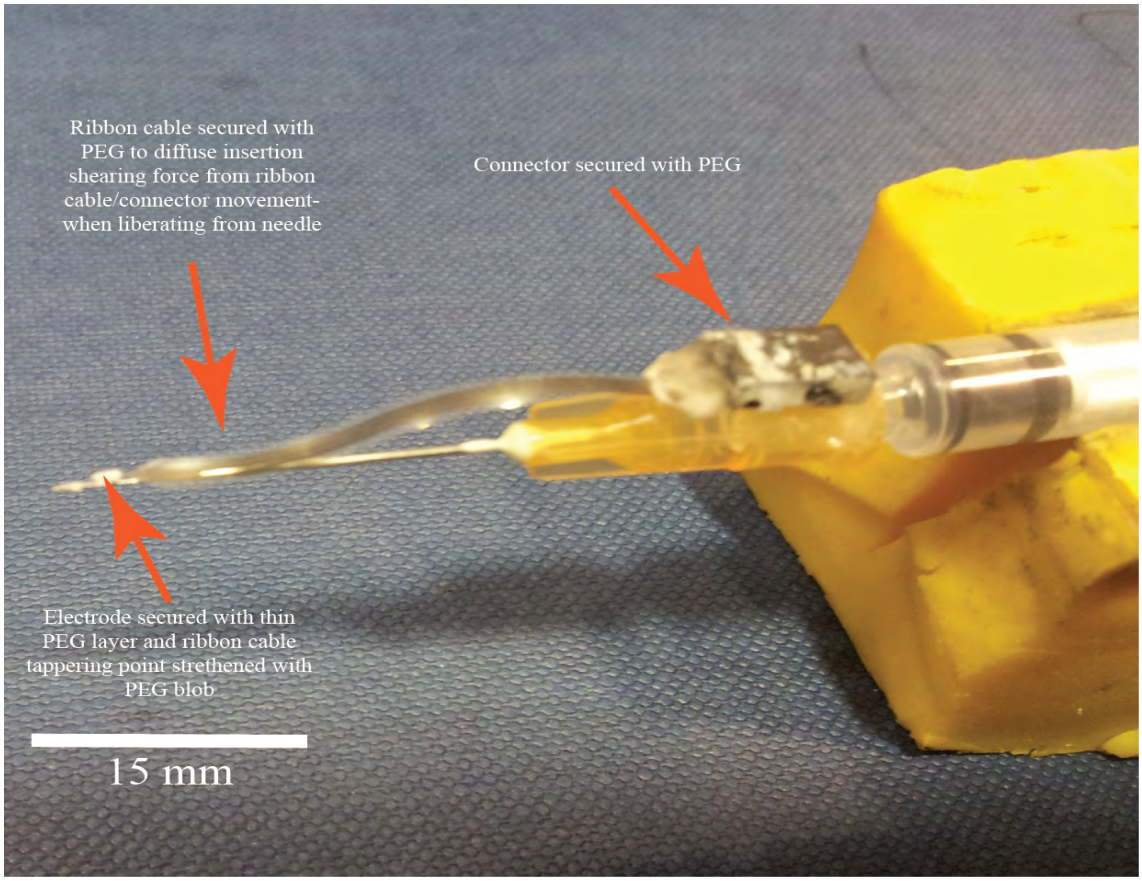

Figure 3.20. Optimised device release to prevent horizontal plane movement for electrode post brain insertion. Probes were thermoformed with a heat gun to straighten devices. This allowed for connector attachment to the plastic part of the syringe with PEG. The sinusoidal probe was then attached with a thin PEG layer to the sharp steel electrode contained within the 25 G needle.

Post-surgery, this optimised device insertion method resulted in an increase in functional electrode number, through reduction in electrode breakages (section 4.3). The probe was inserted with a stereotaxic manipulator. Sequentially, the electrode was inserted, connector liberated and the remaining PEG washed away from the tip region. Finally, the carrier was removed from the brain.

3.11 Conclusions

The switch to using conventional lithography compared to lift-off resulted in successful and repeated titanium mask deposition and patterning, leading to successfully patterned parylene-C layers. The increased adhesion between parylene-C and aluminium led to

further device release optimisation with TMAH, resulting in high functional yields. Post-device release, silver paint bonding of the connector was the optimal connector bonding method. The second batch electrode had reduced impedance compared to the first owing to optimised: metal etching leading to less critical dimension loss, mask alignment, post-device release and device handling after release. Although impedance rises were seen for electrodes left over a three-week period post-wiring, good impedance values can be regained upon DC stimulation and subsequent PEG application to prevent further REDOX reactions. A fine tipped steel electrode, placed inside 25 G needles, was the optimum device insertion method due to reduced invasiveness. Horizontal connector movement during probe detachment post insertion was minimised with ribbon cable thermoforming and further PEG attachment of the ribbon cable to the syringe.

Chapter 4: Device testing *in Vivo*

4.1 Introduction

To analyse recording longevity, electrodes are surgically implanted into appropriate brain regions. Neuronal activity is then observed for the electrodes, relative to a ground (single ended)/or reference and can include single-unit recordings, local field potentials and receptive fields. Classical spiking activity, related to the activation of individual neurons, is characterised as single-unit recordings (Hubel, 1957, 1959). Local field potentials (LFP) is the summation of synaptic field activity from nearby neurons, which is thought to be from the dendrites (Scherberger et al., 2005, Buzsaki et al., 2012).

High frequency spikes occur between 400-3000 Hz and LFP between 1-250 Hz, although this is dependent on specific high and low pass filter settings.

Neuronal activity can be observed and analysed over a chronic time period (> 24 hours). This can be the peak-to-peak voltage amplitude of the signal, the signal-to-noise ratio and *in-vivo* impedance measurements (Moxon et al., 2004, Vetter et al., 2004, Suner et al., 2005, Ward et al., 2009, Kozai et al., 2012a). Changes in the observed neuronal activity values can be used to evaluate chronic electrode performance.

This chapter will analyse the effectiveness of the sinusoidal probe as a chronic implant. The sinusoidal probe was compared to conventional microwire electrodes (Nicolelis et al., 2003) over chronic time points with implantation into the rabbit brain. Appropriate analyses have been made to evaluate chronic performance for spiking and LFP neuronal recordings, analysis of which will be further explained and expanded in later sections.

In this chapter, we showed that the sinusoidal probe had more stable chronic recordings in terms of SNR for high voltage spindle responses (140 day period) and spiking activity (678 day period) when compared to microwire electrodes. A longer chronic recording period was achieved with the sinusoidal probe for the first generation. Further, we also showed that our probe was more stable in terms of LFP power (163 day period). However, results for both spiking activity and LFP recordings, although promising, needed to be further examined due to the low number of sample recordings obtained.

4.2 Methods

4.2.1 Electrode wiring-Sinusoidal probe first generation

A steel formvar insulated wire (0.12 mm diameter; Advent, United Kingdom), length 2-3 inches, was stripped at both ends with a scalpel. One end of the wire was crimped to a pin that would form a constituent of the connector. The other end was connected to the electrode bondpad. The electrode and the wire were aligned with 3 pieces of rubber, with one acting as a base and two small pieces used as an alignment tool and weights to hold the wire and electrode in place (Figure 4.1). The end of a 25G (0.5 x 16 mm) needle (Terumo, Belgium) applied silver paint to the aligned end of the steel formvar wire and electrode bond pad. To ensure that an electrical contact had been successful, the electrode impedance at 1 kHz was measured in saline.

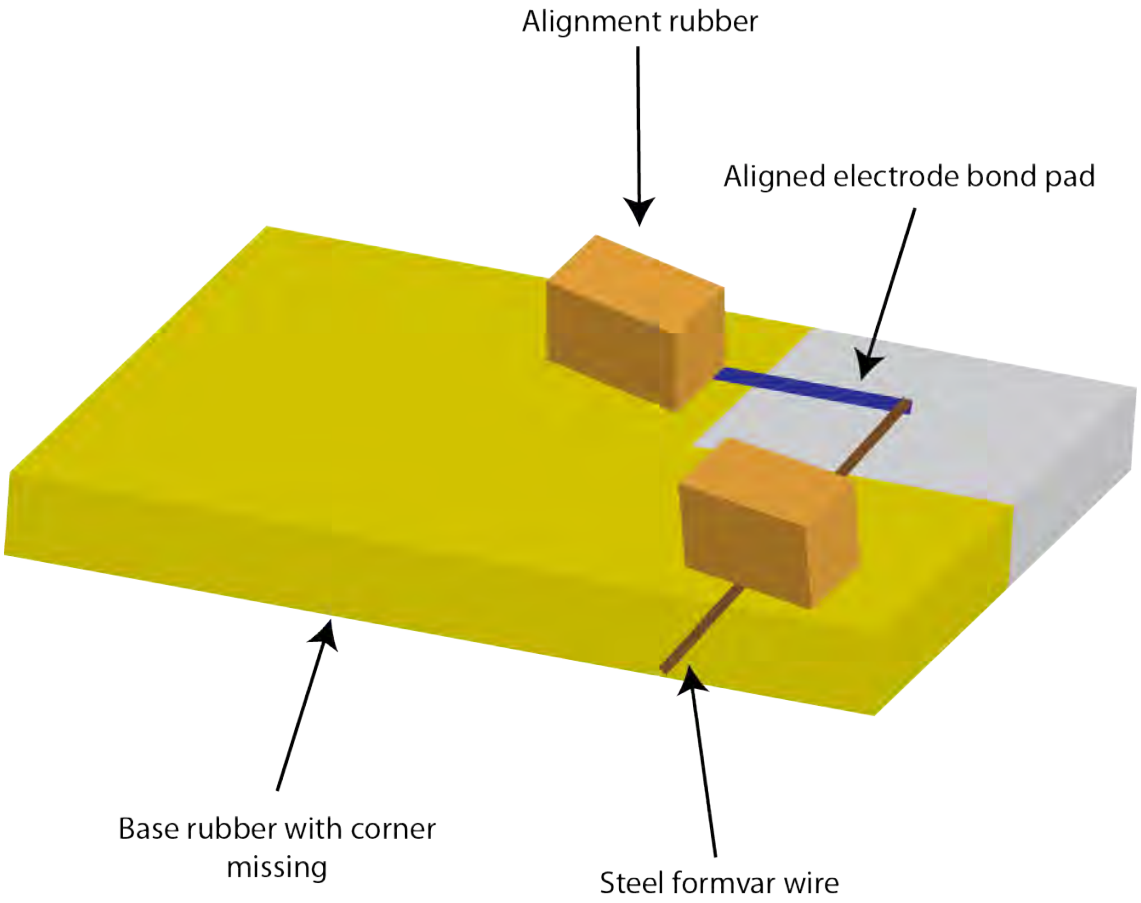

Figure 4.1. Alignment of electrode and steel formvar wire using rubber weights primed for silver paint application to realise an electrical connection

After a successful electrical connection, slow-drying epoxy (Araldite: Farnell, UK) was applied with a 16 G needle to insulate the silver paint. Polyimide (PI-2555) was also

utilised but was unsuccessful due to high curing temperatures needed (200-350^{o}C); this temperature would damage parylene-C.

A PI anchor was applied to the recording end with the use of a 25G needle and soft baked in accordance to manufacturer's guidelines. The electrode sites were re-exposed by dipping the tip in Tetra methyl ammonium hydroxide (TMAH) for 1-2 minutes. The successful re-exposure of the recordings sites was confirmed by optical microscopy and 1 kHz impedance measurement.

4.2.2 Electrode wiring-Sinusoidal probe second generation

Optimising wiring reasoning for the sinusoidal probe second generation has been described elsewhere (section 3.4). In short, a 3 contact Omnetics PS1 connector was aligned to the individual bondpads. Silver paint was used to make an electrical connection. To ensure that an electrical contact had been successful, the electrode impedance at 1 kHz was measured in saline. After a successful electrical connection, two coats of slow-drying epoxy (Araldite, Farnell, UK) was applied with a 16G needle to insulate the silver paint. A PI anchor was applied to the recording end as described above.

4.2.3 Electrode wiring-Microwire

Teflon-insulated stainless steel microwire (0.12 mm diameter; Advent, United Kingdom) was used for the microwire electrode. One end of the wire was stripped and crimped to a pin that would form a constituent of a connector. The uncrimped end of the microwire was bent at a 90^{o} with plastic tweezers to the same length as the novel sinusoidal probe.

4.2.4 Preparation of the electrodes for insertion

Completed electrodes and carriers were placed in ethanol. Under sterile conditions electrodes were attached to sharp steel electrodes (0.229 mm diameter, 2-3 µm tips; Microprobe inc, USA) contained within a 25 g needle attached to a syringe, with heated Polyethylene glycol. The syringe was placed between a cut groove in ethanol soaked rubber to keep it stationary. Initially, autoclaved blu-tack (Bostick, UK) was used to attach and manipulated the sinusoidal probe via the connector to ensure successful electrode aligned with the sharp steel electrode. Successful alignment entailed ensuring that the sharp tip would enter the brain before the electrode. For latter electrodes, the ribbon cable was thermoformed with a heat gun to straighten and the connector attached with PEG. After alignment, the electrode ribbon cable was attached with PEG with the use of a syringe and 25 G needle to hold the electrode in place. For the electrode shaft, a PEG "blob" was diluted with warm saline and applied, with a thin layer applied to the electrode tip and shaft. Individual microwires were hand manipulated, aligned and PEG was applied to attach the wire onto the sharp steel electrode.

Successfully attached electrodes were stored in an autoclaved transparent container and sealed in a sterile surgical bag (Figure 4.2). For further sterilisation, the entire surgical bag containing the boxed electrodes was placed under a ultra-violet (UV) source in a class II fume hood for a three-hour period. UV sterilisation was performed the day before surgery.

Figure 4.2. Attached electrodes prepared for surgical implantation.

4.2.5 Animals

For this study 8 *Oryctolagus cuniculus* (New Zealand white rabbit) were used to monitor recording longevity (table 4.1). All rabbits had electrodes implanted into the sensorimotor representation (Figure 4.3).

Rabbit ID	**Number of implants**	**Indwelling period**	**Data recorded**	**Additional comments**
Rabbit-N	4 mw 4 s First generation	>24 months	Spiking on 1 s electrode	Before thesis commencement, data analysed during thesis period
Rabbit-L	4 mw 4 s First generation	6 months	Spiking on 2 mw electrode	Sinusoidal probe breakages and electrode length not optimal for rabbit brain
Rabbit-P	4 mw 4 s First generation	12 months	No activity was recorded	Same as above
Rabbit-H	4 mw 5 s second generation	3 days	No activity was recorded	Post surgical complications leading to termination
Rabbit-J	4 mw 5 s second generation	163 days	LFP on 1 s and 2 mw	Other electrodes compromised
Rabbit-R	4 mw 8 s second generation	140 days	Fast LFP on 5 s and 2 mw	Other electrodes compromised
Rabbit-Lo	4 mw 8 s second generation	3 days	Spiking 1 s and 2 mw	Post surgical complications leading to termination
Rabbit-Ni	4 mw 6 s second generation	3 days	No activity was recorded	Post surgical complications leading to termination

Table 4.1. Summary of rabbit surgeries and data collected over the study duration. mw= microwire. S=sinusoidal probe.

4.2.6 Surgery

For all animals, electrodes were inserted according to anterior/posterior co-ordinates relative to bregma (Figure 4.3). These co-ordinates were chosen according to the literature (Gould, 1986, Swadlow, 1989, 1990, 1994, Swadlow and Hicks, 1996). A midline incision was made using a diathermy. Skull screws were inserted to anchor the electrode implant and to act as a ground. Holes were drilled for electrode insertion purposes at the specific anterior/posterior co-ordinates relative to bregma, with locations marked by a stereotaxic manipulator. The same stereotaxic frame moved a down post, which held the electrode carrier with the attached electrode. Electrodes were inserted with a fast insertion speed (Bjornsson et al., 2006) manually using the carrier and liberated from the steel insertion electrode by dissolving the polyethylene glycol with warm saline, after obtaining the required insertion depth. The insertion device was removed from the brain via the same carrier. For the microwire electrode, the pin was placed in a connector housing. All wires were glued down to the to the skull, and dental cement filled the craniotomy and held the connector housing in place. For a ground reference, a multi-stranded steel wire was used with the uncrimped end wrapped around a pre-inserted skull screw for single ended recording.

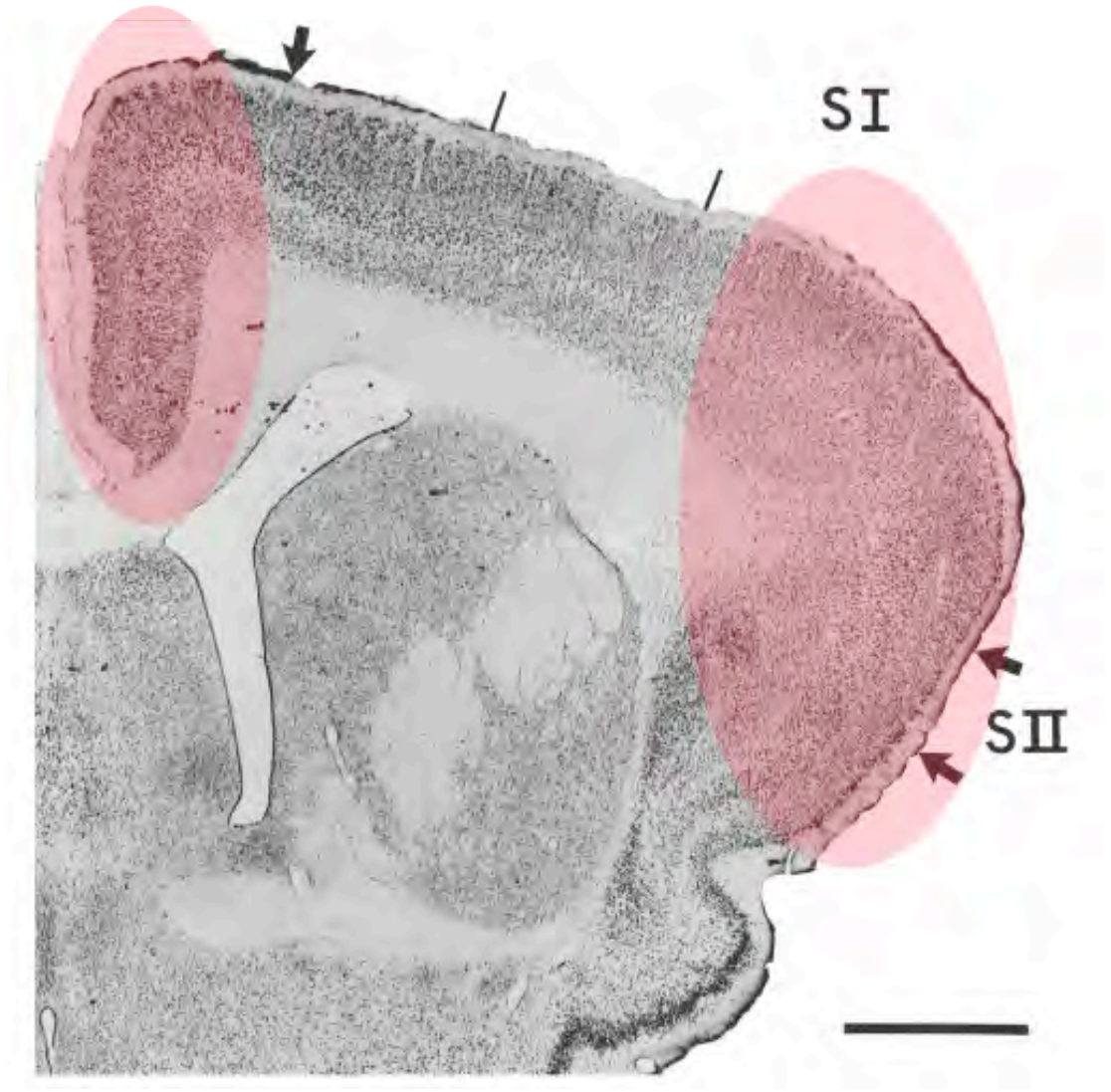

Figure 4.3. A saggital section of the brain showing the regions (red) targeted by our inserted electrodes. The gray matter was targeted, which is where neuron cell somas can be found producing spiking signals, scale bar indicates 2 mm. AP locations varied from A4 to P4 targeting both fore- and hind-limb regions in the rabbit (Gould, 1986).

4.2.7 Electrophysiology data acquisition

Tri-weekly recording sessions started for all animals, one week post-surgery.

Neuronal activity was recorded and logged from electrodes relative to ground with the use of a programmable gain amplifier (1,000 gain; Multichannel systems, Germany), connected to a 1401 CED systems box (Cambridge Electronic Design, UK). The 1401 allowed computer data logging with use of Spike 2 software (Cambridge Electronic Design, UK). For the recording sessions a low pass of 10 kHz and a high pass 0.5 kHz were used, with a sampling rate of 25,000 Hz for all channels. For local field potential

acquisition, a sampling rate of 1000 Hz was used and a low pass of 100 Hz and a high pass of 1 Hz.

4.3 Functional Electrode number post-surgery for second generation

The percentage of functional electrodes post-surgery was calculated through 1 kHz impedance measurements. Electrodes that gave impedance values below 5 MΩ were considered electrically functional for single unit recordings (Ludwig et al., 2006, Ludwig et al., 2011). Figure 4.4 shows the overall trend of an increase in functional electrodes every surgery. This is due to a combination of refined surgical and device insertion manufacturing techniques.

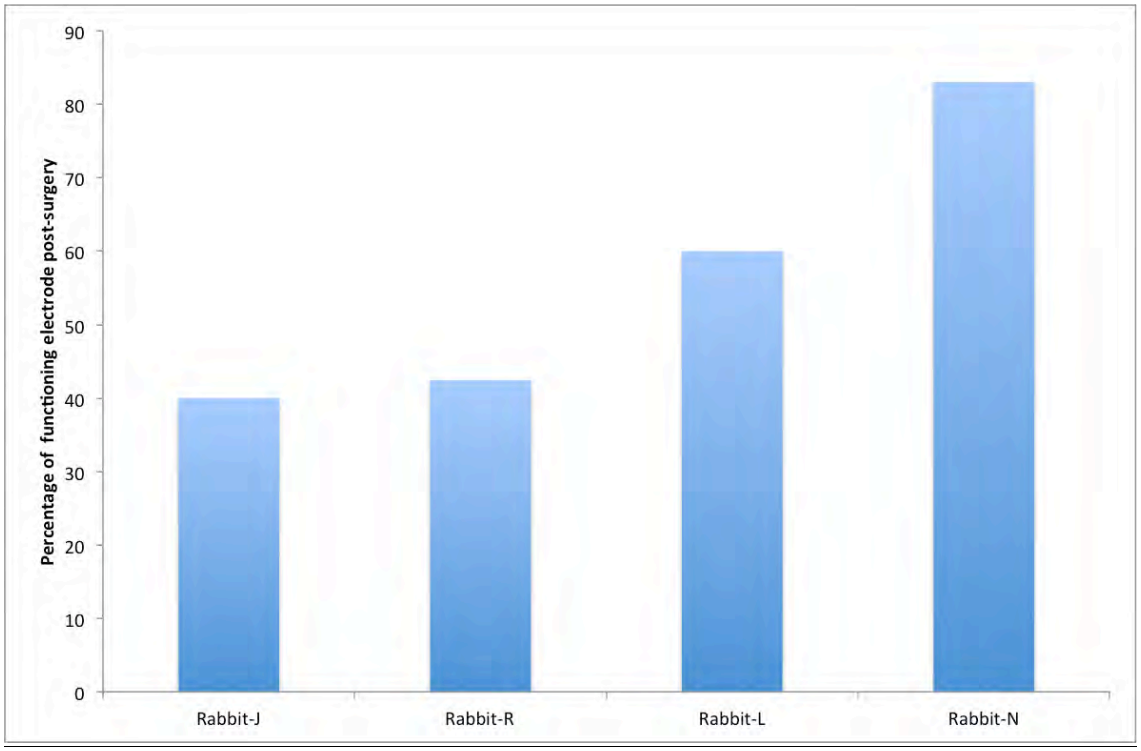

Figure 4.4. Functional sinusoidal probe second generation (%) post-surgery. Rabbit-J, Rabbit-R, Rabbit-Lo and Rabbit-N had 5,12, 10 and 6 Sinusoidal probes implanted respectively.

4.4 Chronic recording performance for the Sinusoidal probe

Recording performance was evaluated in terms of mean peak-to-peak amplitude, noise, SNR and where appropriate, *in-vivo* impedance for LFP and spiking activity. As a measure of recording stability the standard deviation (Suner et al., 2005, Ward et al., 2009) or standard error (Vetter et al., 2004) is taken across the entire recording period and compared for each individual electrode type. Using the standard error for mean values across the entire recording period was not appropriate due to limitation in accounting for varying recording period length per session. The longer the recording session, the higher the number of samples, therefore lowering expected standard error values. Therefore the standard deviation was a more appropriate measure to compare the two individual electrode types.

For statistical analysis, percentile-bootstrapping techniques (Li et al., 2013) were employed due to unequal sample sizes for each recording measure: one sinusoidal probe had three recording sites compared to one microwire recording site. Bootstrapped data sets were constructed by resampling the original data randomly with replacement, so the same number of samples was contained in each data set. This was repeated 10000 times and the difference in means calculated. The null hypothesis mean was zero. The null hypothesis was rejected, if the null hypothesis mean value did not fall between the 2.5 and 97.5 % percentile range calculated from the bootstrap mean value for each recording measure.

All analysis was performed within the Matlab environment (2009a, MathWorks, USA).

4.4.1 Local field potentials

LFP could be potential control signals for brain-machine-interfaces and has long been associated with movement preparation (Scherberger et al., 2005) .

LFP recordings were analysed from Rabbit-J in terms of LFP power across a specific frequency band. A sampling rate of 1 kHz was used.

From neuronal traces corresponding to appropriate electrodes, a power spectrum was constructed using fast-Fourier transformation to observe which frequency bands gave definitive peaks between the two electrode types. Once identified, the power values across the specific frequency band were summated giving a total power for the

frequency band per recording day. Further, the daily peak frequency value for recorded for specific frequency bands.

For Rabbit-J, the beta (12-30 Hz) and theta (4-8 Hz) frequency bands were compared over a 163 day period (Figure 4.5). One sinusoidal probe and two microwire electrodes gave LFP recordings.

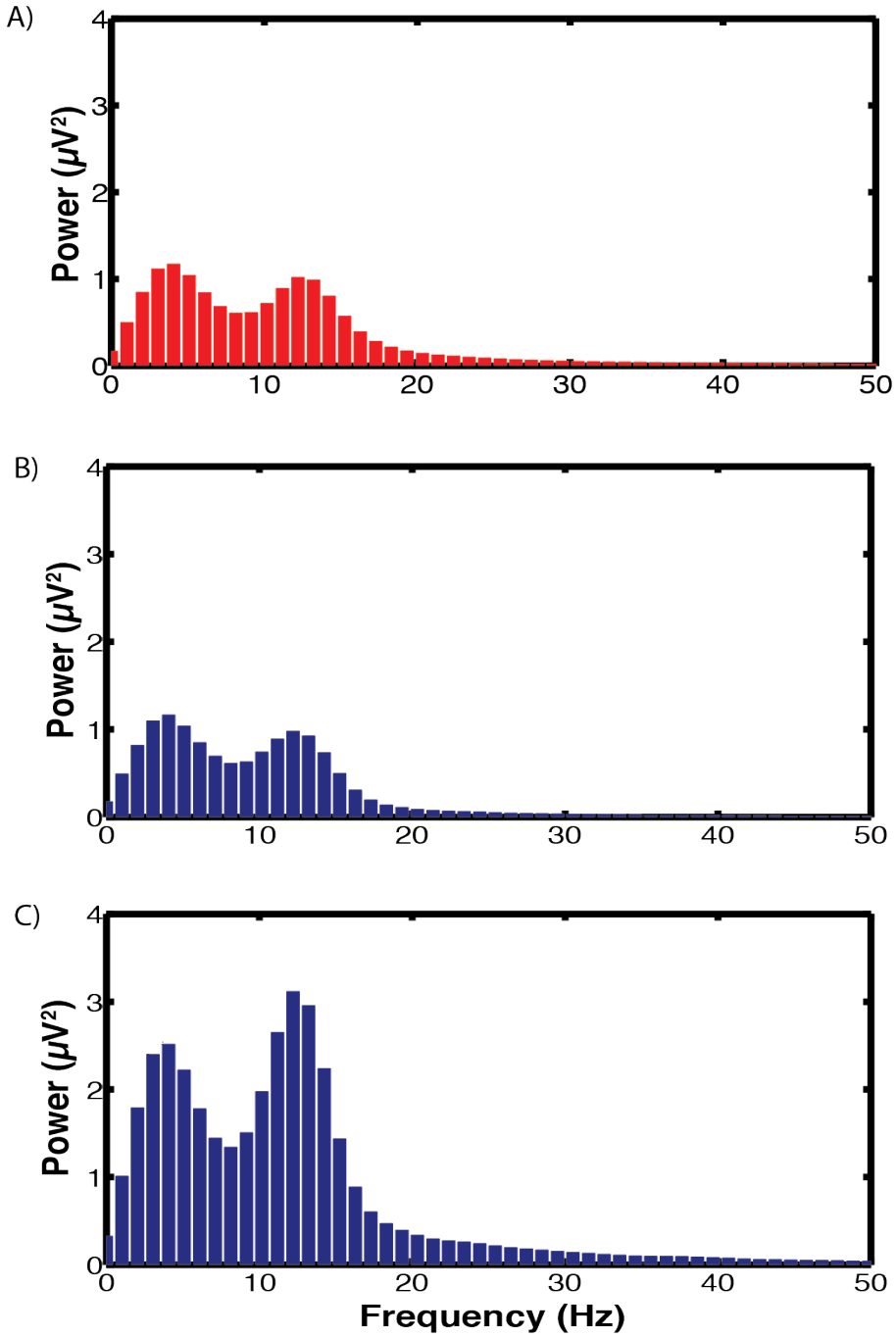

Figure 4.5. An example LFP power spectrum obtained from the sinusoidal (A) and two microwire (B,C) electrodes showing that theta and beta bands can be compared.

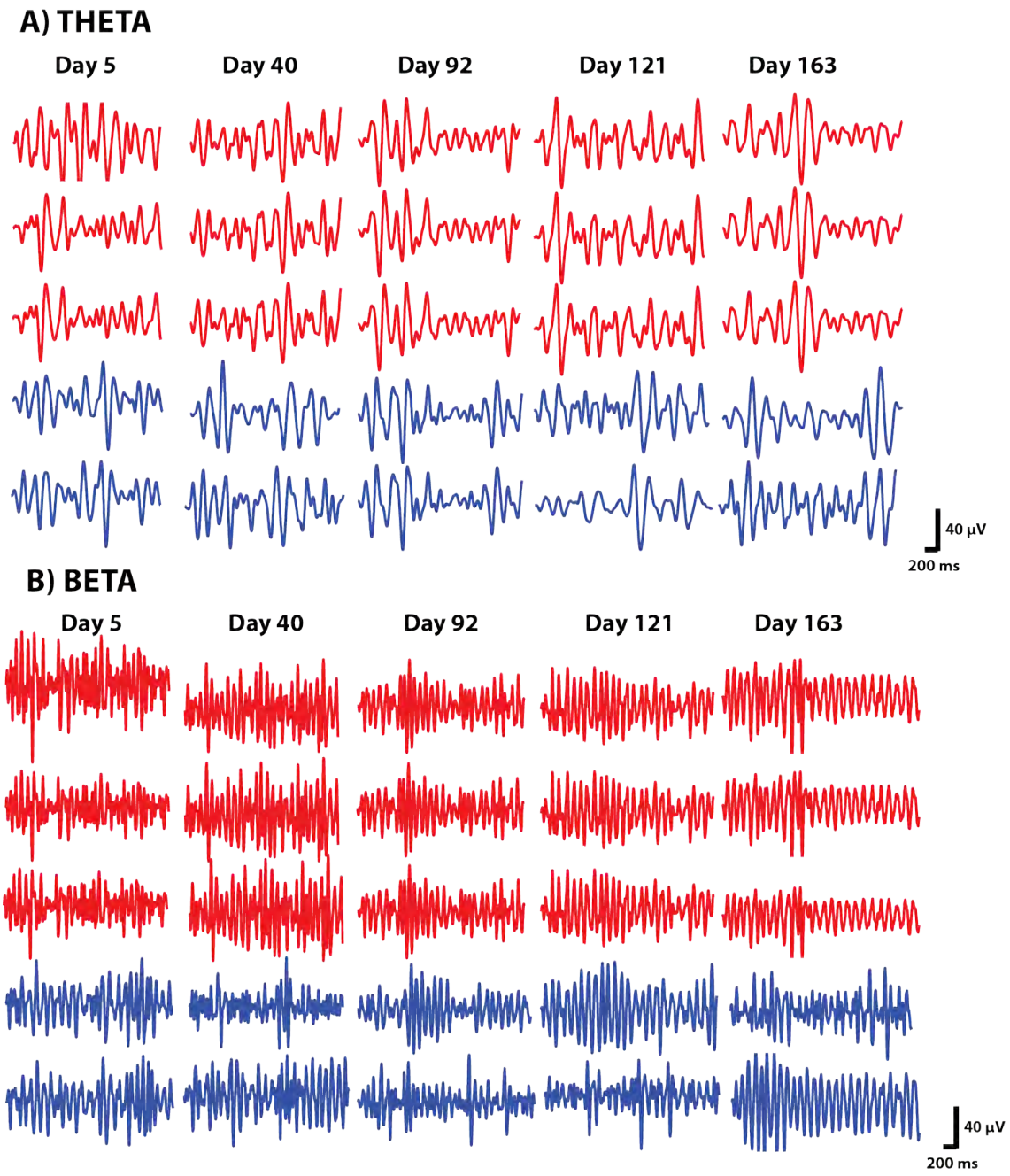

Figure 4.6. Sinusoidal probe (red) and microwire (blue) filtered waveforms over a 163 day indwelling period for Rabbit-J. For theta and beta activity, the microwire electrode have a larger peak-to-peak amplitude than the sinusoidal probe.

Figure 4.6 shows filtered wave form traces for selected days over the 163 day recording period. The same LFP signal was recorded on all three of the sinusoidal probe recording sites across the entirity of the indwelling period ($r=1$, $P<0.05$). Although the microwire electrode appeared to have higher LFP power values (Figure 4.8), the sinusoidal probe was more stable in maintaining similar LFP power as corroborated by lower LFP power

standard deviation values across the entire recording period (Figure 4.7). Therefore stable LFP power was sustained for the sinusoidal probe.

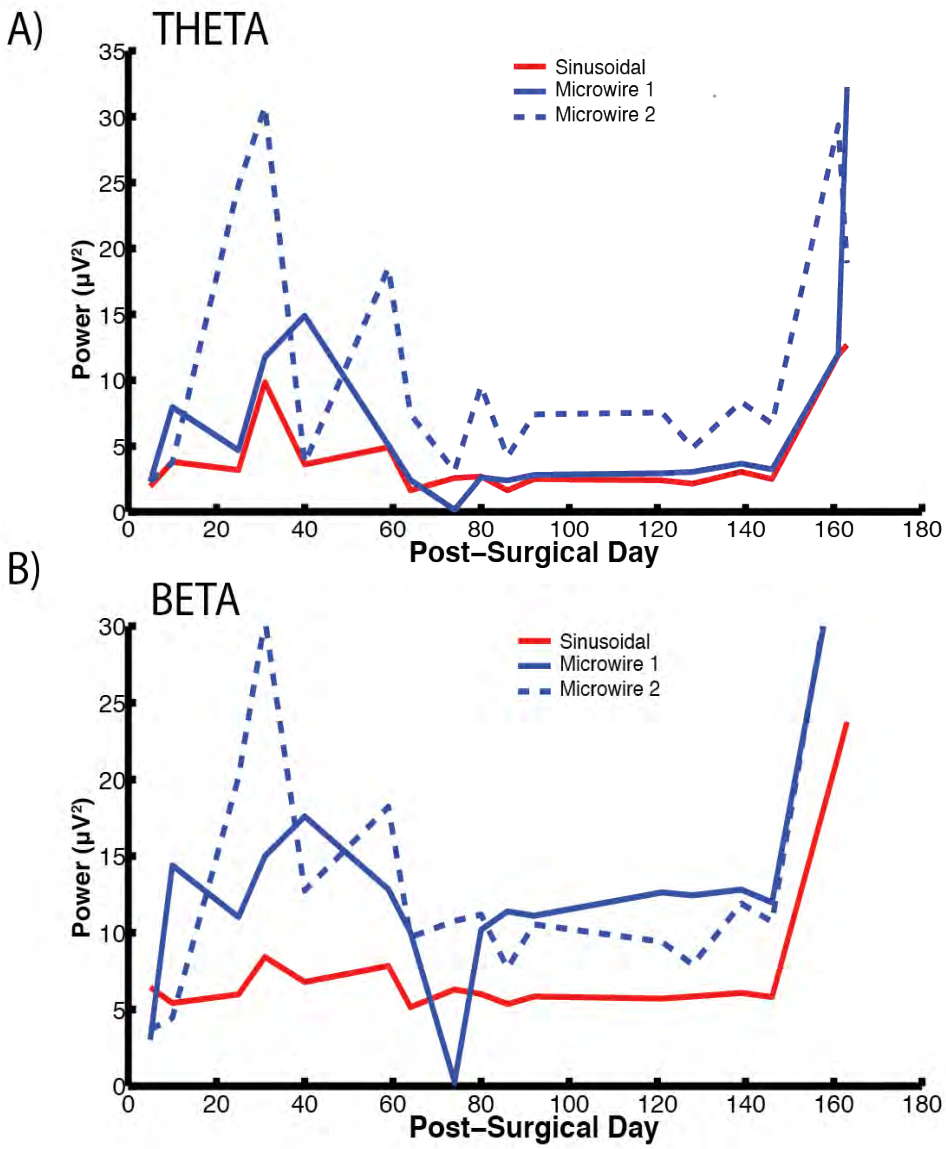

Figure 4.7. Sinusoidal probe (red) and microwire (blue) chronic performance over a 163 day indwelling period for Rabbit-J. Power values are shown for theta (A) and beta (B) activity. Overall, the microwire electrodes have higher power, however the sinusoidal probes were more stable over the recording period. Across the recording period standard deviation values of 3.5, 7.8 and 9.9 and 5.5, 11.2, and 11.6 were obtained for the sinusoidal and two microwire electrodes respectively for theta and beta activity. There was an increase in activity on day 160 for both beta and theta bands as the rabbit had a heightened state of arousal for this recording session.

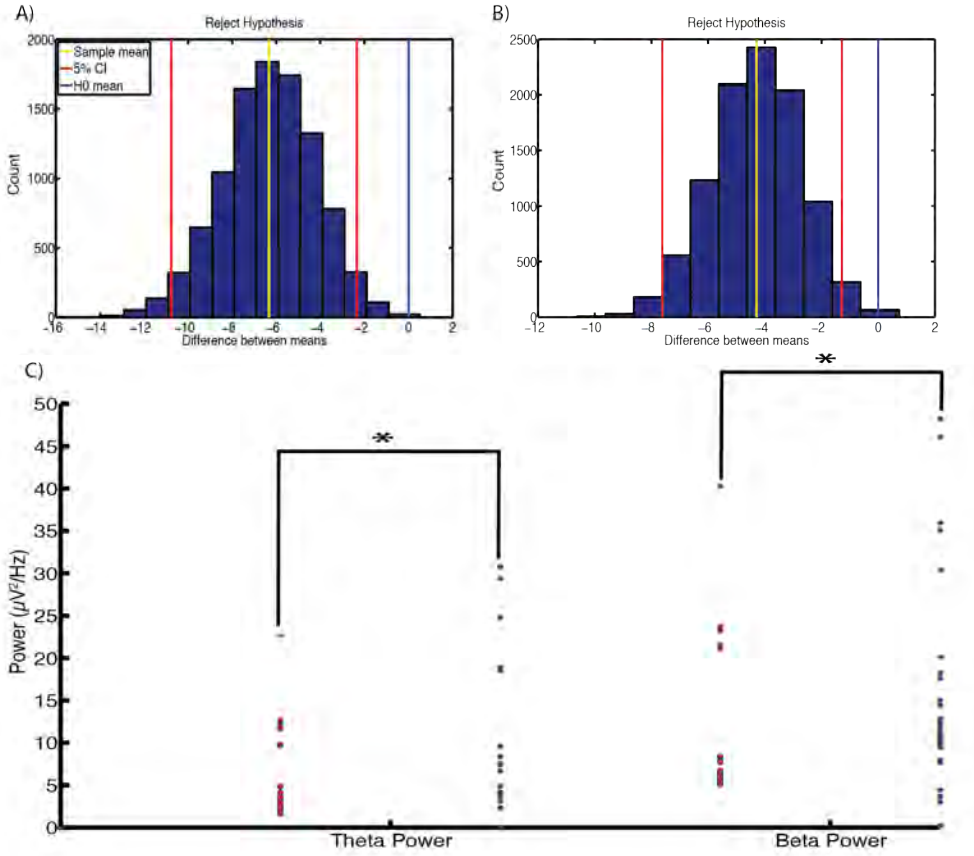

Figure 4.8. Bootstrapping distribution histograms comparing the power for theta (A) and Beta (B) activity. Differences were found between the power values compared between microwire and sinusoidal probes for theta and beta activity (C). H0 mean = hypothesis mean. Cl= confidence interval. * = null hypothesis mean value did not fall between the 2.5 and 97.5 % percentile range calculated from the bootstrap mean values between electrodes.

Peak frequency values were also measured as a function of post-surgical day for both theta and beta activity (Figure 4.9). For theta activity mean ± SEM values for peak frequency of 4.0±0.09, 4.05±0.06 and 4.24±0.16 were obtained for the sinusoidal and two microwire electrodes, respectively. For beta activity mean ± SEM values for peak frequency of 13.0±0.24, 12.4±0.17 and 12.9±0.24 were obtained for the sinusoidal and two microwire electrodes, respectively. Similar peak frequency values recorded across the recording period for both theta and beta activity for both electrode types. No differences were observed between both electrode types for theta and beta bands in terms of peak frequency (Figure 4.10). These results suggest that variability from external factors, which may have influenced recording were kept minimal as similar

peak frequency values were obtained. Further, this showed that the electrodes were recording from similar brain regions, therefore validating the comparison between both electrode types in terms of total LFP power across both theta and beta bands.

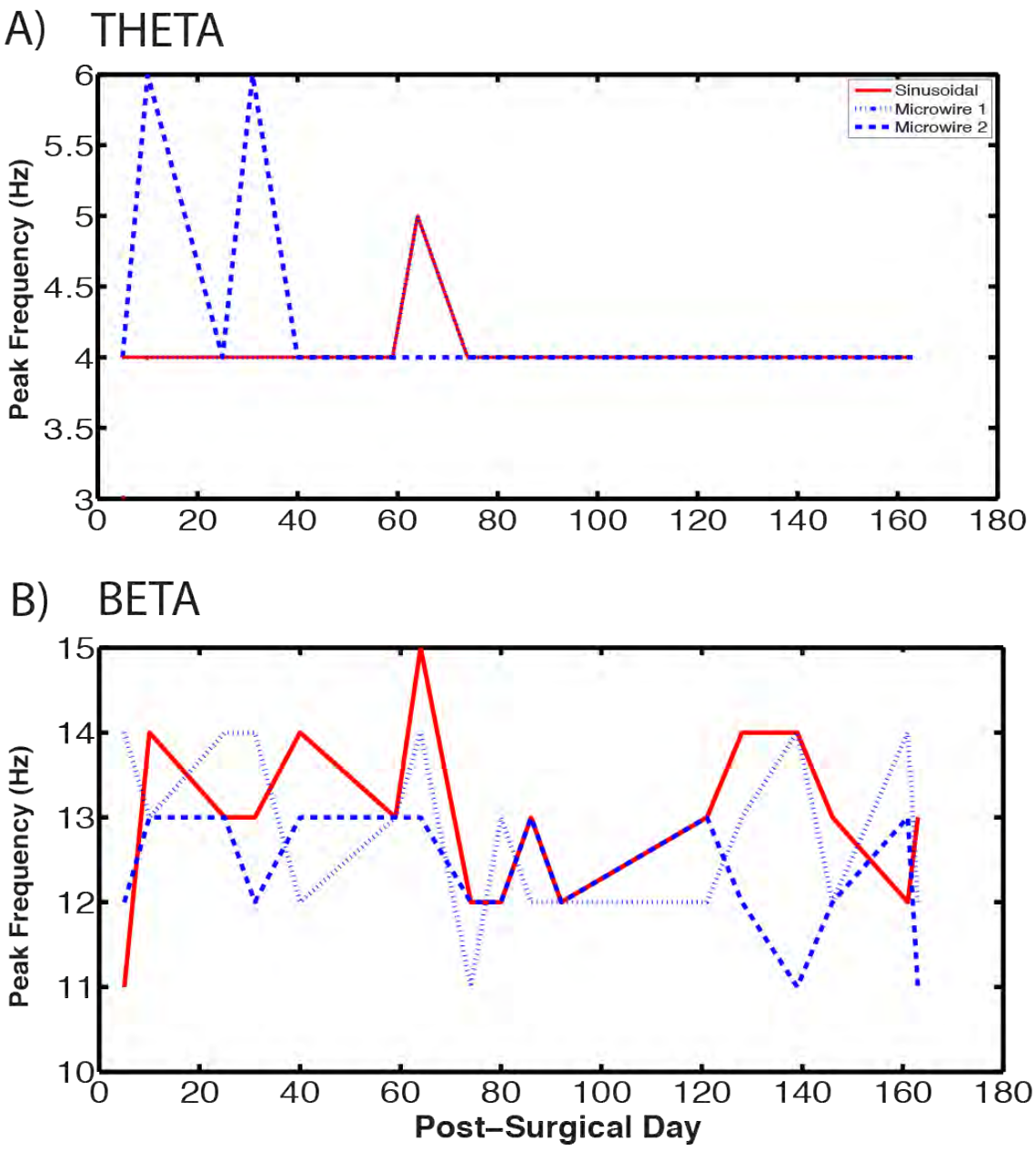

Figure 4.9. Sinusoidal probe (red) and microwire (blue) chronic performance over a 163 day indwelling period for Rabbit-J. Peak frequency values are shown for theta (A) and beta (B) activity. Overall, similar peak frequency values were obtained for both electrode types for theta and beta activity. For theta activity mean ± SEM values for peak frequency of 4.0±0.09, 4.05±0.06 and 4.24±0.16 were obtained for the sinusoidal and two microwire electrodes, respectively. For beta activity mean ± SEM values for peak frequency of 13.0±0.24, 12.4±0.17 and 12.9±0.24 were obtained for the sinusoidal and two microwire electrodes, respectively. The first microwire and sinusoidal electrode had very similar activity recording in terms of peak frequency for beta activity.

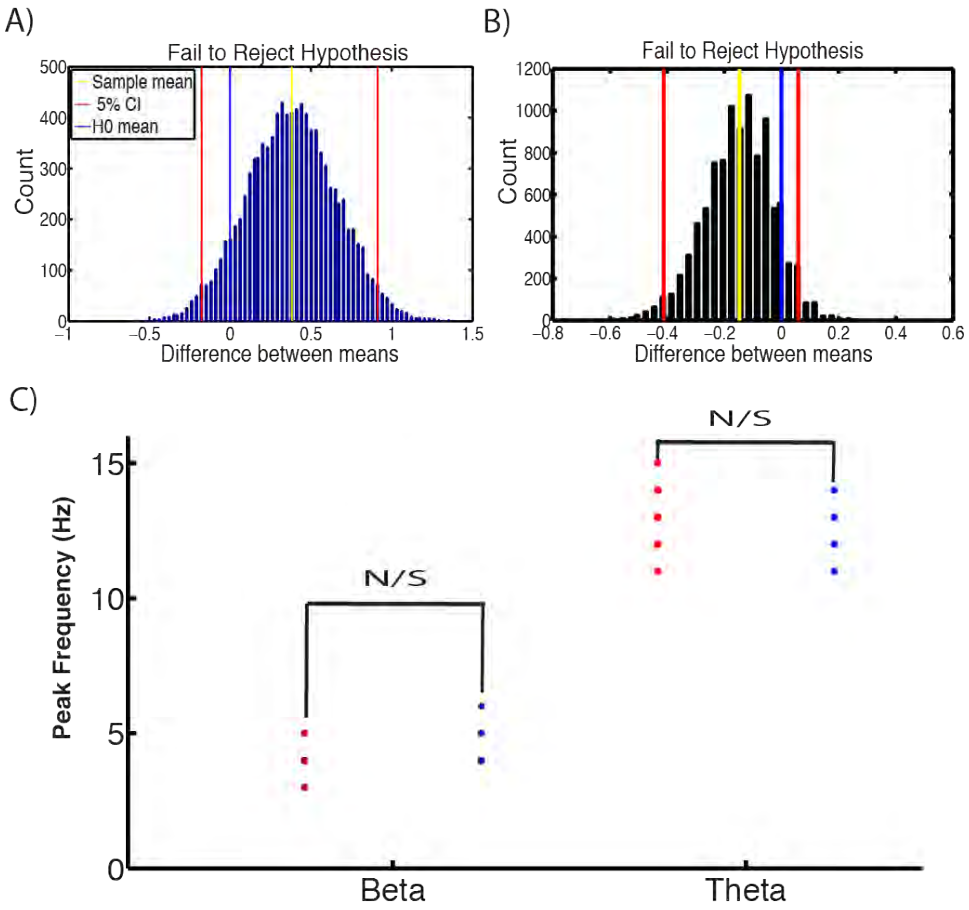

Figure 4.10. Bootstrapping distribution histograms comparing the peak power for theta (A) and Beta (B) activity. No differences were found for the peak frequency values compared between microwire and sinusoidal probes for theta and beta activity (C). H0 mean = hypothesis mean. CI= confidence interval. N/S= not significant in bootstrap test.

4.4.2 High Voltage Spindles

A high voltage spindle response was observed in rabbit-R. Although the filters were set to capture spiking activity, a 600 Hz bursting response was recorded on majority of functioning electrodes. Interestingly, electrodes implanted on the same side of the brain were similar in the activity elicited, hence discounting any potential artefact obtained from the ground. Further, ground to ground recording was not conducive in eliciting such activity. This activity is similar to that reported by Buzsaki and colleagues in rodents (Buzsaki et al., 1988). Raw waveform examples for selective days are shown in Figure 4.11.

This activity was discounted as being genuine spiking activity. Individual electrodes implanted in the same hemisphere and independent of electrode type, recorded similar synchronous responses (Figure 4.11). If genuine spiking activity was being recorded, this would not be the case and individual electrodes would show differing activity. Such a synchronous response is characteristic of the rodent sensorimotor cortex (Buzsaki et al., 1988).

For this response, SNR values were calculated in accordance to Suner and colleagues (Suner et al., 2005), although the equation was slightly modified. For the signal, the peak-to-peak amplitude (A) of the mean signal waveform was calculated. For the noise, the peak-to-peak amplitude of the mean noise waveform was calculated from a section of data where no signal was present. Noise was then calculated as 2 x the average standard deviation of the mean noise waveform (ε). SNR was then calculated as A/ ε.

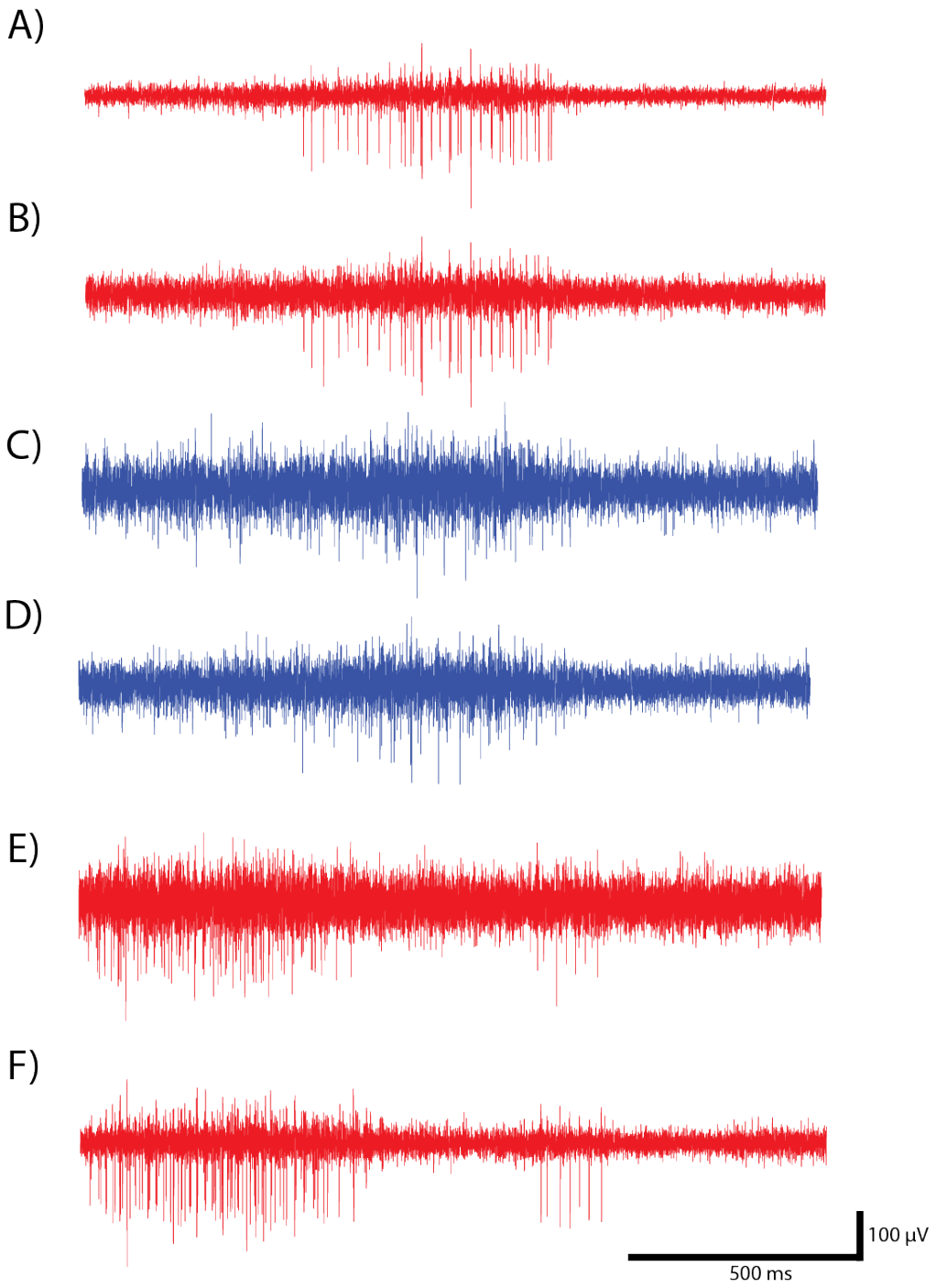

Figure 4.11. Example raw traces from individual electrodes implanted on the right (A-D) or left (E-F) side of the brain. Sinusoidal and microwire electrode recording sites are shown in red and blue respectively. This activity was not counted as spiking activity due to the highly synchronous nature of the activity found on all electrodes, which was hemisphere dependent. This activity is a feature of the rabbit sensorimotor cortex.

Figure 4.12 shows overlain waveforms for selected days over a 140-day period. In general, the sinusoidal probes had higher mean peak-to-peak amplitude per recording session compared to the microwire electrode.

The overall response for average mean peak-to-peak amplitude, mean noise amplitude, SNR and impedance over the recording period is shown for both sinusoidal (n= 15 recording sites) and microwire (n= 2 recording sites) electrodes in Figure 4.13.

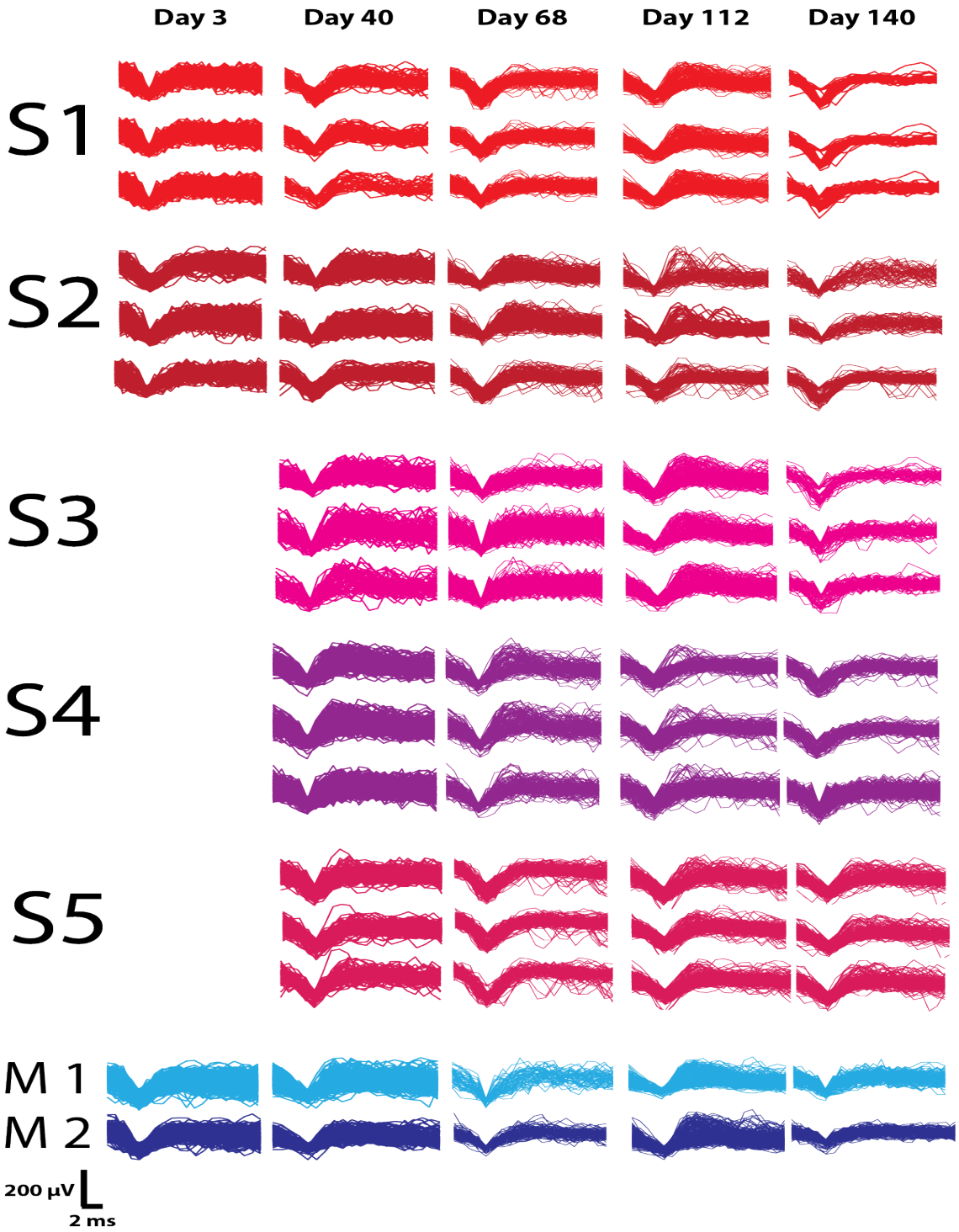

Figure 4.12. Overlain waveforms for 5 sinusoidal probes (S1-5, red triplet shades are individual recording sites) and 2 microwire electrodes (M1-2, bottom two blue shades) over a 140 day indwelling period. Overall the sinusoidal probe gave higher peak-to-peak amplitude over the indwelling period.

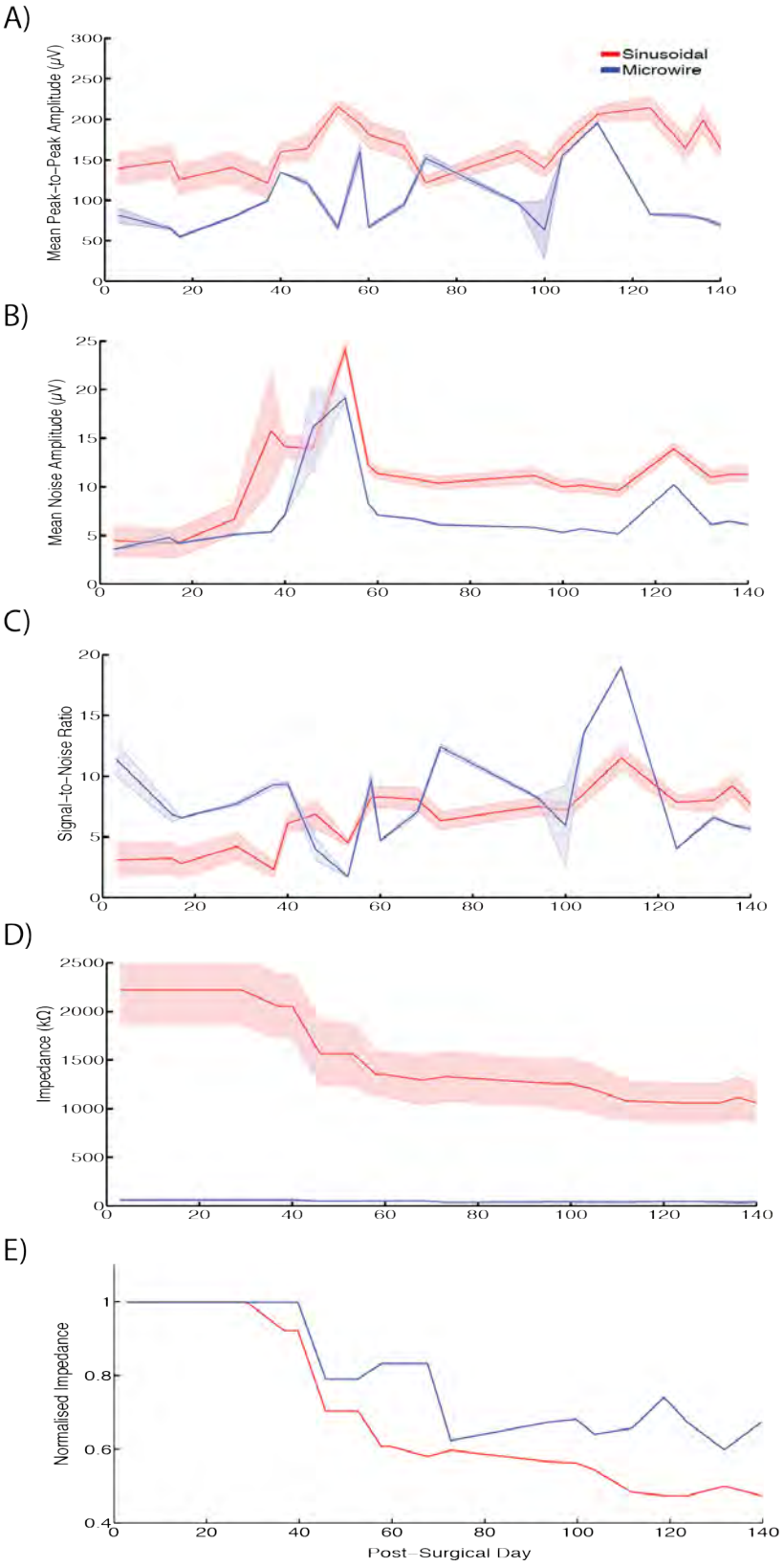

Figure 4.13. Overall sinusoidal (n=15 recording sites) and microwire (n=2 recording sites) chronic performance over a 140 day indwelling period. Shaded error bars show SEM for specific measured recording parameters. A) Average mean peak to peak amplitude recorded per recording session. B) Average noise amplitude recorded per recording session C) Signal-to-noise ratio over the entire recording period (values from A/B). D) Impedances over the entire recording period as a function of post surgical day. E) Impedance normalised in accordance to the first recording session for every electrode across the recording period. There

was an overall decrease in impedance for the sinusoidal (R^2=0.84) and microwire (R^2=0.78) electrode over the indwelling period. Error bars indicate maximum, minimum and mean standard deviation recorded over the entire recording period.

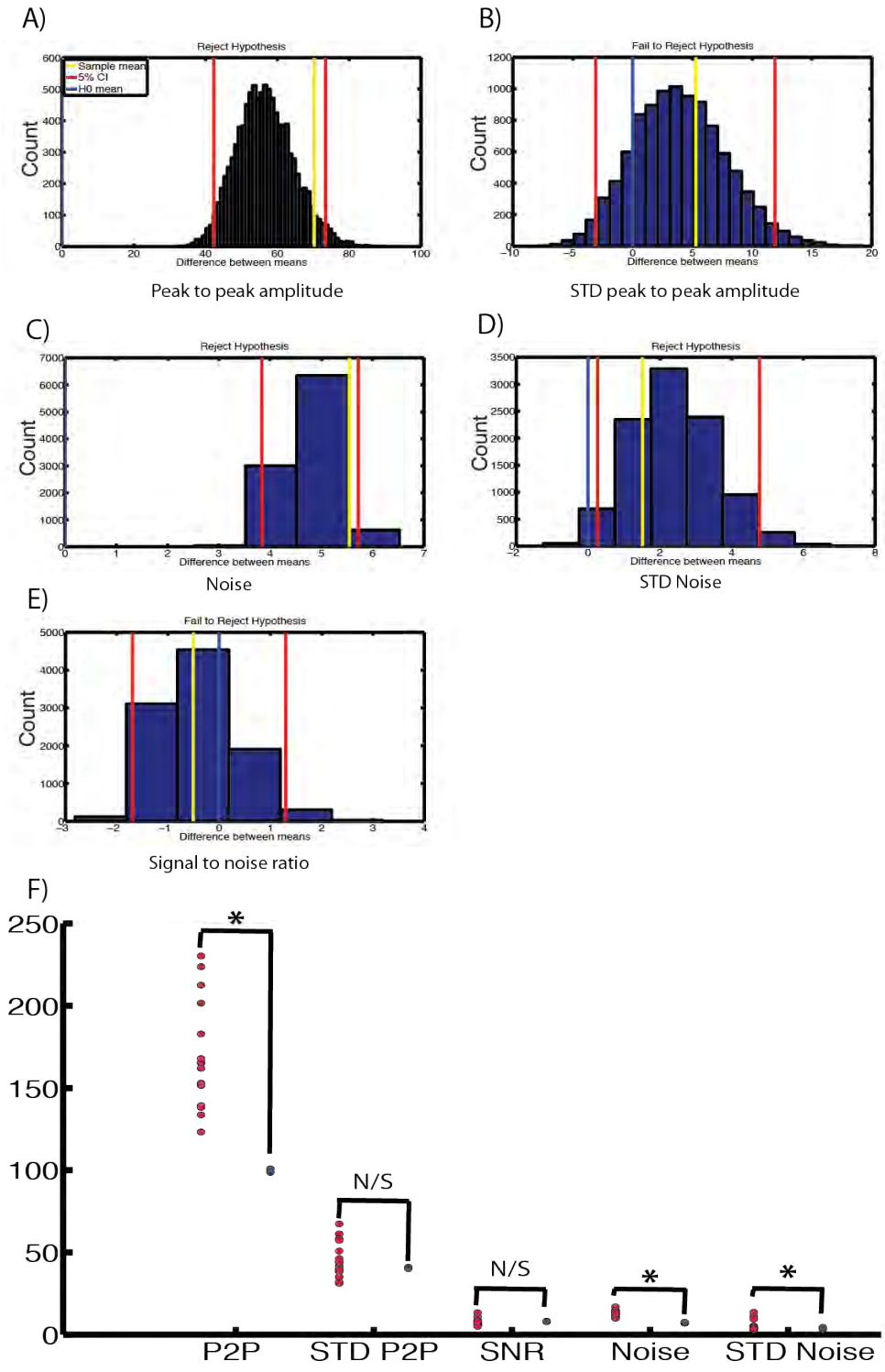

Figure 4.14. Comparison histograms of daily mean peak-to-peak amplitude (A, P2P), standard deviation of mean peak-to-peak amplitude (B, STD P2P), mean peak-to-peak noise amplitude (C), standard deviation of the noise amplitude (D, STD noise) and signal-to-noise ratio (E, SNR)) using bootstrapping methods between the two electrode types. The sinusoidal probe had higher peak-to-peak amplitudes and noise. However, there was no difference for the daily SNR values (F). H0 mean = hypothesis mean. Cl= confidence interval. P2P

amplitude and noise values in µV. * = null hypothesis mean value did not fall between the 2.5 and 97.5 % percentile range calculated from the bootstrap mean values between electrodes. N/S= not significant.

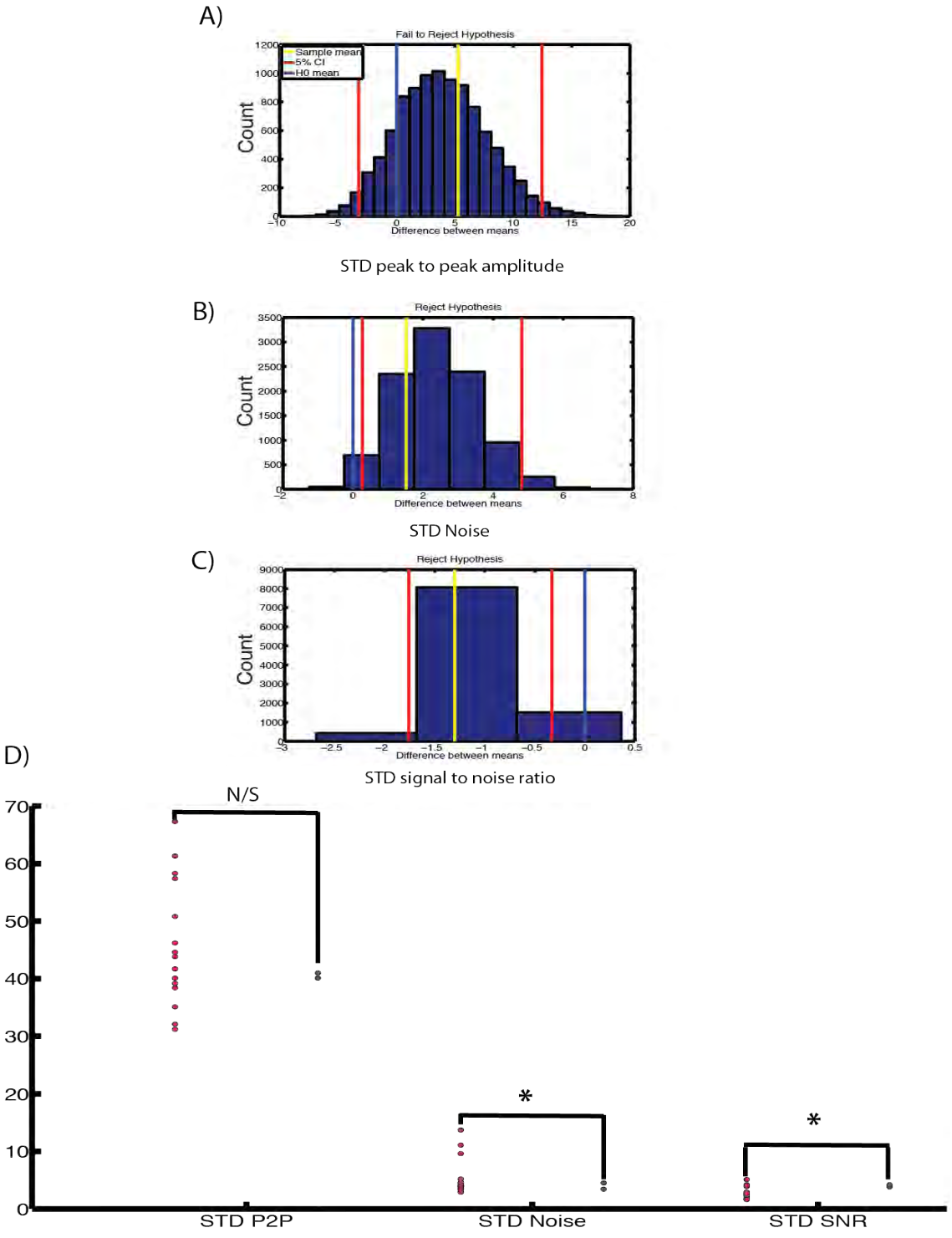

Figure 4.15. Comparison histograms of standard deviation values obtained across the entire recording period for mean peak-to-peak amplitude (A, STD P2P), noise (B, STD Noise) and SNR (C, STD SNR) using bootstrapping methods between the two electrode types. The sinusoidal probe (red) had higher variation in peak-to-peak and noise. However, there was less variation for the SNR values (D). H0 mean = hypothesis mean. Cl= confidence interval. STD P2P amplitude and STD noise values in µV. * = null hypothesis mean value did not fall between the 2.5 and 97.5 % percentile range calculated from the bootstrap mean values between electrodes. N/S= not significant

Figure 4.14 and 4.15 show the overall recording parameters compared between the two electrode types via bootstrapping methods. Overall, the sinusoidal probes had higher mean peak-to-peak values compared to the microwire electrode (Figure 4.14A). The sinusoidal probe had a higher noise floor (Figure 4.14C). There was no difference in the SNR between the two electrode types (Figure 4.14E). To compare the stability of the two electrode types, bootstrapping measures were employed for standard deviation values obtained across the entire recording period (Figure 4.15). However, this comparison was treated with caution as only 2 microwire values were compared to 15 sinusoidal values. The sinusoidal probe was more stable in terms of SNR (Figure 4.16, Figure 4.15C) but worse for noise stability (Figure 4.15B). There appeared to be no difference for mean peak-to-peak amplitude stability across the entire recording period for both electrode types (Figure 4.15A).

In summary, the sinusoidal probe gave scope to record higher mean peak-to-peak amplitude values with comparable stability to the microwire electrodes. Further, higher noise floor values were obtained for our electrode, with worse stability over the indwelling period. Similar SNR values were obtained (Figure 4.16), however our electrode had more stable SNR values across the recording period.

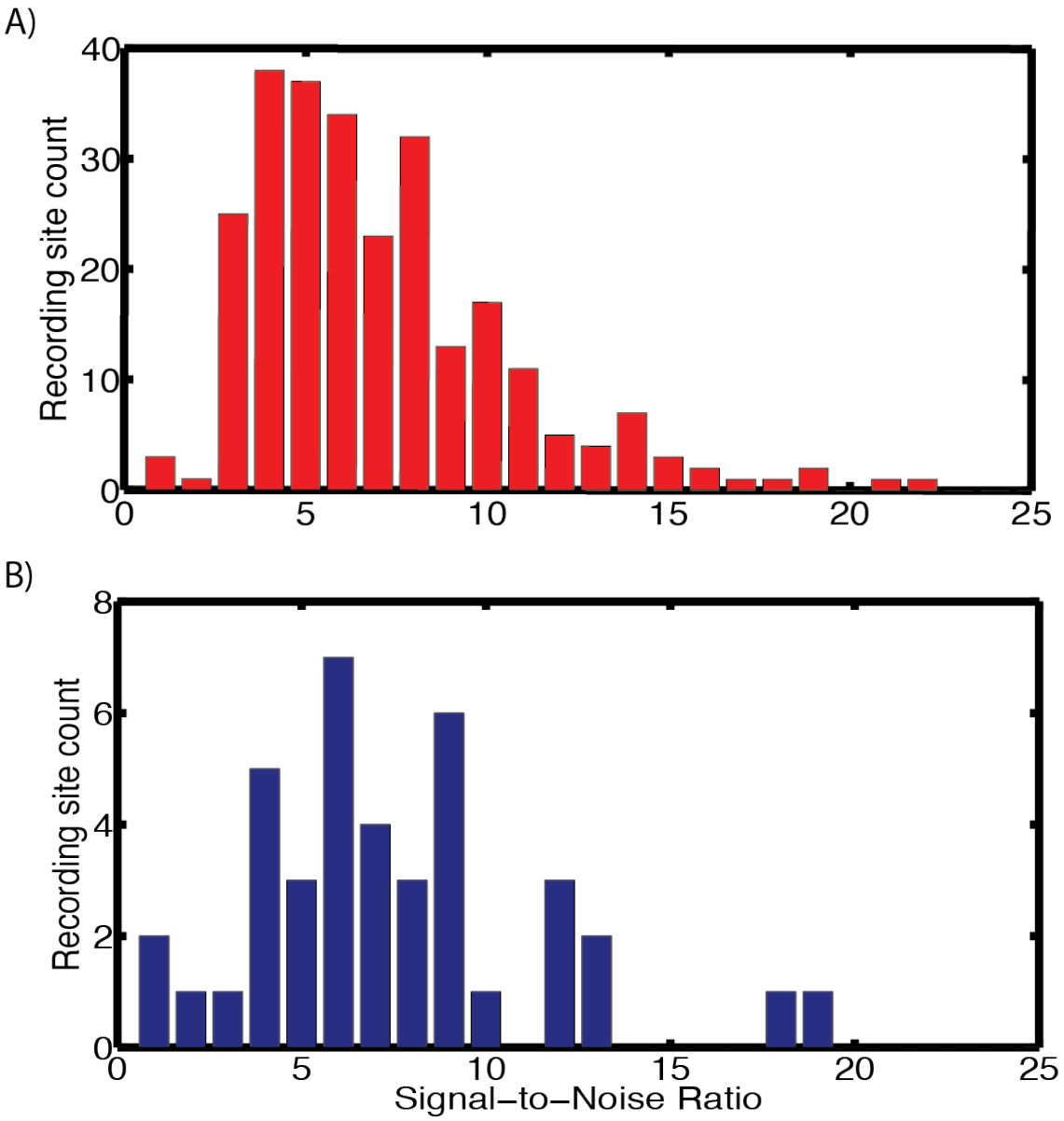

Figure 4.16. SNR histograms for all recording sites over the recording period for Sinusoidal (A) and Microwire (B) electrodes. Bootstrapping methods showed no differences between the two electrode types.

4.4.2.1 Impedance correlation with neuronal signal

Impedance values were correlated with both mean peak-to-peak amplitude and noise across all electrodes using the "regress" function on Matlab (Matlab 2009a, Mathworks,USA). There was no correlation between mean peak-to-peak amplitude (R^2=0.037)/noise (R^2=0.015) and *in-vivo* impedance.

These results suggest that *in vivo* impedance measurements are a poor indicator of chronic electrode performance possibly owing to the complex *in vivo* environment.

4.4.3 Spiking activity

For spiking activity, principle component analysis spike sorting was performed with the custom written software GetSpike. This enabled spikes to be sorted by cluster cutting and times recorded. Individual single units were confirmed with interspike interval histogram construction, with clear obtainment of a refractory period (Jackson and Fetz, 2007).

Accepted waveforms consisted of sections 5 sampling points before and 15 after the threshold crossing. Data was imported into Matlab, where the signal-to-noise ratio per spike was calculated in accordance to Suner and colleagues (Suner et al., 2005). For the signal, the peak-to-peak amplitude (A) of the mean waveform was calculated. For the noise, the mean waveform was subtracted from all waveforms, with the standard deviation calculated from the resulting values. Noise was then calculated as 2 x the average standard deviation (ε). SNR was then calculated as A/ ε.

Spiking was recorded from two rabbits, N and L. Rabbit-N provided chronic recording data for a singular sinusoidal first generation electrode and Rabbit-L data for two microwire electrodes.

For the new electrode generation, spiking activity was recorded for a one day period from Rabbit-Lo before post-surgical complications lead to animal termination.

Figure 4.17-4.19 show example raw recording trace, overlain waveforms, mean peak-to-peak amplitude with corresponding noise floor and SNR for the sinusoidal probe for rabbit-N and the two microwire electrodes from Rabbit-L over the indwelling period. Interestingly, a chronic recording period of 678 days was obtained for the sinusoidal probe and only a 79 and 31 day period respectively for the two microwire electrodes.

Generally, the microwire electrodes obtained higher mean peak-to-peak amplitude and SNR for 10 days post-surgery, before the recording measures began to decline.

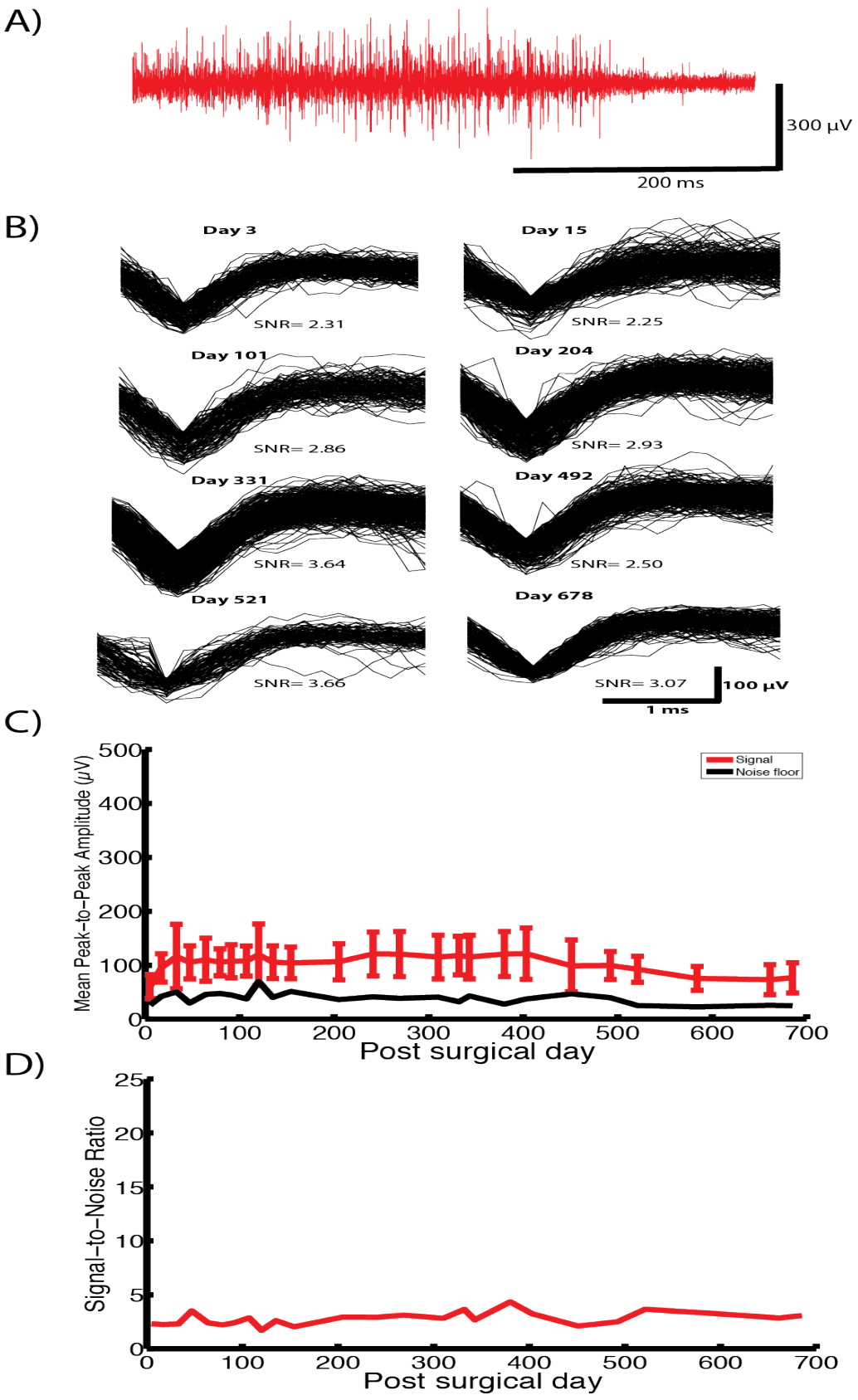

Figure 4.17. Spiking activity from sinusoidal probe in rabbit-N. A) Example raw waveform B) overlain waveforms from selected days over indwelling period, where multi-unit activity is primarily observed . C) Mean peak-to-peak amplitude over indwelling period, which was stable across the 678 day indwelling period. D) Signal-to-noise ratio stability over indwelling period.

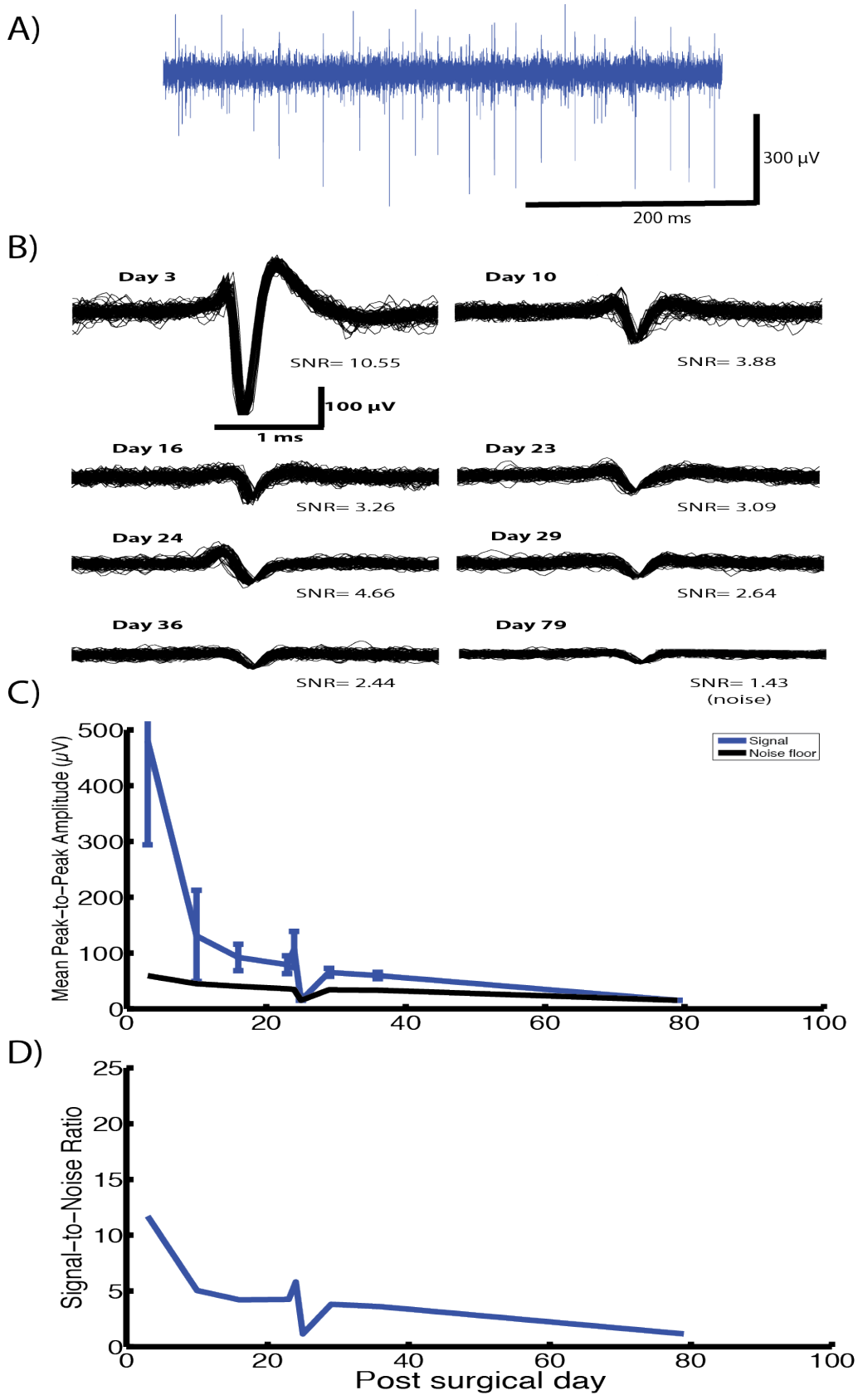

Figure 4.18. Spiking activity from a microwire elecrode in rabbit-L. A) Example raw waveform B) overlaid waveforms from selected days over indwelling period. Single unit activity is obtained on day 3, although multi-unit activity ensues from day 10 onwards. C) Mean peak-to-peak amplitude over indwelling period. D) Signal-to-noise ratio over indwelling period.

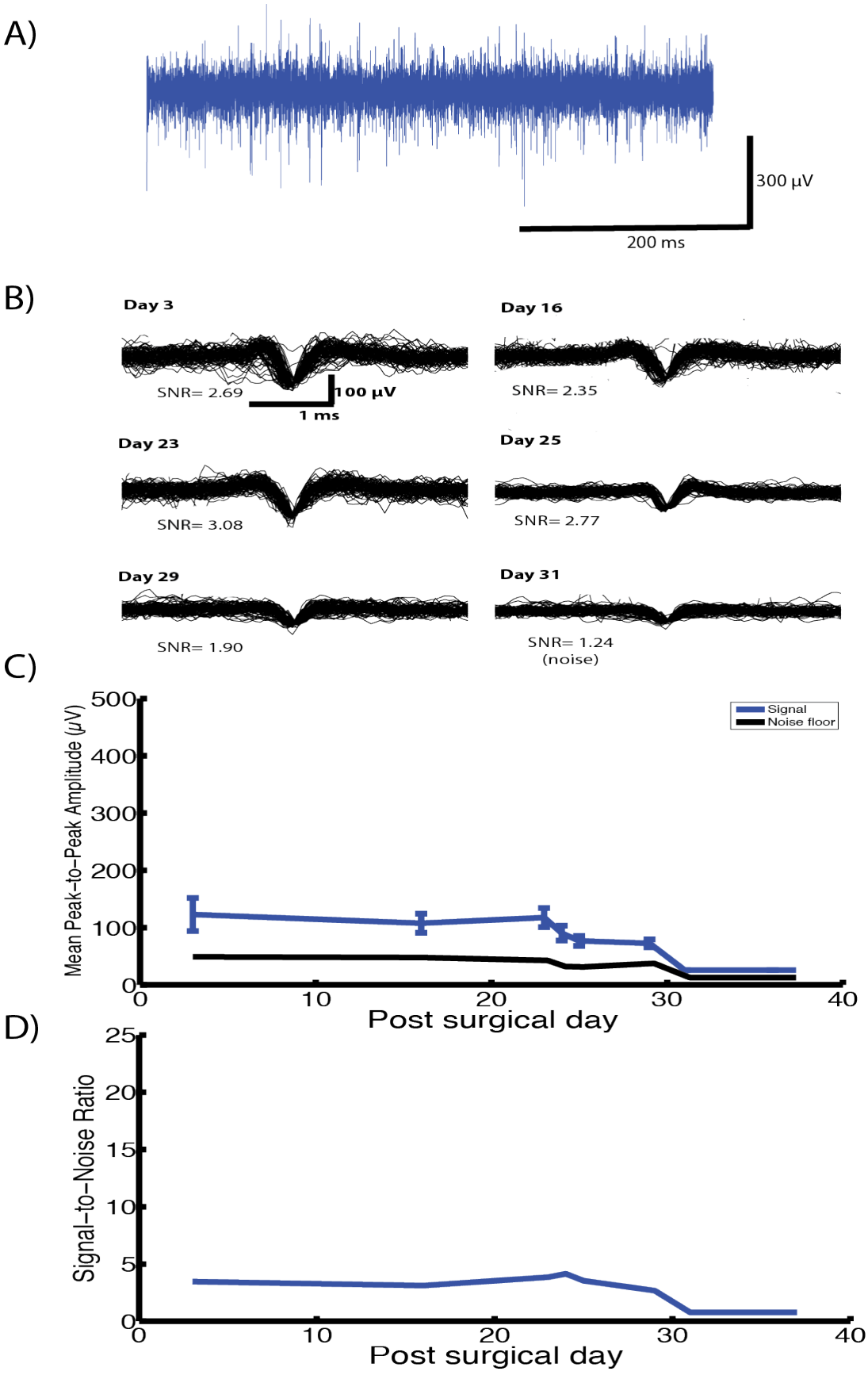

Figure 4.19. Spiking activity from a microwire elecrode in rabbit-L. A) Example raw waveform B) overlain waveforms from selected days over indwelling period, where multi-unit activity is primarily found. C) Mean peak-to-peak amplitude over indwelling period. D) Signal-to-noise ratio over indwelling period.

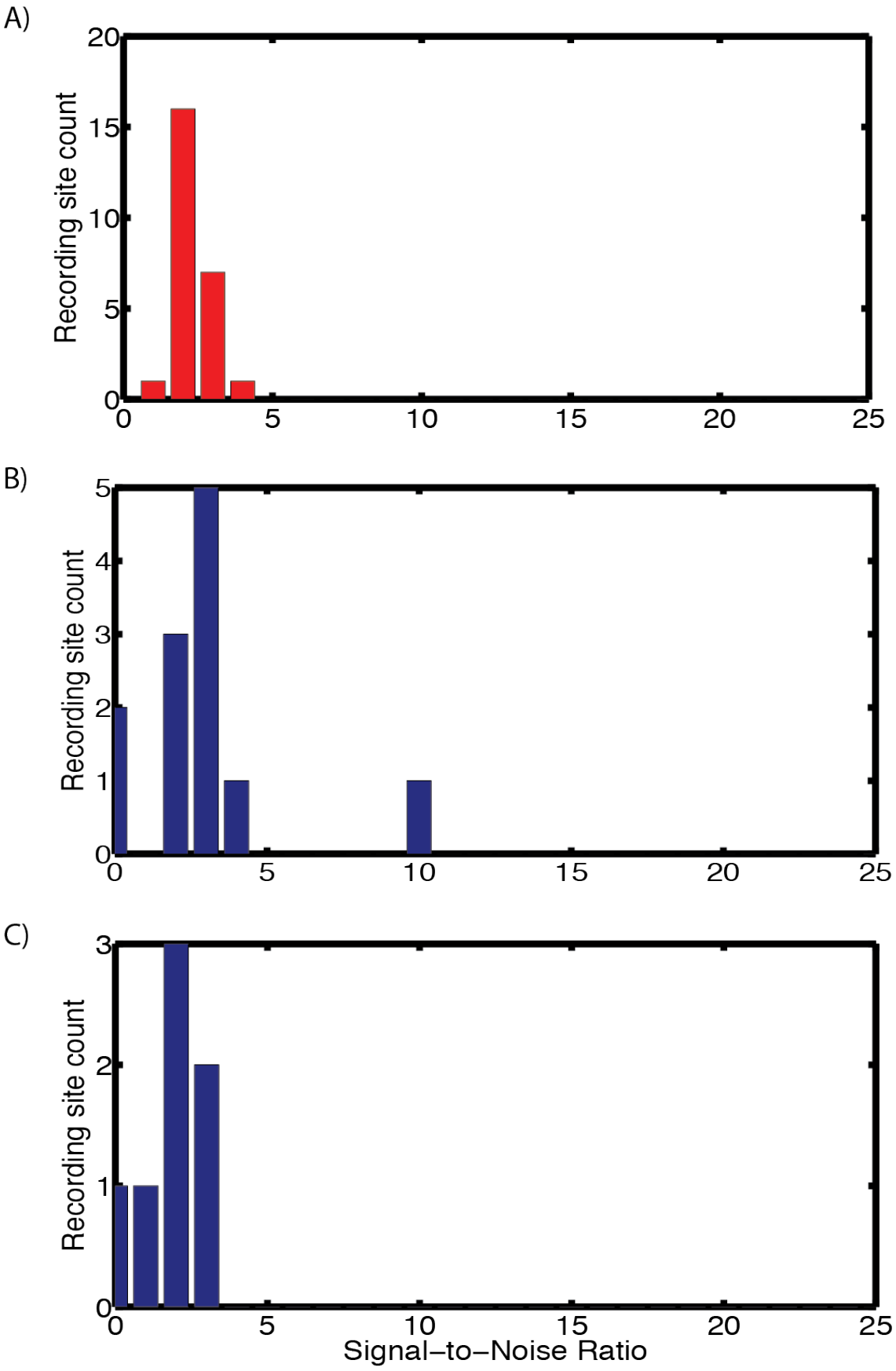

Figure 4.20. SNR histograms for Sinusoidal (A) and Microwire (B,C) electrodes over a 678, 79 and 31 day recording period respectively. Percentile bootstrapping methods showed no difference between the SNR between the electrodes for spiking activity.

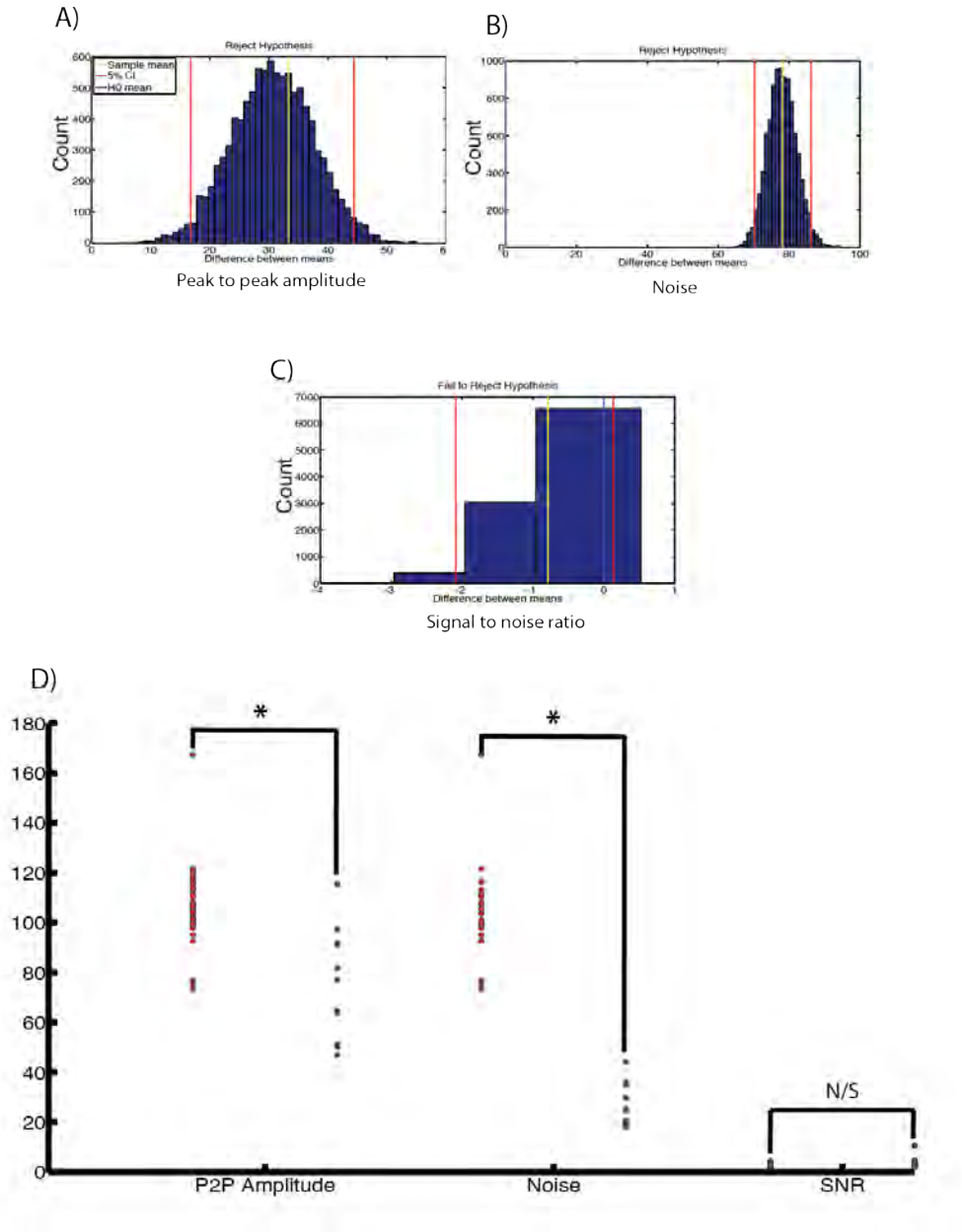

Figure 4.21. Comparison of spiking activity via bootstrapping methods for mean peak-to-peak amplitude (P2P amplitude, A), Noise (B) and Signal-to-Noise ratio (C, SNR) over the indwelling period. Differences were found for both peak-to-peak amplitude and noise only (D). H0 mean = hypothesis mean. Cl= confidence interval. P2P amplitude and noise values in µV. * = null hypothesis mean value did not fall between the 2.5 and 97.5 % percentile range calculated from the bootstrap mean values.

The sinusoidal probe gave higher mean peak-to-peak amplitude values with a higher noise floor (Figure 4.21). However, there appeared to be no difference for the SNR values between the two electrode types (Figure 4.20-4.21).

As only one sinusoidal probe gave spiking activity, bootstrapping methods were not used to compare electrode stability across the entire recording period. However, the sinusoidal probe had a lower standard deviation value for mean peak-to-peak amplitude

and SNR, with a comparable value obtained for the noise. Therefore, it appeared that the sinusoidal probe is more stable for recording spiking activity across the entire recording period (table 4.2).

	Sinusoidal	MW 1	MW 2
Mean peak-to-peak amplitude (µV)	103.7	113.3	72.2
STD peak-to-peak amplitude (µV)	16.7	146.17	21.2
Mean Noise (µV)	38.8	22	27.2
STD Noise (µV)	10.7	12.4	7.6
Mean SNR	2.79	3.79	2.3
STD SNR	0.61	3.04	1.1

Table 4.2. Average mean peak-to-peak, noise and SNR values with corresponding standard deviation (STD) values for spiking activity measured on sinusoidal and microwire electrodes. Overall the sinusoidal probe has more stable peak-to-peak amplitude and SNR values. The noise floor values were higher for the sinusoidal probe, although the noise stability was similar over the indwelling period.

Figure 4.22 shows a putative single unit obtained across all three electrode recording sites for the novel electrode generation three day post-surgery in Rabbit-Lo. The unit had differing SNR and mean peak-to-peak amplitude, which allowed for unit isolation. A custom written Matlab script, Tetcom (courtesy of Prof. Stuart Baker) was used to calculate the best combination SNR. This algorithm optimises linear correlation and for the three individual recording sites, SNR values of 2.01, 4.71, and 7.57 was obtained. A combination value of 11.87 was obtained overall. This shows the usefulness of recording the same single unit across three electrode recording sites.

The microwire electrode had a higher SNR from a putative single unit recorded in the same animal. However, this was a common trend found in spiking data for early stage microwire recording (Figure 4.18-4.19).

For the new electrode generation, putative single units were difficult to record as the animal model used became unreliable. Three rabbits were lost due to post-surgical complications not directly related to the electrode site implants. Therefore further characterisation for spiking activity was not possible during the thesis duration. There is

an inherent need to characterise the chronic performance spiking activity in a more reliable animal model.

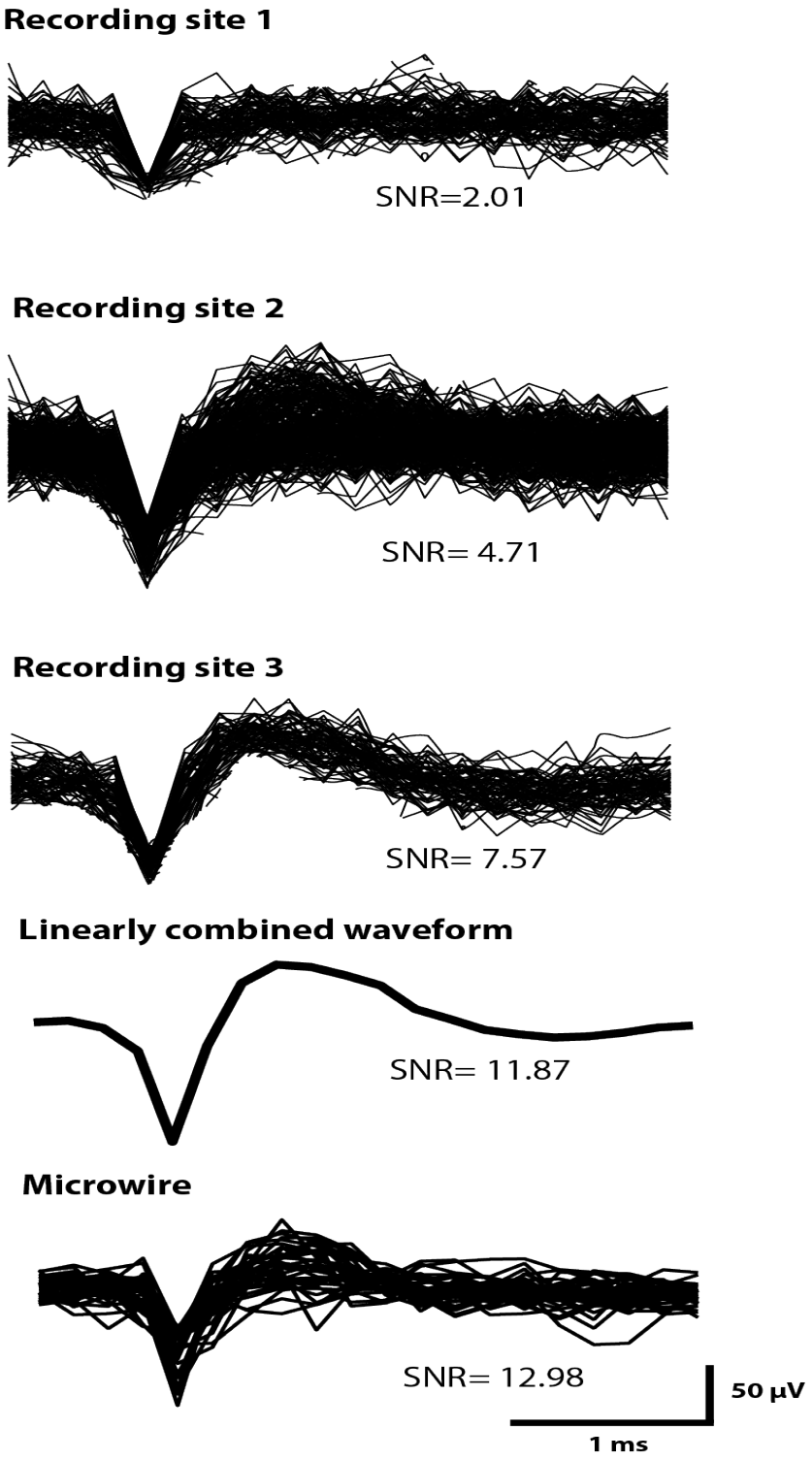

Figure 4.22. Overlain waveforms 3 days post-surgery for Rabbit-Lo. The same unit can be recorded across all three electrode recording sites, allowing for unit isolation based upon differing signal amplitudes and individual SNR. An algorithm optimising linear correlation has been used to produce a linearly combined waveform. A combined SNR of 11.87 was achieved showing the usefulness of recording the same unit across the three electrode recording sites. This combined SNR is higher than that achieved from a solitary sinusoidal probe recording site. Again the microwire electrode has a higher SNR than the sinusoidal probe.

4.5 Conclusions

Electrodes were successfully implanted and analysed for chronic performance with increasing implantation success each surgery. For LFP recordings our electrode gave stable power over the recording period with similar neuronal signals recorded across all three recording sites. For the high voltage spindle responses our electrode gave higher peak-to-peak amplitudes and noise floor values with better or comparable stability across the recording period. Similar SNR values were obtained and our electrode gave a more stable SNR across the recording period. For spiking activity, our electrode first generation gave a longer chronic recording period with a more stable SNR across the recording period, with better mean peak-to-peak amplitude values. Although these finds are initially promising, further testing is needed to support this find as we only have shown this for one electrode. For the new electrode generation, it was possible to record the same single unit across all three recording sites.

Overall our probe always gave higher noise floor values owing to smaller electrode recording site area compared to the microwire electrode.

From the results our electrode was better in terms of electrode recording parameter stability. However, further chronic testing is needed to evaluate electrode performance for putative single units for the new electrode generation.

There is a need to develop a more robust animal model to further test chronic electrode performance, as three rabbits were lost due to complications not directly related to the implanted electrodes.

4.6 Discussion

The sinusoidal probe appeared to be more stable than the microwire electrode in terms of recording stability, however due to the relatively small n numbers, further testing is still needed to corroborate these promising initial findings. To compare our electrode performance with other commercially available electrodes a commonly used SNR measure was used. For our electrode, peak SNR values were obtained at 4-6 and 2-3 for high voltage spindles and spiking respectively. For the high voltage spindle response, a more appropriate comparison would be SNR from multi-unit activity. Jackson and colleagues obtained values around 7 for their microwire electrode (Jackson and Fetz,

2007). For spiking, our electrodes were similar to Suner and colleagues, showing units had SNR values of 3-4 for their Utah array electrode over a 81 day recording period (Suner et al., 2005). Interestingly Ward and colleagues obtained values between 6-7 for multiple electrode types including Utah array, microwire and Michigan probe electrodes over a 30 day recording period (Ward et al., 2009). For novel carbon fibre electrodes, SNR values of 3-8 were obtained over a 5 week indwelling period (Kozai et al., 2012a). Our electrode had comparable or slightly lower SNR values, although variability in recording stability was less than the microwire electrode.

Signal amplitudes of 60-400 μV (Ward et al., 2009), 120-250 μV (Suner et al., 2005), 60-100 μV (Vetter et al., 2004) and 60-200 μV (Kozai et al., 2012a) have been obtained for multiple electrode types, Utah array, Michigan probe and carbon fibre electrode respectively for chronic recording. We show recording amplitudes of 130-230 and 80-100 μV for high voltage spindle responses and spiking, which is comparable to these electrode types.

Noise values are rarely reported in chronic electrode studies, however from the Michigan probe, a value of 6-13 μV has been reported (Vetter et al., 2004). We report values of 7-13 μV for high voltage spindle responses and 38 μV for spiking recording. The former is highly comparable to the Michigan probe electrode. Interestingly, our second-generation sinusoidal probe has approximately 3 times less noise than the first generation. The three recording sites had to be fused when wire bonding for the first generation, hence the possible summation of noise values.

The measure we employed for electrode stability was the standard deviation from average mean values of recording parameters. Jackson and colleagues developed a waveform correlation to observe electrode stability in maintaining similar single units (Jackson and Fetz, 2007). However, this measure should be treated with caution, as similar waveforms may not be wholly indicative of recording from the same unit; units that are the same have been shown to change waveform shape over a chronic recording period. The stability measure we used, combined with waveforms obtained showed that the sinusoidal probe was good at maintaining similar neuronal activity throughout the recording period.

Impedance was not correlated with noise or signal values. For saline testing, thermal noise is the main component of noise as there is no neuronal activity present. *In vivo*, SNR should follow impedance trends as thermal noise is directly related to the electrode

impedance (Ludwig et al., 2006). As there was no correlation, it is possible that other sources of noise (e.g. biological or instrumentation noise) may have dominated the overall noise floor, as sources of noise summate in quadrature. High impedance electrodes did not show lower SNR values, although impedance >4 MΩ made signal amplitude obtainment difficult for our electrode. Interestingly, Ward and colleagues for multiple electrode types showed no correlation between SNR and impedance (Ward et al., 2009). Further, Suner and colleagues report that signals with high SNR were recorded from electrodes with a wide range of impedances and there was no ideal electrode impedance for Utah array chronic recording. However, electrode impedance was better correlated to signal amplitudes in one monkey (Suner et al., 2005). Therefore impedance measurements may not be the best indicator for chronic electrode performance.

Overall, our electrode had stable or initially declining impedances that stabilised over the indwelling period, which was similar to the microwire electrode. In contrast, silicon based probes have increasing impedances over both a 30 (Ward et al., 2009) and 81 (Vetter et al., 2004) day indwelling period. For the Utah array there is a drop in impedance > 1 year post-implant, which is related to electrode degradation.

For high voltage spindle recording, a few electrodes had drops in impedance after >20 days post-surgery, relating to better recording parameters. This may be related to the polyimide ball anchor. As the anchor was not fully cured it was possible that slow dissolution may have given access to more electrode recording site area over the indwelling period. For future iterations, an alternate anchor may be required.

There is a need to characterise putative single units for the second-generation sinusoidal probe. The unreliability of the rabbit animal model prevented further characterisation during the thesis period. Three out of six rabbits survived the initial surgery. Post-surgical complications leading to rabbit mortality was unrelated to the electrode recording sites. Rabbits are known after an extended anaesthesia period to not recover well if any post-surgical complications arise (surgical experience and personal communication with veterinary staff). Therefore using a more suitable animal that can sustain long period (>4 hours) anaesthesia and more resilient to potential post-surgical complications is needed.

Chapter 5: Device histology

5.1 Introduction

The glial reaction leads to electrode failure. It is paramount that glial markers are analysed around electrode implants to evaluate the damage to surrounding neuronal tissue. The majority of studies analysing the glial response around the electrode only account for the tissue where the tip resides, using horizontal sections (Biran et al., 2007, Winslow et al., 2010a, Winslow and Tresco, 2010). However, a better approach is to observe the tissue response around the whole device interface to determine neuronal tissue damage in regions above the electrode tip. This is important as damage in the area above the recording tip can influence the tissue where the tip resides (Kozai et al., 2010b).

To analyse the glial reaction around our electrode implants, we used horizontal sections corresponding to the electrode profile at different depths to observe gliosis around the whole of the device interface. Using this approach, many slices can be obtained to quantify the effect of gliosis around our electrode implants. The sections were tested for the presence of microglia, astrocytes and viable neurons with the use of appropriate markers. Animals were sacrificed at appropriate time-points to allow gliosis quantification to assess the effectiveness for the sinusoidal probe as a chronic implant.

The markers chosen for this study were Isolectin-B4, GFAP and SMI-32 for microglia, astrocyte and neurofilament staining respectively. Isolectin-B4 has been used in numerous studies marking for microglia expression upon trauma to the brain (Wang et al., 2009). GFAP is found in astrocytes, Bergmann glia and chondrocytes of elastic cartilage (Winslow et al., 2010a). Therefore it is an ideal marker to be used for our specific application in observing the astrocytic reaction around neuronal implants (Polikov et al., 2005). SMI 32 is used to visualise neuronal cell bodies, dendrites and some thick axons in the CNS and PNS, but thin axons are not normally revealed (Polikov et al., 2005). This marker can reveal the degree of neuronal integration around an implant, where the dendrites can be shown to interact with the implant to form a stable tissue-electrode interface (Bartels et al., 2008, Winslow et al., 2010a).

In this chapter, for the bottom/tip representation, we show that the sinusoidal probe had less of a microglial response over a 12-24 month time point. There was also an increase

in neuronal integration as shown by neurofilament staining over 12-24 month time period. There was a decreased astrocytic response for both a 6 and 24 month time point. This chapter highlights the possible reduction of micromotion-induced damage with the sinusoidal probe.

5.2 Methods

Histology protocols were performed to determine gliosis. All animals was perfused transcardially with phosphate buffered saline (PBS) and then formal saline whilst under a hypnorm (0.3ml/kg i.m.) and midazolam (2 mg/kg i.v.) anaesthetic regimen to fix the brain. The relevant brain regions were removed and transferred to a 10 % sucrose solution. The day before microtome sectioning, the extracted brain was transferred to a 30% wt sucrose solution for cryoprotection. For microtome sectioning, relevant brain regions were dissected and 50 μm thick sections were obtained according to the electrode profile.

For immunohistochemistry, horizontal slices were stained for microglia, astrocytes and neurofilament relating the top, middle and bottom of the electrode profile (Figure 5.1). Slices were incubated with 3% normal horse serum (Vector Labs, UK: S-2000) for 1 hour to prevent non-specific binding. Sectioned slices were incubated overnight with relevant concentrations of the primary antibodies GFAP (Sigma-Aldrich, UK), isolectin-b4 (Vector Labs, UK: Biotinylated Griffonia (Bandeiraea) Simplicifolia Lectin 1, B-1105) and where appropriate, SMI-32 (Cambridge Biosciences, UK: R-500) made up with PBS-triton on a rocker at 4^{o}C (table 5.1). GFAP and Neurofilament slices underwent incubation with biotinylated antimouse for two hours. All slices were then incubated with horse radish peroxide streptavidin (HRP strep, Vector Labs, UK: SA-5004) for one hour. After every incubation stage three, five minutes washes with PBS were performed on the slices on a rocker.

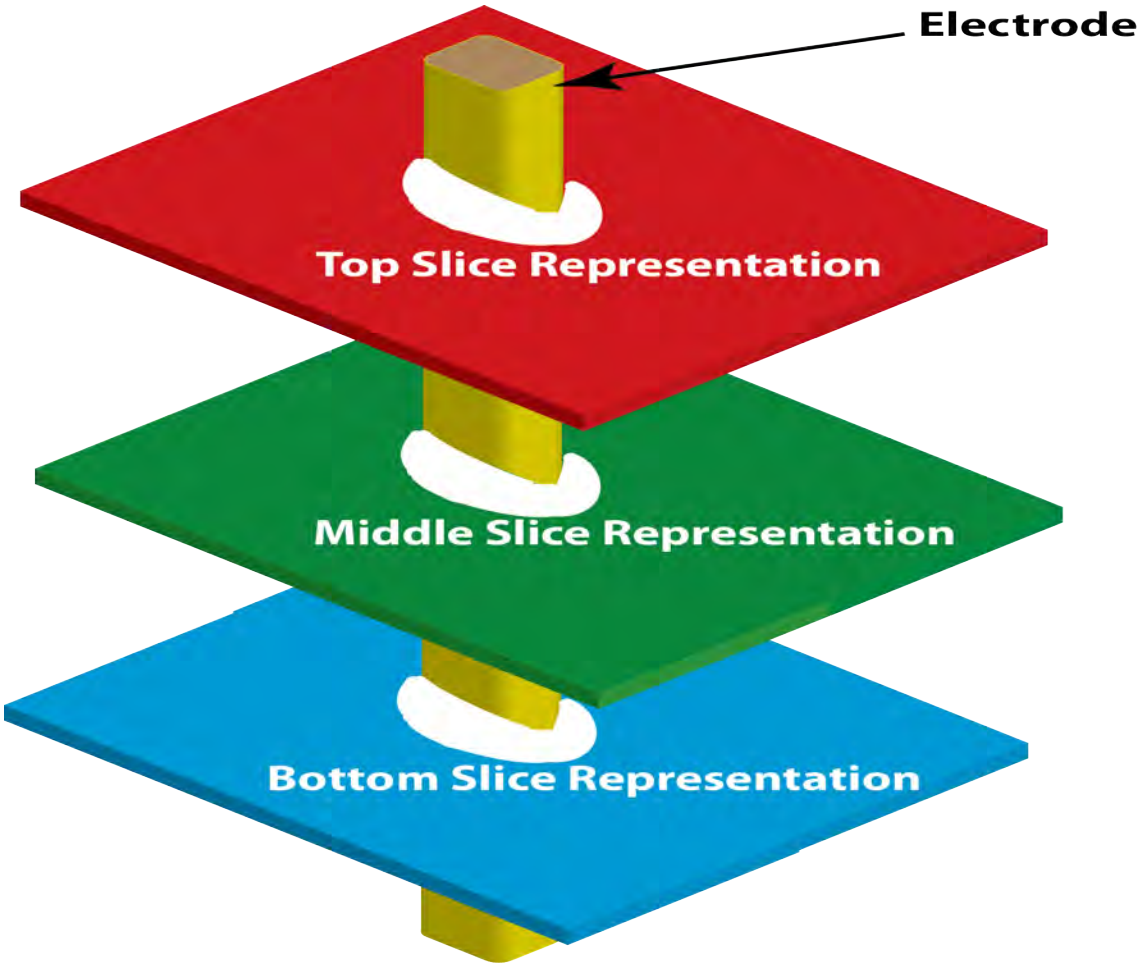

Figure 5.1 Illustration showing where slices were taken relative to the electrode for the different depth profiles. For each depth profile, multiple sections were taken until a thickness of 1 mm was reached. This related to the 3 mm length for both electrode types.

Finally, the Diaminobenzidine (DAB) reaction was performed. One tablet per 5 ml of PBS of peroxide and urea hydrogen was formulated (Sigma-Aldrich, UK). Slices were incubated with DAB for 5 minutes before being transferred into PBS filled wells. Slices were mounted on gelatin-coated slides according to electrode profile and staining and were left to dry overnight. The slices then underwent a series of alcohol (5 minutes of 70%, 95%, 100%, 100%) and two, 10 minute histoclear washes (Sigma-Aldrich, UK), before cover slips were mounted with histomount (Sigma-Aldrich, UK).

Stain	Target	Antibody type	Concentration
GFAP	Astrocytes	Primary	1:500
SMI 32	Neurofilament	Primary	1:1000
Isolectin-b4	Microglia	Primary	1:200
HRP strep	-----	-----	1:200
Biotinylated antimouse	-----	-----	1:200

Table 5.1. Antibodies and relative concentrations used for analysing the immune response around electrode implants. All antibodies were diluted in PBS-triton.

5.2.1 Statistical analyses

For immunohistochemisty, slices were examined under an optical microscope at x10 magnification and images taken of electrode tracks and background at a pre-saturation exposure time dependent on the staining with the use of axiovision software (Carl Zeiss Microimaging, Germany). Each image was then normalised in accordance to endogenous background staining in the Matlab environment (2009a, MathWorks, USA) and inverted. Background images were taken at least 1 mm away from the electrode implantation site. Overall background intensity values were subtracted from electrode tract images to leave the glial response around electrodes (Figure 5.2). Images were imported into ImageJ64 software (NIH, USA) and the radial distribution intensity taken for slices from microwire and sinusoidal probes, centred on the implant sites and according to the electrode shaft profile. This analysis was carried out on all sections for microglia, astrocytes and where appropriate neurofilament. Normalised integrated intensity and distance from the electrode values were obtained for each slice for all identifiable electrode tracks at the three electrode shaft profiles (top, middle and bottom). To analyse the overall effect of the electrode implants, the mean of at least 15 electrode implantation sites for each depth profile were compared between the two electrode types. An overall effect was analysed as gliosis may change from one electrode implant site to another (Rousche and Normann, 1998).

Further analysis was then carried out in the Matlab environment (2009a, MathWorks, USA), where graphs were constructed for the mean intensity values obtained from both electrodes types across all identifiable electrode tracks at the specific electrode profiles for both the microglial and astrocytic response. Paired t-tests were performed comparing both electrode types on specific intensity values corresponding to 50-500 µm away from the electrode implantation centre across all electrode tracts and profile depths, at 50 µm spacing. Results were significant if $P<0.05$. This was in accordance to literature to allow for comparison purposes (Winslow et al., 2010a, Winslow and Tresco, 2010, Potter et al., 2012). The sinusoidal probe generally had a larger implantation hole than the microwire electrode (e.g. Figure 5.3). Therefore distance comparisons were corrected to account for differing implantation site sizes.

To account for multiple comparison error, the Bonferroni correction was performed. The smallest p-value obtained for each depth profile comparison had to be smaller than 0.05 divided by the total number of t-tests performed (10) to account for multiple comparison error. If this was the case, all t-tests performed were accepted for the specific depth profile comparison. Results presented in this chapter have passed the Bonferroni correction, unless otherwise indicated.

The probability of a false positive (type I error) being reported without the Bonferroni correction is given by $1-(1-\alpha)^n$, where α is the confidence interval and n is the number of t-tests performed. For our study this gives a value of 0.40. A summary of histology analysis is shown in Figure 5.2.

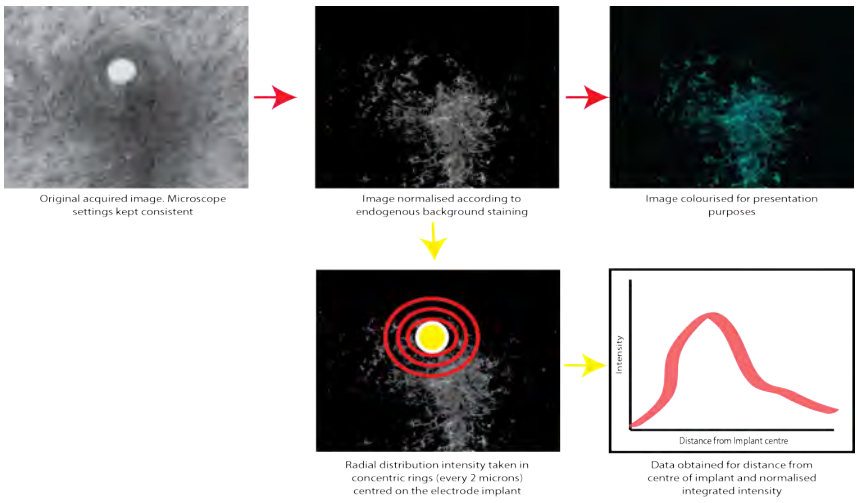

Figure 5.2. Summary of image processing for histology analysis. Red arrows indicate image processing and yellow arrows indicate image analysis.

5.3 Six month time point- Second Generation

The glial reaction was analysed at a 6 month time period for the new electrode generation in Rabbit-R and J. For the 6 month time point, microgliosis was not analysed due to failed staining techniques in both rabbit brains. Staining protocols were successfully optimised between the first and second brain after initial failed staining on test brain slices. However, staining failed in the second rabbit brain.

In Rabbit-J and R (Figure 5.3-5.7), a reduction in astrocytosis was apparent for the sinusoidal probe at the bottom (tip representation), especially in the close vicinity of the probe 0-200 μm. Interestingly, astrocytic interactions were found between microwire implantation sites (Figure. 5.3).

The combined data set also showed a significant reduction in astrocytosis around the sinusoidal probe for the bottom profile representation (Figure 5.7).

5.3.1 Astrocytic Response- Rabbit-J

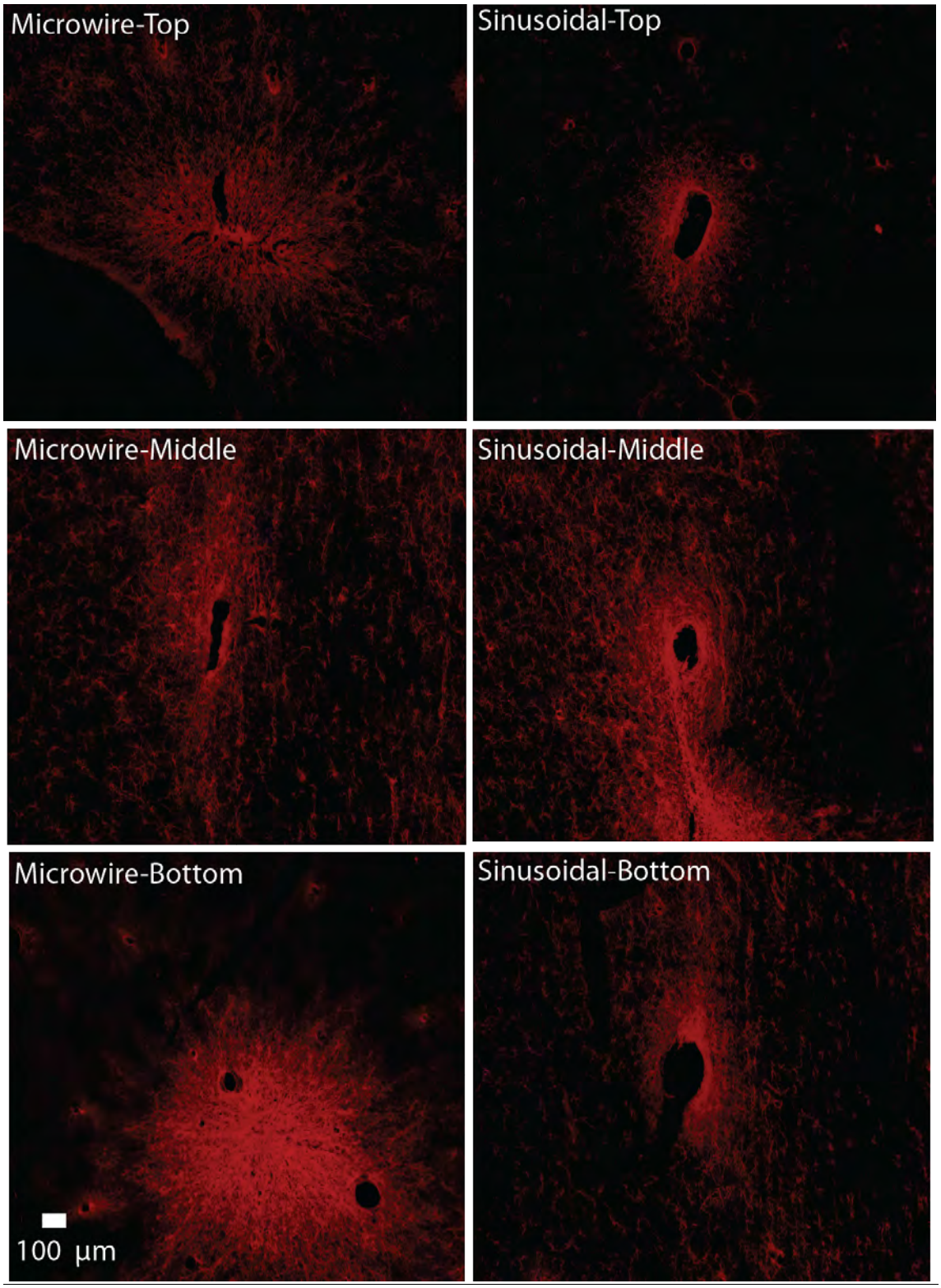

Figure 5.3. Representative images for the astrocytic reaction for both microwire and sinusoidal probe at 6 months. Interestingly, for the bottom representation, there was a clear interaction of recording sites for the microwire electrode. There was also a reduction in the astrocytic response for our probe.

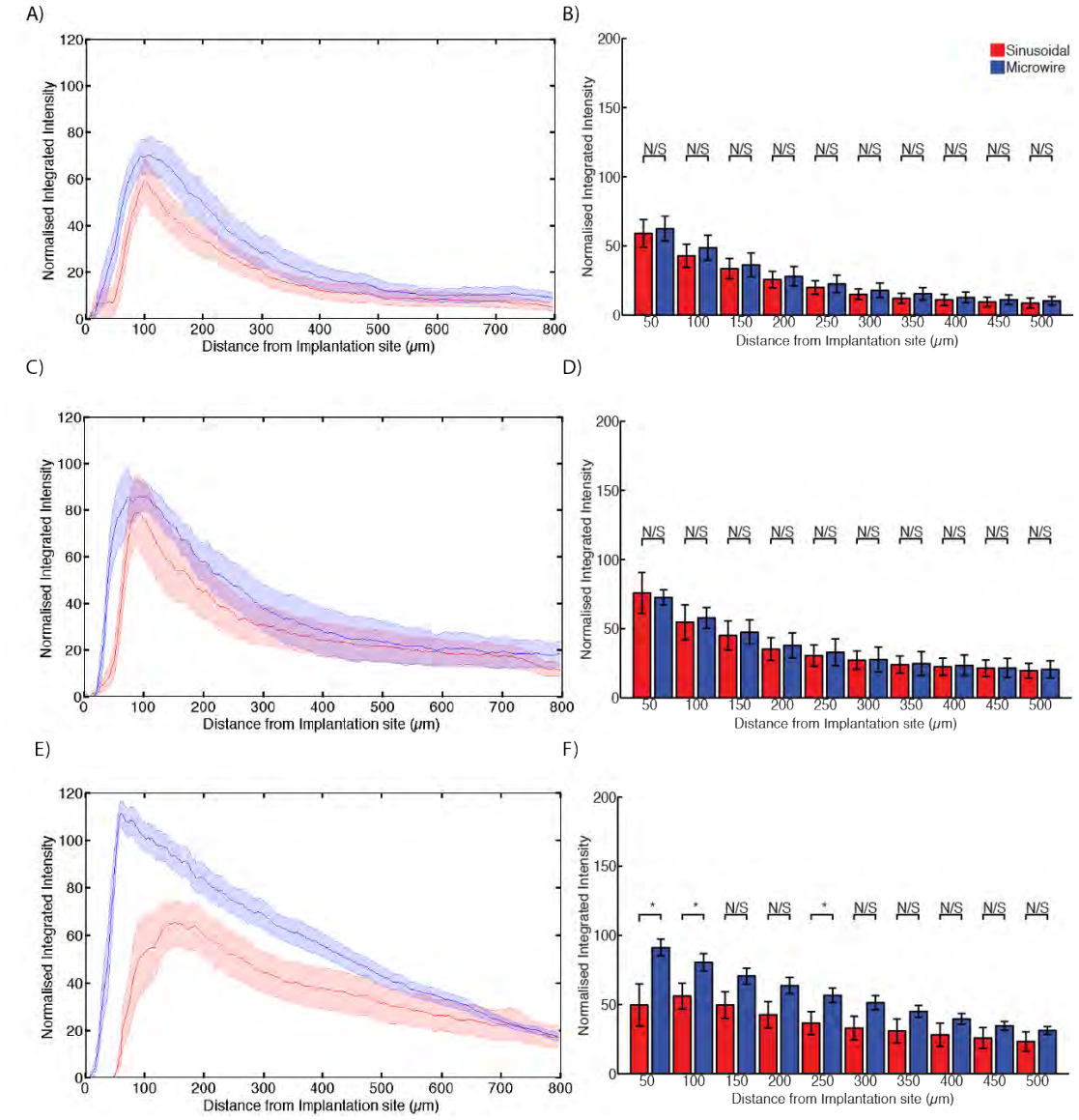

Figure 5.4. Overall astrocytic response to both electrode types (n= 4 microwire and 5 sinusoidal probes) in Rabbit-J at a 6 month time point. Overall normalised integrated intensity response (±SEM) are shown for the top, middle and bottom (tip) profile representation for both electrode types for the astrocytic reaction. All sections used were normalised according to endogenous background staining by subtracting mean grey scale intensity values obtained from background images taken at least 1 mm away from the site of gliosis. * = $p<0.05$; N/S = not significant. For the top and middle profile representation, no significant differences were found at any distance away from the electrode implantation site. For the bottom profile representation, significant differences were found at 50 ($t(15)=2.54, P<0.05$) ,100 ($t(15)=2.17, P<0.05$), and 250 ($t(15)=2.26, P<0.05$) µm away from the electrode implantation site representation. Reduced astrocytosis was evident for the bottom depth profile representation in the close vicinity for sinusoidal probe.

5.3.2 Astrocytic Response- Rabbit-R

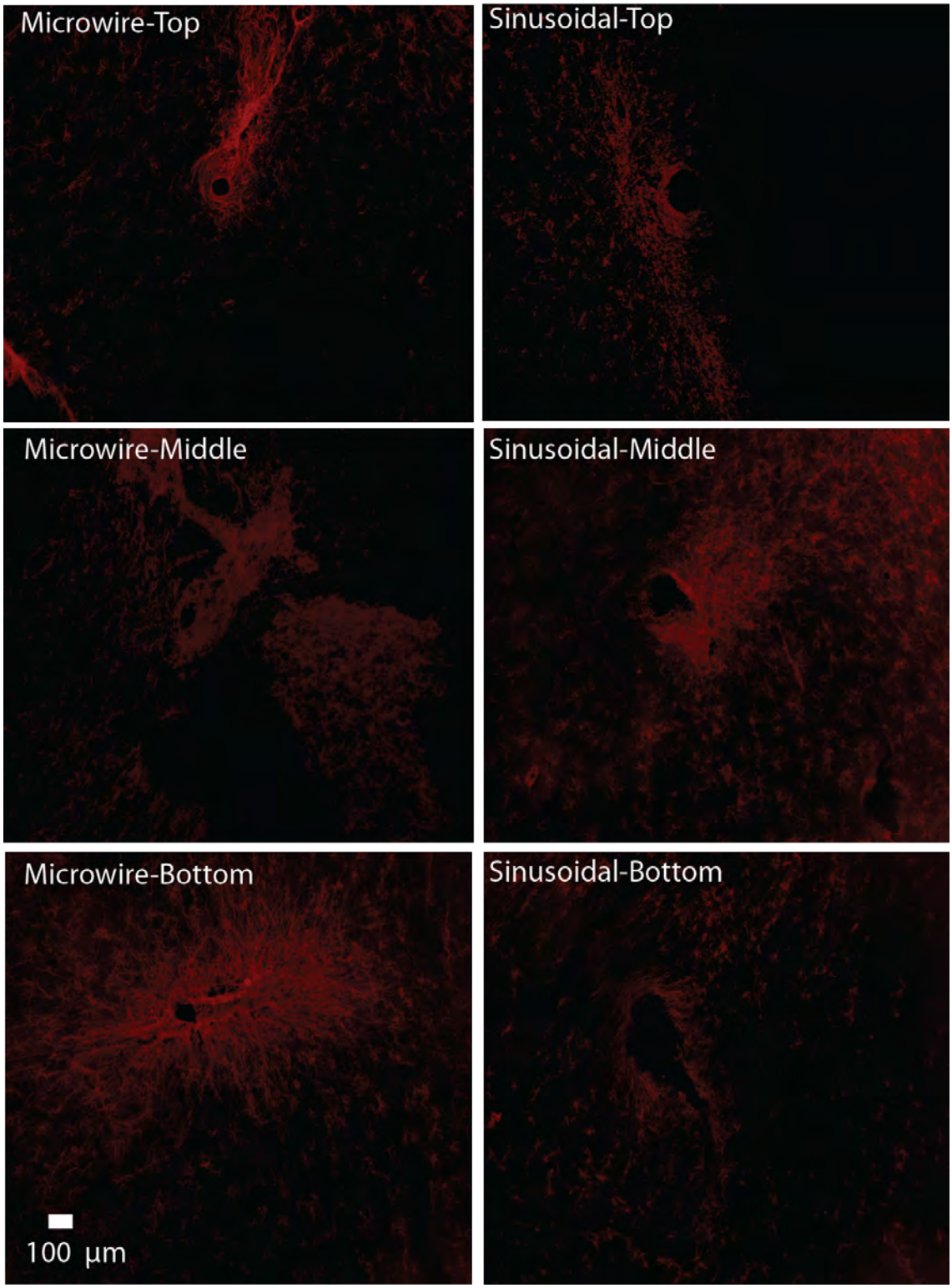

Figure 5.5. Representative images for the astrocytic reaction for both microwire and sinusoidal probe at 6 months for Rabbit-R. Reduction in astrocytosis is apparent for the bottom profile for the sinusoidal probe.

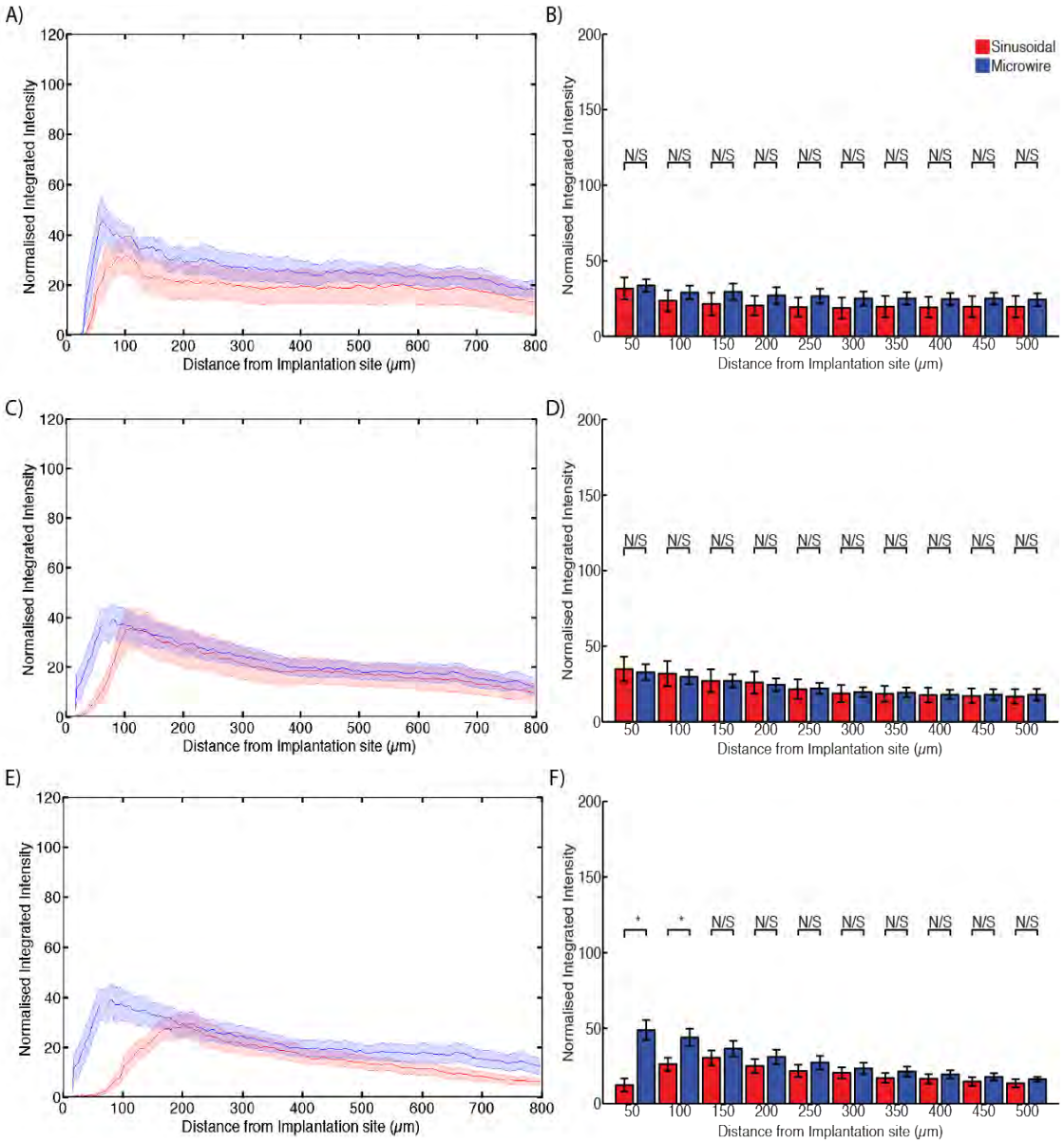

Figure 5.6. Overall astrocytic response to both electrode types (n= 4 microwire and 8 sinusoidal probes) in Rabbit-R for the 6 month timepoint. All sections used were normalised according to endogenous background staining by subtracting mean grey scale intensity values obtained from background images taken at least 1 mm away from the site of gliosis. * = p<0.05; N/S = not significant. Overall normalised integrated intensity response (±SEM) are shown for the top, (A,B) middle (C,D) and bottom (tip) (E,F) profile representation for both electrode types for the astrocytic reaction. For the top and middle profile representation, no significant differences were found at any distance away from the electrode implantation site. For the bottom profile representation, significant differences were found at 50 (t(15)=5.01,P<0.05) and 100 (t(15)=2.40, P<0.05) µm away from the electrode implantation site representation. Reduced astrocytosis was evident for the bottom depth profile representation in the close vicinity for sinusoidal probe.

5.3.3 Combined effect from Rabbit-J and Rabbit-R

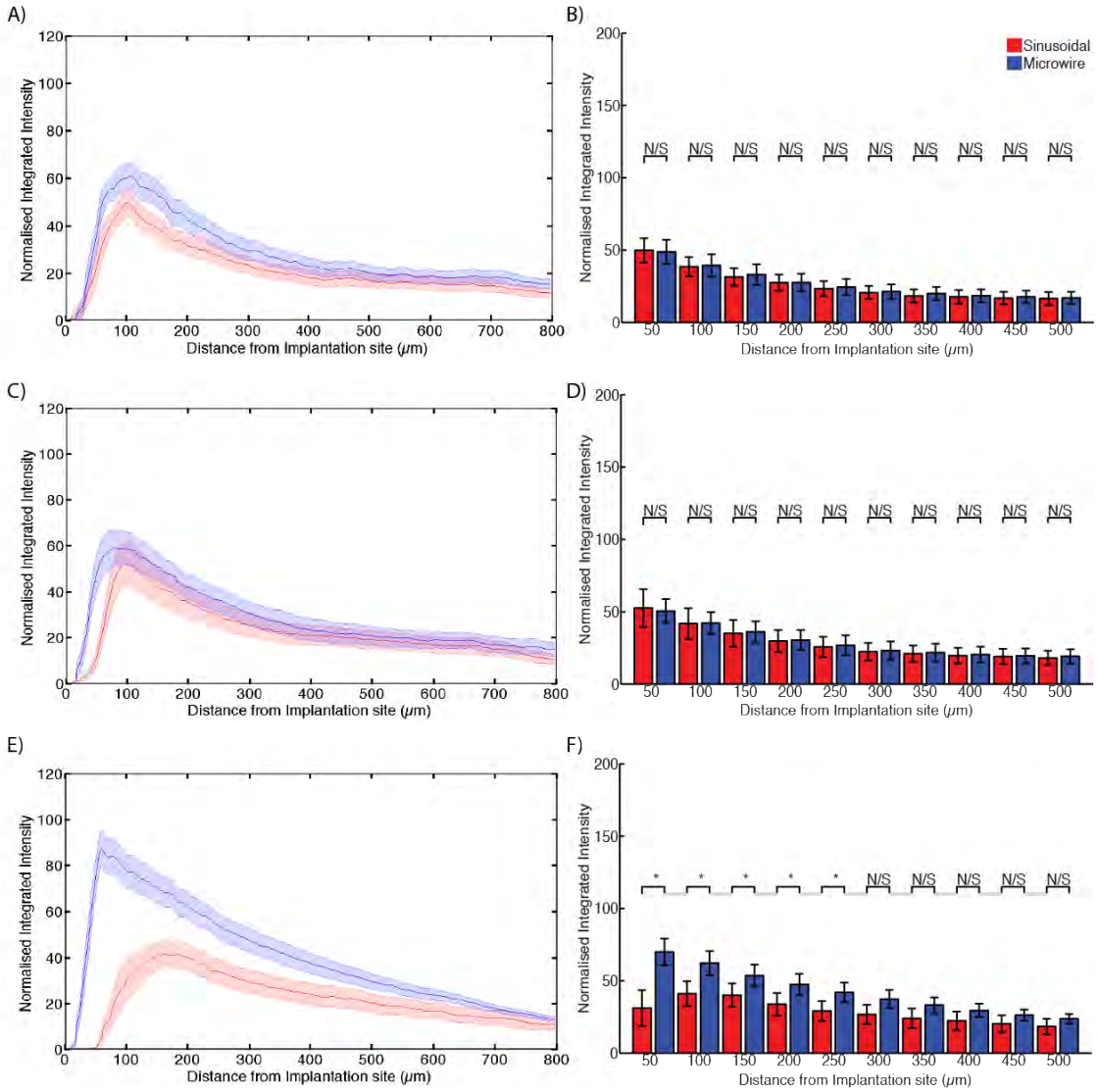

Figure 5.7. Overall astrocytic response to both electrode types from the combined data set in Rabbit-J and Rabbit- R. All sections used were normalised according to endogenous background staining by subtracting mean grey scale intensity values obtained from background images taken at least 1 mm away from the site of gliosis. * = p<0.05; N/S = not significant. Overall normalised integrated intensity response (±SEM) are shown for the top (A,B), middle (C,D) and bottom (tip) (E,F) profile representation for both electrode types for the astrocytic reaction. For the top and middle profile representation, no significant differences were found at any distance away from the electrode implantation site. For the bottom profile representation, significant differences were found at 50 (t(30)=4.47,P<0.05) ,100 (t(30)=3.19,P<0.05), 150 (t(30)=2.15,P<0.05) ,200 (t(30)=2.11,P<0.05), and 250 (t(30)=2.33,P<0.05) µm away from the electrode implantation site. Reduced astrocytosis was evident for the bottom depth profile representation in the close vicinity for sinusoidal probe.

5.4 Twelve month time point- First generation

The gliosis response for the 12 month time point was analysed in rabbit-L. Overall there was decreased microgliosis at the bottom representation for the sinusoidal probe (Figure 5.8-5.9). This was accompanied by an increase in neurofilament staining, which is linked to good neuronal process integration (Figure 5.12-5.13). There was a reduction in astrocytosis at the top and middle profiles, but a similar response was found for the bottom tip representation for both electrode types (Figure 5.10-5.11).

5.4.1 Microglial Response-12 months

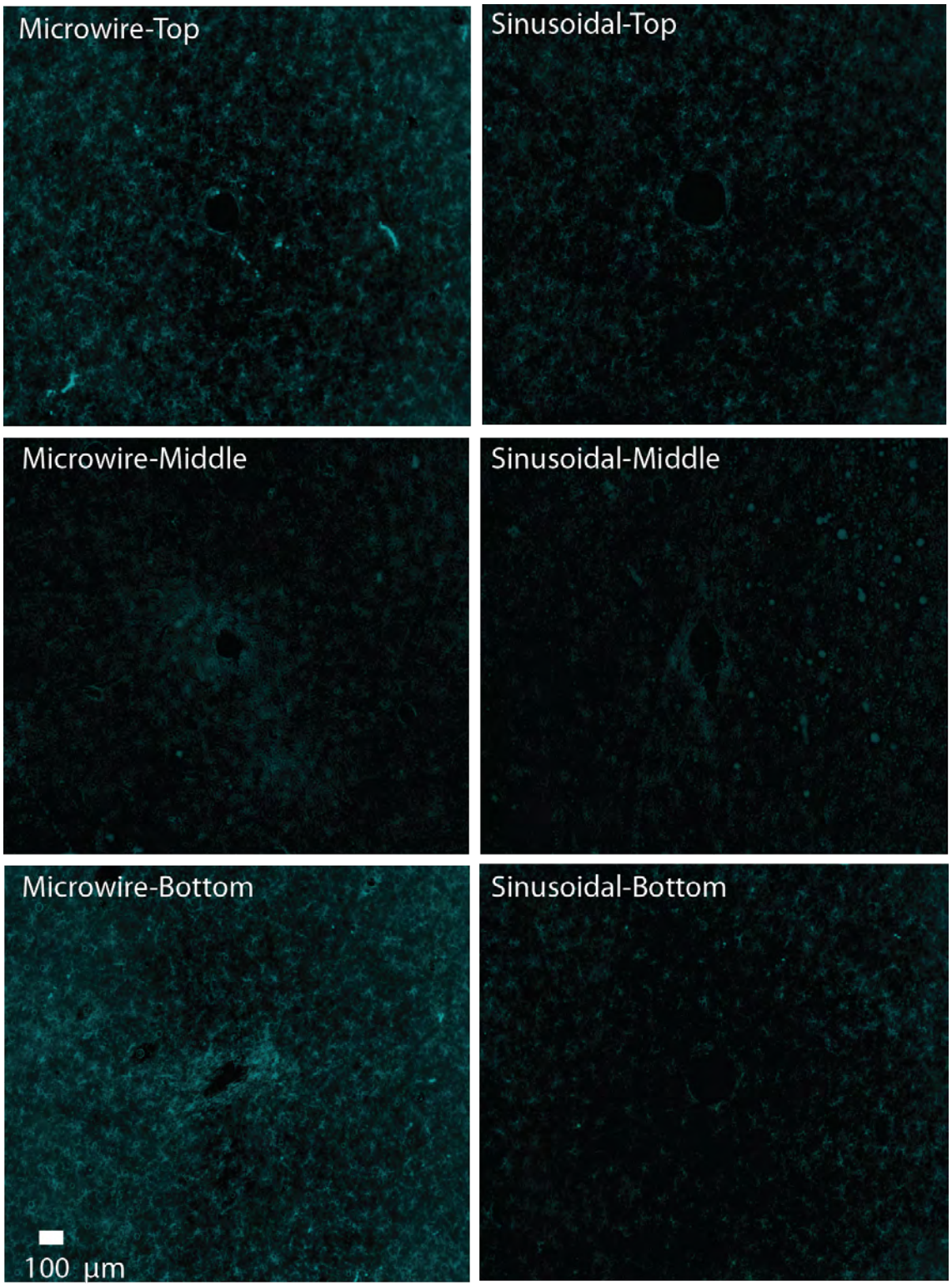

Figure 5.8. Representative images for the microglial reaction for both microwire and sinusoidal probe at 12 months. There was a reduced overall microglial response for all depth profile representation for the sinusoidal probe.

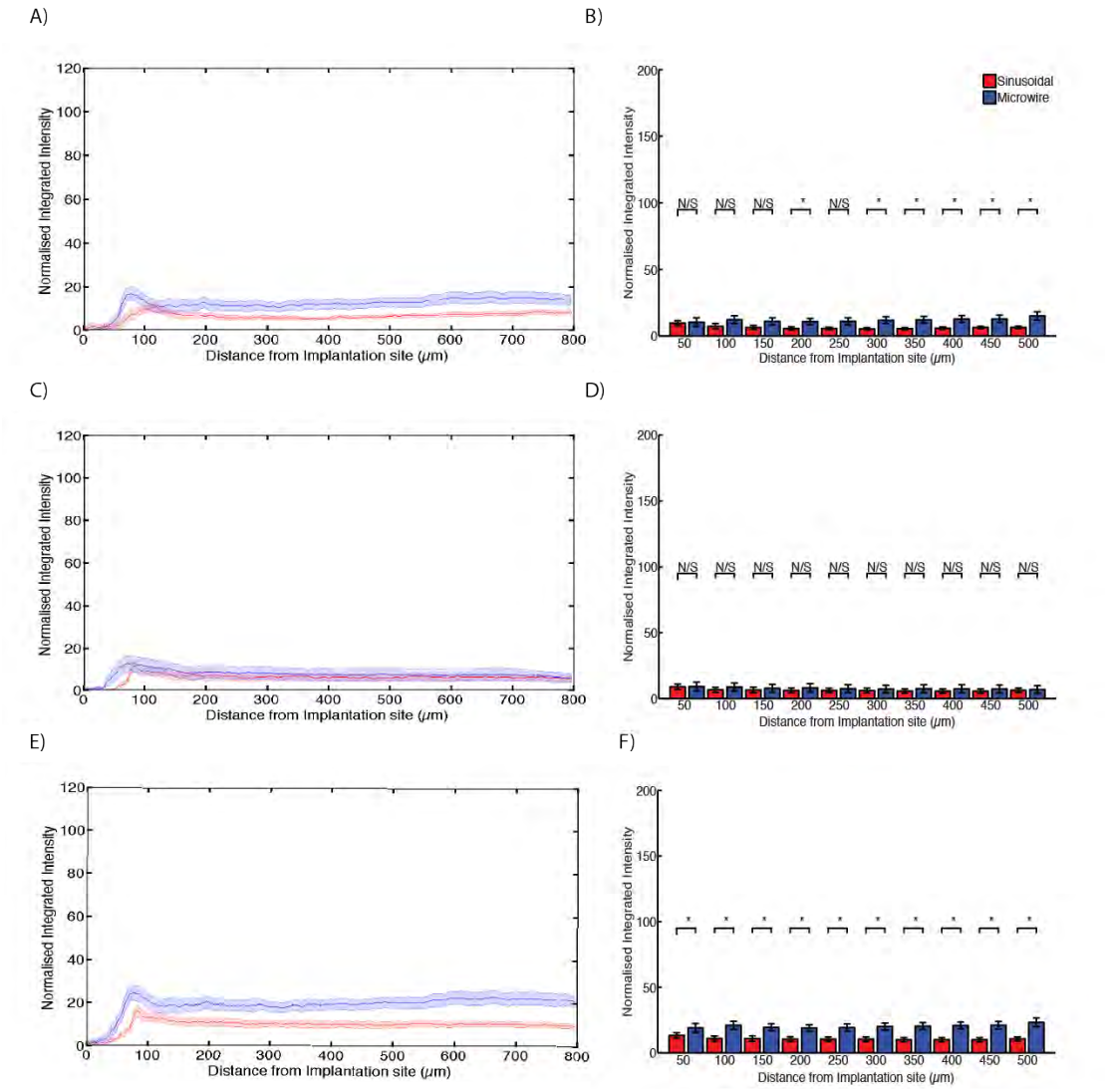

Figure 5.9. Overall microglial response to both electrode types (n= 4 microwire and 4 sinusoidal probes) in Rabbit-L at a 12 month time point. All sections used were normalised according to endogenous background staining by subtracting mean grey scale intensity values obtained from background images taken at least 1 mm away from the site of gliosis. * = p<0.05; N/S = not significant. Overall normalised integrated intensity response (±SEM) are shown for the top (A,B), middle (C,D) and bottom (tip) (E,F) profile representation for both electrode types for the microgliosis reaction. For the top profile representation, significant differences were found at 200 (t(15)=2.18,P<0.05) ,300 (t(15)=2.54,P<0.05), 350 (t(15)=2.74,P<0.05), 400 (t(15)=2.74,P<0.05), 450 (t(15)=2.37,P<0.05), and 500 (t(15)=2.87,P<0.05), away from the electrode implantation site.. For the middle profile representation, no significant differences were found at any distance away from the electrode implantation site. For the bottom profile representation, significant differences were found at 50 (t(15)=2.38,P<0.05) ,100 (t(15)=4.88,P<0.05), 150 (t(15)=5.65,P<0.05) , 200 (t(15)=5.92,P<0.05), 250 (t(15)=4.36 ,P<0.05), 300 (t(15)=4.83, P<0.05), 350 (t(15)=5.67,P<0.05), 400 (t(15)=5.47,P<0.05), 450 (t(15)=5.35,P<0.05) and 500 (t(15)=4.74,P<0.05) µm away from the electrode implantation site representation. Reduced microgliosis was evident for the bottom depth profile representation.

5.4.2 Astrocytic Response- 12 months

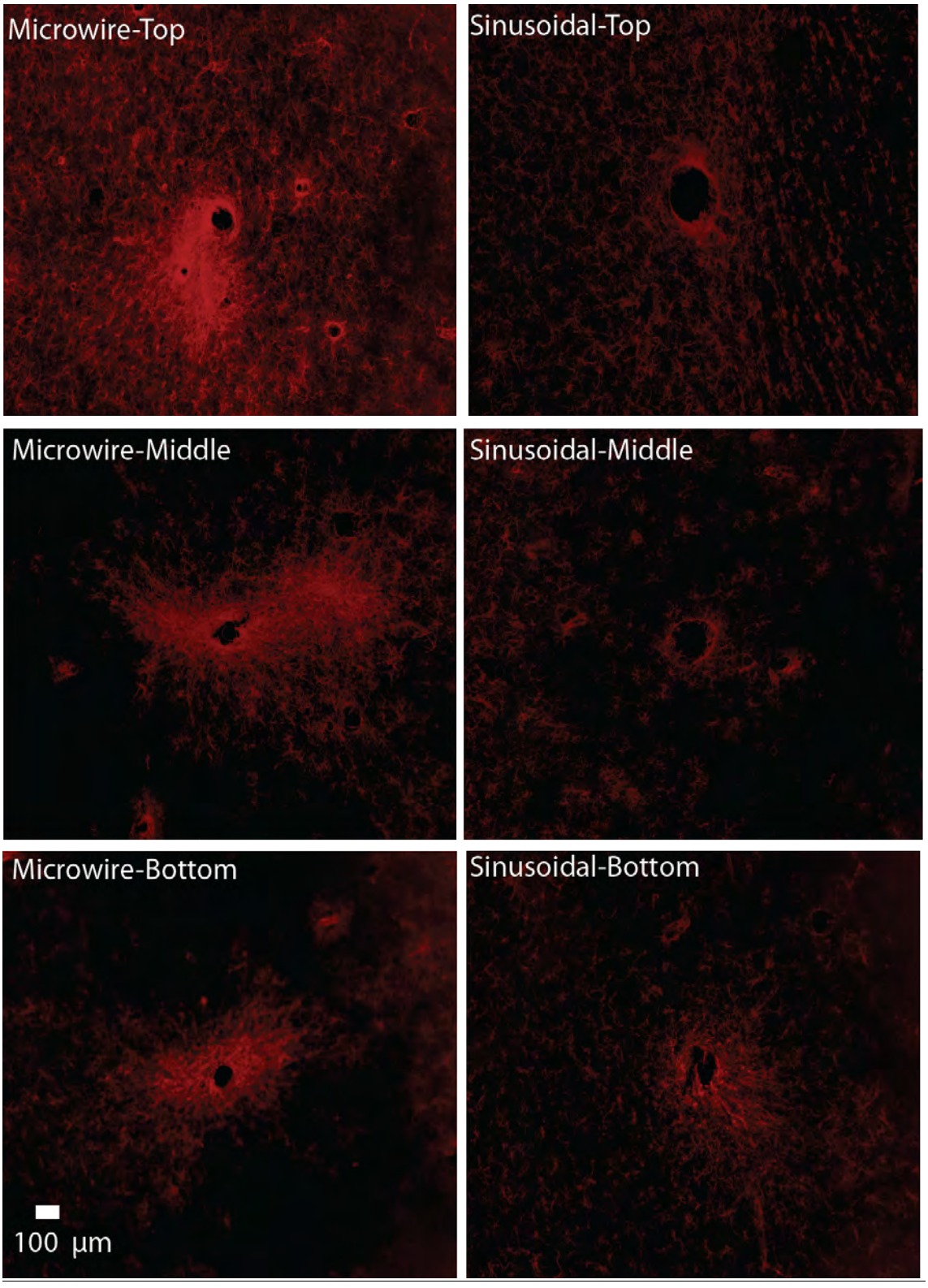

Figure 5.10. Representative images for the astrocytic reaction for both microwire and sinusoidal probe at 12 months.

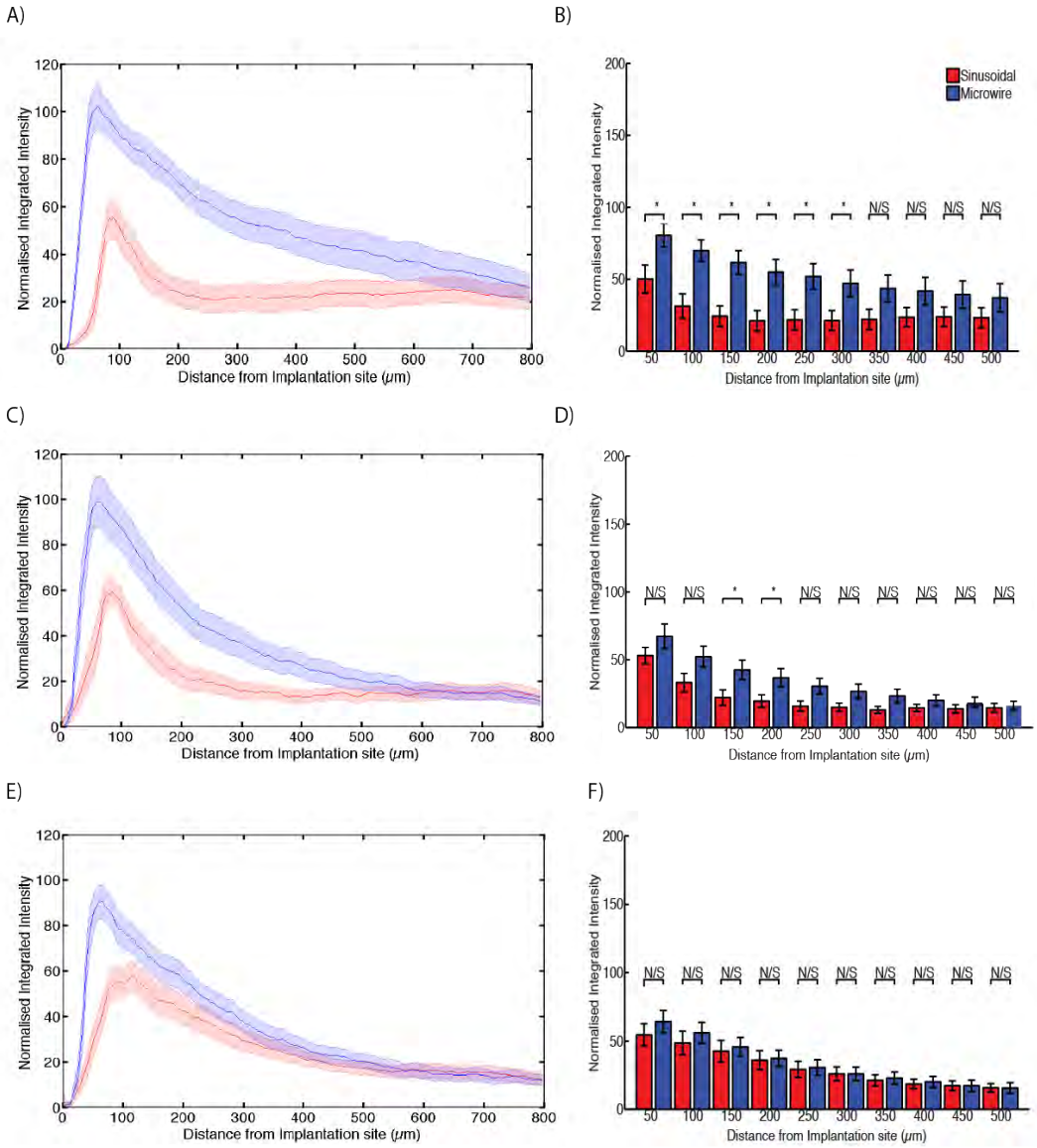

Figure 5.11. Overall astrocytic response to both electrode types (n= 4 microwire and 4 sinusoidal probes) in Rabbit-L at a 12 month time point. All sections used were normalised according to endogenous background staining by subtracting mean grey scale intensity values obtained from background images taken at least 1 mm away from the site of gliosis. * = p<0.05; N/S = not significant. Overall normalised integrated intensity response (±SEM) are shown for the top (A,B), middle (C,D) and bottom (tip) (E,F) profile representation for both electrode types for the astrocytic reaction. For the top profile representation, significant differences were found at 50 (t(15)=2.96,P<0.05) ,100 (t(15)=4.43,P<0.05), 150 (t(15)=4.25,P<0.05), 200 (t(15)=3.57,P<0.05), 250 (t(15)=3.08,P<0.05), 300 (t(15)=2.54,P<0.05) and 350 (t(15)=2.02,P<0.05) µm away from the electrode implantation site. For the middle profile representation, significant differences were found at 150 (t(15)=2.25,P<0.05) and 200 (t(15)=2.18,P<0.05) µm away from the electrode implantation site. representation. Similar responses were found for the top and middle representation. No significant differences were found for the bottom representation between the two electrode types.

5.4.3 Neurofilament-12 months

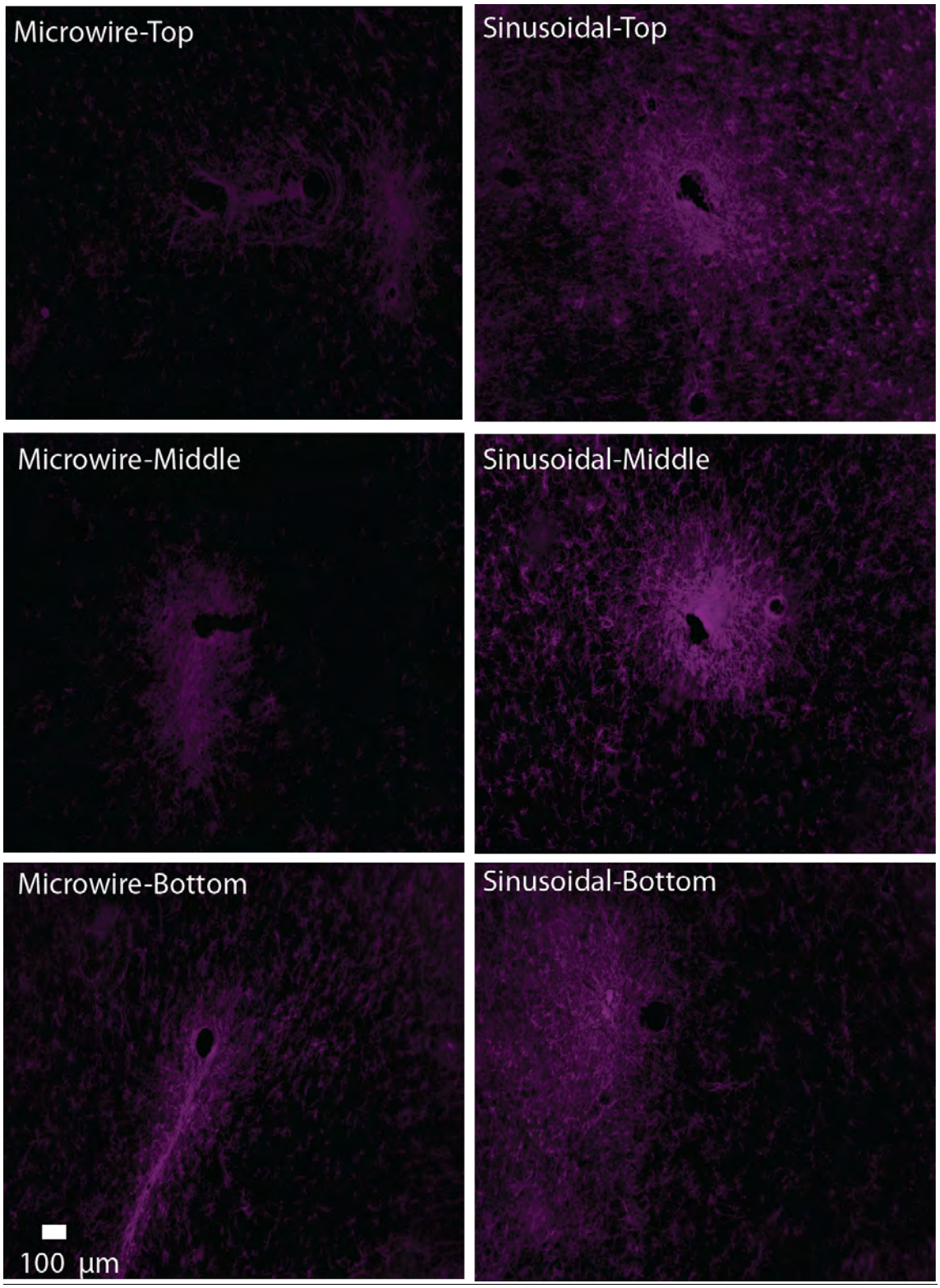

Figure 5.12. Representative images for neurofilament response for both microwire and sinusoidal probe at 12 months. There was an increase in neurofilament staining, especially for the bottom representation for the sinusoidal probe.

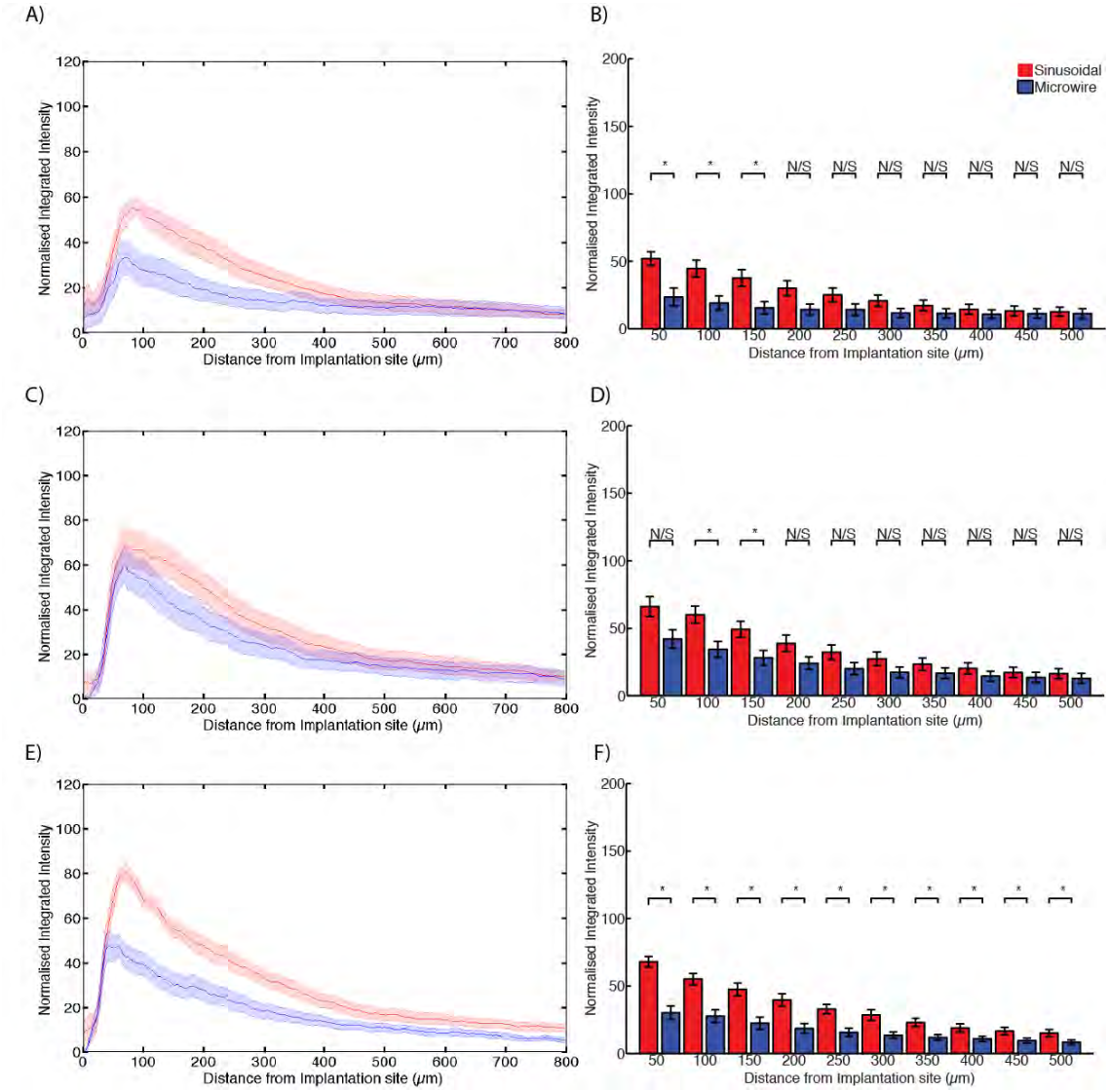

Figure 5.13. Overall neurofilament response to both electrode types (n= 4 microwire and 4 sinusoidal probes) in Rabbit-L at a 12 month time point. All sections used were normalised according to endogenous background staining by subtracting mean grey scale intensity values obtained from background images taken at least 1 mm away from the site of gliosis. * = p<0.05; N/S = not significant. Overall normalised integrated intensity (±SEM) response are shown for the top (A,B), middle (C,D) and bottom (tip) (E,F) profile representation for both electrode types for the microglial reaction. The sinusoidal probe has lower intensity values descending down the electrode indicative of a reduced immune response. For the top profile representation, significant differences were found at 50 (t(15)=3.05,P<0.05) , 100 (t(15)=2.81,P<0.05) and 150 (t(15)=2.66,P<0.05) µm away from the electrode implantation site. For the middle profile representation, significant differences were found at 100 (t(15)=2.32,P<0.05) and 150 (t(15)=2.28,P<0.05) µm away from the electrode implantation site. For the bottom profile representation, significant differences were found at 50 (t(15)=5.92 ,P<0.05) ,100 (t(15)=4.16,P<0.05), 150 (t(15)=3.55,P<0.05), 200 (t(15)=3.72,P<0.05), 250 (t(15)=3.66,P<0.05), 300 (t(15)=3.28,P<0.05), 350 (t(15)=3.03,P<0.05), 400 (t(15)=2.27,P<0.05), 450 (t(15)=2.16,P<0.05) and 500 (t(15)=2.15,P<0.05) µm away from the electrode implantation site. There was a significant increase in neurofilament staining at the bottom profile representation, showing better neuronal integration for the sinusoidal probe.

5.5. Twenty-four month time point-first generation

Overall there was decreased microgliosis at both the top and bottom electrode profiles for the sinusoidal probe. (Figure 5.14-5.15). A decrease in astrocytosis was found at the bottom representation (Figure 5.16-5.17). Interestingly, this decreased gliosis could be linked to the stable spiking recordings obtained for Rabbit-N, where activity was recorded for 678 days with a more stable SNR over the recording period (Section 4.4.3).

5.5.1 Microglial Response-24 months

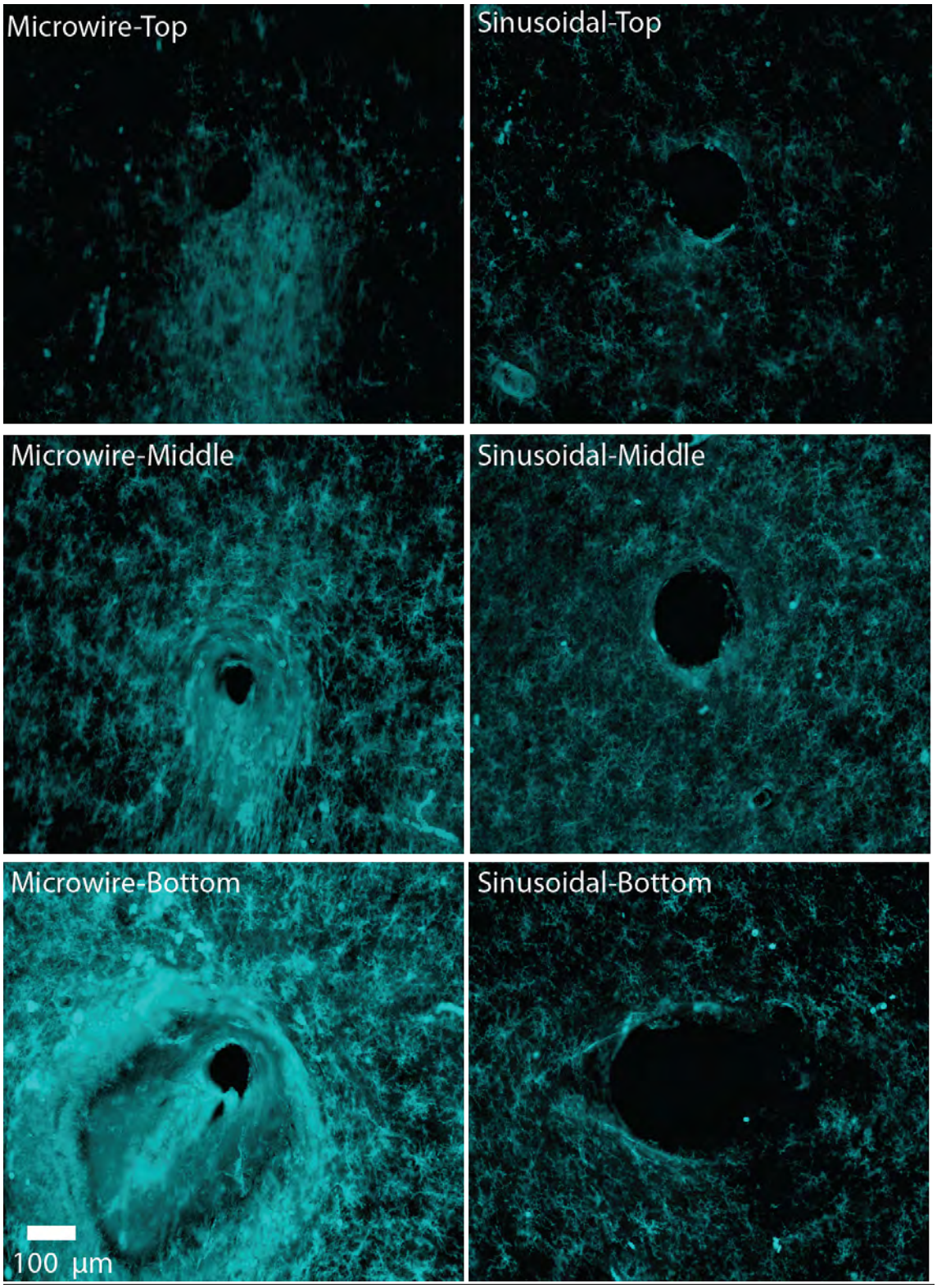

Figure 5.14. Representative images for the microglial reaction for both microwire and sinusoidal probe at 24 months. There was a decrease microglial response over all depth profile respresentations for the sinusoidal probe compared to the microwire.

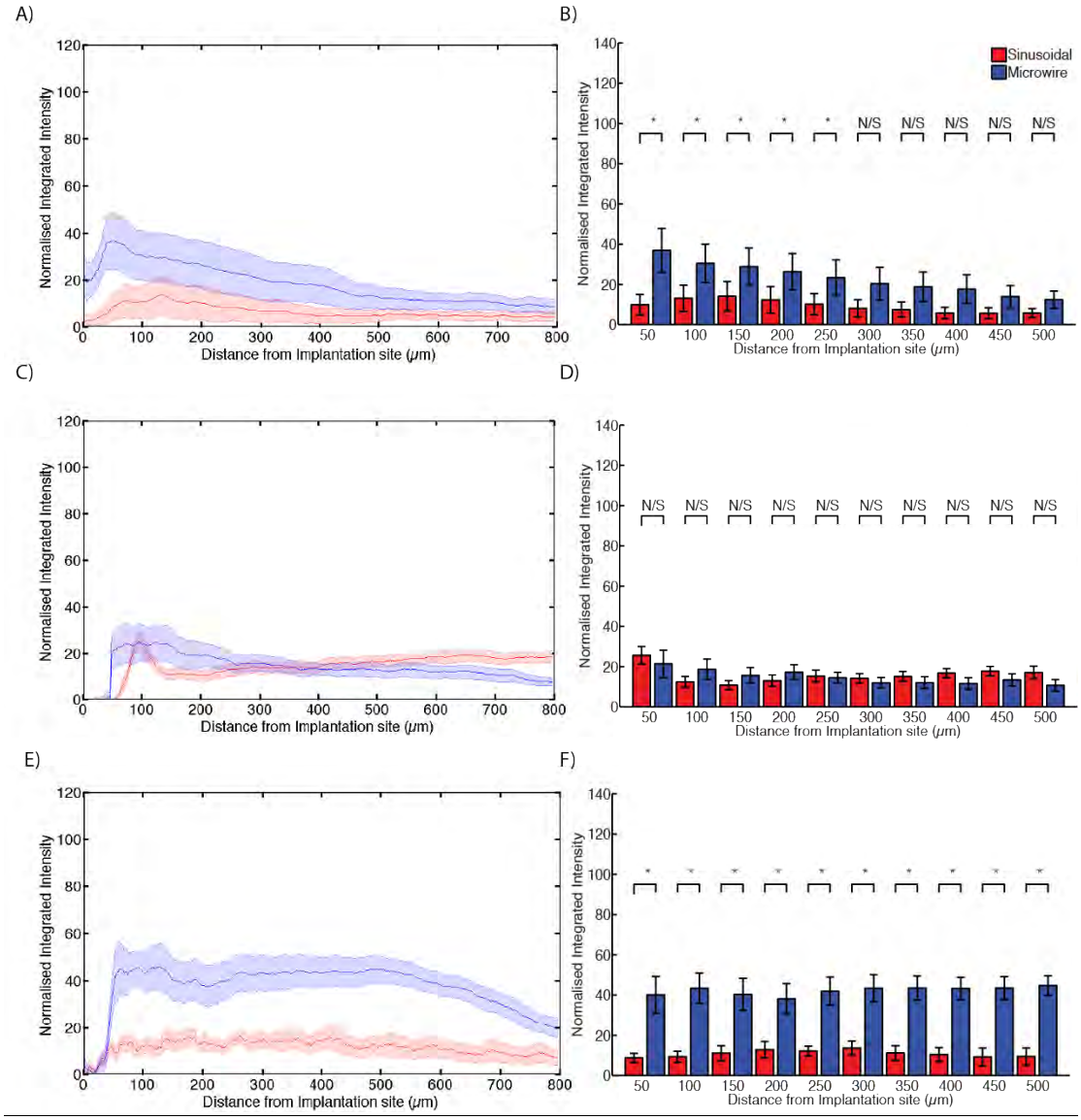

Figure 5.15. Overall microglial response to both electrode types (n= 4 microwire and 4 sinusoidal probes) in Rabbit-N at a 24 month time point. All sections used were normalised according to endogenous background staining by subtracting mean grey scale intensity values obtained from background images taken at least 1 mm away from the site of gliosis. * = p<0.05; N/S = not significant. Overall normalised integrated intensity (±SEM) response are shown for the top (A,B), middle (C,D) and bottom (tip) (E,F) profile representation for both electrode types for the microglial reaction. The sinusoidal probe has lower intensity values descending down the electrode indicative of a reduced immune response. For the top profile representation, significant differences were found at 50 (t(15)=2.62,P<0.05) , 100 (t(15)=2.62,P<0.05), 150 (t(15)=2.62,P<0.05), 200 (t(15)=2.62,P<0.05), 250 (t(15)=2.62,P<0.05) µm away from the electrode implantation site. For the middle profile representation, no significant differences were found. For the bottom profile representation, significant differences were found at 50 (t(15)=2.98,P<0.05) ,100 (t(15)=3.37,P<0.05), 150 (t(15)=2.51,P<0.05), 200 (t(15)=2.36,P<0.05), 250 (t(15)=3.11,P<0.05), 300 (t(15)=3.03,P<0.05), 350 (t(15)=3.42,P<0.05), 400 (t(15)=3.79,P<0.05), 450 (t(15)=3.78,P<0.05) and 500 (t(15)=4.16,P<0.05) µm away from the electrode implantation site. There was a significant reduction in the microglial response especially at the bottom profile representation.

5.5.2 Astrocytic Response-24 months

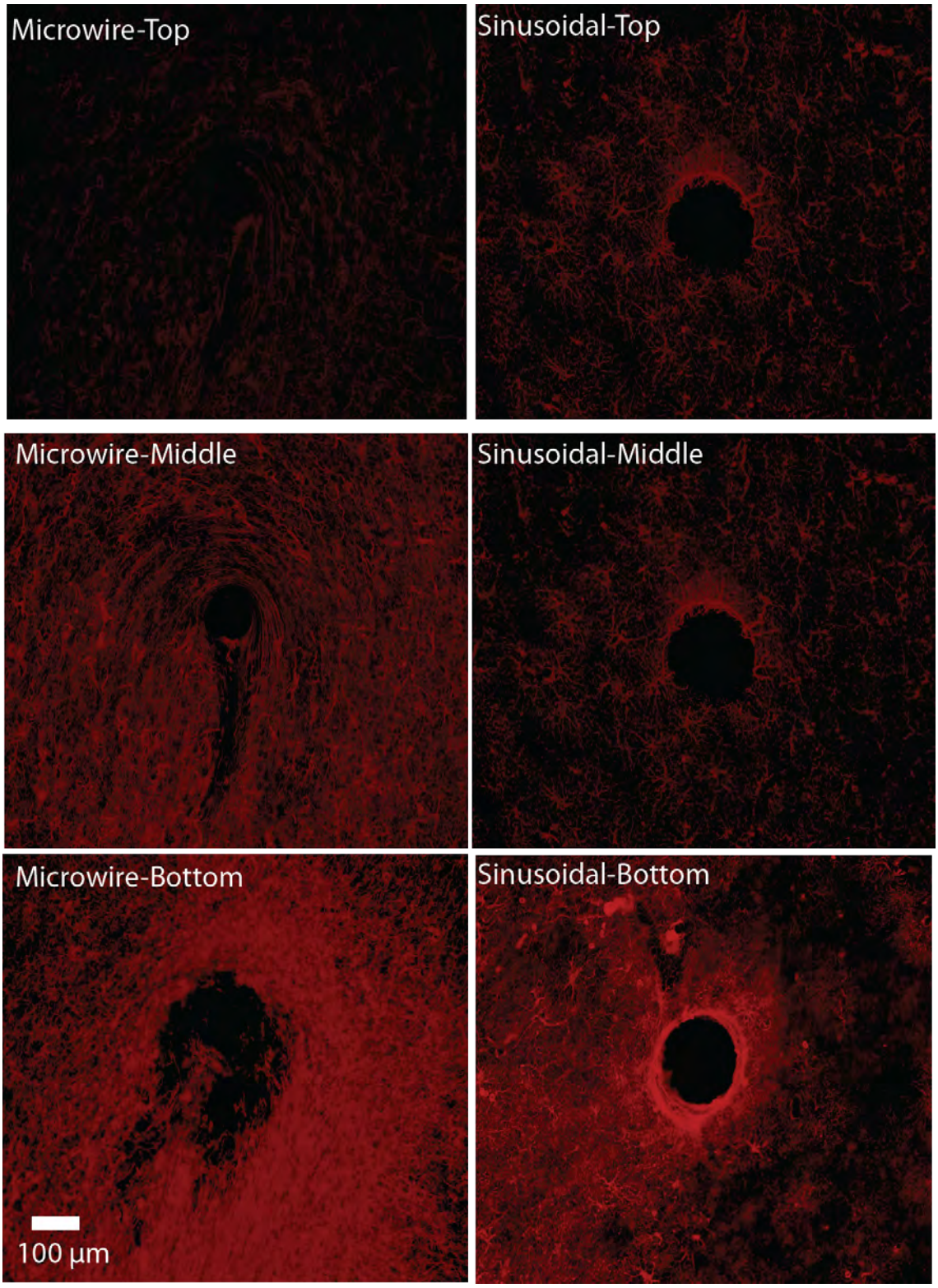

Figure 5.16. Representative images for the astrocytic reaction for both microwire and sinusoidal probe at 24 months. A reduced astrocytic response was observed around the sinusoidal probe especially at the bottom representation.

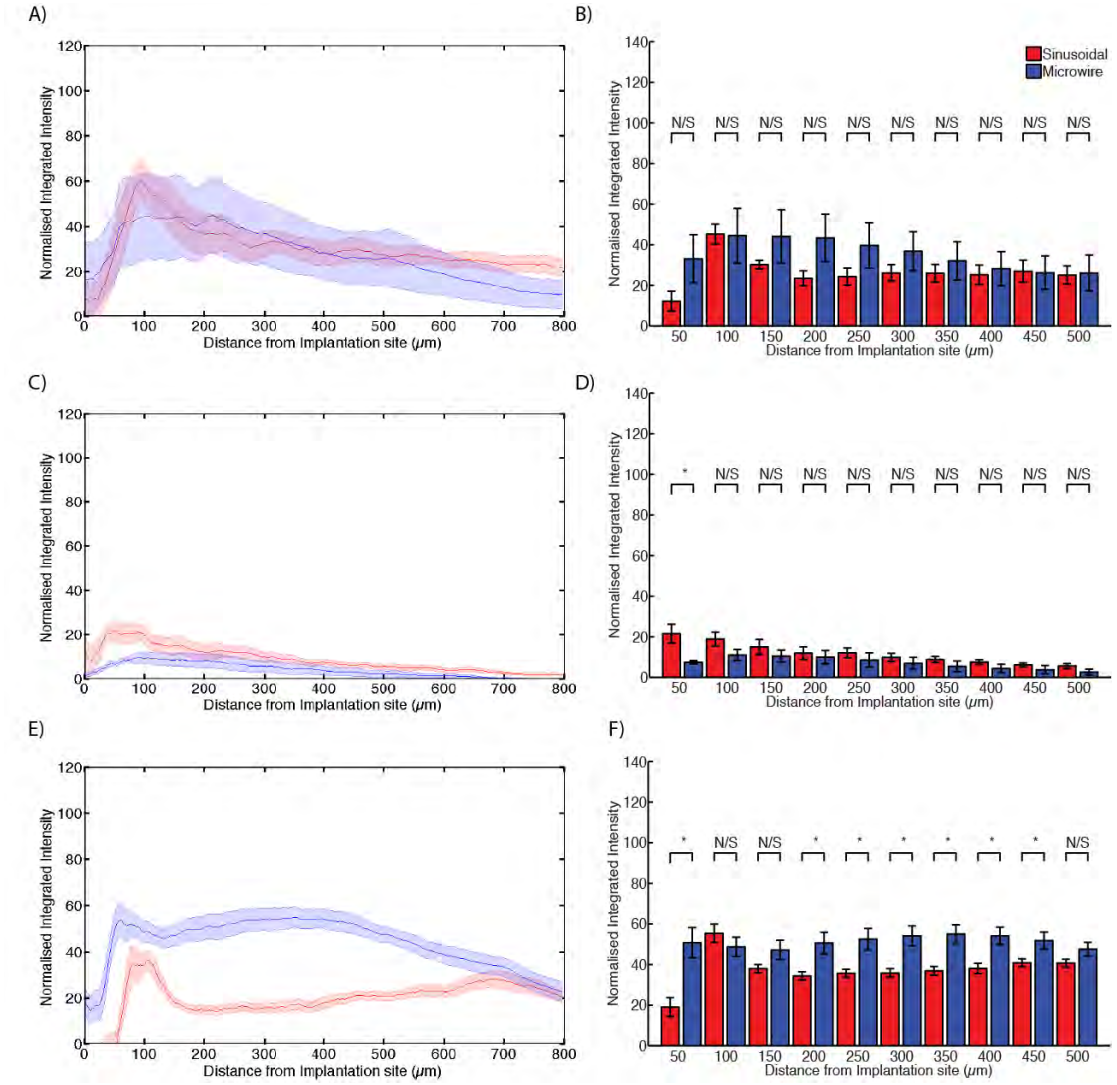

Figure 5.17. Overall astrocytic response to both electrode types (n= 4 microwire and 4 sinusoidal probes) in Rabbit-N at a 24 month time point. All sections used were normalised according to endogenous background staining by subtracting mean grey scale intensity values obtained from background images taken at least 1 mm away from the site of gliosis. * = p<0.05; N/S = not significant. Overall normalised integrated intensity response (±SEM) are shown for the top (A,B), middle (C,D) and bottom (tip) (E,F) profile representation for both electrode types for the astrocytic reaction. For the top profile representation, no significant differences were found over all the distances away from the implantation site. For the middle profile representation, significant differences was found only at 50 (t(15)=2.01,P<0.05) µm away from the electrode implantation site. For the bottom profile representation, significant differences were found at 50 (t(15)=2.85,P<0.05) ,150 (t(15)=1.68,P<0.05), 200 (t(15)=3.04,P<0.05), 250 (t(15)=3.40,P<0.05), 300 (t(15)=4.55,P<0.05), 350 (t(15)=4.35,P<0.05), 400 (t(15)=4.66,P<0.05) and 450 (t(15)=3.23,P<0.05) µm away from the electrode implantation site. Similar responses were found for the top and middle representation. There was a significant reduction in the astrocytic response between 200-450 µm for the sinusoidal probe, this is where the classical astrocytic response is found.

5.5 Conclusions

Table 5.2 shows a summary of the results for the Sinusoidal probe compared to the microwire electrode over all the time points in terms of gliosis. Overall it appeared that the sinusoidal probe had similar responses to the microwire electrode for the top and middle profile. However reduced gliosis is apparent for the bottom representation across all the timepoints.

Timepoint	Top profile	Middle profile	Bottom profile
6 month Astrocytes	Similar	Similar	Reduced
12 months Astrocytes	Reduced	Reduced	Similar
12 months microglia	Similar	Similar	Reduced
12 months Neurofilament	Increased	Increased	Increased
24 months Astrocytes	Similar	Similar	Reduced
24 months Microglia	Reduced	Similar	Reduced

Table 5.2. Summary of the results for the sinusoidal probe compared to the microwire electrode across all time points.

5.6 Discussion

In this study, the sinusoidal probe was compared to the microwire electrode. Although the probe was not compared to standard silicon probes, an emergent hierarchy is evident from the literature. In general silicon probes give a heightened immune response in relation to microwire style probes (Winslow and Tresco, 2010, Kozai et al., 2012a). As we show decreased overall gliosis at multiple timepoints, it is reasonable to assume that we should also have a decreased response when comparing to standard silicon probes.

The sinusoidal probe had decreased overall gliosis in terms of astrocytosis for the 6 month time point and both astrocytosis and microgliosis for the 12 and 24 month time point. Interestingly, there was an increase in neurofilament staining around the sinusoidal probe at the 12 month timepoint. Therefore it appears that electrode designs that incorporate micromotion reducing measures can reduce overall gliosis.

Intriguingly individual microwire recording sites can interact with one another (Figure 5.3), in terms of glial scarring. This is not ideal, as interaction between two electrode sites may induce biological noise and alter overall network effects for the specific recording cells of interest.

Seemingly at more chronic time points, the degree of microgliosis and astrocytosis seems to extend beyond a 500 μm distance (Polikov et al., 2005, Winslow et al., 2010a). Therefore it appears that on-going gliosis will endure to spread to regions far beyond the original implantation site.

Isolectin-b4 staining for microglia appeared to be unreliable especially when comparing the two electrode types at the six month time point. Even though all protocols were kept consistent between all the time points, failed staining still arose. From literature many groups consistently use ED-1 as a marker for microglia and blood-born macrophages infiltrating from the damaged blood-brain barrier resulting from electrode insertion (Winslow et al., 2010a, Potter et al., 2012). Therefore a change to using this marker should be considered for both reliability and comparative purposes in future histology.

Two additional markers should be considered for future histology: NeuN and a marker for peri-neuronal nets (PNN). NeuN staining has been used to quantify viable neurons around an electrode implant after chronic implantation and it will be useful to show this for the sinusoidal probe, combined with neuronal integration through neurofilament staining (Biran et al., 2007). PNN have been shown to aggregate at the site of a glial

scar and also inhibit axon regeneration and growth through the release of chondroitin sulphate proteoglycan (CSG) (Rhodes and Fawcett, 2004). Combined with neurofilament staining, this will promote our understanding for the reasoning behind an increase in neurofilament staining around our sinusoidal probe. A decrease in PNN formation and an increase in neurofilament staining may indicate that the sinusoidal probe does not inhibit axonal regeneration and promotes plasticity over chronic time points.

Occasionally it was difficult to track electrode tracts as the horizontal sections contained blood vessels. Through histology experience, hydrogen peroxide can be used to remove vasculature from slices, however the overall integrity of the tissue is often affected resulting in degradation and difficulties in slicing handling. Pre-coating the electrode with a dye might be a potential solution to track electrode tracts, although the glial response to this approach will need to be examined. Interactions with potential dyes and PEG would also need to be elucidated.

Although relative animals numbers at each time point is low, this is an inherent issue with chronic studies. Further testing is needed to corroborate the results from this study although this is always a challenge in a defined thesis period, especially for the more extreme chronic time-points. This study covered the chronic indwelling time period from 6-24 months. Early time periods, such as 1 or 2 weeks post implantation should be investigated to evaluate the role of the insertion method on gliosis and overall acute stage, gliosis around both electrode types.

Chapter 6: General Discussion

6.1 Summary of results and achievements

Electrodes with an integrated ribbon cable were successfully fabricated and tested. High functional yields were obtained through optimised release techniques. Electrodes were successfully inserted into the rabbit brain with the use of sharp steel electrodes placed in 25g needles and PEG. Chronic testing revealed that the sinusoidal probe was more stable in recording parameters than the microwire electrode in terms of LFP power and SNR. Histology analysis revealed that there was a decrease in overall gliosis especially at the bottom representation for our electrode over the extreme chronic indwelling time-points. Therefore the stability in the recordings appeared to have been linked to the decrease in the glial response to the sinusoidal probe. However for our electrode the number of animals used is only 1 for both LFP and spiking activity. Therefore, further chronic testing is needed to further quantify chronic recordings and histology for the second electrode generation due to the unreliability of the animal model.

In a very demanding thesis period, I have chronically tested the first generation sinusoidal probes in terms of chronic recording and ad-hoc histology. Further, I have optimised the sinusoidal probe design leading to effective microfabrication of the second generation. This was performed with no prior knowledge of microfabrication or engineering techniques. Further, efficient microfabrication meant that we were able to test the electrodes *in-vivo* and obtain histology from our new electrode generation for a 6-month time period. Although we have low n numbers in this study for testing our electrodes, we currently have very high functional yields ensuring ample electrode yields are available for further testing that was not possible during this thesis period.

6.2 Sacrificial layer

Aluminium was chosen over silicon dioxide to enhance device release through decreased etch time taken. Although the ethanol release method was used due to weak adhesion for the first electrode batch, this could not be used for the second electrode batch due to enhanced adhesion. This enhanced adhesion is most likely caused by the change in interface between the first parylene-C layer and aluminium. Aluminium roughness is unlikely to have been a contributing factor in this increased adhesion due

to constant deposition parameters between the batches. The interface between parylene-C and aluminium is not as simple as two components. Aluminium has a tendency to develop a thin native oxide over time and this can interact with the silane based adhesion promoter used for parylene-C. Literature suggests that a greater oxide formation combined with silane will lead to enhanced adhesion between parylene-C and aluminium (Mitchell et al., 2006) . The delay in processing between the aluminium and first parylene-C layer deposition stages may have caused aluminium oxide growth, leading to increased adhesion for our second batch. Similarly, the silane quantity used by the external company could have differed in the processing between first and second batches.

TMAH device release resulted in a higher functional yields being obtained than the ethanol release mechanism, so therefore an increased adhesion between aluminium and parylene-C is beneficial.

Although the ethanol release method did result in all devices being released, the maximum functional yield obtained was never over 50%. However, if this method does need to be used, a shallow petri-dish ethanol soaking method should be considered to release devices, rather than a wetting and peeling method.

Kozai & Kipke released their flexible based devices by etching an aluminium sacrificial layer with KOH (Kozai and Kipke, 2009). When this was tried for our devices, the effervescent nature of the reaction caused device delamination through decreased parylene-C to parylene-C adhesion.

TMAH as that found in dilute volumes in photoresist developer is a good etchant for aluminium. Device release was controlled resulting in high functional yields with TMAH use and the dilute concentration ensured that clean room users do not need to use a wet bench to release devices.

With the advent of both ethanol and TMAH device release, we have developed a method to release electrodes that is fail safe, regardless of the inclusion of relatively large features, such as the ribbon cable.

A surprising finding was etching of WTi with Al etch for the second batch device release. Extensive testing had previously shown that the electrodes should not be damaged by Al etch (Figure 2.5). A constituent of Al etch is phosphoric acid. This acid has been reported to have a 2.5 nm/min etch rate for TiW (10/90 wt%) (Williams et al.,

2003). Therefore it is possible that WTi was etched to a degree affecting overall WTi to parylene-C adhesion.

6.3 Problems with Polyimide

Polyimide was shown to be a poor dielectric layer due to non-uniform layer deposition and increased air bubble formation, which can lead to enhanced dielectric layer breakdown. Stieglitz and colleagues have shown this effect. However, recent flexible electrodes from this group still use polyimide as an insulating layer and maintain that polyimide is a good insulating layer, through biocompatibility and *in-vivo* testing, although this is confined to peripheral implants (Stieglitz et al., 2011). This might be due to the simplicity in deposition compared to other dielectrics such as parylene-C, rather than optimal dielectric selection for biomedical purposes.

The discrepancy between polyimide and parylene-C for non-uniformity and bubble formation may be related to the spin-deposition method used. Facilities only permit manual polyimide pastette dispensation before the spin process. This could lead to unequal polyimide layer growth and bubbling as has been shown.

However, even with an automatic dispenser, problems will still arise, as most polyimides have to be deposited and spun on, more than once to achieve the acquired film thickness, leading to unequal film growth.

6.4 Variations in electrode impedances

Wafer to wafer impedance varied for our electrodes. Metal oxidation, alignment error, the wire bonding method and polyimide ball delamination can account for this variation.

Tungsten based electrodes are susceptible to oxidation. As wafers were singularly processed due to equipment constraints, it is reasonable to assume that the tungsten based electrodes which were stored for second layer parylene-C deposition could have oxidised over time, changing their electrical properties. However, hydrofluoric acid used to remove the titanium mask layer after parylene-C layer etching can also etch any tungsten oxide formed. Interestingly, Patrick and colleagues suggest that at cell equilibrium potential compared to the standard hydrogen electrode (0.4v vs SHE) any

underlying tungsten oxide should dissolve to expose the tungsten surface during open circuit potential measured over a 15-day period calculated from obtained Pourbaix diagrams. Thus the formation of tungsten oxide should dissolve upon biological solution immersion or *in vivo* (Patrick et al., 2011). However, as tungsten was combined with titanium, the electrochemistry for the metal may differ from standard tungsten resulting in an increased likelihood of oxidation. Simple wetting with saline did not expose the underlying WTi surface as indicated by stable, non-falling impedances during saline testing.

Mask alignment error could contribute to varying electrode impedances. Although mask alignment was good throughout leading to functional electrodes, the natural alignment error in optical lithography for processing was 1-2 um. Therefore some electrodes could have more or less of the electrode recording sites exposed leading to higher or lower impedances. The surface area for the electrode site exposed is highly dependent on the alignment process. Our electrode recording sites can be consider to be a cuboid with 4 faces exposed to the elements; the other two faces blocked by the first parylene-c layer and electrode track formation. The top face protrusion from the parylene-C disc, is expected to be 3 μm from the design, which gives a 90 μm^2 in total recording site area. An alignment error of ±2 μm can result in 48 μm^2 and 138 μm^2 in total recording site area, respectively (Figure 6.1). However, as shown by a single dominant impedance range per electrode wafer released, it is acknowledged that vast fluctuations in alignment error is unlikely to be a major contributor to impedance fluctuations per wafer, due to optimised microfabrication techniques. However, impedance outliers for each electrode wafer released can be potentially explained by this phenomenon.

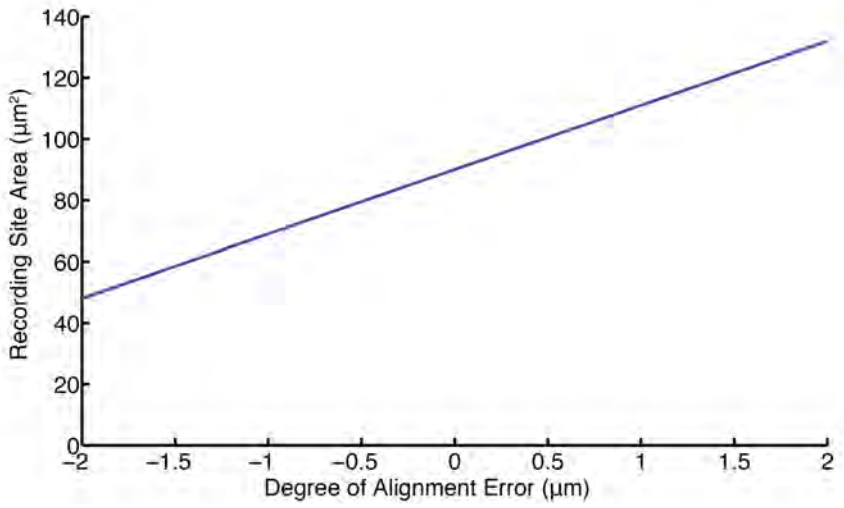

Figure 6.1. The effect of alignment error on total recording site area

Further compounding alignment error was the 10 μm parylene-C layer and 40 nm titanium layer that obstructed alignment mark visualisation through changing refractive indices.

Alignment error for future electrode designs can be minimised with a slight (2-3 μm) increase in electrode recording site protrusion from the rounded recording tip. Alignment error due to changes in refractive indices of the materials can be minimised with thinner dielectric. This will affect overall probe flexibility and potentially device lifetime. However, even with natural equipment alignment error, electrodes were still produced with acceptable impedances for single unit recordings.

If insufficient silver paint quantity was used to wire bond the connector, this resulted in varying impedances across the electrode. However, if the silver paint was removed and re-applied, this resulted in lower and consistent impedances. Insulating the silver paint with epoxy sometimes resulted in connector movement due to viscosity and stickiness, resulting in a compromised connector-electrode bonding. This could also create higher impedances. However, through every processed wafer such wire bonding issues were minimised.

The polyimide ball added could have contributed to varying impedances. Due to the low glass transition temperature for parylene-C, the polyimide anchor could not be fully cured. Electrode recording sites were re-exposed with TMAH etching of polyimide, and at this point had consistent impedance measurement as that pre-polyimide application.

Post-surgery, electrode impedances fall for some electrodes. This could be related to the complete PEG dissolution resulting in more electrode recording area exposed. However, some electrodes had further impedance falls one month post-implant. This could be related to the polyimide anchor. As the anchor is not fully cured, during insertion it is possible that the anchor could have shifted to further insulate the electrode recording sites. Post-surgery the slow polyimide ball degradation could cause electrode isolation from the surround tissue leading to higher recorded impedances. Complete polyimide ball degradation could be related to the fall in impedance. An alternative anchor material should be considered for future electrode iterations.

Desiccator use, either with a vacuum or inert gas, may limit resulting metal reaction with air, post-wiring (Hassler et al., 2011). However, a similar effect was achieved with PEG application to the tip post-polyimide ball application. Further, thorough device cleaning, after saline impedance testing, limited the significant rise in impedances.

Problems in electrode impedance rises with unwired electrodes left in petri-dishes over-time were not seen (data not shown). Therefore, impedance rises were only associated with wired electrodes, which hints at electrochemical changes.

6.5 Metal enhancement to resist reactivity

Although tungsten is a good recording metal, the susceptibility to become oxidised over time remains an issue, as shown with WTi. This will result in higher impedances and thus an increase in noise threshold for recordings. An alternative metal to use would be platinum due to chemical inertness. Patrick and colleages show through impedance spectroscopy and cyclic voltammetry that platinum electrodes are highly inert with unreactive species formed on electrode recording sites (Patrick et al., 2011). This is further corroborated by Cogan and colleagues (Cogan, 2008). Thereby, platinum is a good electrode material for *in-vivo* chronic applications.

Lift-off strategies for thick metal layers would need to be fully optimised as platinum at 1 μm thick, cannot be etched through conventional lithography. Ion-milling can be used to etch relatively thinner layers, 100 nm, through clean room observations. An alternative approach is capping the WTi metal with the deposition of another inert metal to preserve electrode impedances. A prime candidate would be platinum. Utah array fabrication uses a combination of platinum, iridium and titanium for their recording metal, thereby corroborating platinum-use in intracortical electrode design. Platinum addition might enhance electrode recordings through impedance stability due to metal inertness.

An additional masking step would be required to produce the capping for WTi. Figure 6.2 shows the proposed electrode fabrication step. A thin platinum layer, up to 100 nm should be deposited and patterned using ion milling. This step can be performed either after WTi deposition or after second layer parylene-C deposition, although the latter risks surface roughening the outer parylene-C layers if the etch time is not finely controlled.

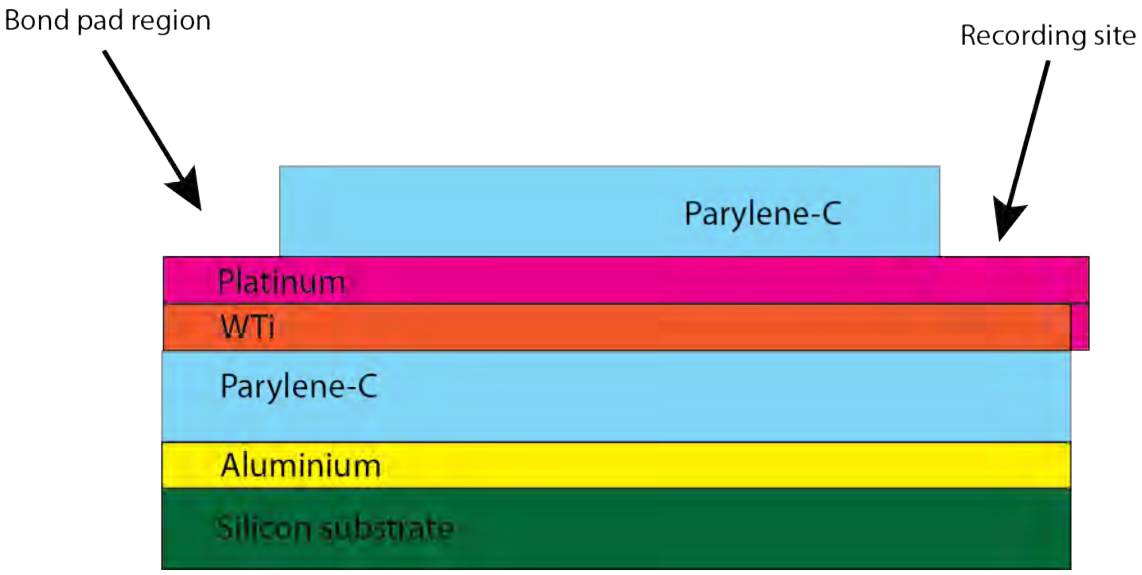

Figure 6.2. The use of platinum to improve the electrochemical stability of the electrode recording sites

Electro-deposition of appropriate materials (e.g. PEDOT) on metal recording sites could prevent impedance rises, electrode reactivity and lower overall impedances. However, deposition of such materials is always linked to adhesion problems, resulting in the gradual loss of the layer, within the first six months of chronic implantation (Kozai et al., 2010a).

6.6 Potential electrode redesign

While electrodes were successfully implanted into the brain with increasing success per surgery, shearing forces from ribbon cable movement was transmitted to the tapering interface between the probe and the ribbon cable, resulting in electrode breakages. Many electrode designs incorporating a ribbon cable are designed in this way, however the electrode shanks are normally thicker (200 μm) than our electrode (35 μm), which reduces the likelihood of breakages (although data directly relating to this from the studies are scarce). Two alternative designs are considered in potentially diffusing the degree of shearing forces experienced by the electrode upon insertion. The first design has curved tapering rather than the commonly used straight tapering (Figure 6.3B). This design would be better at potentially dispersing forces, such a design would still be ineffective at minimising forces due to horizontal plane movement during insertion. A more effective redesign of this particular electrode would be the inclusion of an "insertion shock region." Such a design feature will further restrict force transmission solely to the electrode (Figure 6.3C). From observations, the ribbon cable can absorb

multi dimensions of stress without a compromise in the electrode tracks. Inclusion of such a feature in the electrode design should restrict the force propagated directly to the electrode, with potential reduction in electrode breakages. A recent study from Stieglitz and colleagues have such a design, with curved tapering at the point of probe thickness change, however insertion success and chronic performance data is lacking for the probe (Hassler et al., 2011).

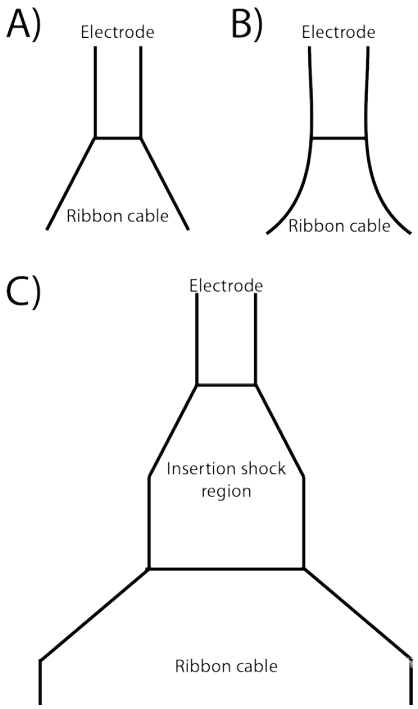

Figure 6.3. Illustrative potential electrode redesigns to minimise electrode breakages during insertion. Two electrode re-designs are considered from the original design (A) for the electrode-ribbon interface. The first is with curved tapering (B) and the second includes a ribbon cable extension with an insertion shock region (C).

6.7 Electrode recording site optimisation

Recent literature suggests that recording site location at the tip or around the edge, rather than centrally located on a probe is optimal for chronic recordings (Seymour et al., 2011, Stoetzner et al., 2012). Recording site location for our electrode is already optimal, with tip based sites.

Table 6.1 shows the recording site surface area for conventional electrodes.

Electrode	Recording site area (μm^2)	Impedance (kΩ)	Reference
Utah Array	1760	50-200	(Nordhausen et al., 1994)
Michigan probe	177	400-500	(Vetter et al., 2004)
Microwire (50 µm)	1963	200-400	This study
Sinusoidal	96	500-1200	This study

Table 6.1. Electrode comparison of 1 kHz impedance measurements in saline.

What is striking is that our electrode recording sites are far smaller, however they give saline-impedance values that are comparable to conventional probes. Although, this might depend on the resistivity of the metal used, other factors such as porosity and surface roughness play a role in reducing impedance (Nordhausen et al., 1994). Figure 6.4 shows an image for WTi before and after Parylene-C RIE. After the second parylene-C layer etching, the recording sites are exposed. Further etching of the first parylene-C layer is required to define the electrode shape. Thus, this leads to surface roughness and a potential increase in metal porosity and surface area, as the metal is bombarded with high-energy electrons from the RIE process during the etching of the first parylene-C layer. This is potentially an explanation for the low impedance values observed with respect to the small recording sites, due to an increase in surface area as shown by the larger grain size.

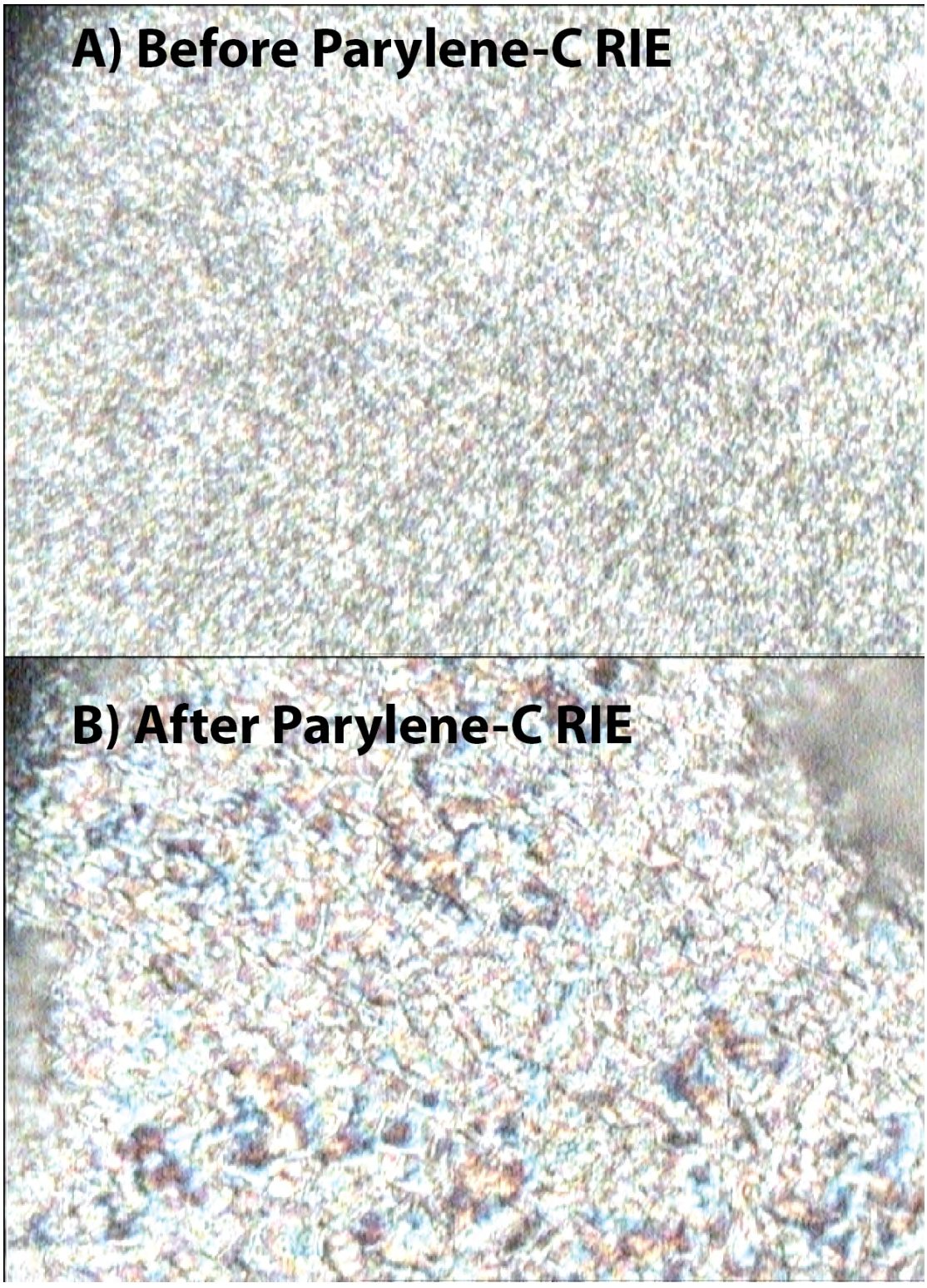

Figure 6.4. Surface area for electrode recording site is enhanced during the Parylene-C RIE process

Making the electrode into a multi-shank array is problematic, as the electrodes would need individual insertion needles attaching in a highly compact area. However, time to insert 10-12 electrodes takes 2 hours, which gives the recording capability from 30-36 channels. The electrodes can also be individually manipulated and angled to record

from multiple brain regions, and to avoid regions that are highly surface vascularised, which is beneficial for chronic performance (Kozai et al., 2010c). Electrodes of varying lengths might be useful for future designs to target deeper or shallower brain regions.

The need to make an array of electrodes is not of great necessity, as the time taken to insert individual electrodes would be acceptable for human surgery.

6.8 Electrode Flexibility Comparison

The flexibility of a neuronal probe can be estimated by using the equation to measure the stiffness of a rectangular cantilever (Seymour et al., 2011, Kozai et al., 2012a). The equation accounts for rectangular dimensionality and the materials Young's modulus; such can be fitted to most neuronal probe designs as a flexibility estimate.

The equation is:

$$\boldsymbol{k = \frac{Ewt^3}{4L^3}}$$

where E is the Young's modulus of the bulk material (Pa) , w is the beam width (m), t is thickness (m) and L the length (m). The value k in Nm^{-1}, can be calculated and compared for each intracortical electrode.

The primary electrode material determines the overall electrode stiffness. Consider our electrode with dimensions L =~ 3.2 mm, w=35 μm, t(total)=21 μm, E=2.86 GPa (Parylene-C) and 400 GPa (tungsten). A single tungsten track will have dimensions L=3.2 mm, w=5 μm, t=1 μm and E=400 GPa. This gives a k value of 1.53 $x10^{-5}$ Nm^{-1}. For three tracks this can be simplified to 3 k (tungsten), which gives 4.58 x 10^{-5} Nm^{-1}. For the parylene-C layers, the k value for 20 μm is 7.10 x 10^{-3} Nm^{-1}. Overall the stiffness of the metal is negligible, and the main material used in the electrode design (parylene-c) determines the overall probe stiffness.

Table 6.2 shows the calculated k values for most major intracortical electrode designs for a single electrode shank with electrodes ranked in flexibility order for the main contributing material in their electrode design.

Electrode Type	k/Nm^{-1}	Dimensions reference
Fish-Bone (4 mm)	6.64×10^{-4}	(Fan et al., 2011)
Sinusoidal (5 mm)	1.60×10^{-3}	This Study
Sinusoidal (3 mm)	7.10×10^{-3}	This Study
Sinusoidal (1 mm)	1.34×10^{-1}	This Study
Michigan probe (10 μm thick)	2.75×10^{-1}	(Kipke et al., 2003)
Michigan probe (15 μm thick)	9.29×10^{-1}	(Kipke et al., 2003)
MW Tungsten (5 mm)	2.25	Manufacturer Information
MW Stainless steel (5mm)	2.25	Manufacturer Information
MW Tungsten (3mm)	5.00	Manufacturer Information
Utah array (1.5 mm)	1.04×10^{1}	(Branner et al., 1999)
MW Stainless steel (3 mm)	1.04×10^{1}	Manufacturer Information
Utah array (1.0mm)	2.31×10^{1}	(Campbell et al., 1991)
Utah array (0.5 mm)	6.16×10^{1}	(Branner et al., 1999)

Table 6.2. *k*-values for major intracortical electrodes arranged in order of flexibility. MW= microwire and have 50 μm diameter. Brackets indicate probe length, unless stated otherwise.

The sinusoidal probe, at current dimensions, is more flexible than majority of the current intracortical electrodes from the estimated flexibility. The Fish-Bone electrode is the most flexible, however the use of polyimide as a dielectric is not suited for chronic application due to eventual device delamination.

By using such a measure we can estimate the effect of dimension and material changes on the overall flexibility of the sinusoidal probe for future iterations.

6.9 Chronic Recordings and Histology

The sinusoidal probe was more stable in recording parameters across the multiple indwelling periods. Interestingly, results from histology show that the sinusoidal probe elicits less of a glial response over a 6-24 month time period. Therefore this stability in recording parameters could be linked to the decrease in gliosis around the sinusoidal probe. Such a decrease in gliosis should enhance recording longevity with a decrease in overall biological noise and minimising neuronal tissue damage. The sinusoidal probe

is designed to anchor in place, with the shaft counteracting micromotion related movement. Interestingly, the movement of the shaft relative to the anchored recording tip did not seem to augment the gliosis at either the top or middle probe profile representations compared to microwire implants.

This study is the first to quantify the response of chronically implanted electrodes over a 24 month indwelling period. The overall magnitude for the glial reaction seems to expand to distances far greater than that observed in the literature, where a 12 weeks indwelling period is the extreme timepoint in rodents (Winslow et al., 2010a, Winslow and Tresco, 2010, Potter et al., 2012). This suggests that an on-going gliosis response will spread to regions far exceeding the initial electrode implant with distances > 500 μm. Therefore a reduction in gliosis is crucial for prolonging the lifetime of chronic implants in terms of recording parameter stability.

6.10 Future directions

There is an inherent need to change the animal model so that more chronic recordings can be observed and characterised for the sinusoidal probe. A different rabbit species or minipig should be considered for future studies.

Although the insertion method was successful for rabbit implantation, an automated insertion system should be considered for translational purposes in primates. Such an insertion method could rely on suction methods with electrodes placed in a pre-defined position and simply attached via a vacuum to insertion needles with strategic holes to allow for suction. Such a method will potentially reduce the time taken per electrode insertion, thus reducing surgery time.

Histology was time consuming as multiple horizontal slices and images had to be taken to analyse gliosis around the specific electrode types. Similarly, such methods offer only a snapshot for the glial response at specific time points. Interestingly, recent methods relying on two-photon microscopy have been developed to track changes to vasculature (Kozai et al., 2010b) and the glial response around electrode implants in real time (Kozai et al., 2012b). Mice containing fluorescent GFP markers for microglia (Kozai et al., 2012b) and astrocytes (Bardehle et al., 2013) have been successfully used

to track changes to glial response over chronic time periods with silicon probes and in a model of acute brain trauma. Currently, such methods only reliably allow imaging with depths up to 200 μm with the silicon implants being angled to reside within cortex at this depth. However, with advances in imaging methods, the glial response around multiple electrode types can be tracked real-time over a chronic indwelling period. This will enable a detailed understanding of the glial response to a particular electrode type.

Similarly, whole brain imaging will now be a possibility with the invention of a new histological technique known as Clear, Lipid-exchanged, Anatomically Rigid, Imaging/immunostaining compatible, Tissue hYdrogel (CLARITY) (Chung et al., 2012, Chung et al., 2013). The method relies on removing the opaque lipids in the brain and replacing them with a hydrogel for structural support purposes. Multiple staining can then be used to specifically tag different cell types by using appropriate washout methods after every specific primary and secondary antibody combination. By using one-photon microscopy it is possible to view the cell types stained. Such a whole brain staining approach may allow for unprecedented resolution and understanding of the glial response around the individual electrode types without brain slicing post-perfusion.

Both techniques may allow for a further understanding of gliosis around the sinusoidal probe over chronic indwelling periods.

Bibliography

References

Abbadie C, Bhangoo S, De Koninck Y, Malcangio M, Melik-Parsadaniantz S, White FA (2009) Chemokines and pain mechanisms. Brain Res Rev 60:125-134.

Allaman I, Gavillet M, Belanger M, Laroche T, Viertl D, Lashuel HA, Magistretti PJ (2010) Amyloid-beta aggregates cause alterations of astrocytic metabolic phenotype: impact on neuronal viability. J Neurosci 30:3326-3338.

Bardehle S, Kruger M, Buggenthin F, Schwausch J, Ninkovic J, Clevers H, Snippert HJ, Theis FJ, Meyer-Luehmann M, Bechmann I, Dimou L, Gotz M (2013) Live imaging of astrocyte responses to acute injury reveals selective juxtavascular proliferation. Nat Neurosci.

Barranco VP, Solomon H (1973) Eczematous dermatitis caused by internal exposure to nickel. South Med J 66:447-448.

Bartels J, Andreasen D, Ehirim P, Mao H, Seibert S, Wright EJ, Kennedy P (2008) Neurotrophic electrode: method of assembly and implantation into human motor speech cortex. J Neurosci Methods 174:168-176.

Beck H, Semisch M, Culmsee C, Plesnila N, Hatzopoulos AK (2008) Egr-1 regulates expression of the glial scar component phosphacan in astrocytes after experimental stroke. Am J Pathol 173:77-92.

Bekar LK, He W, Nedergaard M (2008) Locus coeruleus alpha-adrenergic-mediated activation of cortical astrocytes in vivo. Cereb Cortex 18:2789-2795.

Biber K, Vinet J, Boddeke HW (2008) Neuron-microglia signaling: chemokines as versatile messengers. J Neuroimmunol 198:69-74.

Biran R, Martin DC, Tresco PA (2005) Neuronal cell loss accompanies the brain tissue response to chronically implanted silicon microelectrode arrays. Exp Neurol 195:115-126.

Biran R, Martin DC, Tresco PA (2007) The brain tissue response to implanted silicon microelectrode arrays is increased when the device is tethered to the skull. J Biomed Mater Res A 82:169-178.

Bjornsson CS, Oh SJ, Al-Kofahi YA, Lim YJ, Smith KL, Turner JN, De S, Roysam B, Shain W, Kim SJ (2006) Effects of insertion conditions on tissue strain and vascular damage during neuroprosthetic device insertion. J Neural Eng 3:196-207.

Blau A, Murr A, Wolff S, Sernagor E, Medini P, Iurilli G, Ziegler C, Benfenati F (2011) Flexible, all-polymer microelectrode arrays for the capture of cardiac and neuronal signals. Biomaterials 32:1778-1786.

Borkholder D (1998) Cell Based Biosensors using microelectrodes. Stanford University PhD Thesis.

Borton DA, Yin M, Aceros J, Nurmikko A (2013) An implantable wireless neural interface for recording cortical circuit dynamics in moving primates. J Neural Eng 10:026010.

Brambilla R, Persaud T, Hu X, Karmally S, Shestopalov VI, Dvoriantchikova G, Ivanov D, Nathanson L, Barnum SR, Bethea JR (2009) Transgenic inhibition of astroglial NF-kappa B improves functional outcome in experimental autoimmune encephalomyelitis by suppressing chronic central nervous system inflammation. J Immunol 182:2628-2640.

Branner A, Stein RB, Normann RA (1999) Selective stimulation and recording using a slanted multielectrode array. In: [Engineering in Medicine and Biology, 1999 21st Annual Conf and the 1999 Annual Fall Meeting of the Biomedical Engineering Soc] BMES/EMBS Conference, 1999 Proceedings of the First Joint, vol. 1, p 377 vol.371.

Buzsaki G, Anastassiou CA, Koch C (2012) The origin of extracellular fields and currents--EEG, ECoG, LFP and spikes. Nat Rev Neurosci 13:407-420.

Buzsaki G, Bickford RG, Ponomareff G, Thal LJ, Mandel R, Gage FH (1988) Nucleus basalis and thalamic control of neocortical activity in the freely moving rat. J Neurosci 8:4007-4026.

Calkins MJ, Vargas MR, Johnson DA, Johnson JA (2010) Astrocyte-specific overexpression of Nrf2 protects striatal neurons from mitochondrial complex II inhibition. Toxicol Sci 115:557-568.

Campbell PK, Jones KE, Huber RJ, Horch KW, Normann RA (1991) A silicon-based, three-dimensional neural interface: manufacturing processes for an intracortical electrode array. IEEE Trans Biomed Eng 38:758-768.

Cao X, Zhang Y, Zou L, Xiao H, Chu Y, Chu X (2010) Persistent oxygen-glucose deprivation induces astrocytic death through two different pathways and calpain-mediated proteolysis of cytoskeletal proteins during astrocytic oncosis. Neurosci Lett.

Capadona JR, Shanmuganathan K, Tyler DJ, Rowan SJ, Weder C (2008) Stimuli-responsive polymer nanocomposites inspired by the sea cucumber dermis. Science 319:1370-1374.

Chen Y, Miles DK, Hoang T, Shi J, Hurlock E, Kernie SG, Lu QR (2008) The basic helix-loop-helix transcription factor olig2 is critical for reactive astrocyte proliferation after cortical injury. J Neurosci 28:10983-10989.

Chen YY, Lai HY, Lin SH, Cho CW, Chao WH, Liao CH, Tsang S, Chen YF, Lin SY (2009) Design and fabrication of a polyimide-based microelectrode array: application in neural recording and repeatable electrolytic lesion in rat brain. J Neurosci Methods 182:6-16.

Choi MS, Cho KS, Shin SM, Ko HM, Kwon KJ, Shin CY, Ko KH (2010) ATP induced microglial cell migration through non-transcriptional activation of matrix metalloproteinase-9. Arch Pharm Res 33:257-265.

Chung K, Kim S, Zalocusky KA, Mattis JH, Gradinaru S, Kalyanasundaram SM, Pak SM, Ramakrishnan C, Mirzabekov JJ, Deisseroth K (2012) Clarity: Technology for rapid, whole, intact-brain imaging with molecular phenotyping. Society for Neuroscience, Annual Meeting 2012 208.10/DDD53.

Chung K, Wallace J, Kim SY, Kalyanasundaram S, Andalman AS, Davidson TJ, Mirzabekov JJ, Zalocusky KA, Mattis J, Denisin AK, Pak S, Bernstein H, Ramakrishnan C, Grosenick L, Gradinaru V, Deisseroth K (2013) Structural and molecular interrogation of intact biological systems. Nature.

Cogan SF (2008) Neural stimulation and recording electrodes. Annu Rev Biomed Eng 10:275-309.

Conover JC, Doetsch F, Garcia-Verdugo JM, Gale NW, Yancopoulos GD, Alvarez-Buylla A (2000) Disruption of Eph/ephrin signaling affects migration and proliferation in the adult subventricular zone. Nat Neurosci 3:1091-1097.

de Jong EK, Dijkstra IM, Hensens M, Brouwer N, van Amerongen M, Liem RS, Boddeke HW, Biber K (2005) Vesicle-mediated transport and release of CCL21 in endangered neurons: a possible explanation for microglia activation remote from a primary lesion. J Neurosci 25:7548-7557.

Desai SA, Rolston JD, Guo L, Potter SM (2010) Improving impedance of implantable microwire multi-electrode arrays by ultrasonic electroplating of durable platinum black. Frontiers in Neuroengineering 3:1-11.

Di Giorgio FP, Carrasco MA, Siao MC, Maniatis T, Eggan K (2007) Non-cell autonomous effect of glia on motor neurons in an embryonic stem cell-based ALS model. Nat Neurosci 10:608-614.

Dickey AS, Suminski A, Amit Y, Hatsopoulos NG (2009) Single-unit stability using chronically implanted multielectrode arrays. J Neurophysiol 102:1331-1339.

Edell DJ, Toi VV, McNeil VM, Clark LD (1992) Factors influencing the biocompatibility of insertable silicon microshafts in cerebral cortex. IEEE Trans Biomed Eng 39:635-643.

Ejserholm F, Kohler P, Bengtsson M, Jorntell H, Schouenborg J, Wallman L (2011) A polymer based electrode array for recordings in the cerebellum. In: Neural Engineering (NER), 2011 5th International IEEE/EMBS Conference on, pp 376-379.

Fan W, Maesoon I, Euisik Y (2011) A flexible fish-bone-shaped neural probe strengthened by biodegradable silk coating for enhanced biocompatibility. In: Solid-State Sensors, Actuators and Microsystems Conference (TRANSDUCERS), 2011 16th International, pp 966-969.

Farina C, Aloisi F, Meinl E (2007) Astrocytes are active players in cerebral innate immunity. Trends Immunol 28:138-145.

Fawcett JW, Asher RA (1999) The glial scar and central nervous system repair. Brain Res Bull 49:377-391.

Fetz EE (1999) Real-time control of a robotic arm by neuronal ensembles. Nat Neurosci 2:583-584.

Figiel M, Maucher T, Rozyczka J, Bayatti N, Engele J (2003) Regulation of glial glutamate transporter expression by growth factors. Exp Neurol 183:124-135.

Freeman DK, Heine WF, Passaglia CL (2010) Single-unit in vivo recordings from the optic chiasm of rat. J Vis Exp.

Gadea A, Schinelli S, Gallo V (2008) Endothelin-1 regulates astrocyte proliferation and reactive gliosis via a JNK/c-Jun signaling pathway. J Neurosci 28:2394-2408.

Geddes LA (1997) Historical evolution of circuit models for the electrode-electrolyte interface. Ann Biomed Eng 25:1-14.

Geddes LA, Roeder R (2003) Criteria for the selection of materials for implanted electrodes. Ann Biomed Eng 31:879-890.

George PM, Lyckman AW, Lavan DA, Hegde A, Leung Y, Avasare R, Testa C, Alexander PM, Langer R, Sur M (2005) Fabrication and biocompatibility of polypyrrole implants suitable for neural prosthetics. Biomaterials 26:3511-3519.

Giaume C, Koulakoff A, Roux L, Holcman D, Rouach N (2010) Astroglial networks: a step further in neuroglial and gliovascular interactions. Nat Rev Neurosci 11:87-99.

Gilletti A, Muthuswamy J (2006) Brain micromotion around implants in the rodent somatosensory cortex. J Neural Eng 3:189-195.

Gould HJ, 3rd (1986) Body surface maps in the somatosensory cortex of rabbit. J Comp Neurol 243:207-233.

Gray CM, Maldonado PE, Wilson M, McNaughton B (1995) Tetrodes markedly improve the reliability and yield of multiple single-unit isolation from multi-unit recordings in cat striate cortex. J Neurosci Methods 63:43-54.

Green RA, Lovell NH, Wallace GG, Poole-Warren LA (2008) Conducting polymers for neural interfaces: challenges in developing an effective long-term implant. Biomaterials 29:3393-3399.

Griffith RW, Humphrey DR (2006) Long-term gliosis around chronically implanted platinum electrodes in the Rhesus macaque motor cortex. Neurosci Lett 406:81-86.

Gris P, Tighe A, Levin D, Sharma R, Brown A (2007) Transcriptional regulation of scar gene expression in primary astrocytes. Glia 55:1145-1155.

Hamilton NB, Attwell D (2010) Do astrocytes really exocytose neurotransmitters? Nat Rev Neurosci 11:227-238.

Harris JP, Capadona JR, Miller RH, Healy BC, Shanmuganathan K, Rowan SJ, Weder C, Tyler DJ (2011a) Mechanically adaptive intracortical implants improve the proximity of neuronal cell bodies. J Neural Eng 8:066011.

Harris JP, Hess AE, Rowan SJ, Weder C, Zorman CA, Tyler DJ, Capadona JR (2011b) In vivo deployment of mechanically adaptive nanocomposites for intracortical microelectrodes. J Neural Eng 8:046010.

Hassibi A, Navid R, Dutton RW, Lee TH (2004) Comprehensive study of noise processes in electrode electrolyte interfaces. Journal of Applied Physics 96:1074-1082.

Hassler C, Guy J, Nietzschmann M, Staiger JF, Stieglitz T (2011) Chronic intracortical implantation of saccharose-coated flexible shaft electrodes into the cortex of rats. In: Engineering in Medicine and Biology Society,EMBC, 2011 Annual International Conference of the IEEE, pp 644-647.

Hatsopoulos NG, Donoghue JP (2009) The science of neural interface systems. Annu Rev Neurosci 32:249-266.

He W, McConnell GC, Bellamkonda RV (2006) Nanoscale laminin coating modulates cortical scarring response around implanted silicon microelectrode arrays. J Neural Eng 3:316-326.

Herrmann JE, Imura T, Song B, Qi J, Ao Y, Nguyen TK, Korsak RA, Takeda K, Akira S, Sofroniew MV (2008) STAT3 is a critical regulator of astrogliosis and scar formation after spinal cord injury. J Neurosci 28:7231-7243.

Hess AE, Capadona JR, Shanmuganathan K, Hsu L, Rowan SJ, Weder C, Tyler DJ, Zorman CA (2011) Development of a stimuli-responsive polymer nanocomposite toward biologically optimized, MEMS-based neural probes. Journal of Micromechanics and Microengineering 21:054009.

Hetke JF, Lund JL, Najafi K, Wise KD, Anderson DJ (1994) Silicon ribbon cables for chronically implantable microelectrode arrays. IEEE Trans Biomed Eng 41:314-321.

Hochberg LR, Bacher D, Jarosiewicz B, Masse NY, Simeral JD, Vogel J, Haddadin S, Liu J, Cash SS, van der Smagt P, Donoghue JP (2012) Reach and grasp by people with tetraplegia using a neurally controlled robotic arm. Nature 485:372-375.

Hochberg LR, Serruya MD, Friehs GM, Mukand JA, Saleh M, Caplan AH, Branner A, Chen D, Penn RD, Donoghue JP (2006) Neuronal ensemble control of prosthetic devices by a human with tetraplegia. Nature 442:164-171.

Hoogerwerf AC, Wise KD (1991) A three-dimensional neural recording array. In: Solid-State Sensors and Actuators, 1991 Digest of Technical Papers, TRANSDUCERS '91, 1991 International Conference on, pp 120-123.

Hoogerwerf AC, Wise KD (1994) A three-dimensional microelectrode array for chronic neural recording. Biomedical Engineering, IEEE Transactions on 41:1136-1146.

Huang R, Tai YC (2009) Parylene to silicon adhesion enhancement. In: Solid-State Sensors, Actuators and Microsystems Conference, 2009 TRANSDUCERS 2009 International, pp 1027-1030.
Hubel DH (1957) Tungsten Microelectrode for Recording from Single Units. Science 125:549-550.
Hubel DH (1959) Single unit activity in striate cortex of unrestrained cats. J Physiol 147:226-238.
Hubel DH, Wiesel TN (1959) Receptive fields of single neurones in the cat's striate cortex. J Physiol 148:574-591.
Inoue K (2007) UDP facilitates microglial phagocytosis through P2Y6 receptors. Cell Adh Migr 1:131-132.
Jackson A, Fetz EE (2007) Compact movable microwire array for long-term chronic unit recording in cerebral cortex of primates. J Neurophysiol 98:3109-3118.
John GR, Lee SC, Brosnan CF (2003) Cytokines: powerful regulators of glial cell activation. Neuroscientist 9:10-22.
John GR, Lee SC, Song X, Rivieccio M, Brosnan CF (2005) IL-1-regulated responses in astrocytes: relevance to injury and recovery. Glia 49:161-176.
Jones KJ, Korb E, Kundel MA, Kochanek AR, Kabraji S, McEvoy M, Shin CY, Wells DG (2008) CPEB1 regulates beta-catenin mRNA translation and cell migration in astrocytes. Glia 56:1401-1413.
Kato YX, Maki K, Furukawa S, Kashino M (2008) A photosensitive polyimide based method for an easy fabrication of multichannel neural electrodes. Conf Proc IEEE Eng Med Biol Soc 2008:5802-5805.
Kato YX, Saito I, Takano H, Mabuchi K, Hoshino T (2009) Comparison of neuronal cell adhesiveness of materials in the diX (Parylene) family. Neurosci Lett 464:26-28.
Kawano T, Kunz A, Abe T, Girouard H, Anrather J, Zhou P, Iadecola C (2007) iNOS-derived NO and nox2-derived superoxide confer tolerance to excitotoxic brain injury through peroxynitrite. Journal of Cerebral Blood Flow and Metabolism 27:1453-1462.
Kazemi M, Basham E, Sivaprakasam M, Wang G, Rodger D, Weiland J, Tai YC, Liu W, Humayun M (2004) A test microchip for evaluation of hermetic packaging technology for biomedical prosthetic implants. Conf Proc IEEE Eng Med Biol Soc 6:4093-4095.
Kennedy PR (1989) The cone electrode: a long-term electrode that records from neurites grown onto its recording surface. J Neurosci Methods 29:181-193.
Kennedy PR, Bakay RA (1998) Restoration of neural output from a paralyzed patient by a direct brain connection. Neuroreport 9:1707-1711.
Kennedy PR, Mirra SS, Bakay RA (1992) The cone electrode: ultrastructural studies following long-term recording in rat and monkey cortex. Neurosci Lett 142:89-94.
Khuda, II, Koide N, Noman AS, Dagvadorj J, Tumurkhuu G, Naiki Y, Komatsu T, Yoshida T, Yokochi T (2009) Astrocyte elevated gene-1 (AEG-1) is induced by lipopolysaccharide as toll-like receptor 4 (TLR4) ligand and regulates TLR4 signalling. Immunology 128:e700-706.
Kim DH, Martin DC (2006) Sustained release of dexamethasone from hydrophilic matrices using PLGA nanoparticles for neural drug delivery. Biomaterials 27:3031-3037.
Kim S, Bhandari R, Klein M, Negi S, Rieth L, Tathireddy P, Toepper M, Oppermann H, Solzbacher F (2009) Integrated wireless neural interface based on the Utah electrode array. Biomed Microdevices 11:453-466.

Kim S, Normann RA, Harrison R, Solzbacher F (2006) Preliminary study of the thermal impact of a microelectrode array implanted in the brain. Conf Proc IEEE Eng Med Biol Soc 1:2986-2989.

Kim S, Tathireddy P, Normann RA, Solzbacher F (2007) Thermal impact of an active 3-D microelectrode array implanted in the brain. IEEE Trans Neural Syst Rehabil Eng 15:493-501.

Kipke DR, Vetter RJ, Williams JC, Hetke JF (2003) Silicon-substrate intracortical microelectrode arrays for long-term recording of neuronal spike activity in cerebral cortex. IEEE Trans Neural Syst Rehabil Eng 11:151-155.

Kitzmiller JP, Hansford DJ, Fortin LD, Obrietan KH, Bergdall VK, Beversdorf DQ (2007) Micro-field evoked potentials recorded from the porcine sub-dural cortical surface utilizing a microelectrode array. J Neurosci Methods 162:155-161.

Koehler RC, Gebremedhin D, Harder DR (2006) Role of astrocytes in cerebrovascular regulation. J Appl Physiol 100:307-317.

Kohler P, Linsmeier CE, Thelin J, Bengtsson M, Jorntell H, Garwicz M, Schouenborg J, Wallman L (2009) Flexible multi electrode brain-machine interface for recording in the cerebellum. In: Engineering in Medicine and Biology Society, 2009 EMBC 2009 Annual International Conference of the IEEE, pp 536-538.

Koizumi S, Shigemoto-Mogami Y, Nasu-Tada K, Shinozaki Y, Ohsawa K, Tsuda M, Joshi BV, Jacobson KA, Kohsaka S, Inoue K (2007) UDP acting at P2Y6 receptors is a mediator of microglial phagocytosis. Nature 446:1091-1095.

Koyama S, Chase SM, Whitford AS, Velliste M, Schwartz AB, Kass RE (2009) Comparison of brain-computer interface decoding algorithms in open-loop and closed-loop control. Journal of Computational Neuroscience 1-15.

Kozai TD, Kipke DR (2009) Insertion shuttle with carboxyl terminated self-assembled monolayer coatings for implanting flexible polymer neural probes in the brain. J Neurosci Methods 184:199-205.

Kozai TD, Langhals NB, Patel PR, Deng X, Zhang H, Lahann J, Kotov N, Kipke DR (2010a) In vivo chronic cortical recordings using novel ultra-small carbon fiber based implantable microthread ultramicroelectrodes. Society for Neuroscience Annual Meeting 2010 227.6.

Kozai TD, Langhals NB, Patel PR, Deng X, Zhang H, Smith KL, Lahann J, Kotov NA, Kipke DR (2012a) Ultrasmall implantable composite microelectrodes with bioactive surfaces for chronic neural interfaces. Nat Mater 11:1065-1073.

Kozai TD, Marzullo TC, Hooi F, Langhals NB, Majewska AK, Brown EB, Kipke DR (2010b) Reduction of neurovascular damage resulting from microelectrode insertion into the cerebral cortex using in vivo two-photon mapping. J Neural Eng 7:046011.

Kozai TD, Vazquez AL, Weaver CL, Kim SG, Cui XT (2012b) In vivo two-photon microscopy reveals immediate microglial reaction to implantation of microelectrode through extension of processes. J Neural Eng 9:066001.

Kozai TDY, Marzullo TC, Hooi F, Langhals NB, Majewska AK, Brown EB, Kipke DR (2010c) Reduction of neurovascular damage resulting from microelectrode insertion into the cerebral cortex using in vivo two-photon mapping. Journal of Neural Engineering 7.

Kruger J, Caruana F, Volta RD, Rizzolatti G (2010) Seven years of recording from monkey cortex with a chronically implanted multiple microelectrode. Front Neuroeng 3:6.

LaManna JC, McCracken KA, Patil M, Prohaska OJ (1989) Stimulus-activated changes in brain tissue temperature in the anesthetized rat. Metab Brain Dis 4:225-237.

Lee HS, Han J, Lee SH, Park JA, Kim KW (2010) Meteorin promotes the formation of GFAP-positive glia via activation of the Jak-STAT3 pathway. J Cell Sci 123:1959-1968.
Lee kk (2004) Polyimide-based intracortical neural implant with improved structural stiffness. J Micromech Microeng 14:32-37.
Leis JA, Bekar LK, Walz W (2005) Potassium homeostasis in the ischemic brain. Glia 50:407-416.
Li JC, Cui Y, Chan W (2013) Bootstrap confidence intervals for the mean correlation corrected for Case IV range restriction: a more adequate procedure for meta-analysis. J Appl Psychol 98:183-193.
Li LB, Toan SV, Zelenaia O, Watson DJ, Wolfe JH, Rothstein JD, Robinson MB (2006) Regulation of astrocytic glutamate transporter expression by Akt: evidence for a selective transcriptional effect on the GLT-1/EAAT2 subtype. J Neurochem 97:759-771.
Limatola C, Lauro C, Catalano M, Ciotti MT, Bertollini C, Di Angelantonio S, Ragozzino D, Eusebi F (2005) Chemokine CX3CL1 protects rat hippocampal neurons against glutamate-mediated excitotoxicity. J Neuroimmunol 166:19-28.
Lind G, Gallentoft L, Danielsen N, Schouenborg J, Pettersson LM (2012) Multiple implants do not aggravate the tissue reaction in rat brain. PLoS One 7:e47509.
Liu GJ, Nagarajah R, Banati RB, Bennett MR (2009) Glutamate induces directed chemotaxis of microglia. Eur J Neurosci 29:1108-1118.
Loeb GE, Bak MJ, Salcman M, Schmidt EM (1977a) Parylene as a chronically stable, reproducible microelectrode insulator. IEEE Trans Biomed Eng 24:121-128.
Loeb GE, Walker AE, Uematsu S, Konigsmark BW (1977b) Histological reaction to various conductive and dielectric films chronically implanted in the subdural space. J Biomed Mater Res 11:195-210.
Ludwig KA, Langhals NB, Joseph MD, Richardson-Burns SM, Hendricks JL, Kipke DR (2011) Poly(3,4-ethylenedioxythiophene) (PEDOT) polymer coatings facilitate smaller neural recording electrodes. J Neural Eng 8:014001.
Ludwig KA, Uram JD, Yang J, Martin DC, Kipke DR (2006) Chronic neural recordings using silicon microelectrode arrays electrochemically deposited with a poly(3,4-ethylenedioxythiophene) (PEDOT) film. J Neural Eng 3:59-70.
Mallard C, Wang X, Hagberg H (2009) The role of Toll-like receptors in perinatal brain injury. Clin Perinatol 36:763-772, v-vi.
Meng E, Yu-Chong T (2005) Parylene etching techniques for microfluidics and bioMEMS. In: Micro Electro Mechanical Systems, 2005 MEMS 2005 18th IEEE International Conference on, pp 568-571.
Merrill DR, Bikson M, Jefferys JG (2005) Electrical stimulation of excitable tissue: design of efficacious and safe protocols. J Neurosci Methods 141:171-198.
Miller K, Chinzei K, Orssengo G, Bednarz P (2000) Mechanical properties of brain tissue in-vivo: experiment and computer simulation. J Biomech 33:1369-1376.
Mitchell CJ, Yang G-R, Senkevich JJ (2006) Adhesion aspects of poly(p-xylylene) to SiO2 surfaces using -methacryloxypropyltrimethoxysilane as an adhesion promoter. Journal of Adhesion Science and Technology 20:1637-1647.
Moxon KA, Leiser SC, Gerhardt GA, Barbee KA, Chapin JK (2004) Ceramic-based multisite electrode arrays for chronic single-neuron recording. IEEE Trans Biomed Eng 51:647-656.
Murphy JA, Archibald ML, Chauhan BC (2010) The role of endothelin-1 and its receptors in optic nerve head astrocyte proliferation. Br J Ophthalmol.
Musa S, Welkenhuysen M, Prodanov D, Eberle W, Bartic C, Nuttin B, Borghs G (2009) In vitro and in vivo electrochemical characterization of a microfabricated neural probe. Conf Proc IEEE Eng Med Biol Soc 2009:7143-7146.

Myllymaa S, Myllymaa K, Korhonen H, Toyras J, Jaaskelainen JE, Djupsund K, Tanila H, Lappalainen R (2009) Fabrication and testing of polyimide-based microelectrode arrays for cortical mapping of evoked potentials. Biosens Bioelectron 24:3067-3072.

Najafi K, Ji J, Wise KD (1990) Scaling limitations of silicon multichannel recording probes. Biomedical Engineering, IEEE Transactions on 37:1-11.

Neary JT, Kang Y, Tran M, Feld J (2005) Traumatic injury activates protein kinase B/Akt in cultured astrocytes: role of extracellular ATP and P2 purinergic receptors. J Neurotrauma 22:491-500.

Negi S, Bhandari R, Rieth L, Solzbacher F (2010) In vitro comparison of sputtered iridium oxide and platinum-coated neural implantable microelectrode arrays. Biomed Mater 5:15007.

Nicolelis MA, Dimitrov D, Carmena JM, Crist R, Lehew G, Kralik JD, Wise SP (2003) Chronic, multisite, multielectrode recordings in macaque monkeys. Proc Natl Acad Sci U S A 100:11041-11046.

Nisbet DR, Crompton KE, Horne MK, Finkelstein DI, Forsythe JS (2008) Neural tissue engineering of the CNS using hydrogels. J Biomed Mater Res B Appl Biomater 87:251-263.

Nordhausen CT, Rousche PJ, Normann RA (1993) Chronic recordings of visually evoked responses using the utah intracortical electrode array. In: Engineering in Medicine and Biology Society, 1993 Proceedings of the 15th Annual International Conference of the IEEE, pp 1391-1392.

Nordhausen CT, Rousche PJ, Normann RA (1994) Optimizing recording capabilities of the Utah Intracortical Electrode Array. Brain Res 637:27-36.

Pang C, Cham J, Nenadic Z, Musallam S, Tai YC, Burdick J, Andersen R (2005) A new multi-site probe array with monolithically integrated parylene flexible cable for neural prostheses. Conf Proc IEEE Eng Med Biol Soc 7:7114-7117.

Patrick E, Orazem ME, Sanchez JC, Nishida T (2011) Corrosion of tungsten microelectrodes used in neural recording applications. J Neurosci Methods 198:158-171.

Pichili VB, Rao KV, Jayakumar AR, Norenberg MD (2007) Inhibition of glutamine transport into mitochondria protects astrocytes from ammonia toxicity. Glia 55:801-809.

Pocock JM, Kettenmann H (2007) Neurotransmitter receptors on microglia. Trends Neurosci 30:527-535.

Polikov VS, Tresco PA, Reichert WM (2005) Response of brain tissue to chronically implanted neural electrodes. J Neurosci Methods 148:1-18.

Potter KA, Buck AC, Self WK, Capadona JR (2012) Stab injury and device implantation within the brain results in inversely multiphasic neuroinflammatory and neurodegenerative responses. J Neural Eng 9:046020.

Purcell EK, Seymour JP, Yandamuri S, Kipke DR (2009a) In vivo evaluation of a neural stem cell-seeded prosthesis. J Neural Eng 6:026005.

Purcell EK, Singh A, Kipke DR (2009b) Alginate composition effects on a neural stem cell-seeded scaffold. Tissue Eng Part C Methods 15:541-550.

Purcell EK, Thompson DE, Ludwig KA, Kipke DR (2009c) Flavopiridol reduces the impedance of neural prostheses in vivo without affecting recording quality. J Neurosci Methods 183:149-157.

Rao KV, Panickar KS, Jayakumar AR, Norenberg MD (2005) Astrocytes protect neurons from ammonia toxicity. Neurochem Res 30:1311-1318.

Retterer ST, Smith KL, Bjornsson CS, Neeves KB, Spence AJ, Turner JN, Shain W, Isaacson MS (2004) Model neural prostheses with integrated microfluidics: a

potential intervention strategy for controlling reactive cell and tissue responses. IEEE Trans Biomed Eng 51:2063-2073.
Reyes-Haro D, Muller J, Boresch M, Pivneva T, Benedetti B, Scheller A, Nolte C, Kettenmann H (2010) Neuron-astrocyte interactions in the medial nucleus of the trapezoid body. J Gen Physiol 135:583-594.
Rhodes KE, Fawcett JW (2004) Chondroitin sulphate proteoglycans: preventing plasticity or protecting the CNS? J Anat 204:33-48.
Rietze RL, Reynolds BA (2006) Neural stem cell isolation and characterization. Methods Enzymol 419:3-23.
Robinson DA (1968) The electrical properties of metal microelectrodes. Proceedings of the IEEE 56:1065-1071.
Rohatgi P, Langhals NB, Kipke DR, Patil PG (2009) In vivo performance of a microelectrode neural probe with integrated drug delivery. Neurosurg Focus 27:E8.
Rolls A, Shechter R, Schwartz M (2009) The bright side of the glial scar in CNS repair. Nat Rev Neurosci 10:235-241.
Rousche PJ, Normann RA (1990) A System For Impact Insertion Of A 100 Electrode Array Into Cortical Tissue. In: Engineering in Medicine and Biology Society, 1990, Proceedings of the Twelfth Annual International Conference of the IEEE, pp 494-495.
Rousche PJ, Normann RA (1998) Chronic recording capability of the Utah Intracortical Electrode Array in cat sensory cortex. J Neurosci Methods 82:1-15.
Rubehn B, Stieglitz T (2007) Measurement of defects in spin coated polyimide films. Conf Proc IEEE Eng Med Biol Soc 2007:183-185.
Santos AM, Calvente R, Tassi M, Carrasco MC, Martin-Oliva D, Marin-Teva JL, Navascues J, Cuadros MA (2008) Embryonic and postnatal development of microglial cells in the mouse retina. J Comp Neurol 506:224-239.
Sasaki T, Beppu K, Tanaka KF, Fukazawa Y, Shigemoto R, Matsui K (2012) Application of an optogenetic byway for perturbing neuronal activity via glial photostimulation. Proc Natl Acad Sci U S A 109:20720-20725.
Scherberger H, Jarvis MR, Andersen RA (2005) Cortical local field potential encodes movement intentions in the posterior parietal cortex. Neuron 46:347-354.
Schmidt EM, Bak MJ , McIntosh, JS (1976) Long-term recordings from cortical neurons. Exp Neurol 52:496-506.
Schmidt EM, McIntosh JS, Bak MJ (1988) Long-term implants of Parylene-C coated microelectrodes. Med Biol Eng Comput 26:96-101.
Schwartz AB (2004) Cortical neural prosthetics. In: Annual Review of Neuroscience, vol. 27, pp 487-507.
Seymour JP, Kipke DR (2007) Neural probe design for reduced tissue encapsulation in CNS. Biomaterials 28:3594-3607.
Seymour JP, Langhals NB, Anderson DJ, Kipke DR (2011) Novel multi-sided, microelectrode arrays for implantable neural applications. Biomed Microdevices 13:441-451.
Sharma A, Rieth L, Tathireddy P, Harrison R, Oppermann H, Klein M, Topper M, Jung E, Normann R, Clark G, Solzbacher F (2011) Evaluation of the packaging and encapsulation reliability in fully integrated, fully wireless 100 channel Utah Slant Electrode Array (USEA): Implications for long term functionality. In: Solid-State Sensors, Actuators and Microsystems Conference (TRANSDUCERS), 2011 16th International, pp 1204-1207.
Sharma A, Rieth L, Tathireddy P, Harrison R, Solzbacher F (2010) Long term in vitro stability of fully integrated wireless neural interfaces based on Utah slant electrode array. Applied Physics Letters 96:073702-073702-073703.

Shimada A, Kasai N, Furukawa Y, Nyberg T, Torimitsu K (2009) Neural signal transmission measurements with a conductive polymer microelectrode array. IEEJ Transactions on Electronics, Information and Systems 129:267-271+210.

Simeral JD, Kim SP, Black MJ, Donoghue JP, Hochberg LR (2011) Neural control of cursor trajectory and click by a human with tetraplegia 1000 days after implant of an intracortical microelectrode array. J Neural Eng 8:025027.

Simpson JE, Ince PG, Lace G, Forster G, Shaw PJ, Matthews F, Savva G, Brayne C, Wharton SB (2008) Astrocyte phenotype in relation to Alzheimer-type pathology in the ageing brain. Neurobiol Aging 31:578-590.

Song J, Lee, S, Jung, SH, Gook, CC, Mun, MS (2009) Improved Biocompatibility of Parylene-C Films Prepared by Chemical Vapor Deposition and the Subsequent Plasma Treatment. Journal of Applied Polymer Science 112:3677–3685.

Spataro L, Dilgen J, Retterer S, Spence AJ, Isaacson M, Turner JN, Shain W (2005) Dexamethasone treatment reduces astroglia responses to inserted neuroprosthetic devices in rat neocortex. Exp Neurol 194:289-300.

Stefano L, Racchetti G, Bianco F, Passini N, Gupta RS, Panina Bordignon P, Meldolesi J (2009) The surface-exposed chaperone, Hsp60, is an agonist of the microglial TREM2 receptor. J Neurochem 110:284-294.

Stieglitz T, Meyer JU (1999) Implantable microsystems. Polyimide-based neuroprostheses for interfacing nerves. Med Device Technol 10:28-30.

Stieglitz T, Schuettler M, Rubehn B, Boretius T, Badia J, Navarro X (2011) Evaluation of polyimide as substrate material for electrodes to interface the peripheral nervous system. In: Neural Engineering (NER), 2011 5th International IEEE/EMBS Conference on, pp 529-533.

Stoetzner C, Sari-Perez A, Hullinger R, Carlson D, Wu Q, Carin.L, Seymour JP, Hetke J, Vetter RJ, Shain W, Kipke DR (2012) Investigating chronic failure of silicon microelectrodes in rodents. Society for Neuroscience, Annual Meeting 2012 277.19/NN18.

Sun SH (2010) Roles of P2X7 receptor in glial and neuroblastoma cells: the therapeutic Potential of P2X7 receptor antagonists. Mol Neurobiol 41:351-355.

Sun Y, Lacour SP, Brooks RA, Rushton N, Fawcett J, Cameron RE (2009) Assessment of the biocompatibility of photosensitive polyimide for implantable medical device use. J Biomed Mater Res A 90:648-655.

Suner S, Fellows MR, Vargas-Irwin C, Nakata GK, Donoghue JP (2005) Reliability of signals from a chronically implanted, silicon-based electrode array in non-human primate primary motor cortex. IEEE Trans Neural Syst Rehabil Eng 13:524-541.

Swadlow HA (1989) Efferent neurons and suspected interneurons in S-1 vibrissa cortex of the awake rabbit: receptive fields and axonal properties. J Neurophysiol 62:288-308.

Swadlow HA (1990) Efferent neurons and suspected interneurons in S-1 forelimb representation of the awake rabbit: receptive fields and axonal properties. J Neurophysiol 63:1477-1498.

Swadlow HA (1994) Efferent neurons and suspected interneurons in motor cortex of the awake rabbit: axonal properties, sensory receptive fields, and subthreshold synaptic inputs. J Neurophysiol 71:437-453.

Swadlow HA, Hicks TP (1996) Somatosensory cortical efferent neurons of the awake rabbit: latencies to activation via supra--and subthreshold receptive fields. J Neurophysiol 75:1753-1759.

Szarowski DH, Andersen MD, Retterer S, Spence AJ, Isaacson M, Craighead HG, Turner JN, Shain W (2003) Brain responses to micro-machined silicon devices. Brain Res 983:23-35.

Takahashi K, Rochford CD, Neumann H (2005) Clearance of apoptotic neurons without inflammation by microglial triggering receptor expressed on myeloid cells-2. J Exp Med 201:647-657.

Takano T, Oberheim N, Cotrina ML, Nedergaard M (2009) Astrocytes and ischemic injury. Stroke 40:S8-12.

Takeuchi S, Yoshida Y, Ziegler D, Mabuchi K, Suzuki T (2004) Parylene flexible neural probe with micro fluidic channel. In: Micro Electro Mechanical Systems, 2004 17th IEEE International Conference on (MEMS), pp 208-211.

Thanawala S, Palyvoda O, Georgiev DG, Khan SP, Al-Homoudi IA, Newaz G, Auner G (2007) A neural cell culture study on thin film electrode materials. J Mater Sci Mater Med 18:1745-1752.

Thelin J, Jorntell H, Psouni E, Garwicz M, Schouenborg J, Danielsen N, Linsmeier CE (2011) Implant size and fixation mode strongly influence tissue reactions in the CNS. PLoS One 6:e16267.

Vandecasteele M, M S, Royer S, Belluscio M, Berenyi A, Diba K, Fujisawa S, Grosmark A, Mao D, Mizuseki K, Patel J, Stark E, Sullivan D, Watson B, Buzsaki G (2012) Large-scale recording of neurons by movable silicon probes in behaving rodents. J Vis Exp e3568.

Vetter RJ, Williams JC, Hetke JF, Nunamaker EA, Kipke DR (2004) Chronic neural recording using silicon-substrate microelectrode arrays implanted in cerebral cortex. IEEE Trans Biomed Eng 51:896-904.

Wahjudi PN, Oh JH, Salman SO, Seabold JA, Rodger DC, Tai YC, Thompson ME (2009) Improvement of metal and tissue adhesion on surface-modified parylene C. J Biomed Mater Res A 89:206-214.

Wang Q, van Hoecke M, Tang XN, Lee H, Zheng Z, Swanson RA, Yenari MA (2009) Pyruvate protects against experimental stroke via an anti-inflammatory mechanism. Neurobiol Dis 36:223-231.

Wang X, Arcuino G, Takano T, Lin J, Peng WG, Wan P, Li P, Xu Q, Liu QS, Goldman SA, Nedergaard M (2004) P2X7 receptor inhibition improves recovery after spinal cord injury. Nat Med 10:821-827.

Ward MP, Rajdev P, Ellison C, Irazoqui PP (2009) Toward a comparison of microelectrodes for acute and chronic recordings. Brain Res 1282:183-200.

Weiland JD, Humayun MS, Eckhardt H, Ufer S, Laude L, Basinger B, Tai YC (2009) A comparison of retinal prosthesis electrode array substrate materials. In: Proceedings of the 31st Annual International Conference of the IEEE Engineering in Medicine and Biology Society: Engineering the Future of Biomedicine, EMBC 2009, pp 4140-4143.

White RL, Gross TJ (1974) Evaluation of Resistance to Electrolysis of Metals for Use in Biostimulation Microprobes. Ieee Transactions on Biomedical Engineering Bm21:487-490.

Widge AS, Jeffries-El M, Cui X, Lagenaur CF, Matsuoka Y (2007) Self-assembled monolayers of polythiophene conductive polymers improve biocompatibility and electrical impedance of neural electrodes. Biosensors and Bioelectronics 22:1723-1732.

Williams JC, Rennaker RL, Kipke DR (1999) Long-term neural recording characteristics of wire microelectrode arrays implanted in cerebral cortex. Brain Res Brain Res Protoc 4:303-313.

Williams KR, Gupta K, Wasilik M (2003) Etch rates for micromachining processing-Part II. Microelectromechanical Systems, Journal of 12:761-778.

Winslow BD, Christensen MB, Yang WK, Solzbacher F, Tresco PA (2010a) A comparison of the tissue response to chronically implanted Parylene-C-coated

and uncoated planar silicon microelectrode arrays in rat cortex. Biomaterials 31:9163-9172.

Winslow BD, Shao H, Stewart RJ, Tresco PA (2010b) Biocompatibility of adhesive complex coacervates modeled after the sandcastle glue of Phragmatopoma californica for craniofacial reconstruction. Biomaterials 31:9373-9381.

Winslow BD, Tresco PA (2010) Quantitative analysis of the tissue response to chronically implanted microwire electrodes in rat cortex. Biomaterials 31:1558-1567.

Witteveen JA, Suyatin DB, Gallentoft L, Schouenborg J, Danielsen N, Prinz CN (2010) Gelatin/glycerol coating to preserve mechanically compliant nanowire electrodes from damage during brain implantation. Journal of Vacuum Science & Technology B: Microelectronics and Nanometer Structures 28:C6K13-C16K16.

Woo MS, Park JS, Choi IY, Kim WK, Kim HS (2008) Inhibition of MMP-3 or -9 suppresses lipopolysaccharide-induced expression of proinflammatory cytokines and iNOS in microglia. J Neurochem 106:770-780.

Yong VW, Agrawal SM, Stirling DP (2007) Targeting MMPs in acute and chronic neurological conditions. Neurotherapeutics 4:580-589.

Yu Z, Tsay C, Lacour SP, Wagner S, Morrison B (2006) Stretchable microelectrode arrays--a tool for discovering mechanisms of functional deficits underlying traumatic brain injury and interfacing neurons with neuroprosthetics. Conf Proc IEEE Eng Med Biol Soc Suppl:6732-6735.